Thermal Conductivity Measurements of Thin Films using a Novel 3 Omega Method

Manuel Dominik Bogner

PhD

2017

Thermal Conductivity Measurements of Thin Films using a Novel 3 Omega Method

Manuel Dominik Bogner

A thesis submitted in partial fulfilment
of the requirements of the
University of Northumbria at Newcastle
for the degree of
Doctor of Philosophy

Research undertaken in the
Faculty of Engineering and Environment

September 2017

Declaration

I hereby declare that the work presented in this thesis has not been submitted for any other award and that it is entirely my own work. I also confirm that this work fully acknowledges ideas and contributions from the work of others. Any ethical clearance for the research presented in this thesis has been approved. Approval has been sought and granted by the University Ethics Committee (Oct/2015).

I declare that the Word Count of this Thesis is 51,266 words.

Name: Manuel Dominik Bogner

_____

Date:

_____

Acknowledgements

Firstly and foremost, I owe my heartfelt gratitude to my principle supervisor, Dr. Richard Fu, at the Northumbria University in Newcastle. Dr. Fu guided me along the stony path of doing a PhD. He pushed me, he assured me and he helped me whenever necessary; and he knew when it was necessary. He was a constant source of advice and encouragement. Constructive discussions with him and his valuable input and comments were very important to the success of my studies. I also thank the people at the Northumbria University and at the Faculty of Engineering and Environment who gave me the opportunity to do a PhD and who supported my work. I would like to express my gratitude to my second supervisor Dr. Terence Liu for his helpful modifications of my thesis.

Secondly, I would like to thank Prof. Dr. Günther Benstetter, who made my PhD studies at the Deggendorf Institute of Technology, Germany, possible. I am grateful for his guidance and his expertise and for his provision of the resources for my studies. I also thank him for his advice and valuable contributions with respect to the publications and this thesis.

I am indebted to the Deggendorf Institute of Technology, for supporting my studies in every respect. A special thank you to Prof. Dr. Werner Frammelsberger, who performed the verification of my experimental data and who was continually interested in the progress of my work.

I am grateful to all of my colleagues at the Deggendorf Institute of Technology, who supported me in many respects. My particular thanks go to my colleagues in the Institute of Quality and Material Analysis (IQMA): Edgar Lodermaier and Heiko Ranzinger, for their assistance with SEM and EDX measurements.

I would like to express my heartfelt gratitude to Dr. Chang Yang, University in Leipzig, Germany, who provided the CuI thin film samples for my thermal conductivity analysis.

Hermann Gruber from Infineon Technologies in Regensburg, Germany, deserves my thanks for providing important 3ω thin film samples.

I am grateful to my father and brother, Johann Bogner and Christian Bogner, and also my deceased grandmother, Irmgard Bogner, who always believed in me and never became tired of supporting me and without whom I would not be who I am. I also thank my parents-in-law, Brigitte Kröninger and Alois Kröninger, for their encouragement and their support.

Finally, I would like to thank the most important person who was the greatest source of strength and inspiration, and to whom I dedicate this thesis, Nicole Kröninger, for her patience, her understanding, her love and her never-ending support during all these years.

The work was supported by the German BMBF.

Abstract

For most micro- and nanoelectronic devices based on thin films applied for effective heat dissipation and thermoelectric devices for energy harvesting, thermal management is a critical subject for their device performance and reliability. This thesis focuses on the investigation of the cross- and in-plane thermal conductivities of both high- and low-thermal conductive thin film materials. Aluminum nitride (AlN), with its high thermal conductivity, has been studied, as it is a promising candidate for effective heat conductors in microelectronic devices. Copper iodide (CuI) has also been investigated in this thesis, because of its great interest in novel energy harvesting applications with low thermal conductivity and outstanding thermoelectric properties. Thermal conductivities of thin films tend to be substantially different from those of their bulk counterparts, which is generally caused by oxygen impurities, dislocations, and grain boundary scattering, all of which can reduce the thermal conductivity of the films. These effects also influence cross- and in-plane heat conduction differently, so that the thermal conductivities of the thin films are generally anisotropic in these two directions.

Therefore, experimental work and theoretical analysis have been conducted to understand the effects of crystallinity, grain sizes, and interfacial structures of AlN and CuI films on their thermal conductivities as a function of film thickness. An improved differential multi-heater 3ω method was established and used to study the thickness-dependency of cross- and in-plane thermal conductivities of CuI and AlN thin films sputtered on p-type doped silicon substrates with film thicknesses varied between 70 - 400 nm and 100 – 1000 nm, respectively. Furthermore, our newly proposed 3ω Microscopy method, which combines the advantages of both the conventional 3ω method and atomic force microscopy (AFM) technology, was applied to quantitatively measure the local thermal conductivities of CuI and AlN thin films, with a spatial resolution in sub-micrometer range.

Results revealed that both the cross- and in-plane thermal conductivities of the CuI and AlN thin films were significantly smaller than those of their bulk counterparts. The cross- and in-plane thermal conductivities were strongly dependent on the film thickness. Both the X-ray diffraction and 3ω Microscopy results indicated that the grain size of thin films significantly affected their thermal conductivity due to the scattering effects from the grain boundaries. Finally, the 3ω Microscopy has been proven to provide additional experimental findings, which cannot be identified or detected using conventional thermal characterization methods such as the standard 3ω technique. Its good spatially-resolved resolution for quantitative local thermal characterization, its nondestructive characteristic and without a need for sample preparation, make the 3ω Microscopy a promising thermal characterization method.

Contents

List of Figures

List of Tables

List of Abbreviations and Symbols

Abbreviations

AC	Alternating electrical current
AFM	Atomic force microscopy
Al	Aluminum
AlN	Aluminum nitride
Au	Gold
BTE	Boltzmann transport equation
CuI	Copper iodide
DA	Differential operational amplifier
DC	Direct electrical current
EDX	Energy dispersive X-ray spectroscopy
FEM	Finite element method
FWHM	Full width half maximum
HF	Hydrofluoric acid
IC	Integrated circuit
IR	Infrared
LED	Light emitting diode
LSM	Laser scanning microscopy
MBE	Molecular beam epitaxy
MC	Monte Carlo
MEMS	Micro electro mechanical systems
MFP	Mean free path
Pd	Palladium
PECVD	Plasma enhanced chemical vapor deposition

PLD	Pulsed laser deposition
RF	Radio frequency
RMS	Root mean square
SAW	Surface acoustic wave
SEM	Scanning electron microscopy
Si	Silicon
Si_3N_4	Silicon nitride
SiO_2	Silicon dioxide
SThM	Scanning thermal microscopy
TCR	Temperature coefficient of resistance
TDTR	Time-domain thermoreflectance technique
Ti	Titanium
XRD	X ray diffraction spectroscopy

Greek Symbols

α	Temperature coefficient of electrical resistance
β	Line broadening at half the maximum intensity
β_{th}	Temperature coefficient of thermal conductivity
γ	Fitting constant of 3ω temperature oscillation
ε_f	Film emissivity
θ	Bragg angle
Δ	Laplace operator
λ	Thermal penetration depth
λ_{wave}	X-ray wavelength
μ_p	Hole mobility
ρ	Density
σ	Electrical conductivity
φ	Phase shift of 3ω voltage and temperature signal

ω	Angular modulation frequency

Roman Symbols

A	Area
a	Thermal diffusivity
b	Half width of the metal heater
C	Specific heat capacity per volume
c_p	Specific heat capacity
D_p	Grain size of polycrystalline thin film
d	Thickness
d_f	Film thickness
d_n	Mean size of the grain distribution
E_g	Energy bandgaps
h	Heat transfer coefficient
h_{rad}	Linearized radiation coefficient
$I(t)$	Periodical AC heating current
K	Dimensionless shape factor of Scherrer equation
K_0	Zeroth order modified Bessel function of the second kind
k	Thermal conductivity
k_0	Single crystal thermal conductivity
k_B	Boltzmann coefficient
k_e	Heat conduction dominated by electrons and/or and holes
$k_{f\parallel}$	Film in-plane thermal conductivity
$k_{f\perp}$	Film cross-plane thermal conductivity
k_{ph}	Heat conduction predominantly by phonon scattering
k_{pp}	Thermal conductivity of single crystal
k_s	Thermal conductivity of the substrate
L	Lorenz factor

l	Length of metal heater
l_0	Single crystal phonon MFP
l_g	Phonon mean free path
P	Power
P_l	Heating power per unit length
p	Hole concentration
Q	Quantity of heat
q	Heat flow
R_h	Metal strips electrical resistance
R_k	Interface thermal resistance (Kapitza resistance)
r	Radius
r_{th}	Thermal exchange radius
S	Seebeck coefficient
T	Temperature
$\Delta T_{2\omega}$	Temperature oscillation of the 3ω heater
T_0	Reference ambient temperature
T_∞	Environmental temperature
T_o	Operating temperature
t	Time
V	Voltage
V_ω	First harmonic voltage amplitude
$V_{3\omega}$	Third harmonic voltage amplitude
v	Average sound velocity
v_g	Group velocity of phonons or electrons
ZT	Thermoelectric dimensionless figure of merit

List of Publications

Journal papers:

- **M. Bogner**, A. Hofer, G. Benstetter, H. Gruber, Y.Q. Fu, Differential 3ω method for measuring thermal conductivity of AlN and Si_3N_4 thin films, **Thin Solid Films** 591 (2015) 267–270. DOI: 10.1016/j.tsf.2015.03.031

- C. Yang, D. Souchay, M. Kneiß, **M. Bogner**, H.M. Wei, M. Lorenz, O. Oeckler, G. Benstetter, Y.Q. Fu, M. Grundmann, Transparent flexible thermoelectric material based on non-toxic earth-abundant p-type copper iodide thin film, **Nature Communications** 8 (2017) 16076. DOI: 10.1038/ncomms16076

- T. Berthold, G. Benstetter, W. Frammelsberger, **M. Bogner**, R. Rodríguez, M. Nafría, Protective nanometer films for reliable Cu-Cu connections, **Microelectronics Reliability** (2017). DOI: 10.1016/j.microrel.2017.07.001

- **M. Bogner**, G. Benstetter, Y.Q. Fu, Application of a combined 3 omega-microscopy method to study the correlation between thermal properties and morphology of AlN thin films, **Scanning (Wiley)**, (planned)

- **M. Bogner**, G. Benstetter, Y.Q. Fu, Thermal Characterization of Thermoelectric Materials and Thin Films, using a Bottom Heater Geometry of the 3 Omega Technique, (planned)

- **M. Bogner**, G. Benstetter, Y.Q. Fu, Temperature dependent cross- and in-plane thermal conductivity of AlN thin films measured using differential multi-heater 3 omega technique, (planned)

Conference papers:

- **M. Bogner**, G. Benstetter, Y.Q. Fu, C. Yang, M. Grundmann: Nanoscale thermal properties of next generation transparent/flexible thermoelectric copper iodide films, **Nano Today**, (planned)

Contributions to conferences:

- **M. Bogner**, A. Hofer, G. Benstetter, H. Gruber, Y.Q. Fu, Differential 3ω method for measuring thermal conductivity of AlN and Si_3N_4 thin films, **16th International Conference on Thin Films (ICTF16)**, Dubrovnik, Croatia, October 13-16, 2014, poster presentation

- **M. Bogner**, G. Benstetter, Y.Q. Fu, Cross- and in-plane thermal conductivity of AlN thin films measured using differential 3-omega method, **8th International Conference on Technological Advances of Thin Films and Surface Coatings (ThinFilms 2016)**, Singapore, July 12-15, 2016, poster presentation

- T. Berthold, G. Benstetter, W. Frammelsberger, **M. Bogner**, R. Rodríguez, M. Nafría, Protective nanometer films for reliable Cu-Cu connections, **28th European Symposium on Reliability of Electron Devices, Failure Physics and Analysis (ESREF 2017)**, Bordeaux, France, September 25-28, 2017, presentation

- **M. Bogner**, G. Benstetter, Y.Q. Fu, C. Yang, M. Grundmann: Nanoscale thermal properties of next generation transparent/flexible thermoelectric copper iodide films, **5th Nano Today Conference**, Hawaii, USA, December 6-10, 2017, poster presentation

Chapter 1: Introduction

Advances in nanotechnology have enabled the fabrication of materials and devices with characteristic lengths that can now approach to a few nanometers. These nanostructured materials are becoming increasingly important in our daily life, because of their unusual properties that they exhibit when their length scale is scaled down. Examples of these novel nanostructures include nanotubes, nanowires, thin films and superlattices. They encompass a great number of different applications. Some well-known examples include photovoltaics, which aims at converting sunlight into direct current electricity, or thermoelectrics, which aims at transforming thermal energy from temperature gradients into electrical energy. These novel technologies seem to be promising alternatives to the increasing environmental issues and limited energy resources.

Our progressive understanding of matters' behavior at the nanoscale has enabled the successful management of electron and photon based technologies. In particular, the control of electrons in semiconductor materials resulted in the breakthrough of solid-state transistors, giving rise to all modern electronic devices [1,2]. Analogously, photonic engineering has led to fundamental changes in society, with the development of optical networks and telecommunications. The ability to effectively engineer the electromagnetic spectra is evidenced by various electromagnetic based technologies now available [3]. These applications have been developed throughout a wide range of frequencies, which extend over 16 orders of magnitudes [3]. For example, at frequencies lower than 10^6 Hz, daily life applications such as amplitude and frequency modulated radios have been developed; whereas at the frequencies higher than 10^{22} Hz, technologies such as gamma radiation imaging in nuclear medicine have also been developed [3].

As in case of electromagnetic radiation, quantum mechanics dictates that the vibrational energy must be an integer multiple of the universal quantum, which is proportional to the

frequency. The quanta of crystal lattice vibrations are called phonons [2,3]. Although innovative methods to effectively manipulate photons and electrons (the quanta of electromagnetic radiations) have been developed, satisfactory understanding and control of phonons have not been accomplished so far [3]. The main reason is that, unlike photons and electrons, interactions involving phonons of different frequencies can occur among them, i.e. producing various wavelengths [4]. This mechanism turns the prediction and control of phonon behavior into a much more challenging task.

Phonons are responsible for the conduction of sound and heat in solids [3]. Low frequency vibrations, smaller than 10^{11} Hz, correspond to sound, whereas higher frequency ones could be strongly linked with heating effects [3]. Phonons are involved practically in all types of electrical, optical, mechanical and thermal phenomena. They play a major role in heat transfer and are related to a variety of interesting mechanisms, including phase transitions, ferroelectricity and superconductivity. Advances in nanotechnology and emergence of various types of nanostructured materials have provided new possibilities to accomplish numerous degrees of control of the phononic spectrum, as shown in Figure 1.1 [3]. Thus, analysis and modulation of phonon transport may draw a new technological frontier, especially for thermal management and thermoelectric energy harvesting applications.

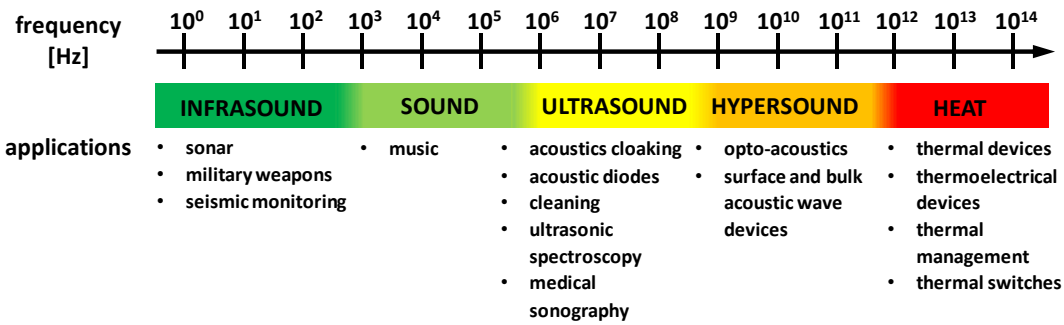

Figure 1.1: Phononic spectrum and its various application areas (adapted and modified from Ref. [3]).

1.1. Thermal management of nanoscale devices and thin films

Detailed understanding of thermal transport in low-dimensional structures is crucial, because of two technological challenges:

(1) The first one is the need of effectively dissipating the heat generated in micro- and nanoelectronic devices;

(2) The second one is associated with inhibiting heat flow in order to develop efficient thermoelectric devices, mostly based on thin films.

The continued trend of electronic industry towards miniaturization causes significant thermal issues, making heat conduction one of the most important limiting factors in electronic system design. This trend can be explained using Moore's law [5], which predicts that the number of transistors in a dense integrated circuit (IC) doubles approximately every two years (see Figure 1.2).

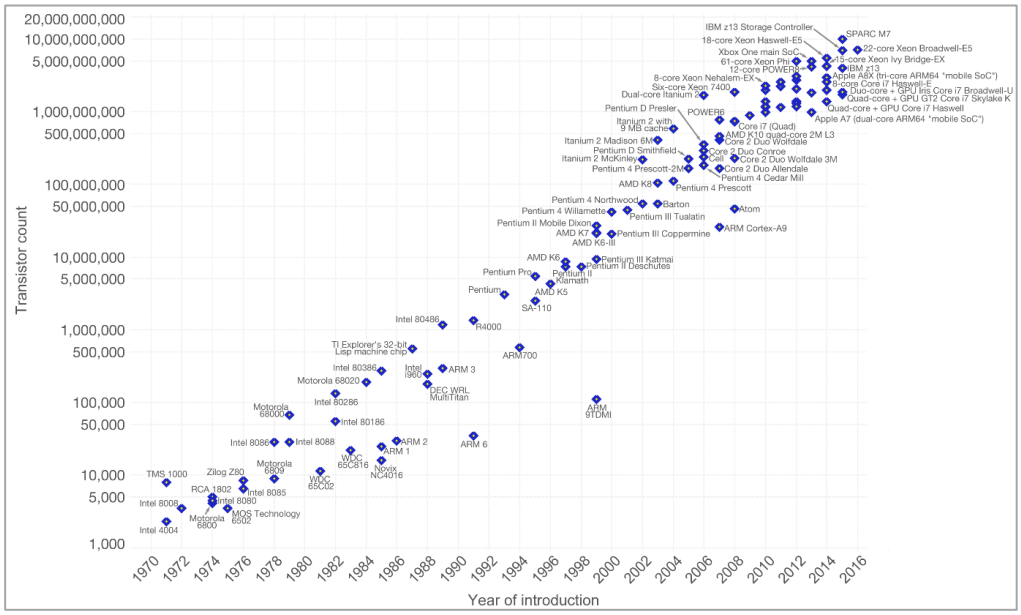

Figure 1.2: Moore's law describes the empirical regularity that the number of integrated circuits doubles approximately every two years. This advancement is important as other aspects of technological progress, such as processing speed or the price of electronic products, are strongly linked to Moore's law (adapted from Ref. [5]).

As the volume density of components in ICs is increased and the characteristic dimensions are scaled down to a few nanometers or even smaller, higher temperatures in localized volumes are reached by means of the Joule effect. The inefficient removal of heat is detrimental to the functionality, reliability and lifetime of the device. Conventional high power microelectronic devices, light emitting diodes (LEDs) and semiconductor lasers are examples of applications that undergo important thermal issues. Optimizing physical properties of their elemental components is therefore desirable to enhance heat conduction processes and overcome thermal issues. While materials with high thermal conductivity are required for thermal management applications, the opposite is true for thermoelectric devices. The performance of thermoelectric devices depends on the dimensionless figure of merit, defined as [6]:

$$ZT = \frac{S^2 \sigma}{k} T_0 \tag{1.1}$$

with σ being the electrical conductivity, S the Seebeck coefficient, T_0 the operating temperature and k the thermal conductivity [6]. Therefore, thermoelectric applications seek to impede heat transfer to ensure significantly large temperature gradients. However, materials that effectively conduct electricity and minimize thermal transport do not occur simultaneously in nature. To achieve a good thermoelectric performance, engineering material's properties is therefore often required. Phonon engineering is a research field that is recently emerged as a consequence of these needs. It aims at applying the understanding of phonon transfer to effectively manipulate the phonon spectrum and adapt the thermal properties of a material for a suitable functionality.

1.2. Thermal conduction in polycrystalline films

Performance and reliability of the above mentioned devices are strongly dependent on the thermal properties of their constitutive materials. In particular, the thermal conductivity of thin films is of critical importance, because of its strong impact on thermal performance.

Thermal conductivities of thin films could be considerably different from those of their bulk counterparts [7–13], which are generally attributed to two main reasons. Firstly, compared to the bulk crystalline materials, thin films prepared using various deposition technologies generally have many impurities, dislocations, small grain boundaries, and columnar microstructures, all of which tend to reduce their thermal conductivities [9,12–14]. Secondly, even though a film with less defects can be prepared, it is still expected to have reduced thermal conductivity due to grain boundary scattering and phonon leakage in the thin film materials. These two effects affect cross-plane and in-plane heat transport differently, so that the thermal conductivities of the thin films are generally anisotropic in these two directions, even though their bulk counterparts have isotropic properties. Therefore, precise measurements of the cross-plane ($k_{f\perp}$) and in-plane ($k_{f\parallel}$) thermal conductivities of polycrystalline thin films are critical for designing or analyzing microelectronic devices. Besides crystal quality and compositions of thin films, the interfacial structure between the film and substrate is another important factor in determining the thermal conductivity of the whole device, and is critical for the reliability and efficiency of the thin film based devices operated at high powers [12,13]. To ensure the best thermal performance of thin films, it is necessary to systematically study the relationship among the process parameters, microstructures such as crystallinity and interfacial properties, and thermal conductivity (cross- and in-plane) of the films [13].

Furthermore, frequently only the cross-plane thermal conductivities of thin films have been investigated. Measurements of the in-plane thermal conductivity of anisotropic thin films are less common than those of the cross-plane direction, and the methods used are more complex and challenging [15]. The simultaneous measurement of cross- and in-plane thermal conductivities of polycrystalline thin films without changing the sample during the measurement, to allows a precise comparison of cross- and in-plane conductivities, has neither been experimentally studied nor explained theoretically. Therefore, structural and thermal characterizations, as well as accurate theoretical description considering the size and

morphology evolutions of grains in polycrystalline films, are desired to further understand the heat transport in these materials.

This thesis reports a new approach to measure both cross- and in-plane thermal conductivities of thin films prepared on substrates, in order to investigate the thickness dependency of the thin film's thermal conductivity. Experimental work and theoretical analysis have been conducted to understand the effects of crystallinity, grain/surface crystallite sizes, and interfacial structures of thin films on their thermal conductivities. It is for the first time that both the cross- and in-plane thermal conductivities of aluminum nitride (AlN) and copper iodide (CuI) thin films were obtained using an improved differential 3ω method. In contrast to other commonly used thermal conductivity measurement methods, such as axial/radial heat flow method [16], steady-state electrical heating method [16], laser flash method [16] or transient thermoreflectance technique (TDTR) [16], the 3ω method is insensitive to radiation errors/losses, because the effective heat volume of the heat source is within the micrometer range [16,17] and it is capable to measure both in- and cross-plane thermal conductivities. Therefore, higher accuracy and better reproducibility of the film's thermal conductivity data can be obtained [13].

Because of its great interests in new technological applications, AlN has been used as a test material for high thermal conductivity applications in this study. Owing to its outstanding performance as a thermal conductor and electric insulating ceramic, AlN has been widely integrated in advanced micro- and optoelectronic devices, where it is typically exploited as a thermal management material [13]. With a thermal conductivity of about 320 $Wm^{-1}K^{-1}$ at room temperature in its bulk form [18], AlN stands as a promising solution to overcome undesirable heating effects that appear in solid-state systems [13]. Furthermore, with decreasing structural dimensions and simultaneously increasing power density of many microelectronic devices, it is urgent to use good thermally conductive and insulating thin films, such as AlN, to replace some conventional dielectric layers such as silicon dioxide

(SiO_2) and silicon nitride (Si_3N_4) [13]. Therefore, AlN is a particularly suitable candidate for our studies.

On the other hand, the increasing requirements for applications of advanced materials in energy harvesting require a fundamental understanding of the underlying physical properties, such as thermal and electrical conductivities of the respective materials. One approach to this, which has been dramatically gained in importance in recent years, is thermoelectric energy conversion [6]. This discipline deals with the motionless solid state-based conversion of temperature differences into electrical energy and vice versa. CuI thin films provide a great potential to improve thermoelectric [6,19] and optoelectronic applications [20,21], such as microscale transparent flexible thermogenerators, due to their excellent thermoelectric properties [6,19,20,22]. However, the room temperature in- and cross-plane thermal conductivity values of CuI films, which are the most critical properties for high conversion efficiency, still remain unknown and investigations are desperately needed. Therefore, the main focus of this thesis is the investigation of cross- and in-plane thermal conductivities of polycrystalline CuI thin films, as these are critical for designing and analyzing thermoelectric devices at room temperature.

1.3. Local thermal properties of thin films

The nanoscale properties of material systems are becoming more important due to the progress in material science and are necessary for the development of novel approaches of thermal management [13] and thermoelectric applications [6]. Electronics and material science have demonstrated a great demand for high-spatially resolving techniques to analyze the respective systems concerning the local quantitatively thermal characteristics [23]. This specifically local thermal characteristic is essentially for studying the heat transport in thin films. Therefore, a quantitative determination of the local thermal conductivity of thin films is mandatory within the fundamental characterizations.

Common thermal characterization techniques such as infrared (IR) thermography [24], transient thermoreflectance technique [16], and macroscopic 3ω method [10,17] have restricted laterally spatial resolution due to their optical diffraction limit or metal strips deposited at the surface of the thin film sample. These characterization methods are not capable to obtain the local thermal conductivity of thin films. Atomic force microscopy (AFM) overcomes these limits and enables to qualitatively record temperature [23] as well as thermal conductivity [23] distributions with high resolutions for both thin films and bulk materials. Modified AFM can utilize a thermo-resistive AFM probe, acting as both heat source and temperature sensor.

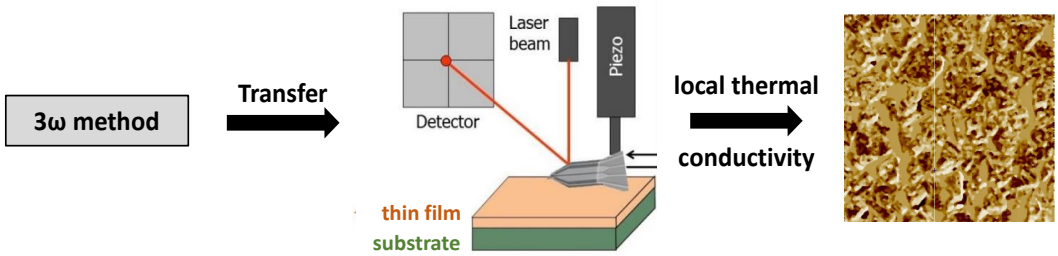

Figure 1.3: Schematic of the 3ω Microscopy technique that combines the experimental setup of an AFM with the basic 3ω principle, to quantitatively determine the local thermal conductivity of thin films.

Moreover, it has already been demonstrated that the AFM, combined with the fundamental 3ω principle, is basically capable to quantitatively determine the local thermal conductivity of bulk materials with a lateral resolution in nanometer range [25,26]. Based on these preliminary studies, we developed a new experimental technique, which merges the basic AFM and differential 3ω method in order to quantitatively determine the local thermal conductivity of thin films, as illustrated in Figure 1.3. To realize this new "3ω Microscopy" technique, the macroscopic 3ω method has been transferred to the microscopic level by combining the AFM with our extended differential 3ω method. Within this thesis, the 3ω Microscopy technique is utilized to quantitatively measure the local thermal conductivities of thin-film-on-substrate systems, in order to demonstrate its potential as an alternative thermal characterization method.

1.4. Main research goals

In brief, four major research aspects on the thermal conduction processes involved in polycrystalline thin films can be identified from the discussion above:

- Novel experimental approaches should be implemented to measure both cross- and in-plane thermal conductivities of thin films simultaneously, without changing the sample during the measurement process, in order to investigate the thickness dependency of their thermal conductivity values. Therefore, the well-established 3ω method has to be extended.

- Studying the cross- and in-plane thermal conductivity of AlN thin films, used for high thermal conductivity applications. Because of the decrease of structural dimensions and simultaneous increase of power density, it is urgent to use high thermally conductive and insulating thin films within microelectronic devices, such as AlN, to replace some traditional dielectric layers such as SiO_2 and Si_3N_4.

- Investigating the cross- and in-plane thermal conductivity of CuI thin films, used to develop novel and high efficient thermoelectric devices.

- A novel experimental technique is developed to determine the local thermal conductivity of thin films in dependence on sample properties (e.g. film thickness and surface particle size) with a high spatial resolution. To implement this specification, the macroscopic 3ω method will be transferred to the microscopic level by combining the AFM with our extended 3ω method.

1.5. Outline of the thesis

Motivated by the need of making progress towards the above four issues, this thesis was devoted to the investigation of the thermal conductivity of nanoscale thin films and explored

the possibility to measure heat transfer in cross- and in-plane direction of these low-dimensional structures.

The thesis is organized in eight chapters, devoted to study the thermal conductivity of different thin film materials. Following this introductory chapter, each chapter will start with an introduction describing the motivation, except for the final chapter, which is about summary and outlook for future work.

- In Chapter 2, a literature review of the thermal properties of thin films and the state-of-art thermal characterization methods are introduced. First, the theoretical description of heat conduction in solids is presented briefly, and the unique thermal properties of polycrystalline thin films are discussed. Then, the state-of-art thermal conductivity measurement techniques are analyzed, focusing on the ability to precisely and reproducibly measure the cross- and in-plane thermal conductivities of anisotropic thin films.

- Since the 3ω method will be the fundamental measurement principle, which has to be analyzed in the context of particular circumstances within this thesis, the functionality and history of this technique will be discussed in Chapter 3, covering the thermal conductivity determination of substrates, thin films and multilayer systems. Furthermore, we will present our novel "multi-heater" 3ω technique to simultaneously measure both cross- and in-plane thermal conductivities of thin films. This novel concept allows a more precise comparison of cross- and in-plane conductivities, compared to what is achievable with the standard in-plane methods.

- Chapter 4 provides a description of the experimental procedures used to synthesize SiO_2, Si_3N_4, AlN and CuI thin films for the 3ω measurements and characterize their structural and chemical properties. This chapter covers the deposition of the investigated thin films, the crystallographic, structural and chemical analysis methods. Finally, the modified experimental setup of our extended macroscopic and

our novel 3ω Microscopy technique are discussed, and the procedures to perform thickness-dependent thermal conductivity measurements are introduced.

- Thickness-dependent cross- and in-plane thermal conductivity measurements of SiO_2, Si_3N_4 and AlN films are studied in Chapter 5. Due to their well-known thermal properties, SiO_2 and Si_3N_4 films are used as reference materials for the 3ω method. Furthermore, experimental work and theoretical analysis have been conducted to understand the effects of crystallinity, grain/surface crystallite sizes, and interfacial structures of the AlN films on their thermal conductivities. The effect of the film-substrate interfaces on the cross- and in-plane thermal conductivities of AlN thin films is studied experimentally by our novel approach, introduced in Chapter 3.

- In Chapter 6, we analyze the thermoelectric properties of CuI thin films. This chapter is mainly focusing on the thickness dependency of the cross- and in-plane thermal conductivities of CuI films. Experimental techniques have been conducted to understand the effects of crystallinity, surface crystalline particle sizes, and interfacial structures of the CuI films on their thermal conductivity values in both cross- and in-plane directions.

- Chapter 7 introduces the novel 3ω Microscopy technique for measuring the local thermal conductivity of thin films. We present that the basic principle of the macroscopic 3ω method can be transferred to the AFM. This chapter provides the actual 3ω-AFM calibration of the thermal probe. Additionally, we develop a thermal model for the local 3ω analysis of thin films.

- Finally, Chapter 8 contains the conclusions to summarize all the results, and an outlook of the perspectives for future work is also given.

1.6. References

[1] M. Planck, On the Law of Distribution of Energy in the Normal Spectrum, Annalen der Physik und Chemie 309 (3) (1901) 553–563.

[2] H. Kragh, Max Planck: The reluctant revolutionary, Physics World 13 (12) (2000) 31–36.

[3] M. Maldovan, Sound and heat revolutions in phononics, Nature 503 (7475) (2013) 209–217.

[4] N. Li, J. Ren, L. Wang, G. Zhang, P. Hänggi, B. Li, Phononics: Manipulating heat flow with electronic analogs and beyond, Reviews of Modern Physics 84 (3) (2012) 1045–1066.

[5] G.E. Moore, Cramming more components onto integrated circuits, IEEE Solid-State Circuits Newsletter 20 (3) (2006) 33–35.

[6] C. Yang, D. Souchay, M. Kneiß, M. Bogner, H.M. Wei, M. Lorenz, O. Oeckler, G. Benstetter, Y.Q. Fu, M. Grundmann, Transparent flexible thermoelectric material based on non-toxic earth-abundant p-type copper iodide thin film, Nature communications 8 (2017) 16076.

[7] Y. Zhao, C. Zhu, S. Wang, J.Z. Tian, D.J. Yang, C.K. Chen, H. Cheng, P. Hing, Pulsed photothermal reflectance measurement of the thermal conductivity of sputtered aluminum nitride thin films, Journal of Applied Physics 96 (8) (2004) 4563–4568.

[8] P.K. Kuo, G.W. Auner, Z.L. Wu, Microstructure and thermal conductivity of epitaxial AlN thin films, Thin Solid Films 253 (1-2) (1994) 223–227.

[9] T.S. Pan, Y. Zhang, J. Huang, B. Zeng, D.H. Hong, S.L. Wang, H.Z. Zeng, M. Gao, W. Huang, Y. Lin, Enhanced thermal conductivity of polycrystalline aluminum nitride thin films by optimizing the interface structure, Journal of Applied Physics 112 (4) (2012) 44905.

[10] S.M. Lee, D.G. Cahill, Heat transport in thin dielectric films, Journal of Applied Physics 81 (6) (1997) 2590–2595.

[11] D.G. Cahill, K. Goodson, A. Majumdar, Thermometry and Thermal Transport in Micro/Nanoscale Solid-State Devices and Structures, Journal of Heat Transfer 124 (2) (2002) 223.

[12] S.R. Choi, D. Kim, S.-H. Choa, S.-H. Lee, J.-K. Kim, Thermal Conductivity of AlN and SiC Thin Films, International Journal of Thermophysics 27 (3) (2006) 896–905.

[13] M. Bogner, A. Hofer, G. Benstetter, H. Gruber, R.Y. Fu, Differential 3ω method for measuring thermal conductivity of AlN and Si3N4 thin films, Thin Solid Films 591 (2015) 267–270.

[14] G.A. Slack, R.A. Tanzilli, R.O. Pohl, J.W. Vandersande, The intrinsic thermal conductivity of AIN, Journal of Physics and Chemistry of Solids 48 (7) (1987) 641–647.

[15] C. Dames, Measuring the Thermal Conductivity of Thin Films: 3 Omega and related Electrothermal Methods, Annual Review of Heat Transfer 16 (1) (2013) 7–49.

[16] D. Zhao, X. Qian, X. Gu, S.A. Jajja, R. Yang, Measurement Techniques for Thermal Conductivity and Interfacial Thermal Conductance of Bulk and Thin Film Materials, Journal of Electronic Packaging 138 (4) (2016) 40802.

[17] D.G. Cahill, Thermal conductivity measurement from 30 to 750 K: The 3ω method, Review of Scientific Instruments 61 (2) (1990) 802–808.

[18] A. Jacquot, B. Lenoir, A. Dauscher, P. Verardi, F. Craciun, M. Stölzer, M. Gartner, M. Dinescu, Optical and thermal characterization of AlN thin films deposited by pulsed laser deposition, Applied Surface Science 186 (1-4) (2002) 507–512.

[19] C. Yang, M. Kneibeta, M. Lorenz, M. Grundmann, Room-temperature synthesized copper iodide thin film as degenerate p-type transparent conductor with a boosted figure of merit, Proceedings of the National Academy of Sciences of the United States of America 113 (46) (2016) 12929–12933.

[20] M. Grundmann, F.L. Schein, M. Lorenz, T. Böntgen, J. Lenzner, H. von Wenckstern, Cuprous iodide: A p-type transparent semiconductor, history, and novel applications, Physica status solidi A (2013) 1671-1703.

[21] G. Lin, F. Zhao, Y. Zhao, D. Zhang, L. Yang, X. Xue, X. Wang, C. Qu, Q. Li, L. Zhang, Luminescence Properties and Mechanisms of CuI Thin Films Fabricated by Vapor Iodization of Copper Films, Materials 9 (12) (2016) 990.

[22] C. Yang, M. Kneiss, F.L. Schein, M. Lorenz, M. Grundmann, Room-temperature Domain-epitaxy of Copper Iodide Thin Films for Transparent CuI/ZnO Heterojunctions with High Rectification Ratios Larger than 10(9), Scientific reports 6 (2016) 21937.

[23] S. Gomès, A. Assy, P.O. Chapuis, Scanning thermal microscopy: A review, Physica status solidi A 212 (3) (2015) 477–494.

[24] M. Grecki, J. Pacholik, B. Wiecek, A. Napieralski, Application of computer-based thermography to thermal measurements of integrated circuits and power devices, Microelectronics Journal 28 (3) (1997) 337–347.

[25] A. Altes, R. Heiderhoff, L.J. Balk, Quantitative dynamic near-field microscopy of thermal conductivity, Journal of Physics D: Applied Physics 37 (6) (2004) 952–963.

[26] G.B.M. Fiege, A. Altes, R. Heiderhoff, L.J. Balk, Quantitative thermal conductivity measurements with nanometre resolution, Journal of Physics D: Applied Physics 32 (5) (1999) 13-17.

Chapter 2: Literature Survey

2.1. Introduction

Recent advances in techniques of synthesis, processing, and microanalysis are enabling the routine production of materials with structures with the length scales down to several micro- to nanometers. Examples are nanotubes, nanowires, thin films and superlattices, widely used in micro- and nanoelectronic devices [1,2]. For most of these novel micro- and nanoelectronic devices based on thin films and nanostructured materials, thermal management is a critical subject for their device performance, and can be divided into groups of high- and low-thermal conductivity applications (see Figure 2.1) [1,2]. Materials with high thermal conductivities are needed for devices such as ICs or LEDs, where an efficient heat dissipation is required [3,4]. On the other hand, thermoelectric applications for energy harvesting such as heat barrier coatings or nanoscale thermogenerators, thin films with a very low thermal conductivity are desperately needed [5–8].

In this thesis, heat conduction processes of dielectric and semiconductive materials are studied, in which heat is predominantly transported by phonons [9], as introduced in Chapter 1. In order to investigate the thermal conductivity of thin films and nanostructures, a general understanding of fundamental heat conduction within solids is absolutely necessary. Therefore, in Section 2.2 the different heat transfer modes are presented. Then, the Fourier's law of heat conduction is given together with the boundary conditions used to solve this equation.

Section 2.3 will summarize the present understanding of thermal conduction in thin films and nanostructured materials. Then the most relevant theoretical and experimental studies concerning the characterization of thermal properties of thin films are discussed, focusing on the film thickness dependency of the thin film thermal conductivity.

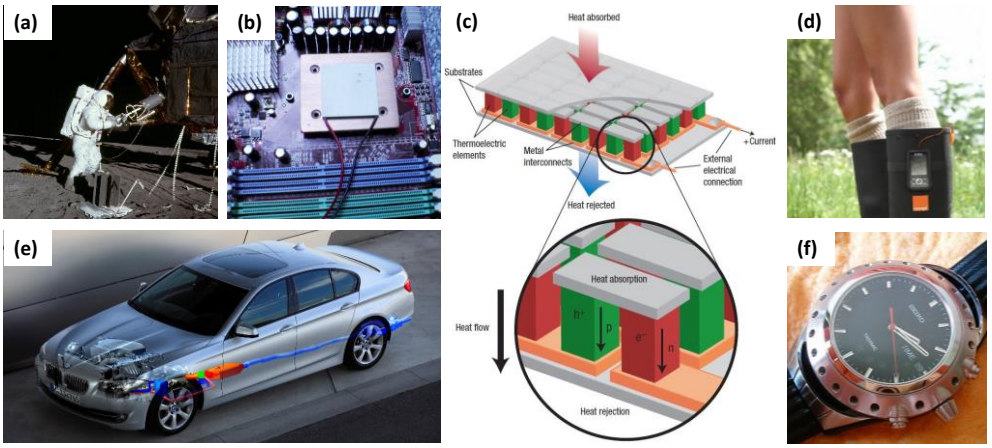

Figure 2.1: Examples of thin films and nanostructured materials used in thermal management and thermoelectric applications: (a) thermoelectric generator of Apollo 12 was used as the power source for the Apollo Lunar Surface Experiments Package [10], (b) thin films with low thermal conductivity are used in Peltier devices for thermoelectric cooling applications, (c) novel thermogenerators to efficiently convert thermal energy into electrical power [11], (d) wellington boots with a power generating sole that converts heat from feet into electrical power to charge battery-powered handhelds [12], (e) thermoelectric devices for energy recuperation used in automotive industry [13], (f) thermoelectric watch is powered by converting body temperature into electricity [14].

Even though different theoretical approaches have been developed to describe the reduced heat conduction within thin films, it is still a challenging task to measure the thermal conductivity of thin films. Accurate experimental data build the fundament for improving the thermal properties of thin films and to understand the significant influences of thin film's thickness and materials composition. For this reason, Section 2.4 summarizes the challenges of thin film thermal conductivity measurements and the state-of-the-art of experimental methods that are utilized to measure thermal conductivity of thin films. Their specific characteristics and appropriate fields of application are also discussed.

2.2. Fundamentals of general heat conduction

2.2.1. Fourier's law

The differential equations describing the distribution of heat demonstrate the most general boundary conditions and convert the special physical problems to pure analytical ones. There

is a continuing requirement of developing new materials with certain thermal characteristics, which have to be analyzed by means of improved thermal characterization methods. Of course, the motivation of this trend is the requirement for materials with improved thermal characteristics for new technical applications. Regardless of the different applications, the theory of heat by Joseph Fourier [15] is still valid, because of its fundamental characteristics. These fundamental characteristics can be expressed mathematically using the heat diffusion through solid bodies [15].

The initial point of this fundamental theory is based on experiments concerning the conduction of heat [15]. Suppose A is the dimension of a finite or infinitely small surface area of a body, which is kept at a constant temperature T. If T_0 describes the temperature of the surrounding atmosphere, and k denotes the thermal conductivity of the external part of the body, the quantity of heat dQ_a, which is transmitted through the area A into the surrounding atmosphere during the time dt is given by:

$$dQ_a = (T - T_0) \cdot k \cdot A \cdot dt \tag{2.1}$$

This law, describing the thermal transfer between a solid body into a gaseous body, is not general, since the validity is limited to small differences in temperature and to the special case where the coefficient k is constant. In spite of this limitation, the validity of this fundamental law has been confirmed by many experiments [16]. Thus, this law is directly obtained from the result of experiments. Since this law only describes the heat flow from a solid body into a gaseous one, and there is still the problem of heat conduction within solids, Fourier [15] developed an instrumental setup in order to verify his basic hypothesis by additional experiments. For these purposes, he investigated theoretically the uniform and linear conduction of heat within an infinite flat plate with defined thickness d, whose interfaces at both sides are kept at constant temperatures T_A and T_B [15]. Assuming the steady-state condition of the plate with respect to the temperatures, he was able to derive that the temperature distribution in z-direction is (see Figure 2.2) [15]:

$$T(z) = T_A + \frac{T_B - T_A}{d} \cdot z \tag{2.2}$$

Fourier's important fundamental conclusions based on Eq. (2.2) are more significant than the trivial nature of this experiment. For example, using simple mathematical relationships, he obtained the identity of the quantity of heat, which is transferred at both boundary layers of the flat plate [15].

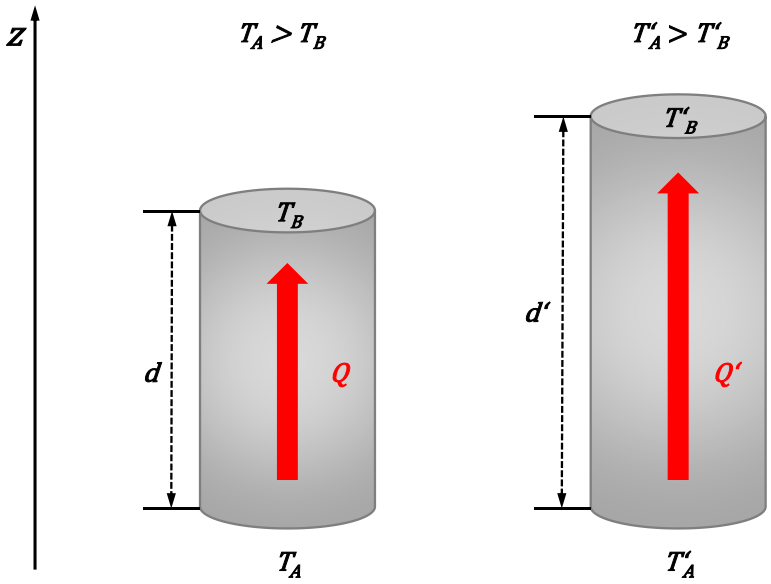

Figure 2.2: Relationship of heat flow through two objects with identical material and form but different dimensions.

In conclusion, it is possible to prove the case for the temperature distribution within the plate of infinite size in x- and y-direction and having limited thickness with its defined boundary temperatures, if the steady-state is reached. Further interpretations comparing two plates with equal thermal characteristic and shape but different values in dimensions as shown in Figure 2.2, has led to the following equation [15,16]:

$$\frac{Q}{Q'} = \frac{\frac{T_B - T_A}{d}}{\frac{T'_B - T'_A}{d'}} = \frac{d'}{d} \cdot \frac{T_A - T_B}{T'_A - T'_B} \tag{2.3}$$

Eq. (2.3) relates the two different quantities of heat Q and Q' passing through the cross-sections of the two plates and different geometries. While this equation provides the

relative relationship between the quantity of heat and the geometrical data, nevertheless, it enables us, by introducing an additional coefficient k, which is dependent of the material, to find an absolute relationship between the density of heat flow per unit time $\dot{q}$ and the according temperature gradient within the material [15,16]:

$$\dot{q} = k \cdot \frac{T_A - T_B}{d} \tag{2.4}$$

Considering the flow of heat in three dimensions, this special relationship can be presented in a more general way by using the temperature distribution between the two boundary layers of the flat plane (see Figure 2.3) out of Eq. (2.2) and finally it leads to the formulation of Fourier's law [15,16]:

$$\vec{\dot{q}} = -k \cdot gradT(x,y,z) \tag{2.5}$$

The coefficient k, which has been originally introduced as the material's specific value characterizing a certain amount of units of heat, is called the thermal conductivity. The thermal conductivity k is not a constant for a unique substance. In theory, it is assumed that the thermal conductivity does vary with temperature [17]. The thermal conductivity of metals is directly proportional to the absolute temperature and mean free path of the molecules. The mean free path decreases with the increase in temperature so that the thermal conductivity decreases with temperature [17]. It should be noted that it is valid for metals, and the presence of impurities in the metal can reverse the trend. However, when the range of temperature is limited, this change in k may be neglected. An approximation to the actual state may be obtained by making k a linear function of temperature T [18]:

$$k = k_0 \cdot [1 + \beta_{th} \cdot (T - T_0)] \tag{2.6}$$

where k_0 is the thermal conductivity at reference temperature T_0 = 0°C and β_{th} is a constant and in fact negative for most substances.

If the temperature is not within this linear regime, the thermal conductivity as a function of temperature $k(T)$ can be approximated by a higher order polynomial [18]:

$$k(T) = k_0[1 + \beta_{th}(T - T_0) + \gamma_{th}(T - T_0)^2 + \delta_{th}(T - T_0)^3 + \cdots] \quad (2.7)$$

The thermal conductivity k can differ in directions within a solid at a constant and homogeneous temperature. The mathematical description becomes more complex in the case of changing the simple geometry into complex ones, when the mathematical description in Cartesian coordinates is no longer applicable. Similarly, the mathematical description becomes more complex, if the boundary conditions are functions of time.

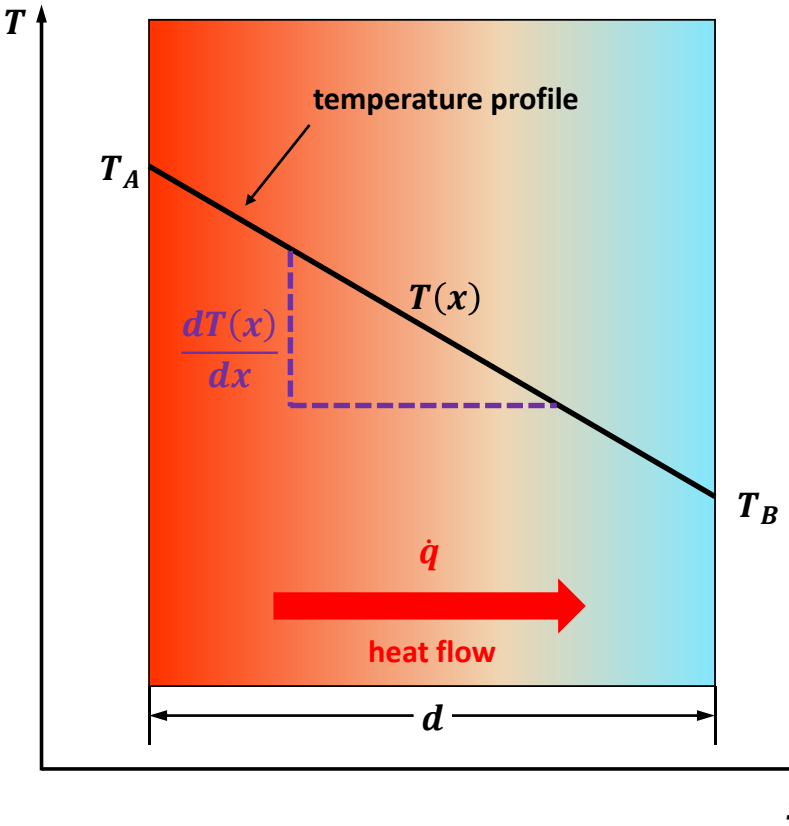

Figure 2.3: Application of Fourier's law to one-dimensional, steady-state heat conduction across a plane layer of constant thermal conductivity k and thickness d.

2.2.2. Equation of continuity

The main objective of studying heat conduction is to determine the temperature distribution and heat flow rates within a medium or to determine the rate of heat flow due to a temperature

difference between two media in contact. While the heat conduction process is visualized at the molecular level as the exchange of kinetic energy between particles in the high and low temperature regions [19], however, in the phenomenological theory of heat conduction, the molecular structure is disregarded and the heat conduction medium is assumed as a continuum [18]. Theoretical investigations in heat conduction adapted from the concept of continuum, begin with the derivation of the heat conduction equation, whereas the heat conduction equation is a mathematical relation expressed by a differential equation between temperature, space and time coordinates.

Analytical investigations in heat conduction adapted from the concept of continuum result in the equation of continuity, which is given by the following differential equation [18]:

$$div(\vec{q}) + \frac{\partial w}{\partial t} = 0 \tag{2.8}$$

where $\partial w/\partial t$ denotes the temporal variation of the heat energy density. Considering an additional heat energy being transformed within the observed volume, Eq. (2.8) must be extended to the general continuity equation of thermodynamics:

$$div(\vec{q}) + \frac{\partial w}{\partial t} = \dot{q}_E \tag{2.9}$$

Where $\dot{q}_E$ indicates the amount of heat generated per unit time and volume.

2.2.3. Relation between heat energy and temperature

To merge the equation of continuity and Fourier's law to one unique comprehensive differential equation, a third physical law, which describes the relationship between temperature and heat energy is required. Similar to Fourier's law, this equation, which relates the variation in heat density to the variation in temperature, is also a fundamental one [15]:

$$\frac{\partial w}{\partial t} = c_p \rho \frac{\partial T}{\partial t} \tag{2.10}$$

where the material specific parameters c_p, ρ denote the specific heat and density of the material, respectively.

Adding Fourier's law (Eq. 2.5), the equation of continuity Eq. (2.9) and Eq. (2.10) to the general differential equation of heat conduction finally leads to [18]:

$$c_p \rho \frac{\partial T}{\partial t} = \frac{\partial}{\partial x}\left(k_x \frac{\partial T}{\partial x}\right) + \frac{\partial}{\partial y}\left(k_y \frac{\partial T}{\partial y}\right) + \frac{\partial}{\partial z}\left(k_z \frac{\partial T}{\partial z}\right) + \dot{q}_E \tag{2.11}$$

Since only the derivative of temperature T appears in this equation, the influence of the absolute temperature can be neglected. Assuming that the material is homogenous $\left(k \neq f(x,y,z)\right)$ and isotropic $\left(k = k_x = k_y = k_z\right)$, Eq. (2.11) can be simplified by introducing the Laplace operator Δ:

$$\frac{\partial T}{\partial t} = a \cdot \Delta T + \frac{\dot{q}_E}{\rho c_p} \tag{2.12}$$

where $a = \frac{k}{\rho c_p}$ indicates the thermal diffusivity of the material.

In case of a steady-state ($\partial T / \partial t$ = 0), Eq. (2.12) can be further reduced into the well-known Poisson equation, which in the special case of volumes without sources, reduces to the so called Laplace equation [18]:

Poisson equation: $$-\Delta T = \dot{q}_E \cdot k^{-1} \tag{2.13}$$

Laplace equation: $$-\Delta T = 0 \tag{2.14}$$

The partial differential equations can now be extracted out of three fundamental physical laws, which provide a comprehensive description of the heat conduction process. Nevertheless, this mathematical description of the physical process is not sufficient yet, which becomes obvious by considering the fact that each spatial and temporal constant temperature distribution $T(x,y,z,t) = T_0$ is a solution of the above mentioned differential equations. To complete the description, it is now required to define boundary (spatial) and initial conditions (temporal).

2.2.4. Boundary conditions

To ascertain the specific temperature distribution of the investigated system, the initial point of each location of the field from which the temporal changes can be assessed has to be known first. Next, the type of interaction of those volume elements must be known, which are located directly at the surface of the entire temperature field and therefore depends on the conditions of the external ambience. These specifications permit to simplify the idealized applied model in order to minimize the complexity of the system in special cases. Because the temporal limiting condition consists of the designation of a scalar function of position $T_0(x, y, z)$, which can be assumed to be continuous or not, there are three different kinds of boundary conditions, summarized in Table 2.1 [20]:

(1) Dirichlet boundary condition:

The first physical model for the interface between the investigated system and the surrounding volume within the observed time is given by the assumption of equating the temperature distribution at the surface of the system T_S with the temperature distribution of the surrounding ambience T_A at this spatial boundary. In fact, this distribution must be defined for the entire surface, but the function itself can either be randomised, continuous or discontinuous with respect to time and space [20]. This so-called Dirichlet condition represents an ideal heat sink [20]. Within this thesis, the Dirichlet condition will be applied for the analysis of the resulting heat flow between the heat source and thin film sample, as a function of the sample's thermal conductivity.

(2) Neumann boundary condition:

While the first boundary condition defines the temperature at the surface of the investigated system, the second and third boundary condition predict the heat flow from the observed region to the outer region. The so-called Neumann boundary

condition defines the heat flow perpendicular to the particular surface element ($n^T \cdot \dot{q}$) and can be separated into the homogeneous and inhomogeneous Neumann conditions [20]. The homogeneous one defines the heat flow of zero. This represents the perfect heat insulation in the physical sense. If the perpendicular component (outwards or inwards) of the heat flow is assumed to be unequal to zero ($q_n \neq 0$) the inhomogeneous Neumann condition will be used.

(3) Robin- or Cauchy-boundary condition:

This boundary condition finally specifies the temperature of the ambience as well as a mathematical law, which allows the calculation of the heat transfer between the surface of the object and the ambience, by relating the quantity of heat dQ, which is emitted via the surface element dF with the temperature T_S during the time dt to the ambience of temperature T_A. This fundamental relationship was first postulated by Newton and the resulting boundary condition can be found usually in literature as Robin- or Cauchy-boundary condition [20]. The coefficient of proportionality h is denoted as the heat transfer coefficient and is depending on several specific characteristics, e.g. surface (smoothness or roughness) or ambient cooling medium (laminar or turbulent). In the most general case, all of the mentioned boundary conditions, which are graphically compared in Figure 2.4, can be applied to different but not necessarily connected parts of a heat conduction model.

Table 2.1: Summary of different kinds of spatial boundary conditions and comparison of resulting mathematical equations [20].

Dirichlet condition	$T_S(x,y,z,t) = T_A(x,y,z,t)$	(2.15)
Neumann condition	$n^T \cdot \dot{q} = -k\left(n_x \cdot \frac{\partial T}{\partial x} + n_y \cdot \frac{\partial T}{\partial y} + n_z \cdot \frac{\partial T}{\partial z}\right) = \dot{q}_n$ (homogeneous: $\dot{q}_n = 0$)	(2.16)
Robin or Cauchy condition	$n^T \cdot \dot{q} = -k \cdot n^T \cdot \nabla T = h \cdot (T_S - T_A)$	(2.17)

In this section, the theoretical descriptions of the most important temperature fields of the common geometrical and temporal heat source characteristics and the fundamentals of general

heat conduction in solids are derived. These descriptions build the theoretical fundamentals of our extended 3ω method and our novel 3ω Microscopy, which will be used to investigate the cross- and in-plane thermal conductivities of different thin films, substrates and multilayer-systems.

As we know, micro- and nanoscale materials, such as thin films, could have very different thermal conductivity values, since the energy carriers (phonons or electrons) can be strongly scattered by the extremely constrained feature size of the material, and their dispersion relation can also be altered. Therefore, the following section provides a review of the thermal properties of thin films and how they are constrained at nanoscale.

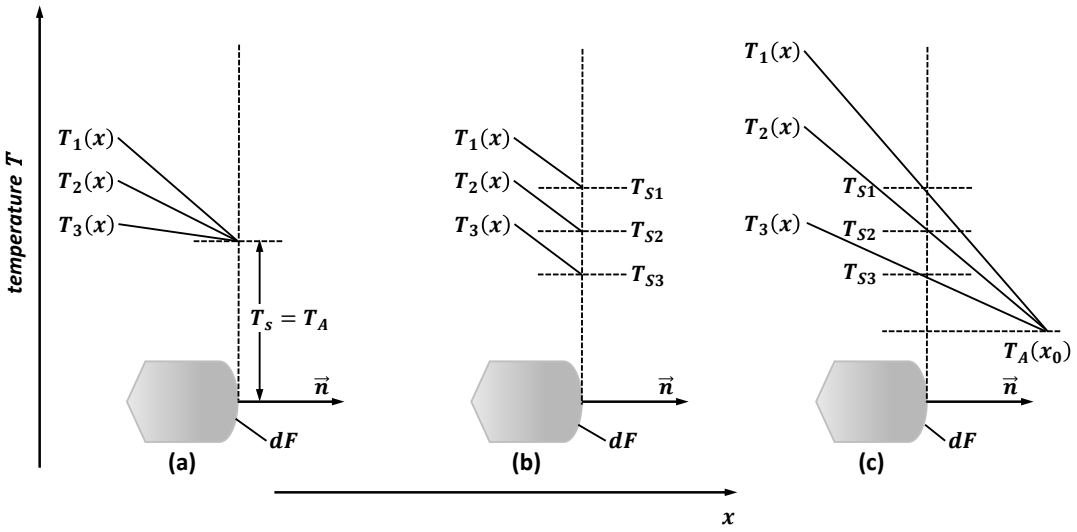

Figure 2.4: Schematic comparison of the three different kinds of boundary conditions: (a) Dirichlet condition, (b) Neumann condition and (c) Robin- or Cauchy-condition (modified from Ref. [20]).

2.3. Thermal properties of thin films

In the following sections, the theoretical advances and thermal transport mechanisms describing the thermal conductivity of polycrystalline thin films will be briefly reviewed. Then, relevant theoretical and experimental studies concerning the thermal conduction of thin films will be discussed, focusing on the thickness dependency of thin film thermal conductivity.

As explained previously, the unique structure of thin films and nanostructured materials makes their thermal properties, especially their thermal conductivity in cross- and in-plane directions, differ significantly from values of their bulk counterparts [1–4,21,22]. In the solid-state, heat conduction is mediated by free electrons and lattice vibrations, which are the harmonic motions of the atoms that form the crystalline lattice. For the electromagnetic waves, the elastic fluctuations in a crystalline solid carry certain amount of thermal energy that is quantized. These energy elements are phonons. The thermal conductivity of a solid is therefore determined by the ability of phonons and electrons to transport thermal energy as they propagate through the crystal, i.e., $k = k_{ph} + k_e$, where the subscript ph and e refer to phonons and electrons, respectively [22,23]. The classic kinetic theory of gases has been widely used to describe the thermal conductivity of metals, isolators and semiconductors, by relating it to the physical properties of their energy carriers [24]:

$$k = \frac{1}{3}\rho c_p v_g l_g \tag{2.18}$$

where ρ is the density of the material (for phonons), c_p the specific heat, v_g the group velocity of phonons or electrons, and l_g the phonons mean free path (MFP). Eq. (2.18) is the so-called "gray approximation", in which the carriers are considered frequency-independent and therefore contribute to heat conduction equally, being indistinguishable or "gray". The product of $\rho c_p v_g l_g$ is normalized over three degrees of freedom to obtain the average value in a given direction. The MFP is defined as the average distance traveled by an energy carrier before experiencing a collision [22]. While the specific heat and group velocity are not sensitive to crystallographic defects, the MFP is affected by the distortion of the crystal symmetry, and it governs the fluctuation of the thermal conductivity due to the size effects [24]. Since polycrystalline films exhibit a large volume fraction of grain boundaries, as well as other common crystallographic imperfections, their thermal conductivity can differ from that of their bulk counterparts by several orders of magnitude [1–4,21].

This thesis addresses thermal conduction in dielectric (SiO_2, Si_3N_4) and semiconductive (AlN, CuI) polycrystalline films. In dielectric or semiconductive materials, transfer of heat is predominated by phonons [9,22]. Thus, the following discussion neglects the conduction by electrons ($k_e \approx 0$), and focuses on the mechanisms by which phonon transport is affected i.e. crystal structure and the length scales involved in the studied thin film samples.

Compared to the bulk or single crystalline materials, many thin films prepared using various deposition technologies have different crystallographic defects, such as dislocations, vacancies, substitutional impurities, interstitial voids and complex grain boundaries, all of which tend to reduce the thermal conductivity of the films [1]. These crystallographic defects affect both cross- and in-plane heat transport differently, so that the thermal conductivities of the thin films are generally anisotropic in these two directions, even though their bulk counterparts have the isotropic properties (see Figure 2.5).

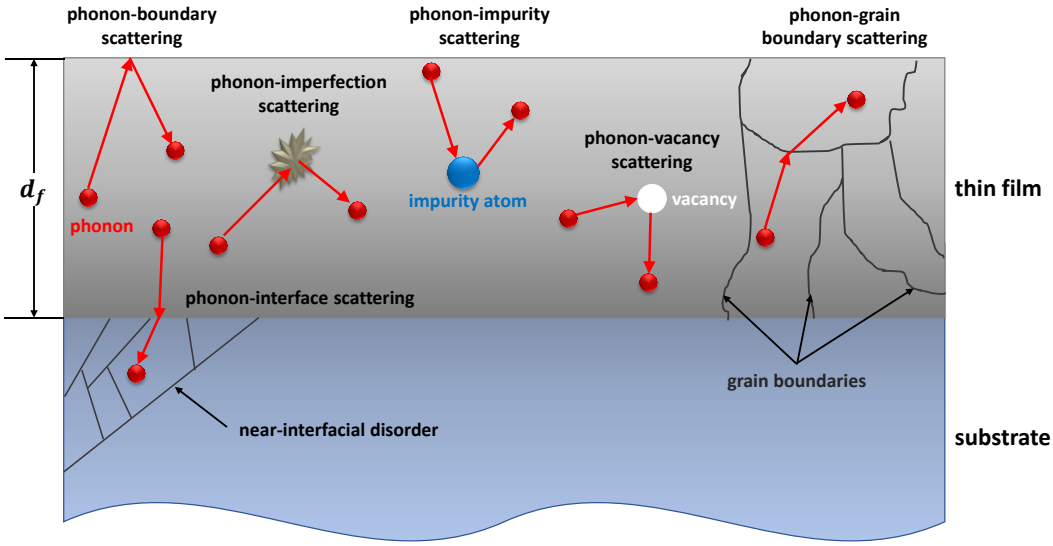

Figure 2.5: Thermal conductivity reduction of polycrystalline thin films compared to that of their corresponding single-crystal counterparts, due to scattering events between phonons and different types of crystallographic defects like phonon-boundary, phonon-impurity, phonon-vacancy, phonon-interface and phonon-grain boundary scattering (modified from Ref. [1]).

Therefore, precise measurement of the cross- and in-plane thermal conductivities of polycrystalline thin films is critical for designing microelectronic devices. Thus, in

multi-crystalline structures, besides phonon-phonon and phonon-boundary interactions, two additional scattering processes affect thermal conduction. In this case, lattice vibrations MFPs are reduced due to increased grain boundary scattering (intergranular transport) and scattering within the grains, owing to the reduced grain size (intragranular transport). The effects become more dominant as the film thickness is comparable to the length of phonon MFP [1–3,21,25].

Experimental and theoretical studies have been extensively performed in order to study the heat conduction in perfect single crystalline thin films. Despite the significant relevance of polycrystalline thin film in micro- and nanoelectronic devices, only little research has been conducted to understand and analytically describe thermal conduction in polycrystalline thin films. Most of the experimental and theoretical studies [1,26,27] reported that the grain size significantly affected the thermal conductivity of thin films due to the existence of phonon-grain-boundaries, because a smaller grain size could decrease the thermal conductivity of the film due to the shorter phonon MFP. Furthermore, Jaramillo-Fernandez *et al*. [28] demonstrated both theoretically and experimentally that cross-plane thermal conductivity was also strongly reduced by phonon-impurity scattering (e.g. oxygen impurities). Recently, Dong *et al*. [29] proposed a simple analytical model. By considering equal spherical crystallites of mean grain size d_n and including size effects, as well as diffusive scattering at grain boundaries, their analysis yields the effective thermal conductivity $k_{eff,}$ of a nanocrystalline material [29]:

$$k_{eff} = \frac{k_0 \left(1 + \frac{l_0}{d_n^{\Lambda}}\right)^{-1}}{1 + R_K \left[\frac{k_0}{(1 + l_0/d_n^{\Lambda})}\right] \cdot d_n^{-1}} \tag{2.19}$$

where k_0 is the corresponding single-crystal thermal conductivity, R_k the interface thermal resistance (Kapitza resistance) and l_0 is the single-crystal phonon MFP. To derive this expression, Dong *et al*. [29] have considered that the intragranular grain thermal conductivity $k_{intra} = k_0/(1 + l_0/d_n)$, can be expressed as an exponential function of the grain size d_n.

Thereby, Λ is an exponent ranging from ½ to ¾, according to the phenomenological theory [30]. This analytical formulation proved to be very useful, because the effective thermal conductivity of the material can be easily obtained if knowing its mean grain size, the single-crystal thermal conductivity, the single-crystal phonon MFP and the Kapitza thermal resistance. However, this formulation does not account for the distribution of the grain shape and size along the growth direction of the film. Furthermore, the model was focused on thermal properties of bulk or freestanding nanocrystalline materials, rather than film-on-substrate systems and therefore does not consider the interfacial thermal resistance between a film and its substrate. In addition, Monte Carlo (MC) [31] and Boltzmann transport equation (BTE) [22,32–34] simulations have proven to be tedious in their implementations, because the quantities that determine the lattice thermal conductivity are frequency-dependent and therefore difficult to obtain, requiring high computation time [35]. MC [31] and BTE [22,32–34] simulations are taking both thin film geometry and interfacial thermal resistance into account. From the literature review about the understanding of phonon transport inside nanocrystalline structures, it appears that early work has been focused on materials composed of equisized grains. Yet, film deposited at room temperature by physical and chemical vapor techniques generally exhibit a grained structure that increases in size and evolves in shape from the bottom to the top of the film, along the cross-plane direction [28]. The need to describe and study the thermal conductivity of polycrystalline thin films is therefore evident.

Therefore, AlN and CuI thin films were systematically investigated in Chapters 5 and 6 by characterizing their cross- and in-plane thermal conductivities, crystal structures, chemical compositions, surface morphologies and interfacial structures using an extended differential 3ω method, X-ray diffraction (XRD), energy dispersive X-ray spectroscopy (EDX), AFM and scanning electron microscopy (SEM).

2.3.1. Thermal conductivity of AlN thin films

AlN thin films have been widely used in surface acoustic wave (SAW) devices [36,37], LEDs [38], and micro-electro-mechanical systems (MEMS), because of their outstanding properties, such as high piezoelectric coupling factor, excellent dielectric properties, wide energy band gap, and high thermal conductivity [39]. With the decrease of structural dimensions and simultaneous increase of power density for many microelectronic devices, it is urgent to use high thermally conductive and insulating thin films, such as AlN, to replace some traditional dielectric layers such as SiO_2. Single crystalline AlN is one of the promising candidates for effective heat conductors in microelectronic devices due to its high thermal conductivity (320 $Wm^{-1}K^{-1}$) at room temperature [40], which makes it an ideal material to solve the thermal management problem. The bulk thermal conductivity of AlN is significantly higher than those of standard dielectric materials such as SiO_2 and Si_3N_4 [41,42].

However, thermal conductivities of thin films could be substantially different from those of their bulk counterparts [2–4,21,39,41,43,44], which are generally attributed to two main reasons. Firstly, compared to the bulk crystalline materials, many thin films prepared using deposition technologies have many impurities, dislocations, and grain boundaries, all of which tend to reduce the thermal conductivity of the films [3,4,39,42]. Secondly, even though a film with less defects can be prepared, it is still expected to have reduced thermal conductivity due to grain boundary scattering and phonon leakage in these thin film materials. These two effects affect cross- and in-plane heat transport differently, so that the thermal conductivities of the thin films are generally anisotropic in these two directions, even though their bulk counterparts have isotropic properties as mentioned on page 27. Besides crystalline quality and compositions of AlN thin films, the interfacial structure between the film and substrate is another important factor in determining the thermal conductivity of the whole device, and is critical for the reliability and efficiency of the AlN based devices operated at high powers [3,4]. To ensure the best thermal performance of AlN thin films, it is necessary

to systematically study the correlations among microstructures such as crystallinity and interfacial properties, and thermal conductivity of the films.

Very few studies have reported thermal conductivity values at room temperature of polycrystalline AlN films deposited on Si substrate by radio frequency (RF) magnetron sputtering and most of the reported values vary from 0.5 to 50 $Wm^{-1}K^{-1}$ [3,4,39,44,45]. The considerable fluctuation of published thermal conductivity values arises from a strong dependence on deposition methods, process parameters as well as the chemical purity (e.g. oxygen content) of the AlN samples [28]. Due to this fluctuation, a comparison of published thermal conductivity values should consider the deposition method and process parameters of the investigated thin films. For example Pan *et al.* [39] showed that the thermal conductivity of AlN thin films increased from 9.9 to 26.7 $Wm^{-1}K^{-1}$, if the film's growth temperature increases from 330 to 560°C. However, all of these studies showed that the cross-plane thermal conductivity values of AlN strongly depend on the film thickness [3]. Zhao *et al*. [41] analyzed their results based on the microstructure and oxygen impurities. They attributed the observed thickness dependence to the decrease of grain size and the increase of oxygen impurities as the films become thinner. Choi *et al*. [4] showed that the microstructures developed at the interfacial region near the substrate could be amorphous due to the lattice mismatch between AlN film and Si substrate. Thus, they attributed the observed trend to the low thermal conductivity in the interfacial region. Pan *et al*. [39] obtained a similar result, which showed that the thermal conductivity values of polycrystalline AlN thin films can be increased by improving the interface between the AlN film and the Si substrate.

More recently, a similar trend for the thickness dependence of the thermal conductivity has been investigated by Duquenne *et al*. [45] and Belkerk *et al*. [44], who studied the thermal properties of AlN films deposited by direct current (DC) balanced and unbalanced magnetron sputtering. The terms "balanced" and "unbalanced" refer to magnetron classification. The balanced one is the standard configuration, while the unbalanced is a technology that uses additional magnetic coils to enhance and intensify the plasma containing the ionic species

[44,45]. Because of the "unbalanced" magnetic field, this magnetron configuration results in higher energies and therefore higher temperatures involved during the deposition process. Duquenne *et al*. [45] and Belkerk *et al*. [44] showed that the balanced magnetron process yielded to thermal conductivities between 2.5 and 50 $Wm^{-1}K^{-1}$ for AlN film thicknesses between 800 and 3500 nm. On the other hand, unbalanced magnetron sputtering led to thermal conductivities between 20 and 130 $Wm^{-1}K^{-1}$ for film thickness varied from 150 to 3500 nm [44,45]. Because of the high measured values, the investigations led to highly thermally conductive AlN thin films. Similarly Choi *et al*. [4], Pan *et al*. [39] and Jaramillo-Fernandez *et al*. [28] also identified substantial differences in the microstructure near the interfacial region between the AlN film and Si substrate, which appeared to be highly disordered within a limited thickness. These studies addressed the thickness-dependence problem by attributing the increase of the cross-plane thermal conductivity with film thickness to deposition parameters, microstructure and average grain/particle size.

Although the above mentioned studies made progress by indicating qualitatively that structural features may be responsible for the changes in thermal conduction, a physical description in terms of both morphology and grain/surface crystallite sizes, along both cross- and in-plane direction of AlN thin films, has not been achieved so far and is highly desirable. Therefore, this thesis will explore a new approach to measure both cross- and in-plane thermal conductivities of AlN thin films prepared on silicon substrates using RF magnetron reactive sputtering, in order to characterize the thickness dependency of the film's thermal conductivity.

2.3.2. Thermal conductivity of CuI thin films

Controlled modulation of phonon transport in thin films promises major new technological developments. Thermal conductivity regulation and heat flow control at small scales are of great interest for a wide range of applications such as thermoelectric devices, energy harvesting applications and thermal management in micro- and nanoelectronics.

Both thermoelectric and thermal barrier applications aim to design the structure of advanced technical materials to adapt their thermal response in order to be as low as possible. One strategy consists in introducing or remove crystallographic defects, which has been confirmed to be an effective means of adjusting thermal conduction. The field of thermoelectrics has experienced remarkable advances in last decades, overcoming the impossibility to find values of the figure of merit ZT, significantly greater than unity [6,8]. Structuring thermoelectric materials at the nanoscale level has achieved surprising values of ZT. Grain boundaries are known to gently increase phonon scattering and are object of active research, in which grain sizes of nanocrystalline materials are engineered to significantly reduce the thermal conductivity and therefore increase the thermoelectric figure of merit (ZT-values) [6,46–49]. This is also valid for thermal barrier coatings, where microstructure of the film plays an important role in decreasing thermal conduction [50–52]. Substitutional impurities are the other means of disturbing the crystal symmetry, such as vacancies and dislocations, and are also used to adapt the thermal response of thin films [6,53–58].

In Chapter 6 of this thesis, we will focus on a static approach of tuning the thermal conductivity of thin films. Therefore, we will investigate the room temperature thermoelectric performances of CuI thin films, since the CuI in its ground-state phase was recently reported as a high performance p-type transparent conductor material [5–8]. Binary CuI is an environment-friendly material composed of non-toxic and naturally abundant elements, copper and iodine [8]. Present in sea water, iodine is the heaviest essential element used widely in our daily life for biological functions [8]. Interestingly, a heavy element such as iodine has a low thermal conductivity, which is necessary for a good thermoelectric performance [8].

However, in spite of these previous experimental and theoretical results, the cross- and in-plane thermal conductivities of CuI thin films, one of the most critical properties for a high thermoelectric conversion efficiency, still remain unknown and further investigations are desperately needed. Therefore, a major research goal of this thesis is the investigation of

cross- and in-plane thermal conductivities of polycrystalline CuI thin films. Therefore, experimental work and theoretical analysis have been performed to understand the effects of crystallinity, grain/surface crystalline sizes, and interfacial structures of the CuI films on their thermal conductivities. It is, for the first time, that both the cross- and in-plane thermal conductivities of CuI thin films were measured as a function of film thickness. The thermal conductivities were obtained using our differential multi-heater 3ω method technique.

Finally, the theoretical description of thermal conduction in polycrystalline thin films have been derived and different approaches to adjust the thermal conductivity of thin films have been presented. The state-of-the-art measurement techniques, which utilize the above described thermal conduction in dependence on the particular geometry and in dependence on the particular temporal characteristic of the heat source, will be discussed in the following, in order to quantitatively determine the thermal conductivity of thin films and bulk materials.

2.4. Thin film thermal conductivity characterization

Accurately experimental determination of the thermal conductivity of thin films is essential for ensuring the performance of nanoscale devices. Since the late 1980s, the scientific community, motivated by its great technological interest, has devoted tremendous efforts into the development of experimental techniques that provide precise thermal conductivity measurements of thin films and nanostructures [1,2,59–64].

Despite the important advances achieved in the past decades, thermal conductivity measurements on these structures remain a highly challenging task, due to the small heat fluxes that have to be detected and the reduced characteristic dimensions of the structures under analysis [65].

Thin films are usually deposited onto a thicker bulk substrate, which serves as the mechanical support structure. Since peeling-off them from the substrate surface is often difficult and costly, thermal measurements are frequently performed on film-on-substrate systems. The

substrate contribution has to be therefore subtracted from the measured properties of the film-on-substrate configuration, which can increase experimental uncertainties. Figure 2.6 represents the typical experimental setup used in cross-plane thermal conductivity measurements, along with associated experimental challenges for film-on-substrate configurations.

To extract the thermal conductivity of the studied film, experimental techniques typically require the determination of heat flux and/or temperature difference between two points of the specimen under analysis. For thin films, the main challenge is to create a heat flux through the film, which is sufficiently high to be detected, without inducing a large temperature increase in the substrate. The second issue is to experimentally measure the small temperature decrease across the sample thickness, which can vary from few nanometers to several microns [66].

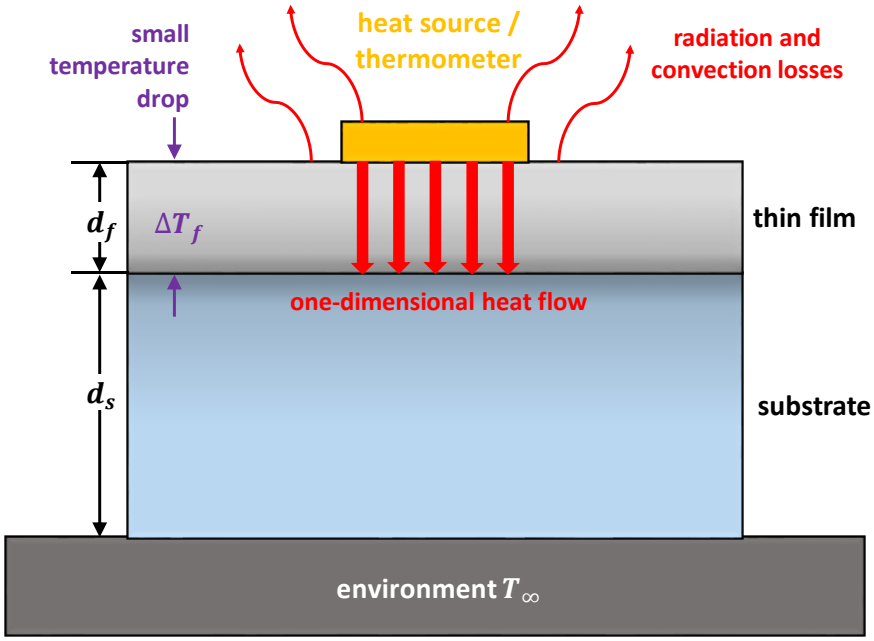

Figure 2.6: Typical experimental setup for thermal measurements on thin films and associated experimental challenges (modified from Ref. [66]).

Thermal conductivity characterization methods can be performed either by steady-state or transient techniques, as presented in Table 2.2. Steady-state experiments, which are performed when the studied system reaches a thermal equilibrium, encounter significant

problems related to the parasitic substrate heat flow (large temperature rise in the substrate), and radiation and convection losses that introduce errors in the measurement [61]. If the thermal resistance of the substrate is dominant in the total thermal resistance of the experiment, the temperature difference through the substrate will be considerably higher than the one across the thin film. Subtracting the substrate contribution to the overall temperature rise will therefore increase the experimental uncertainty. Moreover, since the thermal excitation in direct current experiments is continuous, the thermal response is also sensitive to the boundary conditions between the substrate and the environment. Because such contact resistances are generally not negligible and poorly controlled, they complicate the thermal analysis [67]. On the other hand, at room temperature or above, radiation and convection losses from the sample surface will be dominant in the heat transfer, if the thermal resistance of the substrate is higher than that of the measured film, increasing the experimental uncertainties [67].

Conversely, in transient techniques, the thermal response is studied as a function of time. Transient methods overcome the above mentioned problems by using alternative heating (e.g. alternating current (AC) heating current), which is combined with the reduced characteristic length of the experimental geometry, thus allowing to analyze a very small volume of the sample, and confining the heat wave inside the film-on-substrate system [17,61,67].

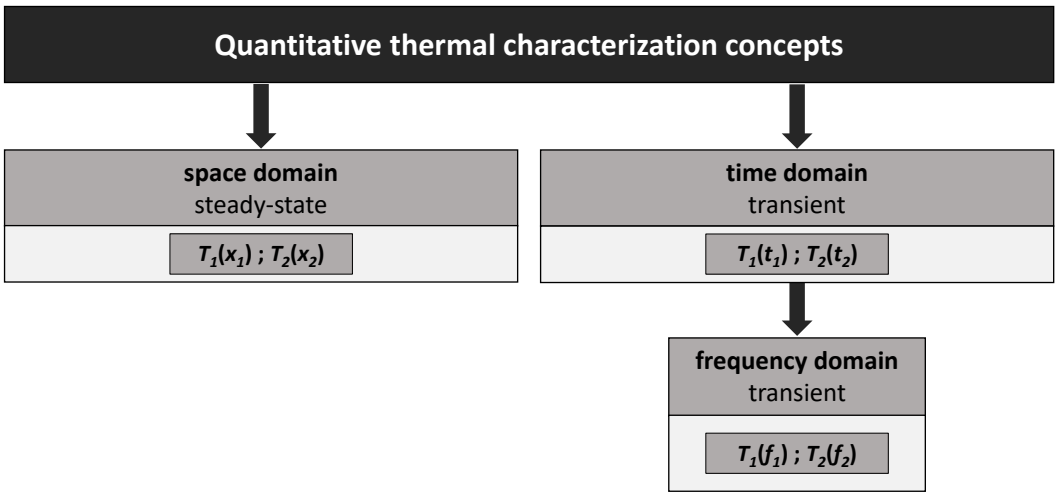

Figure 2.7: Classifications of techniques and concepts for thermal conductivity determination.

2.4.1. Thin film thermal conductivity characterization methods

In general, thermal conductivity characterization methods can be performed either by steady-state (space-domain) or transient techniques (time- and frequency-domain) as illustrated in Figure 2.7. Table 2.2 summarizes the most commonly used measurement techniques. Different measurement methods and concepts including the steady-state techniques (space-domain) and transient methods such as the 3ω method (frequency-domain), and the TDTR (time-domain) will be briefly discussed within the following sections. A more detailed review of thermal conductivity measurement techniques is provided by Zhao *et al.* [61].

Table 2.2: Commonly used characterization techniques to measure the thermal conductivity of thin films and bulk materials (modified from Ref. [61]).

		Bulk materials	Thin films
Steady-state		Axial heat flow method Radial heat flow method	Steady-state electrical heating methods
Transient	time-domain	Laser flash method Transient hot strip method (THS) TDTR technique	TDTR technique
	frequency-domain	3ω method	3ω method

2.4.1.1. Steady-state methods

The thermal characterization based on the analysis within the space-domain can be described by employing the steady-state measurement techniques. These common techniques to determine the thermal conductivity of materials will be firstly introduced. However, since alternative techniques have been developed rapidly, several variations of these techniques have been established and refined by using the improvement in technical equipment and major techniques. These fundamental techniques can be used to create a comprehensive understanding of material specific thermal determinations. In this section, we will present two

common steady-state measurement techniques, which are a) the axial heat flow and b) the radial heat flow methods. A review of further steady-state thermal conductivity measurement techniques is provided by Zhao *et al.* [61].

a) Axial heat flow method

Turning first to the axial heat flow based method, by assuming a linear heat flow, the defining equation for the thermal conductivity k (see Eq. (2.5)) of an isotropic homogeneous body reduces to [61]:

$$k = \frac{\dot{Q}}{A} \cdot \frac{\Delta z}{\Delta T} \tag{2.20}$$

where $\dot{Q}$ denotes the power traversing the specimen of cross-section A, and z denotes the axial- or the radial-direction.

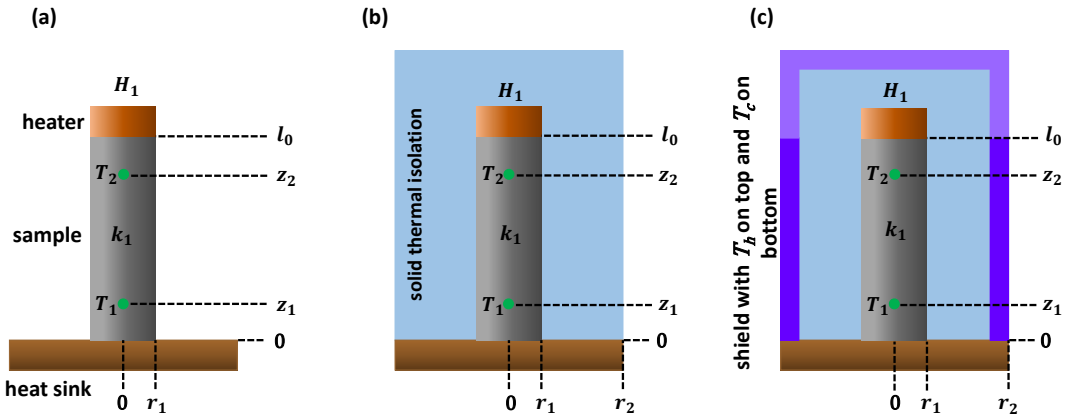

Figure 2.8: Schematic illustration of the axial heat flow systems: (a) specimen of thermal conductivity k_1 and length l_0 mounted on a base plate, (b) reduction of radial heat losses by additional thermal insulation, (c) improved method for the determination of k_1 with temperature shielding included.

The quantitative characterization of k involves the determination of the geometrical parameters A and $\Delta z = z_1 - z_2$, where z_1 and z_2 represent the locations of the temperature sensors. It also involves the measurement of the heat flow rate $\dot{Q}$ and it has to be ensured that all the measured power is responsible for the measured temperature gradient $\Delta T/\Delta z$. Along

with these geometrical parameters and the heat flow rate, the measurement of the temperatures T_1 and T_2 at the presumed locations is essential, since it has to be ensured that T_1 and T_2 correspond to the specimen temperature at z_1 and z_2, respectively (see Figure 2.8).

b) Radial heat flow method

For the radial heat flow based cylindrical thermal conductivity measurement method, a stable electrical current is passed through the core heater, and the radial temperature distribution is observed (see Figure 2.9). After the system reaches the steady-state, the temperatures at two different known radii, the voltage drop across the core heater and the current through the core heater are measured. Assuming a radial heat flow between the cylindrical isothermal surfaces r_1 and r_2, the heat flow rate q, through a cylindrical element of unit axial length is given by [20]:

$$q = -2\pi r k(T) \cdot \frac{dT}{dr} \tag{2.21}$$

Since the mean thermal conductivity k over the temperature range from T_2 to T_1 can be calculated by solving the integral of $k(T)$ with respect to the temperature T, the defining equation for calculating the thermal conductivity in the case of the radial heat flow based method can be derived as [20]:

$$k = P_l \cdot \frac{\ln(r_2/r_1)}{2\pi(T_1 - T_2)} \tag{2.22}$$

where P_l is the power per unit length from the core heater over the specimen midplane and T_n is the temperature at radius r_n. In the axial method, the setup is often arranged to avoid radial heat flow.

In the case of the radial method, the purpose of the setup is exactly opposite. Alternatives to satisfying the assumption of purely radial heat flow by preventing axial heat flow, are given by:

a) introducing interfaces or gaps within the specimen;

b) introducing additional guard heaters at the end of the core heater;

c) introducing similar techniques to simulate infinitely long systems.

These alternatives are described in reference [68].

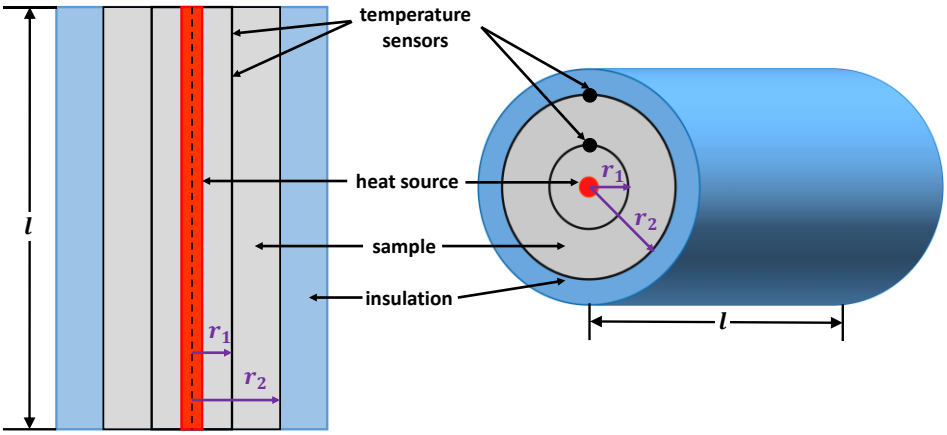

Figure 2.9: Schematic of the radial heat flow method (modified from Ref. [61]).

2.4.1.2. Transient methods

As described in the previous section, the space-domain based characterization, in the case of steady-state condition, is based on Fourier's law (see Eq. (2.5)), which is independent of time t. The analysis within the time-domain is based on the solution of the general differential equation of heat conduction (see Eq. (2.11)). Transient measurement techniques utilize heat sources that generate periodically temperature fluctuations in the investigated sample, in order to determine its thermal properties. The following section provides the basic principles of the two most widely used measurement techniques to obtain the thermal conductivity of thin films and bulk materials, which are the TDTR technique and the 3ω method.

a) Time-domain thermoreflectance technique

The TDTR is a non-contact thermal characterization method, which utilizes an optical heating and measuring system to obtain the thermal properties of thin films and bulk materials [61,69]. This technique is capable to determine the thermal conductivity, heat capacity and interfacial

thermal resistance of a film-on-substrate system [61,69]. Therefore, the investigated specimen has to be coated with a thin metallic layer, usually aluminum, which varies its reflectance as function of the temperature rise due to the optical heating [61,69]. The thermal characteristics of the specimen can be extracted by the reflectance change of the thin metallic coating on top of the specimen [61,69].

Working on the basis of a pump-and-probe process, TDTR uses two laser beams with different beam paths. Firstly, a pump beam is directed onto the surface of the sample, which is heated as a result of absorbing some of the beam power, as illustrated in Figure 2.10.

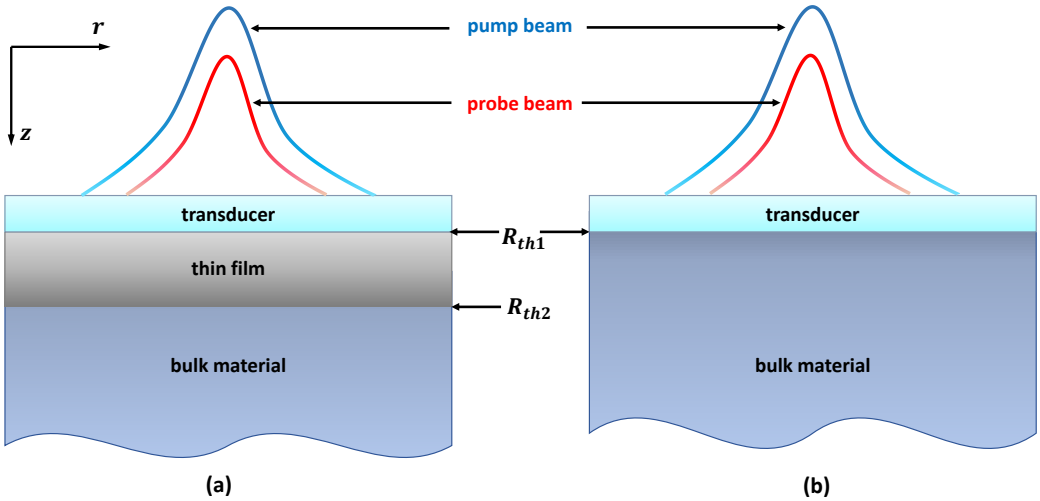

Figure 2.10: Schematic cross-sections of (a) film-on-substrate and (b) substrate/bulk samples utilized for determining thermal characteristics of thin films and substrate/bulk materials using the TDTR method. The thermal boundary resistances between different layers of the investigated samples are represented by R_{th1} and R_{th2} (modified and adapted from Ref. [61]).

Heating and measurement are accomplished by a "pump" using a single high energy, and excimer laser pulse in the order of picoseconds. The laser beam is used to heat the surface of the thin film in an area of a few square microns as the optical energy is absorbed [61,69]. The heat diffusion and temperature on the surface of the sample depend on its properties, in particular the thermal conductivity of the individual layers. The reflectivity, i.e. the proportion of the laser beam that is reflected from the surface of the sample, is influenced by the temperature. This means that the surface temperature can be determined by a probe beam that

falls onto the sample surface after the pump beam with a time delay. The reflected probe beam consequently provides information about the surface temperature of the sample and its thermal properties. The reflected probe beam falls on a photo diode, obtaining the measurement data. The temporal probe pulse width is less than 10 ps, which correlates to an effective thermal penetration depth in the order of nanometers [61]. The general equation of heat conduction (see Eq. (2.11)) is fitted to the acquired measurement data and used to determine the thermal conductivity of the investigated specimen. The unique advantages and drawbacks of the TDTR method are listed in Table 2.3.

Table 2.3: Advantages and disadvantages of the 3ω method and the TDTR technique [1,61,82].

	3ω method	TDTR technique
Advantages	• High results repeatability • Simple experimental setup • High accuracy, particularly for bulk materials and low thermal conductivity dielectric films • Wide temperature range (30 – 1000 K) • Simultaneous measurement of both cross- and in-plane thermal conductivity	• No need for electrical insulation for metals and semiconductors • High spatial resolution • Complex sample geometry can be investigated • Can separate the metal/film interface thermal conductance from the thermal conductivity • High accuracy for metals
Disadvantages	• Cannot distinguish between the thermal conductivity of a film and interface • No local thermal conductivity mapping of thin films (But our 3ω Microscopy fills this gap) • Accuracy for metals is reduced	• Experimental setup is complex and expensive • Medium results repeatability • Accuracy is typically limited to several percent due to uncertainties in experimental parameters (film thickness and heat capacity of metal film) • Only cross-plane thermal conductivity can be measured

A major drawback of the TDTR is that it can only measure the cross-plane thermal conductivity $k_\perp$ of samples that have a smooth, reflective surface and are at least a few tens of nanometers thick [69,70]. The most effective and accurate approach to simultaneously measure the cross- and in-plane thermal conductivities of anisotropic thin films, would be using the extended 3ω method, which will be presented in Section 3.3.2.2. The following section will introduce the basic 3ω method and their application fields.

b) 3ω method

The last measurement technique that we discuss within this chapter is the so-called 3ω method. The 3ω method was originally developed in 1989 by Cahill [17,71] and is commonly utilized to determine thermal conductivities of both thin films [71,72] and bulk materials [17,73]. It is also capable to obtain the thermal conductivity of liquids [74,75] and gases [76]. The 3ω measurement technique was evolved from the conventional hot-wire techniques [77–79] and is predominantly used to measure the cross-plane thermal conductivity of dielectric thin films [3,4,21,60,61,66].

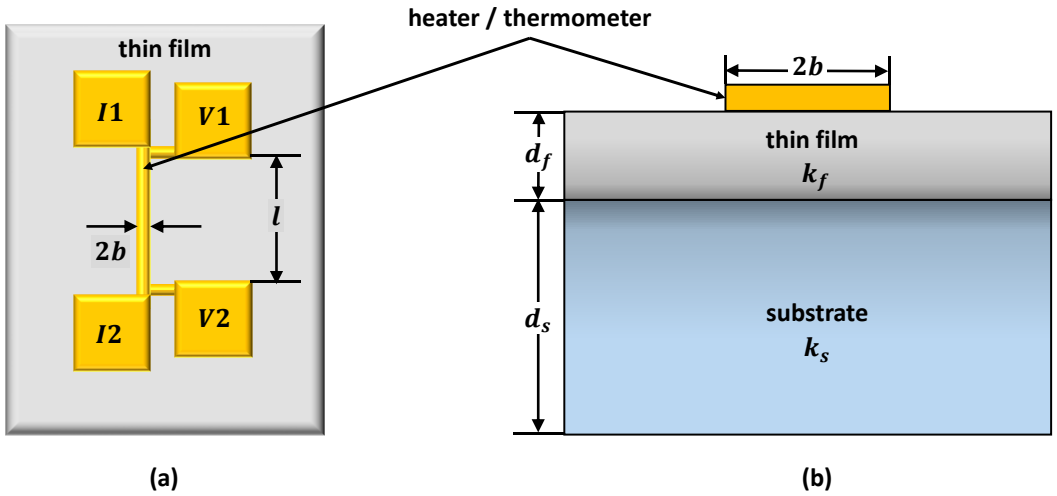

Figure 2.11: (a) Schematic layout of the four-pad test structure used to determine the thermal conductivity of a thin film by the 3ω method. A metal strip serves as both heater and thermometer. The four pads are the connections for current leads ($I1$, $I2$) and voltage leads ($V1$, $V2$). The strip length l is the distance between the current leads and $2b$ represents the strip width; (b) Schematic cross-section of film-on-substrate samples required for the 3ω method.

As shown in Figure 2.11, a thin metal strip, with a width of $2b$ and a resistance R_h, is deposited on top of the thin film sample for simultaneous operations as both a heater and thermometer. An AC current with an angular modulation frequency ω is driven through the metal strip causing Joule heating and induces a temperature oscillation $\Delta T(\omega)$ at a frequency of 2ω. This results in a voltage oscillation $\Delta V(\omega)$ along the heating resistor with a third harmonic, which depends on the temperature oscillation of the heater [3]. The temperature and voltage oscillations are the key parameters of the 3ω method [3]. Using the 3ω method, thermal conductivity of a thin film can be obtained by comparing the temperature oscillation in a film-on-substrate structure with the corresponding value of the substrate. The temperature variation of the film-on-substrate structure can be experimentally measured by detecting the voltage oscillation across the metal heater, which is proportional to the oscillating resistance value [3].

Numerous extensions and enhancements of Cahill's basic 3ω method have been reported in order to investigate the thermal conductivity of thin films and substrate materials [3,21,60,80]. However, the 3ω method provides a large room of improvement in case of determining the thermal conductivity of anisotropic thin films, especially along the in-plane direction. Measurements of the in-plane thermal conductivity are less common than those of the cross-plane direction, while the methods used are more diverse [67]. In-plane measurements can be divided into those for the suspended and those for the supported films. In general, methods for the suspended films are only sensitive for the in-plane thermal conductivity and cannot properly detect the heat flow in the cross-plane direction [81]. Furthermore, the microfabrication to obtain a suspended thin film and the significant impact of radiation losses are serious challenges [67]. Therefore, one of our main goals of this thesis is to develop a new approach to measure both cross- and in-plane thermal conductivities of thin films without changing the sample during the measurement process. This modification and further extensions we developed within this thesis will be presented in Chapter 3.

With our extended 3ω method, it is the first time that the cross- and in-plane thermal conductivity of thin films can be obtained simultaneously. One of the main goals of this thesis is to study the thickness-dependency of cross- and in-plane thermal conductivity of amorphous thin films for thermal management (AlN films [3]) and thermoelectric applications (CuI films [8]).

Thermal properties of thin films and nanostructured material systems gain in importance due to the progress in material science and increasing performances and electronics. There have great demands for high-spatially resolving techniques to analyze the respective systems concerning the local quantitative thermal characteristic. Therefore, the determination of the local thermal conductivity of thin films is mandatory within fundamental characterizations. For this reason, we developed a novel experimental technique to determine the local thermal conductivity of thin films in dependence on their sample properties (e.g. film thickness, surface crystallite size) with a high spatial resolution. To realize this concept, the 3ω method with its numerous advantages and wide range of applications, is transferred to the microscopic level by combining the AFM with our extended 3ω technique. The extensions and modifications of the 3ω method will represent the main research aims of this thesis, as summarized in Section 1.4 of page 9.

The 3ω method provides some unique advantages compared to other steady-state or transient thermal conductivity characterization methods, summarized in Table 2.3, especially for the characterization of both cross- and in-plane thermal conductivities of thin films. In contrast to other commonly used steady-state thermal conductivity measurement methods, such as axial/radial heat flow method [61] or the steady-state electrical heating techniques, the 3ω method is insensitive to radiation errors/losses, because the effective heat volume of the heat source is within the micrometer-range [17,61]. Therefore, higher accuracy and better reproducibility of the film's thermal conductivity data can be obtained [3]. Cahill *et al*. [73] demonstrated that the radiation losses by using the 3ω method are below 2%.

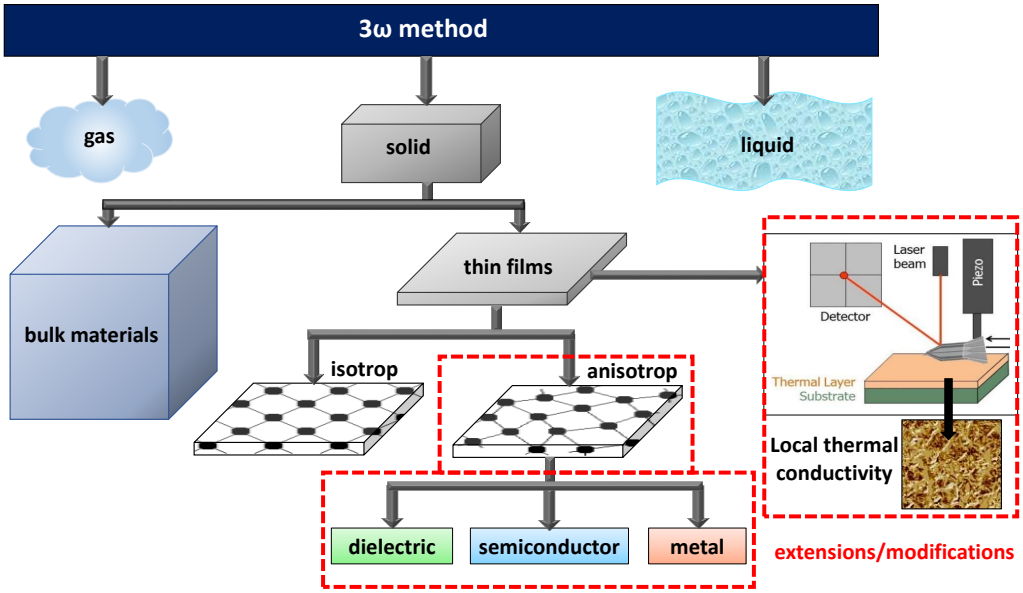

Figure 2.12: The wide field of application of the 3ω method and its extensions. The classic 3ω method is capable to measure the thermal conductivity of bulk materials, but over the years the method has been modified and extended several times to expand its field of application. The 3ω method is now able to obtain the thermal conductivity of solids, gases and fluids, as well as dielectric, semi-conductive, and metallic materials. Within this thesis we extended the method to enable the measurement of anisotropic materials and local thermal conductivities of thin films with a high spatial resolution. Our extensions and improvements are highlighted in red.

Another advantage of the 3ω method is, its wide field of applications, which enables thermal conductivity measurements of dielectric, semiconducting and electrically conducting thin films [60,61,67] (see Figure 2.12). Furthermore, the 3ω method is the only technique, which can be applied to measure the cross- and in-plane thermal conductivity of thin films simultaneously, by using our improved multi-heater approach, presented in Chapter 3.

Considering these points, the 3ω method with all its modifications and specific advantages, is the most suitable thermal characterization technique for our research objectives within this thesis. Therefore, the extended 3ω method is our major characterization tool to perform all the thermal conductivity measurements to study the thermal properties of thin films.

2.4.2. Summary and comparison of thermal conductivity characterization methods

In brief, thermal conductivity characterization methods can be performed either by steady-state (space-domain) or transient techniques (time- and frequency-domain). Figure 2.13 gives an overview of the sample size and required measurement time for commonly used steady-state and transient thermal conductivity measurement techniques.

Usually, steady-state techniques, which are performed when studied systems reach the thermal equilibrium, encounter significant problems related to the parasitic substrate heat flow (large temperature rise in the substrate), and radiation/convection losses that introduce errors in the measurement, as discussed in Section 2.4. If the thermal resistance of the substrate is dominant in the total thermal resistance of the experiment, the temperature difference through the substrate will be considerably higher than the one across the film [3,61]. Subtracting the substrate contribution to the overall temperature rise will therefore increase the experimental uncertainty. Moreover, since the thermal excitation in DC experiments is continuous, the thermal response is also sensitive to the boundary conditions between the substrate and the environment [61,67]. Because such contact resistances are generally not negligible and poorly controlled, they complicate the thermal analysis [67]. On the other hand, at room temperature or above, radiation and convection losses from the sample surface will be dominant in the heat transfer, if the thermal resistance of the substrate is higher than the one of the measured film, increasing the experimental uncertainties [61,67]. Because of these specific drawbacks, steady-state methods are not suitable and accurate enough for measuring the thermal conductivity of thin films and nanostructured materials. Therefore, steady-state methods such as axial and radial heat flow methods as well as the steady-state electrical heating method are normally used for the thermal characterization of bulk materials.

Conversely, in transient techniques, the thermal response is studied as a function of time. Transient methods overcome the above mentioned problems by using alternative heating,

which is combined with the reduced characteristic length of the experimental geometry, allows us to analyze a very small volume of the sample, confining the heat wave inside the film-on-substrate system [61]. Despite this advantage, the transient hot wire method has some difficulties in the sample preparation. Also, the fragility of the long thin wire is another problem when the method is applied on solids and fluids [61]. Therefore, the TDTR method and 3ω methods are both transient methods that can measure the thermal conductivities of thin films in the order of several nanometers to micrometers. They are the most suitable and accurate measurement techniques for thin films and nanostructured materials [82]. Table 2.3 lists the major advantages and disadvantages of both methods.

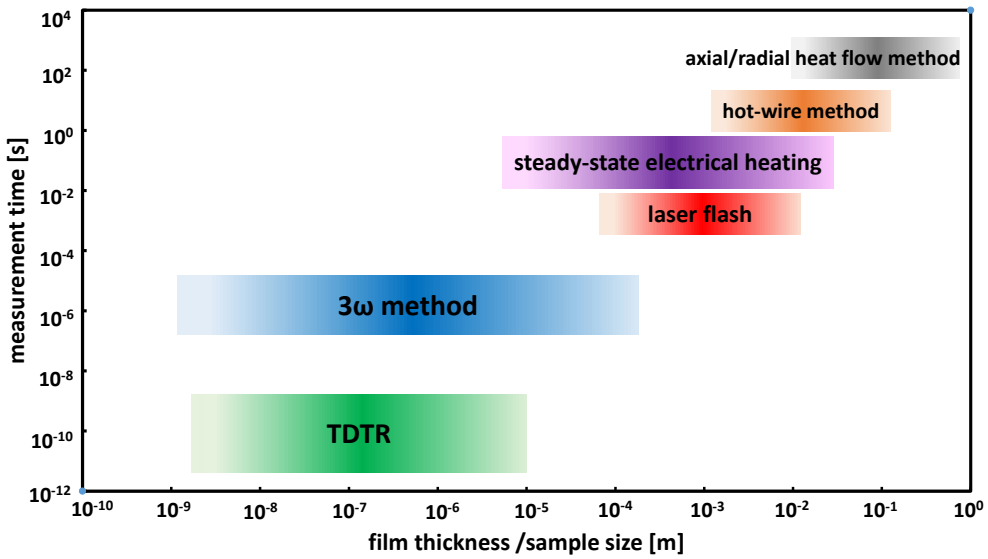

Figure 2.13: Overview of the sample size, which is equal to the film or substrate thickness and required measurement time for commonly used steady-state and transient thermal conductivity measurement techniques. The measurement time describes the time period, which is needed to reach the temperature equilibrium inside the sample. Transient techniques like TDTR and the 3ω method are capable of measuring thinnest film samples in a very short amount of time (modified and adapted from Ref. [61]).

Although many techniques have been developed to measure the thermal conductivity of thin films, currently the 3ω method is one of the most widely used methods because of its low cost, simplicity, and high accuracy [3,61]. Applications of the 3ω method to electrically conducting or semiconducting materials can be challenging, because of the need to electrically

isolate the metal heater from the sample. This additional layer of electrical insulation inevitably introduces an additional thermal resistance between the metal heater and the sample, which can reduce both the sensitivity and accuracy of the technique [67,83].

Because of these challenges, the TDTR with the ability to measure thermal conductivity of electrically conducting thin films was developed. Due to recent advances in both the experimental design and methods for data analysis, the TDTR is now a flexible and accurate tool for measuring the thermal conductivity of bulk materials and thin film that span a range in thermal conductivities from the lowest thermal conductivities ever observed in a fully dense solid [84] to the high thermal conductivities of pure metals [85]. However, for the TDTR technique the equipment used to build up the experimental setup is expensive rendering this method a relatively costly one. Furthermore, at the moment the TDTR method can only measure the cross-plane thermal conductivity of any sample that has a smooth, reflective surface and is at least a few tens of nanometers thick, but it is not possible to obtain reproducible and accurate information about the thermal properties of the in-plane direction [70,86]. Therefore, we chose the 3ω method as the thermal conductivity characterization technique for our thin films, because one of our major research objectives is to study the thickness-dependency of the cross- and in-plane thermal conductivities of AlN and CuI thin films.

2.5. References

[1] D.G. Cahill, P.V. Braun, G. Chen, D.R. Clarke, S. Fan, K.E. Goodson, P. Keblinski, W.P. King, G.D. Mahan, A. Majumdar, H.J. Maris, S.R. Phillpot, E. Pop, L. Shi, Nanoscale thermal transport. II. 2003–2012, Applied Physics Reviews 1 (1) (2014) 11305.

[2] D.G. Cahill, K. Goodson, A. Majumdar, Thermometry and Thermal Transport in Micro/Nanoscale Solid-State Devices and Structures, Journal of Heat Transfer 124 (2) (2002) 223.

[3] M. Bogner, A. Hofer, G. Benstetter, H. Gruber, R.Y. Fu, Differential 3ω method for measuring thermal conductivity of AlN and Si3N4 thin films, Thin Solid Films 591 (2015) 267–270.

[4] S.R. Choi, D. Kim, S.-H. Choa, S.-H. Lee, J.-K. Kim, Thermal Conductivity of AlN and SiC Thin Films, International Journal of Thermophysics 27 (3) (2006) 896–905.

[5] M. Grundmann, F.L. Schein, M. Lorenz, T. Böntgen, J. Lenzner, H. von Wenckstern, Cuprous iodide: A p-type transparent semiconductor, history, and novel applications, Physica status solidi A (2013) 1671-1703.

[6] C. Yang, M. Kneibeta, M. Lorenz, M. Grundmann, Room-temperature synthesized copper iodide thin film as degenerate p-type transparent conductor with a boosted figure of merit, Proceedings of the National Academy of Sciences of the United States of America 113 (46) (2016) 12929–12933.

[7] C. Yang, M. Kneiss, F.-L. Schein, M. Lorenz, M. Grundmann, Room-temperature Domain-epitaxy of Copper Iodide Thin Films for Transparent CuI/ZnO Heterojunctions with High Rectification Ratios Larger than 10(9), Scientific reports 6 (2016) 21937.

[8] C. Yang, D. Souchay, M. Kneiß, M. Bogner, H.M. Wei, M. Lorenz, O. Oeckler, G. Benstetter, Y.Q. Fu, M. Grundmann, Transparent flexible thermoelectric material based on non-toxic earth-abundant p-type copper iodide thin film, Nature communications 8 (2017) 16076.

[9] J.M. Ziman, Electrons and phonons: The theory of transport phenomena in solids, Clarendon Press, Oxford, (2007) (p. 11, 87-89).

[10] NASA HUMAN SPACE FLIGHt, Apollo 12 Image: AS12-46-6790 (19 Nov. 1969), available at https://spaceflight.nasa.gov/gallery/images/apollo/apollo12/html/as12-46-6790.html.

[11] G.J. Snyder, E.S. Toberer, Complex thermoelectric materials, Nature materials 7 (2) (2008) 105–114.

[12] New Atlas Team, Thermoelectric boots charge your mobile phone, 2010, available at http://newatlas.com/thermoelectric-orange-power-wellies-generate-electricity/15346/ (accessed on March 11, 2017).

[13] BMW Group, Research project: Turbosteamer, 2011, available at https://www.press.bmwgroup.com/deutschland/photo/compilation/T0119738DE/auf-der-suche-nach-dem-naechsten-gramm (accessed on March 10, 2017).

[14] EcoFriend Group, Can thermoelectricity ever become a viable source of clean energy generation?, available at http://www.ecofriend.com/thermoelectricity-viable-source-clean-energy-generation.html (accessed on March 10, 2017).

[15] J.B.J. Fourier, The analytical theory of heat by Joseph Fourier, University Press, Cambridge, (1878) 77-86.

[16] H.S. Carslaw, J.C. Jaeger, Conduction of heat in solids, 2nd ed., Clarendon, Oxford, (1959) 1-92.

[17] D.G. Cahill, Thermal conductivity measurement from 30 to 750 K: The 3ω method, Review of Scientific Instruments 61 (2) (1990) 802–808.

[18] Y. Yener, S. Kakaç, Heat conduction, 4th ed., Taylor and Francis, Washington, 2008.

[19] A. Stoffel, Finite Elemente und Wärmeleitung: Eine Einführung, VCH, Weinheim, New York, Basel, Cambridge, 1992.

[20] D.R. Flynn, Thermal Conductivity of Loose-Fill Materials by a Radial-Heat-Flow Method, in: K.D. Maglić, A. Cezairliyan, V.E. Peletsky (Eds.), Compendium of Thermophysical Property Measurement Methods, Springer US, Boston, 1992, 33–75.

[21] S.M. Lee, D.G. Cahill, Heat transport in thin dielectric films, Journal of Applied Physics 81 (6) (1997) 2590–2595.

[22] X. Wang, Experimental micro/nanoscale thermal transport, Wiley, Hoboken, NJ, (2012) 1-45.

[23] M. Kaviany, Essentials of heat transfer: Principles, materials, and applications, Cambridge University Press, Cambridge, New York, (2011).

[24] P.G. Klemens, Theory of Thermal Conduction in Thin Ceramic Films, International Journal of Thermophysics 22 (1) (2001) 265–275.

[25] A. Majumdar, Microscale Heat Conduction in Dielectric Thin Films, Journal of Heat Transfer 115 (1) (1993) 7.

[26] L. Braginsky, N. Lukzen, V. Shklover, H. Hofmann, High-temperature phonon thermal conductivity of nanostructures, Physical Review B 66 (13) (2002).

[27] H.S. Yang, G.R. Bai, L.J. Thompson, J.A. Eastman, Interfacial thermal resistance in nanocrystalline yttria-stabilized zirconia, Acta Materialia 50 (9) (2002) 2309–2317.

[28] J. Jaramillo-Fernandez, J. Ordonez-Miranda, E. Ollier, S. Volz, Tunable thermal conductivity of thin films of polycrystalline AlN by structural inhomogeneity and interfacial oxidation, Physical chemistry chemical physics 17 (12) (2015) 8125–8137.

[29] H. Dong, B. Wen, R. Melnik, Relative importance of grain boundaries and size effects in thermal conductivity of nanocrystalline materials, Scientific reports 4 (2014) 7037.

[30] V.L. Gurevich, Transport in phonon systems, North-Holland, Amsterdam, 1986.

[31] Q. Hao, G. Chen, M.-S. Jeng, Frequency-dependent Monte Carlo simulations of phonon transport in two-dimensional porous silicon with aligned pores, Journal of Applied Physics 106 (11) (2009) 114321.

[32] M. Kazan, S. Volz, Calculation of the lattice thermal conductivity in granular crystals, Journal of Applied Physics 115 (7) (2014) 73509.

[33] K. Miyazaki, T. Arashi, D. Makino, H. Tsukamoto, Heat conduction in microstructured materials, IEEE Transactions on Components and Packaging Technologies 29 (2) (2006) 247–253.

[34] R. Yang, G. Chen, M. Laroche, Y. Taur, Simulation of Nanoscale Multidimensional Transient Heat Conduction Problems Using Ballistic-Diffusive Equations and Phonon Boltzmann Equation, Journal of Heat Transfer 127 (3) (2005) 298.

[35] Z. Tian, S. Lee, G. Chen, Comprehensive review of heat transfer in thermoelectric materials and devices, Annual Review of Heat Transfer 17 (2014) 425–483.

[36] J. Zhou, H.F. Pang, L. Garcia-Gancedo, E. Iborra, M. Clement, M. de Miguel-Ramos, H. Jin, J.K. Luo, S. Smith, S.R. Dong, D.M. Wang, Y.Q. Fu, Discrete microfluidics based on aluminum nitride surface acoustic wave devices, Microfluid Nanofluid 18 (4) (2015) 537–548.

[37] M. Clement, L. Vergara, J. Sangrador, E. Iborra, A. Sanz-Hervas, SAW characteristics of AlN films sputtered on silicon substrates, Ultrasonics 42 (1-9) (2004) 403–407.

[38] H. Witte, A. Rohrbeck, K.-M. Günther, P. Saengkaew, J. Bläsing, A. Dadgar, A. Krost, Electrical investigations of AlGaN/AlN structures for LEDs on Si(111), Physica status solidi A 208 (7) (2011) 1597–1599.

[39] T.S. Pan, Y. Zhang, J. Huang, B. Zeng, D.H. Hong, S.L. Wang, H.Z. Zeng, M. Gao, W. Huang, Y. Lin, Enhanced thermal conductivity of polycrystalline aluminum nitride thin films by optimizing the interface structure, Journal of Applied Physics 112 (4) (2012) 44905.

[40] A. Jacquot, B. Lenoir, A. Dauscher, P. Verardi, F. Craciun, M. Stölzer, M. Gartner, M. Dinescu, Optical and thermal characterization of AlN thin films deposited by pulsed laser deposition, Applied Surface Science 186 (1-4) (2002) 507–512.

[41] Y. Zhao, C. Zhu, S. Wang, J.Z. Tian, D.J. Yang, C.K. Chen, H. Cheng, P. Hing, Pulsed photothermal reflectance measurement of the thermal conductivity of sputtered aluminum nitride thin films, Journal of Applied Physics 96 (8) (2004) 4563–4568.

[42] G.A. Slack, R.A. Tanzilli, R.O. Pohl, J.W. Vandersande, The intrinsic thermal conductivity of AIN, Journal of Physics and Chemistry of Solids 48 (7) (1987) 641–647.

[43] P.K. Kuo, G.W. Auner, Z.L. Wu, Microstructure and thermal conductivity of epitaxial AlN thin films, Thin Solid Films 253 (1-2) (1994) 223–227.

[44] B.E. Belkerk, A. Soussou, M. Carette, M.A. Djouadi, Y. Scudeller, Structural-dependent thermal conductivity of aluminium nitride produced by reactive direct current magnetron sputtering, Applied Physics Letters 101 (15) (2012) 151908.

[45] C. Duquenne, M.P. Besland, P.Y. Tessier, E. Gautron, Y. Scudeller, D. Averty, Thermal conductivity of aluminium nitride thin films prepared by reactive magnetron sputtering, Journal of Physics D: Applied Physics 45 (1) (2012) 15301.

[46] F. Suriano, M. Ferri, F. Moscatelli, F. Mancarella, L. Belsito, S. Solmi, A. Roncaglia, S. Frabboni, G.C. Gazzadi, D. Narducci, Influence of Grain Size on the Thermoelectric Properties of Polycrystalline Silicon Nanowires, Journal of Electronic Materials 44 (1) (2015) 371–376.

[47] M. Gunes, M. Ozenbas, Effect of grain size and porosity on phonon scattering enhancement of Ca3Co4O9, Journal of Alloys and Compounds 626 (2015) 360–367.

[48] H. Wu, J. Carrete, Z. Zhang, Y. Qu, X. Shen, Z. Wang, L.-D. Zhao, J. He, Strong enhancement of phonon scattering through nanoscale grains in lead sulfide thermoelectrics, NPG Asia Materials 6 (6) (2014) 108.

[49] J. Carrete, N. Mingo, S. Curtarolo, Low thermal conductivity and triaxial phononic anisotropy of SnSe, Applied Physics Letters 105 (10) (2014) 101907.

[50] M. Pourbafrani, R.S. Razavi, S.R. Bakhshi, M.R. Loghman-Estarki, H. Jamali, Effect of microstructure and phase of nanostructured YSZ thermal barrier coatings on its thermal shock behaviour, Surface Engineering 31 (1) (2014) 64–73.

[51] N. Schlegel, S. Ebert, G. Mauer, R. Vaßen, Columnar-Structured Mg-Al-Spinel Thermal Barrier Coatings (TBCs) by Suspension Plasma Spraying (SPS), Journal of Thermal Spray Technology 75 (6) (2014) 1497.

[52] Q.L. Li, X.Z. Cui, S.Q. Li, W.H. Yang, C. Wang, Q. Cao, Synthesis and Phase Stability of Scandia, Gadolinia, and Ytterbia Co-doped Zirconia for Thermal Barrier Coating Application, Journal of Thermal Spray Technology 24 (11) (2014) 1.

[53] A. Iskandar, A. Abou-Khalil, M. Kazan, W. Kassem, S. Volz, On the interplay between phonon-boundary scattering and phonon-point-defect scattering in SiGe thin films, Journal of Applied Physics 117 (12) (2015) 125102.

[54] W. Zhao, P. Wei, Q. Zhang, H. Peng, W. Zhu, D. Tang, J. Yu, H. Zhou, Z. Liu, X. Mu, D. He, J. Li, C. Wang, X. Tang, J. Yang, Multi-localization transport behaviour in bulk thermoelectric materials, Nature communications 6 (2015) 6197.

[55] K.F. Murphy, B. Piccione, M.B. Zanjani, J.R. Lukes, D.S. Gianola, Strain- and defect-mediated thermal conductivity in silicon nanowires, Nano letters 14 (7) (2014) 3785–3792.

[56] X. Zhang, Z. Sun, Effects of vacancy structural defects on the thermal conductivity of silicon thin films, Journal of Semiconductors 32 (5) (2011) 53002.

[57] P.E. Hopkins, Thermal Transport across Solid Interfaces with Nanoscale Imperfections: Effects of Roughness, Disorder, Dislocations, and Bonding on Thermal Boundary Conductance, ISRN Mechanical Engineering (2) (2013) 1–19.

[58] G.A. Slack, L.J. Schowalter, D. Morelli, J.A. Freitas, Some effects of oxygen impurities on AlN and GaN, Journal of Crystal Growth 246 (3-4) (2002) 287–298.

[59] D.G. Cahill, W.K. Ford, K.E. Goodson, G.D. Mahan, A. Majumdar, H.J. Maris, R. Merlin, S.R. Phillpot, Nanoscale thermal transport, Journal of Applied Physics 93 (2) (2003) 793–818.

[60] T. Borca-Tasciuc, A.R. Kumar, G. Chen, Data reduction in 3ω method for thin-film thermal conductivity determination, Review of Scientific Instruments 72 (4) (2001) 2139–2147.

[61] D. Zhao, X. Qian, X. Gu, S.A. Jajja, R. Yang, Measurement Techniques for Thermal Conductivity and Interfacial Thermal Conductance of Bulk and Thin Film Materials, Journal of Electronic Packaging 138 (4) (2016) 40802.

[62] L. Shi, C. Dames, J.R. Lukes, P. Reddy, J. Duda, D.G. Cahill, J. Lee, A. Marconnet, K.E. Goodson, J.H. Bahk, A. Shakouri, R.S. Prasher, J. Felts, W.P. King, B. Han, J.C. Bischof, Evaluating Broader Impacts of Nanoscale Thermal Transport Research, Nanoscale and Microscale Thermophysical Engineering 19 (2) (2015) 127–165.

[63] A.M. Marconnet, M.A. Panzer, K.E. Goodson, Thermal conduction phenomena in carbon nanotubes and related nanostructured materials, Reviews of Modern Physics 85 (3) (2013) 1295–1326.

[64] E.S. Toberer, L.L. Baranowski, C. Dames, Advances in Thermal Conductivity, Annual Review of Materials Research 42 (1) (2012) 179–209.

[65] X.C. Tong, Advanced Materials for Thermal Management of Electronic Packaging, 1st ed., Springer Springer Science+Business Media, New York, (2011).

[66] T. Borca-Tasciuc, G. Chen, Experimental Techniques for Thin-Film Thermal Conductivity Characterization, in: Tritt (Hg.) (2004) – Thermal Conductivity, 205–237.

[67] C. Dames, Measuring the Thermal Conductivity of Thin Films: 3 Omega and related Electrothermal Methods, Annual Review of Heat Transfer 16 (1) (2013) 7–49.

[68] K.D. Maglić, A. Cezairliyan, V.E. Peletskii, Compendium of Thermophysical Property Measurement Methods: Volume 2 Recommended Measurement Techniques and Practices, Springer US, Boston, (1992).

[69] D.G. Cahill, Analysis of heat flow in layered structures for time-domain thermoreflectance, Review of Scientific Instruments 75 (12) (2004) 5119–5122.

[70] J.P. Feser, D.G. Cahill, Probing anisotropic heat transport using time-domain thermoreflectance with offset laser spots, The Review of scientific instruments 83 (10) (2012) 104901.

[71] D.G. Cahill, H.E. Fischer, T. Klitsner, E.T. Swartz, R.O. Pohl, Thermal conductivity of thin films: Measurements and understanding, Journal of Vacuum Science & Technology A: Vacuum, Surfaces, and Films 7 (3) (1989) 1259–1266.

[72] D.G. Cahill, M. Katiyar, J.R. Abelson, Thermal conductivity of a-Si: H thin films, Physical Review B 50 (9) (1994) 6077–6081.

[73] D.G. Cahill, R.O. Pohl, Thermal conductivity of amorphous solids above the plateau, Physical Review B 35 (8) (1987) 4067–4073.

[74] B.K. Park, J. Park, D. Kim, Note: Three-omega method to measure thermal properties of subnanoliter liquid samples, The Review of scientific instruments 81 (6) (2010) 66104.

[75] S.R. Choi, J. Kim, D. Kim, 3omega method to measure thermal properties of electrically conducting small-volume liquid, The Review of scientific instruments 78 (8) (2007) 84902.

[76] E. Yusibani, P.L. Woodfield, M. Fujii, K. Shinzato, X. Zhang, Y. Takata, Application of the Three-Omega Method to Measurement of Thermal Conductivity and Thermal Diffusivity of Hydrogen Gas, International Journal of Thermophysics 30 (2) (2009) 397–415.

[77] U. Hammerschmidt, A New Pulse Hot Strip Sensor for Measuring Thermal Conductivity and Thermal Diffusivity of Solids, International Journal of Thermophysics 24 (3) (2003) 675–682.

[78] J.J. Healy, J.J. de Groot, J. Kestin, The theory of the transient hot-wire method for measuring thermal conductivity, Physica B+C 82 (2) (1976) 392–408.

[79] E. van der Held, F.G. van Drunen, A method of measuring the thermal conductivity of liquids, Physica 15 (10) (1949) 865–881.

[80] C.E. Raudzis, F. Schatz, D. Wharam, Extending the 3ω method for thin-film analysis to high frequencies, Journal of Applied Physics 93 (10) (2003) 6050–6055.

[81] Y.S. Ju, K. Kurabayashi, K.E. Goodson, Thermal characterization of anisotropic thin dielectric films using harmonic Joule heating, Thin Solid Films 339 (1-2) (1999) 160–164.

[82] Y.K. Koh, S.L. Singer, W. Kim, J.M.O. Zide, H. Lu, D.G. Cahill, A. Majumdar, A.C. Gossard, Comparison of the 3ω method and time-domain thermoreflectance for measurements of the cross-plane thermal conductivity of epitaxial semiconductors, Journal of Applied Physics 105 (5) (2009) 54303.

[83] J.P. Feser, E.M. Chan, A. Majumdar, R.A. Segalman, J.J. Urban, Ultralow thermal conductivity in polycrystalline CdSe thin films with controlled grain size, Nano letters 13 (5) (2013) 2122–2127.

[84] C. Chiritescu, D.G. Cahill, N. Nguyen, D. Johnson, A. Bodapati, P. Keblinski, P. Zschack, Ultralow thermal conductivity in disordered, layered WSe2 crystals, Science 315 (5810) (2007) 351–353.

[85] J.C. Zhao, X. Zheng, D.G. Cahill, High-throughput diffusion multiples, Materials Today 8 (10) (2005) 28–37.

[86] A.J. Schmidt, X. Chen, G. Chen, Pulse accumulation, radial heat conduction, and anisotropic thermal conductivity in pump-probe transient thermoreflectance, The Review of scientific instruments 79 (11) (2008) 114902.

Chapter 3: Principle and Theory of the 3ω Method

3.1. Introduction

The frequency-domain was introduced in Section 2.4 as a special method within the time-domain ones, providing the opportunity to eliminate unknown quantities by establishing and utilizing more than just one mathematical equation. The so-called 3ω method constitutes a technique within the frequency-domain, and therefore possesses the advantages that the space-domain or time-domain based measurement methods do not have. Since the 3ω method will be the fundamental measurement method, which has to be analyzed and modified in the context of particular circumstances within this thesis, the history, theoretical basics, and modifications of this technique will be discussed in the following sections.

3.1.1. Evolution of the 3ω method

In 1910, Corbino demonstrated that thermal oscillations of a metal wire, generated by an AC heating current provide information about the thermal properties of the investigated material [1]. However, until 1963, Holland took up Corbino's approach in order to measure thermal properties of titanium over a wide temperature range [2]. In 1964 Gerlich also utilized the electrically generated harmonic temperature oscillations to determine the thermal characteristic of bar-shaped germanium (Ge), silicon (Si), and Ge-Si alloys from room temperature up to 1000 K, and emphasized the advantages of the narrow band amplification applicable to this method [3]. In 1966, Holland theoretically analyzed the harmonic periodical temperature variations and discussed therewith the necessary conditions for the simplified assumptions for the first time [4]. After another period of almost 20 years, Birge utilized the same method in order to perform a specific heat spectroscopy of liquids (glycerol) in 1985 [5–7]. To perform this kind of analysis, a thin metal film (electrical heater) was evaporated

onto a glass substrate and the complete setup was immersed in a bath of the liquid sample to be measured.

As the first one in 1987, Cahill [8] considered the theoretical description of the amplitude of the periodical temperature oscillation for an ideal line heat source [9]. Cahill developed a theory linking the metal heater's third harmonic voltage component with the thermal conductivity of the investigated sample [8]. In contrast to Birge's measurements, the narrow metal line serving as a heater and thermometer was deposited onto a substrate, which has to be thermally characterized. Using this method, he investigated the temperature dependence of the thermal conductivity of different kinds of bulk materials (e.g. SiO_2, PMMA, glycerol, glass) in the temperature range from 30 to 1000 K [10,11]. While some scientific groups utilized the third harmonic detection scheme to determine the material specific quantities of an AC current fed into a thin and long specimen itself [12], others employed the 3ω technique to thermally characterize the substrate, where a flat and plane electrical heater has been deposited on its surface [13]. The different geometry of the heater of finite width was considered by assuming a superposition of infinitely thin line heaters located across the complete width of the heater. Moreover, the heater was assumed to have a negligible mass and consequently had no effect on the temperature profile of the medium [14]. Since the thermal conductivity of thin film materials was poorly known, Cahill has also studied the thermal conductivity of thin films using the 3ω method in 1994 [15,16] (see Figure 3.1(b)), although the 3ω method originally was developed to determine thermal quantities of bulk materials (see Figure 3.1(a)). In the following section, the gradual development of the 3ω method is summarized. Figure 3.1 presents an overview of its evolution, developed throughout the decades.

3.1.2. Extension and modifications of the 3ω method

Numerous extensions and enhancements of Cahill's basic 3ω method have been reported in order to investigate the thermal conductivity of thin films and substrate materials [17–20]. For

these purposes, simplifications and assumptions of the heat conduction models are often useful and their validity has been quantitatively discussed by Borca-Tasciuc *et al*. [19]. In 2001, Borca-Tasciuc *et al*. [19] further derived a two-dimensional heat conduction model for a multilayer structure, which considered the substrate thickness, anisotropic thermal conductivity of thin film and substrate materials as well as the finite thickness and heat capacitance of the 3ω heater, so that this heat conduction model covered many relevant layered systems used for research and industrial purposes (see Figure 3.1(c)) [19–21].

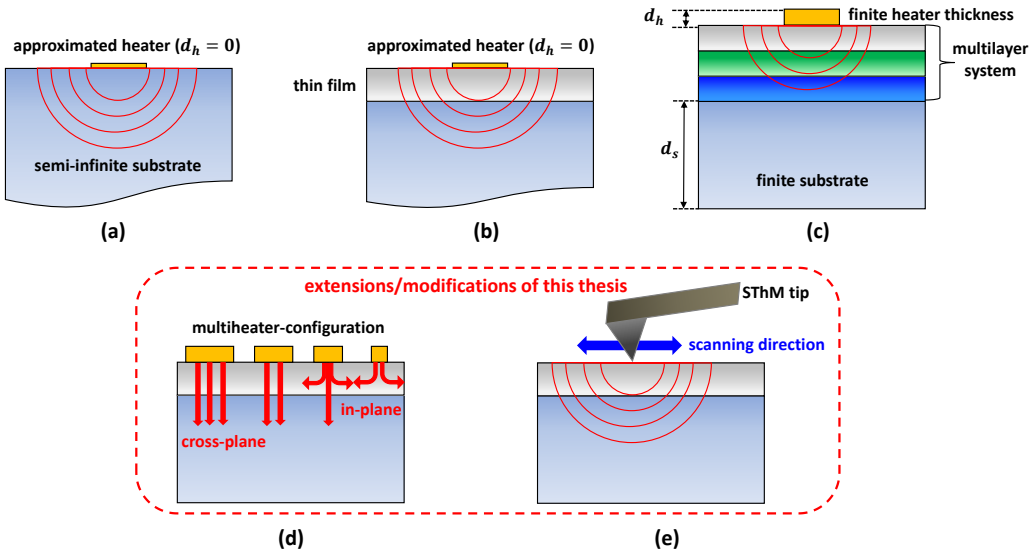

Figure 3.1: Continuous enhancements and modifications of the 3ω method developed throughout the decades: (a) basic 3ω method by Cahill [11] to determine thermal properties of bulk materials (b) Cahill also employed the 3ω method to determine the thermal conductivity of thin films [15] (c) Borca-Tasciuc *et al*. [19] derived a two-dimensional heat conduction equation for a multilayer structure that considers a finite heater and substrate thickness, and anisotropic thermal conductivity of thin films (d) simultaneous determination of in-plane and cross-plane thermal conductivities in anisotropic materials using our multi-heater 3ω method, which utilizes four heaters with different widths (e) our 3ω Microscopy technique to characterize the local thermal conductivities of substrates and thin films.

However, the 3ω method provides a large room of improvement in case of determining the thermal conductivity of anisotropic thin films, especially along the in-plane direction. Measurements of the in-plane thermal conductivity are less common than those of the

cross-plane direction, while the methods used are more diverse [21]. In-plane measurements can be divided into those for the suspended and those for the supported films. In general, methods for the suspended films are only sensitive for the in-plane thermal conductivity and cannot properly detect the heat flow in the cross-plane direction [22]. Furthermore, the microfabrication to obtain a suspended thin film and the significant impact of radiation losses are serious challenges [21]. Therefore, one of our main goals of this thesis is to develop a new approach to measure both cross- and in-plane thermal conductivities of thin films without changing the sample during the measurement.

The 3ω technique has the potential to extract more information from film-on-substrate systems, such as the simultaneous measurement of cross- and in-plane thermal conductivities of anisotropic thin films using our novel multi-heater 3ω method, which utilizes four heaters with different widths [23] (see Figure 3.1(d)). Moreover, the 3ω method is capable to determine thermal conductivity of conductive and semi-conductive films using multilayer systems [17,21,24]. This modification and further extensions we developed within this thesis will be presented in this chapter.

Apart from the application of the macroscopic 3ω method, the basic 3ω measurement principle presented in Section 3.2, can also be utilized to characterize the local thermal conductivities of substrates and thin films, as illustrated in Figure 3.1(e). Based on these preliminary studies of Cahill *et al.* [8,10,11,15,18], we developed a new experimental technique, which merges the basic AFM and 3ω method, in order to quantitatively determine the local thermal conductivity of thin films. To realize this new "3ω Microscopy", the 3ω method has been transferred to the microscopic level by combining the AFM with our extended differential 3ω method (see Section 4.3.2.1), which has never been reported to the best of our knowledge. Within this thesis, the 3ω Microscopy technique is utilized to quantitatively measure the local thermal conductivities of thin-film-on-substrate systems, in order to demonstrate its potential as a promising nanoscale thermal characterization method. The experimental setup of the 3ω Microscopy is described in Section 4.3.2.2.

3.2. Basic principle of the 3ω method

In this section we present and discuss the theoretical fundamentals of the 3ω method. Figure 3.2 shows the typical conductive strip used for the 3ω technique.

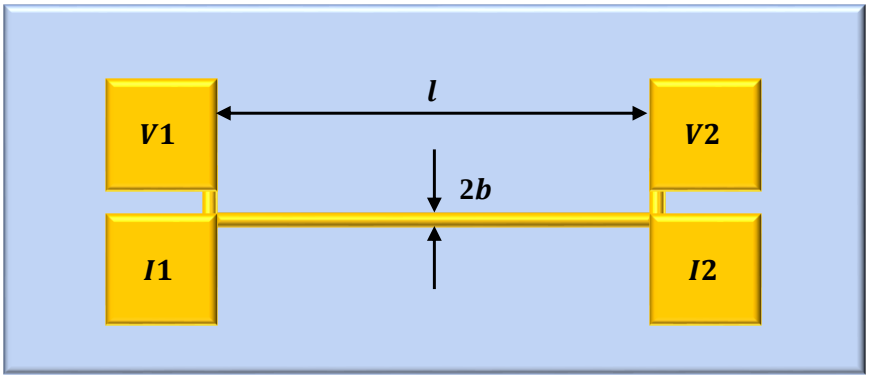

Figure 3.2: Schematic layout of the four pad test structure used to determine the thermal conductivity of a thin film by the 3ω method. A metal strip serves as both heater and thermometer. The four pads are the connections for current leads ($I1, I2$) and voltage leads ($V1, V2$). The strip length l is the distance between the current leads and $2b$ represents the strip width.

In general, a metal strip is directly deposited onto the surface of the specimen, usually by sputtering or lift-off process. To improve the adhesion of the metallic layer to the sample, an additional adhesion layer may be required [17]. The choice of the heater/thermometer material relies on the temperature coefficient of resistance α, that describes the characteristic change of the metal strips electrical resistance R_h as a function of temperature T. Normally, metals have a positive temperature coefficient, meaning that electrical resistance increases with increasing temperature. Most metals and alloys have an approximately linear electrical resistivity variation depending on temperature within a limited temperature range, which depends on the material [25]. If the temperature is not within this linear regime, the electrical resistance as a function of temperature can be approximated by a higher order polynomial [25]:

$$R(T) = R_0[1 + \alpha(T - T_0) + \beta(T - T_0)^2 + \gamma(T - T_0)^3 + \cdots] \quad (3.1)$$

where R_0 is the value of the electrical resistance at a reference temperature T_0 of 0°C. In this thesis measurements have been performed within the linear regime and the constant temperature coefficient of resistance α is therefore defined by:

$$\alpha = \frac{1}{R_{h,0}} \cdot \frac{dR_h(T)}{dT} \tag{3.2}$$

where $R_{h,0}$ is the value of the electrical resistance at a reference temperature T_0. Materials such as gold (Au), platinum (Pt), aluminum (Al) and silver (Ag) are commonly used due to their large temperature coefficients of resistance ($\alpha > 1.0 \times 10^{-3}$ K^{-1}), which are large enough to generate a measurable 3ω voltage signal [17,21,26]. The deposited metallic strip is then microfabricated to obtain four rectangular contact pads connected by pins to the narrow heating strip. The upper two pads serve to apply the AC electrical current that generates the Joule heating and the lower two pads are used for measuring the voltage oscillation across the metal strip, which contains the third harmonic voltage component. The width of the metal heater is defined as $2b$ and the length as l, as it is illustrated in Figure 3.2.

Since an electrical signal should be analyzed in order to determine the thermal conductivity k of a specimen, it is inevitably needed to consider the comprehensive mathematical description of the combined electrical–thermal system. In the following, a brief descriptive derivation of the electrical signal will be described. Firstly, for the heater depicted in Figure 3.2 and Figure 3.3, assuming a long electrical conductive metal strip supplied with a periodic AC current $I(t)$. The current can be written as a function of frequency ω [26],

$$I(t) = I_0 \sin(\omega t) \tag{3.3}$$

Through Joule effect, the dissipated heating power in the metal strip can be written as [26]:

$$P(t) = I(t)^2 R_h = \frac{I_0^2 \cdot R_h}{2}(1 - \cos(2\omega t)) \tag{3.4}$$

Then the resulting periodic power variation $P(t)$ can be further written as:

$$P(t) = P_{DC} + P_{2\omega}\cos(2\omega t) \tag{3.5}$$

As can be seen from Eq. (3.5), the resulting power varies as a function of doubled exciting frequency and thus the temperature oscillation $\Delta T(t)$ also varies at 2ω [26],

$$\Delta T(t) = \Delta T_{2\omega}\cos(2\omega t + \varphi) \tag{3.6}$$

Due to the temperature coefficient α of the material, the resistance of the metal strip is influenced by the time-dependent temperature oscillation $\Delta T(t)$ and the resistance $R_h(t)$ changes to the doubled exciting frequency as well. While the rms value of this resistance $R_{h,0}$ is dependent on the absolute temperature T as well as on the temperature coefficient α, and the periodical resistance variation $\Delta R_{h,0}$ depends on the temperature coefficient α and the amplitude of the periodical temperature variation ΔT, which finally contains the information of the thermal conductivity [26]:

$$R_h(t) = R_{h,0} + \Delta R_h\cos(2\omega t + \varphi) \tag{3.7}$$

The Joule heating is linked with a certain inertia, hence a phase shift φ between the excitation current and the resulting periodical temperature variation appears. Since the voltage drop across the metal strip (simultaneously acting as a heater and thermometer) will be analyzed, the resulting equation for the time-dependent voltage $V(t)$ is still missing. Multiplying the periodical electrical current $I(t)$ by the resistance variation $R_h(t)$ and utilizing the theorem of addition, the analytical description of $V(t)$ can be obtained as [26]:

$$\begin{aligned} V(t) = R_{h,0}\cdot I_0\sin(\omega t) - \frac{R_{h,0}\cdot I_0\cdot\alpha\cdot\Delta T_{2\omega}}{2}\sin(\omega t + \varphi) \\ + \frac{R_{h,0}\cdot I_0\cdot\alpha\cdot\Delta T_{2\omega}}{2}\sin(3\omega t + \varphi) \end{aligned} \tag{3.8}$$

$$V(t) = V_0\cdot sin(\omega t + \gamma) + \frac{V_0\cdot\alpha\cdot\Delta T_{2\omega}}{2}\cdot sin(3\omega t + \varphi) \tag{3.9}$$

At this point, it should be noted that the resulting voltage across the metal strip (see Eq. (3.8)) consists of three different components, where the first two components give the variations at the exciting frequency ω and the last one constitutes the variation at the third harmonic of the exciting frequency 3ω. While the first term varying as a function of ω contains the temperature due to the included rms value of the resistance $R_{h,0}$, the second term varying as a function of ω and the third term varying at 3ω contain the thermal conductivity through $\Delta T_{2\omega}$. Thus, the analysis of the ω component provides information about the superposed temperature and thermal conductivity, while the analysis of the 3ω component provides the information about the isolated material specific thermal conductivity.

Furthermore, the ω and 3ω components of the heater voltage response can be identified in Eq. (3.9). The first term is typically three orders of magnitude greater than the 3ω component, and is more difficult to be utilized in thermal measurements, because it only contains information about the imaginary part of the thermal oscillation [11]. On the other hand, the second term is proportional to the real and imaginary part of the temperature oscillation [11], providing a good alternative to directly measure the thermal transfer function of the studied sample in the frequency-domain. Since the third harmonic response of the voltage is a very small quantity, the lock-in technique is required to extract this signal [11,17,21]. The thermal oscillation can therefore be obtained from the 3ω component (see Eq. (3.10)) in terms of rms (root mean square) quantities, as usually measured by lock-in amplifiers:

$$\Delta T_{2\omega} = \frac{2}{\alpha}\frac{V_{3\omega,rms}}{V_{0,rms}} \tag{3.10}$$

Since in a typical 3ω experiment, V_ω is at least one thousand times greater than $V_{3\omega}$ [11,17,26], the input voltage signal V_0 can be approximately estimated as the first harmonic voltage response V_ω ($V_0 \approx V_\omega$) and Eq. (3.10) becomes:

$$\Delta T_{2\omega} = \frac{2}{\alpha}\frac{V_{3\omega,rms}}{V_{\omega,rms}} \tag{3.11}$$

This relation provides a direct experimental measurement of the thermal wave amplitude $\Delta T_{2\omega}$. The thermal properties of the specimen under analysis can then be obtained by fitting the measured amplitude of the thermal oscillation to an appropriate analytical model of heat conduction.

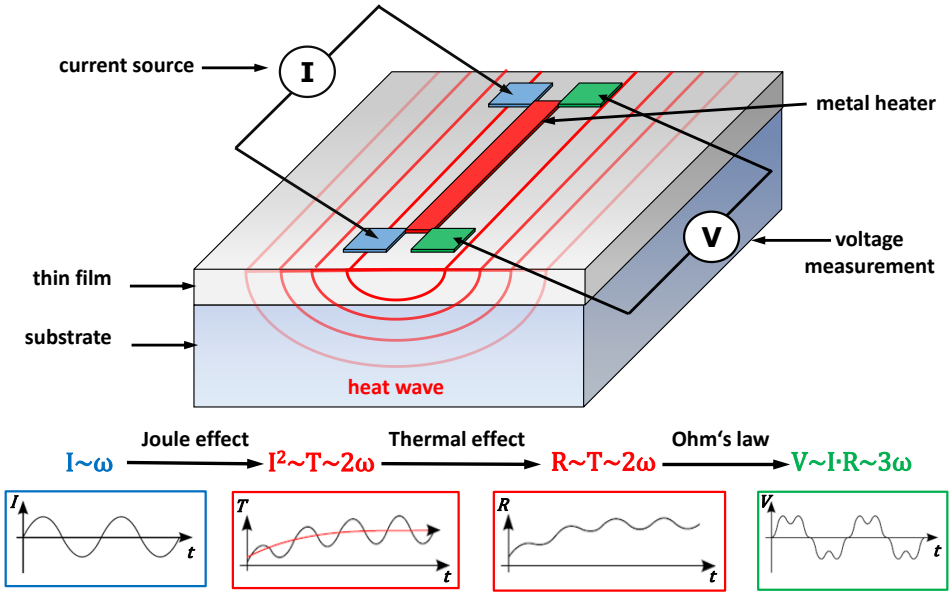

Figure 3.3: The 3ω method uses a single metal strip as both the heater and thermometer. An AC heating current at angular frequency ω heats the surface of the sample at a frequency of 2ω. Since the resistance of a metal increases with temperature, temperature oscillations produce an oscillation of the electrical resistance at a frequency of 2ω. Consequently, the voltage drop across the metal line has a small component at a frequency of 3ω that can be used to measure the temperature oscillations and the thermal response of the film-on-substrate sample.

If the 3ω signal is defined as the signal of interest, there is still the question of how to analyze this signal in order to extract the thermal conductivity quantitatively. Therefore, the next section discusses in details the derivation of the solution to the transient heat conduction equation for a finite width line heater with a finite width $2b$, deposited onto the film-on-substrate system. In order to determine the temperature oscillation of the heater $\Delta T_{2\omega}$, the solution of the heat conduction equation will be discussed. The obtained temperature oscillation of the heater $\Delta T_{2\omega}$ solution will then be used to find a relation with the thermal conductivity of the analyzed sample. For this purpose, we consider first a one-dimensional

line source of heat. Then, the effect of the finite width of the heater will be integrated into the model, allowing the thermal analysis for both the bulk materials and thin films.

3.3. Theoretical basics of the 3ω method for specific layer-systems

The measured 3ω voltage $V_{3\omega}$ is directly related to the thermal wave amplitude $\Delta T_{2\omega}$, which is then compared to a thermal model depending on the excitation frequency ω to determine the thermal conductivity k of thin films and bulk materials. Thus, the 3ω heat conduction model requires the obtained value of the thermal wave amplitude expressed in terms of the first V_{ω} and the third harmonic $V_{3\omega}$ of the measured voltage. Then, to relate the measured quantities with the thermal properties of the specimen, an analytical solution of the thermal wave amplitude as a function of the thermal conductivity $\Delta T_{2\omega}(k)$ of the specimen under analysis has to be found.

The following sections describe this process in detail, providing the fundamentals for the thermal measurements performed in this thesis. First, an expression for the thermal wave as functions of the experimental variables is obtained. Then, data reduction is performed by finding an analytical solution to the temperature oscillation, in the case of an infinitely narrow heater deposited onto the semi-infinite isotropic substrate (in Section 3.3.1.1). The analysis is extended by considering a heater of finite width, as it is the case in 3ω experiments (in Section 3.3.1.2). Finally, an analytical expression of the thermal wave amplitude induced by a thin film deposited onto a substrate is given, and the differential approach is described in Section 3.3.2. The following sections provide a detailed review of the data reduction proposed by Cahill and co-workers for the 3ω method, compiling the whole derivation of the experimental thermal conductivity for bulk materials and thin films, which is scattered into several papers in the literature [8,10,11,15,19,27,28].

3.3.1. Thermal conductivity determination of substrates

Cahill and Pohl [8] derived an approximate solution for the increase of temperature of a heater deposited on an isotropic semi-infinite substrate. Therefore, a heater of width $2b$, which is much smaller than the wavelength of the diffusive thermal wave was used. This particular geometry leads to a cylindrical heat flow pattern through the studied volume, with the temperature gradients in the radial direction (see Figure 3.4). The theoretical background used to obtain the temperature oscillation of the heater, which allows for the direct determination of the thermal conductivity, will be described in the following section.

3.3.1.1. Case of an infinitely narrow heater on a semi-infinite isotropic substrate

It is convenient to begin the analysis with a simplified geometry, consisting of a one-dimensional line source of heat, as can be seen in Figure 3.4(a). An analytical solution of the heat conduction equation, considering an infinitely narrow line source of heat at the surface of a semi-infinite volume, was firstly obtained by Carslaw and Jaeger [9]. The expression for the real part of the thermal wave at a distance $r = \sqrt{x^2 + y^2}$ from the line heat source is given by [9]:

$$\Delta T_{2\omega}(r,t) = \frac{P_l}{k\pi} K_0(qr) \cdot e^{\mathrm{i}2\omega t} \tag{3.12}$$

here P_l is the power per unit length generated by the AC heating current applied through the metal heater, k the thermal conductivity of the specimen, K_0 the zeroth order modified Bessel function of the second kind (see Appendix A for detailed information), with argument qr, and $q = (1+i)\left(2\omega\rho c_p/k\right)$ [9]. The quantity $\lambda = |1/q|$ refers to the penetration depth at which the thermal oscillation propagates into the sample during one cycle of the AC power heating (see Figure 3.4). Therefore, the penetration depth of the thermal oscillation is given by [11]:

$$\lambda = \frac{1}{|q|} = \sqrt{\frac{a}{2\omega}} = \sqrt{\frac{k}{2\omega\rho c_p}} \tag{3.13}$$

where a is the thermal diffusivity, c_p the specific heat capacity and ρ the density of the investigated material.

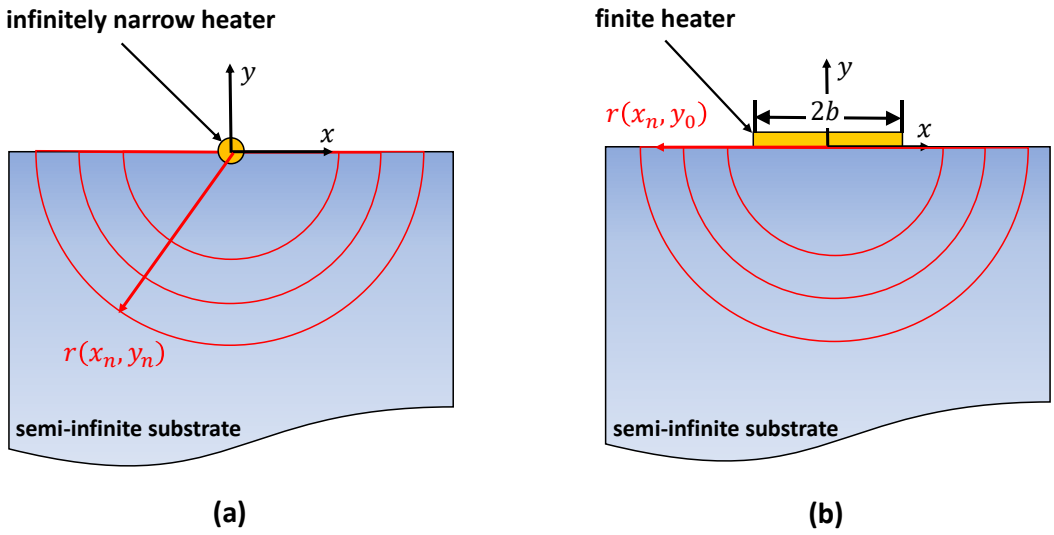

Figure 3.4: Cross-section of different heat sources on the surface of semi-infinite substrate materials: (a) cylindrical heat pattern generated by an infinitely narrow heater (solution from Carslaw and Jaeger [9]) (b) the finite width line heater (solution from Cahill [11]).

The exact solution of the thermal wave amplitude (see Eq. (3.12)) can be derived, if considering that the substrate is a semi-infinite isotropic medium, and assuming zero heat flux through the sample surface [9,11]. Eq. (3.12) is also based on the assumptions that the heater mass can be neglected and the heater behaves as an infinitely good thermal conductor with negligible thickness and heat capacity [9,11,19]. Additionally, it is considered that the metal strip is a uniform line heat source of infinite length in contact with the investigated sample, assuming negligible thermal boundary resistance between the heater and the underlying material.

Figure 3.5 shows the time-evolution of the real part of the temperature oscillation $\Delta T_{2\omega}$ as a function of the distance r [29]. Following the zeroth order Bessel function of the second kind [9], the thermal wave decays rapidly as the function of the distance r away from the heater.

By this means, the use of an AC current allows us to analyze a very small volume of the sample and to be weakly sensitive to heat loss by convection and radiation due to the confinement of the heat wave inside the sample, and to the rapid decay of the temperature oscillations compared to the characteristic radiative time [21,26].

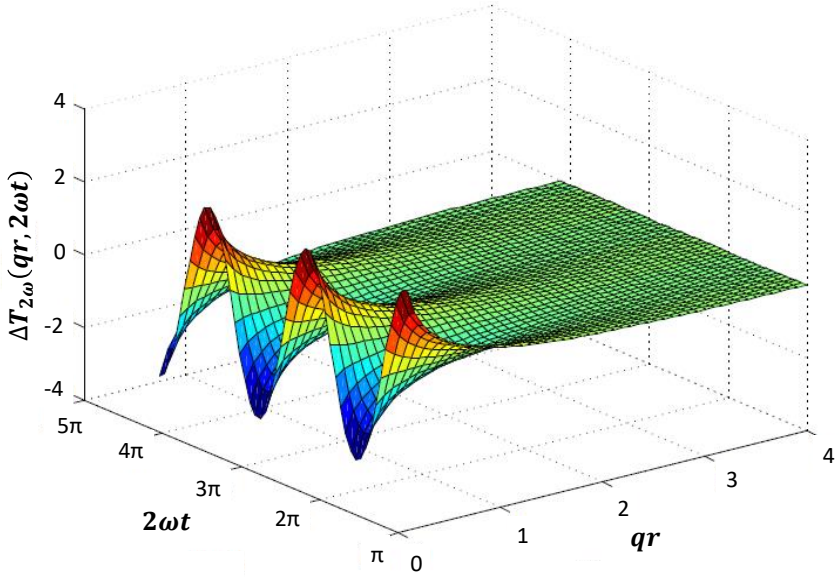

Figure 3.5: Time-evolution of the thermal oscillation amplitude at distance r from an infinitely narrow heater. Visualization of the real part (in-phase) of Eq. (3.12). The oscillations decreases rapidly away from the heater and are even in the time-domain (modified and adapted by Ref. [29]]).

To avoid parasitic edge effects in the measurement, the length l of the heat source used in the experiments must be very long compared to its width $2b$, such that $l \gg 2b$, and the width must be constant along the heat source [11]. Taking into consideration of the semi-infinite medium assumption, Eq. (3.12) is valid if the penetration depth λ of the heat wave is smaller than the thickness of the studied sample, such as that $d_s > \lambda_s$, where subscript s refers to the substrate. Quantitative analysis carried out by Borca-Tasciuc *et al.* [19] suggested that $d_s/\lambda_s > 5$ in order to keep measurement errors under 1%, as the amplitude of the thermal oscillation decays 1% of its value after five thermal wavelengths. However, numerical simulations performed by Jacqout *et al.* [30] showed that even a ratio of $d_s/\lambda_s > 2$ appeared to be acceptable [21].

3.3.1.2. Case of a heater with a finite width

The effect of the finite heater width can be included in the model by adding an infinite number of one-dimensional line heaters along the whole heater width $2b$ [11,31] (see Figure 3.4(b)), which involves a convolution integral. As observed in Figure 3.5, the temperature oscillation is an even function in the time-domain. It is then convenient to use the cosine Fourier transform with respect to the *x*-coordinate [11,32]. The Fourier cosine transform pair in the wave-number-domain η is [11]:

$$\hat{f}(\eta) = \int_0^\infty f(x) \cdot \cos(\eta x)\ dx \tag{3.14}$$

$$f(x) = \frac{2}{\pi} \int_0^\infty \hat{f}(\eta) \cdot \cos(\eta x)\ d\eta \tag{3.15}$$

Considering only the thermal oscillation at the surface of the sample (y = 0) [11], the Fourier transform in the wave-number-domain η of a zeroth order Bessel function of the second kind K_0, is given by [11,29,32]:

$$\Delta T_{2\omega}(\eta) = \int_0^\infty \Delta T_{2\omega}(x) \cos(\eta x)\ dx = \frac{P_l}{\pi k} \int_0^\infty K_0(qx) \cos(\eta x)\ dx = \frac{P_l}{2k} \left(\frac{1}{\sqrt{\eta^2 + q^2}} \right) \tag{3.16}$$

Since the heat in the metal strip follows an even behavior over the width, the thermal wave amplitude for a finite width heater can be obtained by the product of Eq. (3.16) with the Fourier transform of the heat source in the x-space, which in this case can be expressed as a rectangular pulse $rect(x)$, as it is illustrated in Figure 3.6 [11,29]:

$$\Delta T_{2\omega}(\eta) = \frac{P_l}{2k} \left(\frac{1}{\sqrt{\eta^2 + q^2}} \right) \int_0^b rect(x) \cdot \cos(\eta x)\ dx = \frac{P_l}{2k} \cdot \frac{\sin(\eta b)}{\eta b \sqrt{\eta^2 + q^2}} \tag{3.17}$$

Taking the inverse transform of Eq. (3.17) to switch $\Delta T_{2\omega}(\eta)$ back to the space-domain, the above equation can be re-written into [11,29]:

$$\Delta T_{2\omega}(x) = \frac{2}{\pi}\int_0^{\infty} \Delta T_{2\omega}(\eta)\cdot\cos(\eta x)\ d\eta = \frac{P_l}{\pi k}\int_0^{\infty} \frac{\sin(\eta b)}{\eta b\sqrt{\eta^2+q^2}}\cdot\cos(\eta x)\ d\eta \qquad (3.18)$$

Since the temperature measurements are performed over the width of the metal strip, the amplitude of the thermal oscillation $\Delta T_{2\omega}(x)$ is an average value across the metal strip.

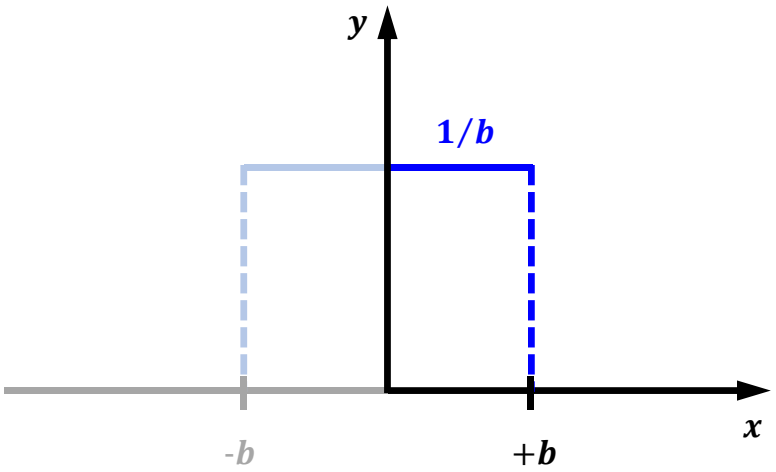

Figure 3.6: Rectangular function to realize the finite heater width $2b$.

Thus, the average temperature increase in the heater can be obtained by integrating Eq. (3.18) in the space-domain from 0 to b [11]:

$$\Delta T_{2\omega|avg} = \frac{1}{b}\int_0^{b} \Delta T_{2\omega}(x)\ dx = \frac{P_l}{\pi k}\int_0^{\infty} \frac{\sin^2(\eta b)}{(\eta b)^2\sqrt{\eta^2+q^2}}\cdot d\eta \qquad (3.19)$$

The integral in Eq. (3.19) has no direct analytical closed form. To obtain an approximate solution, Cahill [11] proposed to analyze its limit when the thermal penetration depth λ is much larger than the metal strips half-width b ($\lambda \gg b$) and when the thermal penetration depth is much smaller than the half-width b of the metal strip ($\lambda \ll b$). Therefore, the average amplitude of the heater's thermal oscillation $\Delta T_{2\omega|avg}$ as a function of heating frequency f can be divided into a linear regime ($\lambda \gg b$) at low frequencies and a planar regime ($\lambda \ll b$) at high frequencies [11].

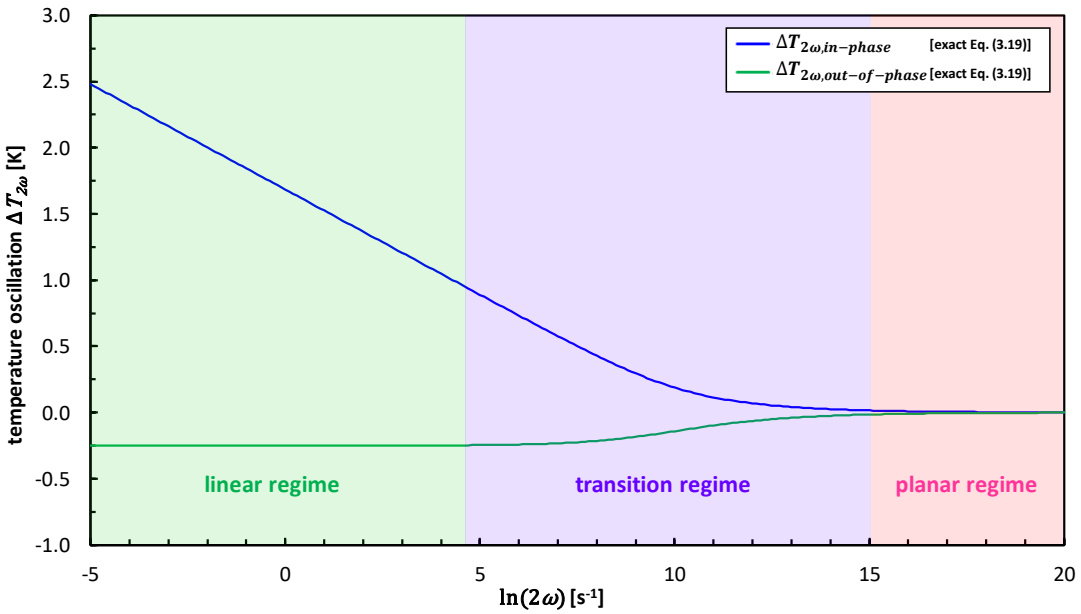

Figure 3.7: The in-phase (blue line) and out-of-phase (green line) components of the average amplitude of the heater's temperature oscillations versus the heating frequency ω according to Eq. (3.19). The rms power per unit length P_l is 1 Wm^{-1}, the heater half width b is 10 µm, the thermal conductivity k is 1 $Wm^{-1}K^{-1}$ and the thermal diffusivity a is 1 mm^2s^{-1}. The average amplitude of the thermal oscillation $\Delta T_{2\omega|avg}$ as a function of the heating frequency ω can be divided into a linear regime (green area) at low frequencies ($\lambda \gg b$) and a planar regime (red area) at high frequencies ($\lambda \ll b$). The transition regime (violet area) is defined between these two cases. The linear regime is used to determine the thermal conductivity of the sample (modified from Ref. [29]).

The transition regime can be defined between these two cases. For the linear regime, Borca-Tasciuc *et al.* [19] suggested that $\lambda/b > 5$ in order to keep measurement errors of the 3ω method under 1%. Furthermore, for the planar regime Koninck [29] recommended that $\lambda/b < 0.2$ in order to keep measurement errors below 1%.

3.3.1.3. Solution of the exact equation

a) Approximate solution for the linear regime

As presented in Figure 3.7, the linear regime is that part where the in-phase (real part) temperature oscillation $\Delta T_{2\omega}$ decreases linearly as a function of thermal excitation frequency 2ω and where the out-of-phase (imaginary part) temperature oscillations component has a

constant negative value. This regime is defined within the low frequencies when the thermal penetration depth is much larger compared to the half-width of the heater ($\lambda \gg b$) [11]. In this case, the wave number of the thermal oscillation is defined over a domain such that $1/\lambda < \eta < 1/b$ [29]. Then the upper limit of the integral in Eq. (3.19) can be replaced by $1/b$. Additionally, $\sin(\eta b)/\eta b$ can be evaluated at the limit where b tends towards 0:

$$\lim_{b\to 0} \frac{\sin(\eta b)}{\eta b} = 1 \tag{3.20}$$

After these, the approximated solution to Eq. (3.19) is given by:

$$\Delta T_{2\omega|avg} = \frac{P_l}{\pi k}\left[\ln\left(\frac{1}{bq} + \sqrt{\frac{1}{(bq)^2}+1}\right) - \ln q\right] \approx \frac{P_l}{\pi k}[\gamma - \ln(bq)] \tag{3.21}$$

where γ is a fitting constant close to 0.923 [14,18], adjusted to fit the experimental data. However, Lee and Cahill [18] demonstrated that γ = 1.05 fits the thermal data more precisely. As $q = (1+\mathrm{i})\left(2\omega\rho c_p/k\right)^{1/2}$, is given in terms of frequency ω, Eq. (3.21) can be further re-written into (see Appendix A for detailed derivation) [11]:

$$\Delta T_{2\omega|avg} = \frac{P_l}{\pi k}\left[\frac{1}{2}\ln\left(\frac{k}{\rho c_p b^2}\right) - \frac{1}{2}\ln(2\omega) + \gamma\right] - \mathrm{i}\frac{P_l}{4k} \tag{3.22}$$

Eq. (3.22) indicates that the thermal conductivity of an isotropic substrate can be obtained from the gradient of the in-phase magnitude of the measured $\Delta T_{2\omega,avg}$ values depending on $\ln(2\omega)$ by [11]:

$$k = \frac{P_l}{2\pi}\left[\frac{d}{d\ln(2\omega)}\Delta T_{2\omega|avg}\right]^{-1} \tag{3.23}$$

Eq. (3.22) is plotted for P_l = 1 Wm^{-1}, half-width of the heater b = 10 µm, substrate thermal conductivity k_s = 1 Wm^{-1}K^{-1}, and thermal diffusivity a = 1 mm^{2}s^{-1}. Figure 3.8 indicates that for the linear regime, the in-phase component decreases logarithmically as the thermal

excitation frequency 2ω increases. However, over the same frequency range, the out-of-phase temperature oscillations keep constant at a negative value.

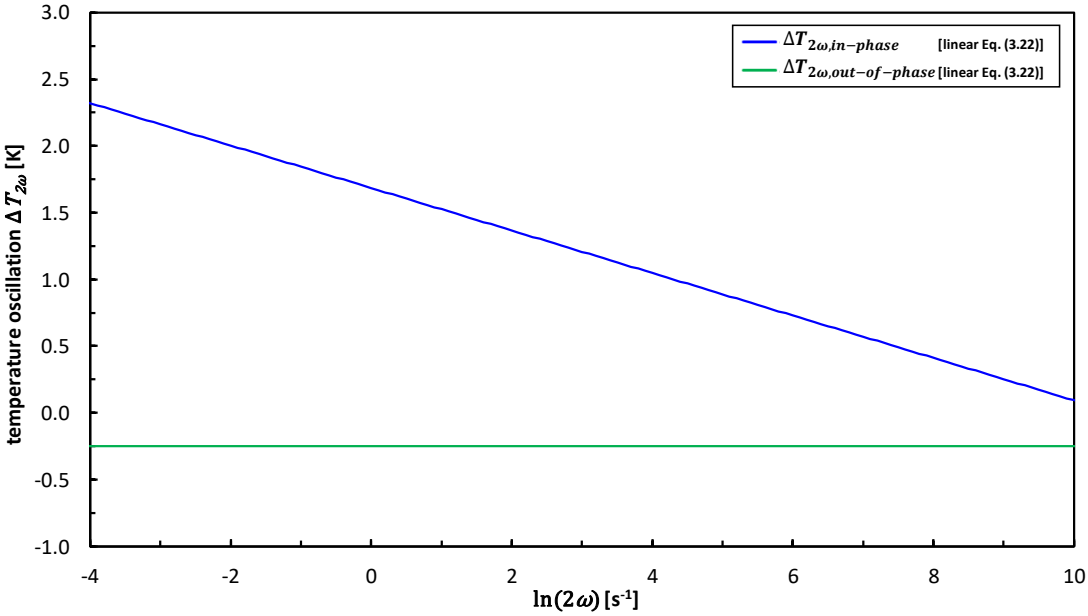

Figure 3.8: Temperature oscillations with respect to the natural logarithm of the thermal excitation frequency 2ω for the linear regime according to Eq. (3.22). The rms power per unit length P_l is 1 Wm^{-1}, the heater half width b is 10 µm, the thermal conductivity k is 1 Wm^{-1}K^{-1} and the thermal diffusivity a is 1 mm^{2}s^{-1} (modified from Ref. [29]).

Substituting Eq. (3.22) in Eq. (3.10) yields the third harmonic voltage $V_{3\omega}$ [29]:

$$V_{3\omega} = -\frac{V_0^3 \alpha}{4\pi l k_s R_{h,0}} \left(\ln(2\omega) + \ln\left(\frac{b^2}{a}\right) - 2\gamma \right) - i\frac{V_0^3 \alpha}{8 l k_s R_{h,0}} \tag{3.24}$$

Determining the slope of the linear relation between the in-phase harmonic voltage and the natural logarithm of the thermal excitation frequency 2ω, we can determine the thermal conductivity of the substrate k_s as follows:

$$k_s = \frac{V_0^3 \alpha}{4\pi l R_{h,0}} \cdot \frac{1}{gradient} \tag{3.25}$$

A direct derivation of k_s is also possible from the imaginary part of the heat wave (out-of-phase oscillation). However, Cahill [11] has experimentally found that Eq. (3.23) and Eq. (3.25) are more reliable and reproducible. This approach is known as the 3ω slope method.

It is advantageous compared to other transient techniques, because it does not require independent measurements of thermal diffusivity or volumetric heat capacity [11,31].

b) Approximate solution for the planar regime

For the in- and out-of-phase temperature oscillations equal in magnitude but opposite in signs, we can define a planar regime at higher frequencies, where the thermal penetration depth λ is considered to be lower than the half-width b of the metal heater ($\lambda \ll b$). Accordingly, we can obtain the following equation [14,29]:

$$\lim_{b\to\infty} \frac{1}{\pi b}\left[\frac{\sin(\eta b)}{\sin(\eta)}\right]^2 = \delta(\eta) \tag{3.26}$$

Substituting Eq. (3.26) in Eq. (3.18) we obtain [29]:

$$\Delta T_{2\omega|avg} = \frac{P_l}{bk}\int_0^\infty \frac{\sin^2(\eta)\,\delta(\eta)}{\eta^2\sqrt{\eta^2+q^2}}\cdot d\eta = \frac{P_l}{2bkq} \tag{3.27}$$

Given that $\sqrt{i} = \frac{1+i}{\sqrt{2}}$, Eq. (3.27) can be written as [29]:

$$\Delta T_{2\omega|avg} = \frac{P_l}{2bk\sqrt{\frac{2\omega}{a}}} e^{\left(-i\frac{\pi}{4}\right)} \tag{3.28}$$

Clearly there is a $-\pi/4$ shift, which indicates a phase delay between the temperature oscillation and the heating power. Furthermore, Eq. (3.28) shows that the real and imaginary parts of the temperature oscillations have the same magnitude while their signs are opposite. Substituting Eq. (3.28) in Eq. (3.10) yields:

$$V_{3\omega} = \frac{V_0^3\,\alpha}{4\sqrt{2}lbR_{h,0}k_s\sqrt{\frac{2\omega}{a}}}(1-i) \tag{3.29}$$

The approximate solutions are compared with the exact solution by plotting Eq. (3.19), Eq. (3.22) and Eq. (3.28) as illustrated in Figure 3.9.

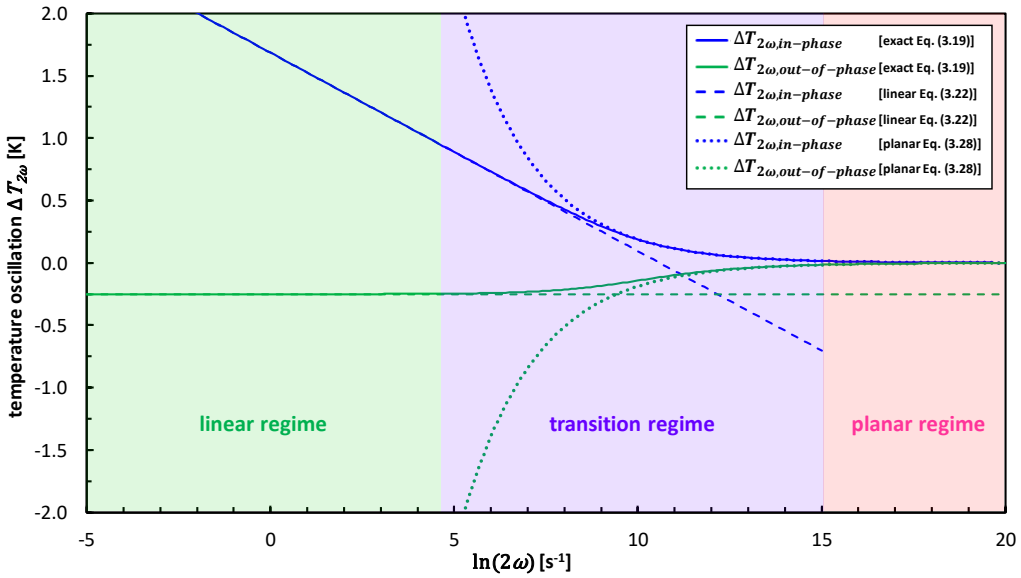

Figure 3.9: Comparison between the exact and appropriate solutions for the linear and planar regimes. The rms power per unit length P_l is 1 Wm^{-1}, the heater half width b is 10 µm, the thermal conductivity k is 1 Wm^{-1}K^{-1} and the thermal diffusivity a is 1 mm^{2}s^{-1}. The average amplitude of the thermal oscillation $\Delta T_{2\omega|avg}$ as a function of the heating frequency ω can be divided into a linear regime (green area, Eq. (3.22)) at low frequencies ($\lambda \gg b$) and a planar regime (red area, Eq. (3.28)) at high frequencies ($\lambda \ll b$). The transition regime (violet area) is defined between these two cases. The linear regime is used to determine the thermal conductivity of the sample (modified from Ref. [29]).

The rms power, the metal heater half-width, the thermal conductivity and thermal diffusivity are the same as in Figure 3.7 and Figure 3.8. The solid lines are the exact solutions while the dotted lines are the approximate solutions for the planar regime and the dashed lines are the approximate solutions of the linear regime. The blue lines represent the in-phase temperature oscillations and the green lines represent the out-of-phase ones.

In order to precisely determine the thermal conductivities of substrate materials, measurements must be performed within the frequency range of the linear regime. In the following section, the boundary conditions restricting the frequency range of the linear regime are defined.

c) Linear regime boundaries

Cahill's equation of the heater's temperature oscillations (Eq. (3.19)) considers an isotropic semi-infinite substrate as explained in Section 3.3.1.1. However, in practice, the substrate has a finite thickness d_s. Therefore the boundaries of the linear regime must be defined according to the thickness of the substrate and the width of the metal heater deposited onto the substrate. To guarantee that the assumption of a semi-infinite substrate is valid, Borca-Tasciuc *et al.* [19] suggested that the ratio between the thickness of the substrate and the penetration depth of the thermal wave should be larger than five ($d_s/\lambda_s > 5$). Furthermore, the substrate must see the 3ω heater as a line source of heat, which can be accomplished if the ratio between the penetration depth of the thermal wave and the heater half-width is also larger than five ($\lambda_s/b > 5$) [19]. Both approximations keep measurement errors of the 3ω method under 1% [19].

3.3.2. Thermal conductivity determination of thin films

Probably one of the most interesting aspects of the 3ω technique is its capability of determining the cross- and in-plane thermal conductivities of thin films deposited onto a substrate. Today, this approach is widely used and is considered as one of the most effective experimental methods for thermal characterization of thin films and nanostructured materials, as shown in Section 2.4. In the following sections, methods used to obtain the cross-plane (Section 3.3.2.1) and in-plane (Section 3.3.2.2) thermal conductivities of thin films will be presented.

3.3.2.1. Determination of cross-plane thermal conductivity

Measurements of the cross-plane thermal conductivity are more common than those of the in-plane conductivities [21]. Since thin films generally exhibit an anisotropic and heterogeneous structure, their thermal conductivity values are often direction-dependent. The experimental technique proposed by Cahill *et al.* [15], which is an extension of the "slope method" presented in Section 3.3.1, provides an approach to perform cross-plane thermal

conductivity measurements on thin films. It is based on the fact that using a metal strip with a width $2b$, which is much larger than the film thickness d_f ($2b \gg d_f$), will lead to a one-dimensional heat flux in the direction normal to the film surface, the so-called "cross-plane direction", as illustrated in Figure 3.10(a).

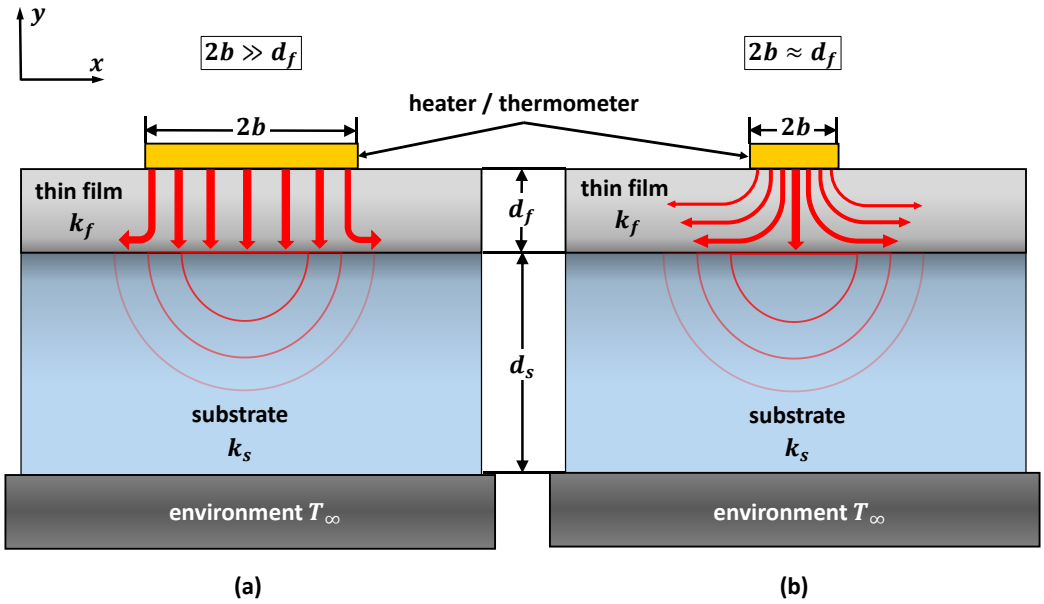

Figure 3.10: Thermal wave produced by (a) a heater much greater than the film thickness $2b \gg d_f$ for cross-plane measurements and (b) a narrow heater for in-plane measurements.

Therefore, the half-width b of the metal heater must be large enough to comply with the following condition [19]:

$$\frac{b}{d_f}\left(\frac{k_{f\perp}}{k_{f\parallel}}\right)^{1/2} \geq 5.5 \tag{3.30}$$

where $k_{f\perp}$ and $k_{f\parallel}$ represent the cross- and in-plane thermal conductivity values of the thin film, and d_f the film thickness, respectively. This behavior can be approximated as a one-dimensional heat conduction model. On the other hand, Kurabayashi *et al.* [22,33] and Borca-Tasciuc *et al.* [28] reported that working with a very narrow heater will results in a divergent heat pattern that spreads along the in-plane direction, as shown in Figure 3.10(b). In this case, the metal strip is sensitive to both the cross- and in-plane thermal conductivity components, and the behavior can be approximated as a two-dimensional heat conduction

model [28]. It is noteworthy to mention that our discussions are focused on both cross- and in-plane thermal conductivity measurements of thin films in this thesis.

In the case of a film with a thermal conductivity k_f smaller than that of the substrate k_s, the film-on-substrate system behaves as a series of thermal resistors [19,21]. Therefore, the studied film contributes to the temperature rise measured along the heater by adding a frequency-independent temperature oscillation (ΔT_f). Considering that the power per unit area transferred from the metal heater is a constant in the y-direction ($Q = P_l/2b$), the temperature drop across the film can be simply obtained by Fourier's law (Eq. (2.5)) [16]:

$$\Delta T_f = \int_0^{d_f} \frac{Q}{k_f}\, dy = \frac{P_l.d_f}{2b \cdot k_f} \tag{3.31}$$

where k_f is the cross-plane thermal conductivity of the studied film. The increase in the amplitude of the thermal oscillation due to the thin film can therefore be written as follows:

$$\Delta T_{2\omega} = \Delta T_f + \Delta T_s \tag{3.32}$$

where the subscript f and s correspond to the film and the substrate, respectively. In consequence, the thermal conductivity of the film can be obtained by subtracting the calculated temperature rise of the bare substrate from the experimental measured temperature rise of the strip, caused by the film-on-substrate system [19].

$$k_f = \frac{P_l \cdot d_f}{2b\left(\Delta T_{2\omega} - \Delta T_{s,calc}\right)} \tag{3.33}$$

Eq. (3.33) allows for the direct measurement of the thermal conductivity of the studied film. It is relevant to mention that, if the film of interest is electrically conductive, the heater has to be necessarily isolated by a dielectric film [21]. In this case a thin SiO_2 or Si_3N_4 film is normally deposited onto the sample surface, as it is illustrated in Figure 3.11(b).

The thermal response of the substrate $\Delta T_{s,calc}$ can be calculated directly from Eq. (3.22) and subtracted from the measured $\Delta T_{2\omega}$. Thermal conductivity of the substrate k_s can also be calculated from the slope of $\Delta T_{2\omega|avg}$ versus $\ln(2\omega)$ as shown by Eq. (3.23) and Eq. (3.25) [11,19]. The frequency range for thin film thermal conductivity measurement depends on the applicable error level in the results when using the linear regime approximation (see Section 3.3.1.3).

The differential technique using a reference sample, is a further extension of the above discussed method. It is particularly useful for analyzing complex systems composed of several films (involving dielectric, nucleation or buffer layers), because it allows for the determination of the thermal conductivity of the specific film in the multilayer structure [21,26,31]. Furthermore, the differential approach is capable to obtain the thermal conductivity values of electrically conductive thin films, such as metals and semiconductors [21,26]. However, a dielectric thin film between the metal 3ω heater and the conductive thin film of interest is required, as illustrated in Figure 3.11. In such systems, the voltage drop across the metal heater depends on the temperature rise caused by the whole multilayer structure. The measured thermal transfer function is therefore the sum of the contributions of the thermal oscillations coming from different components of the system [21,26,31].

To extract the signal changes exclusively caused by the film of interest, the differential approach uses the average temperature difference measured between two similar sets of experiments, one involving the specimen and the other performed on a system without the studied film, which serves as a reference sample. The composition of the reference sample (a) and the multilayer structure (b) including the film of interest are shown in Figure 3.11.

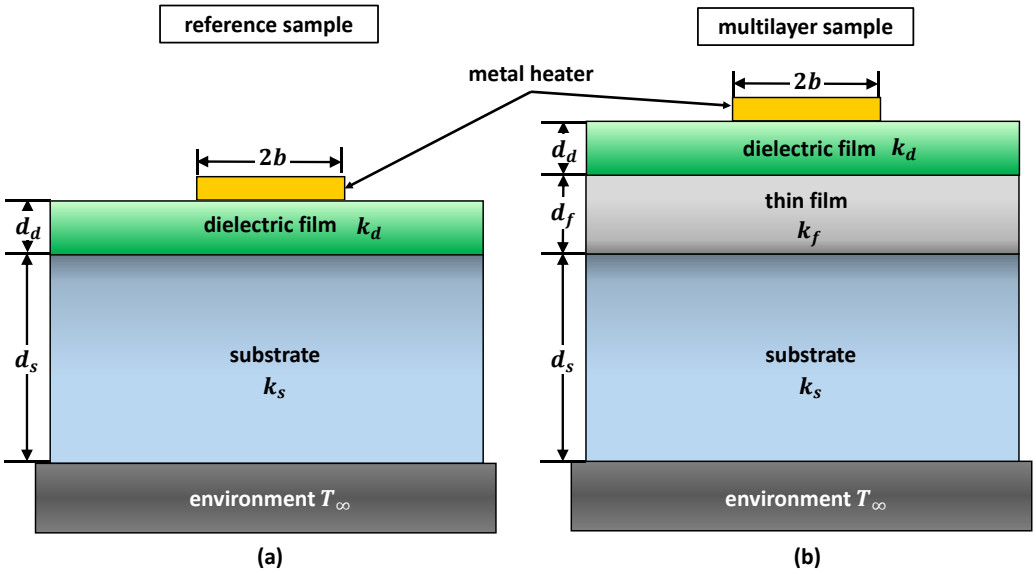

Figure 3.11: Cross-sections of film-on-substrate samples required for the differential 3ω method: (a) reference sample without the film of interest (colored in grey); (b) multilayer sample including the film of interest and the reference film-on-substrate structure. The differential technique is capable to obtain the thermal conductivity values of electrically conductive thin films. Therefore, a dielectric thin film (colored in green) between the 3ω heater and the conductive thin film of interest is required.

By removing the signal of the reference sample from that of the specimen with the studied film, it is possible to subtract the common background contribution of the parasitic interfacial thermal resistance, such as the one between the metal heater and the underlying film, and the one between the substrate and the first deposited layer [19,21,31]. In the same way, the contribution of additional elements, such as buffer or nucleation layers, can also be subtracted from the total experimental temperature rise, which is obtained at comparable power inputs by similar heaters deposited on the specimen and the reference structure [19,21,31]. The temperature oscillations of both the reference sample and the multilayer structure, including the film of interest, are shown in Figure 3.12. Under this condition, the thermal conductivity of the film is given by [19,21,31]:

$$k_f = \frac{d_f}{2}\left[\left(\frac{2 \cdot V_{3\omega} \cdot b}{P_l \cdot \alpha \cdot V_\omega}\right)_{r+f} - \left(\frac{2 \cdot V_{3\omega} \cdot b}{P_l \cdot \alpha \cdot V_\omega}\right)_{r}\right]^{-1}_{avg} \tag{3.34}$$

The subscript $r + f$ and r correspond to the specimen with the studied film and the reference structure, respectively.

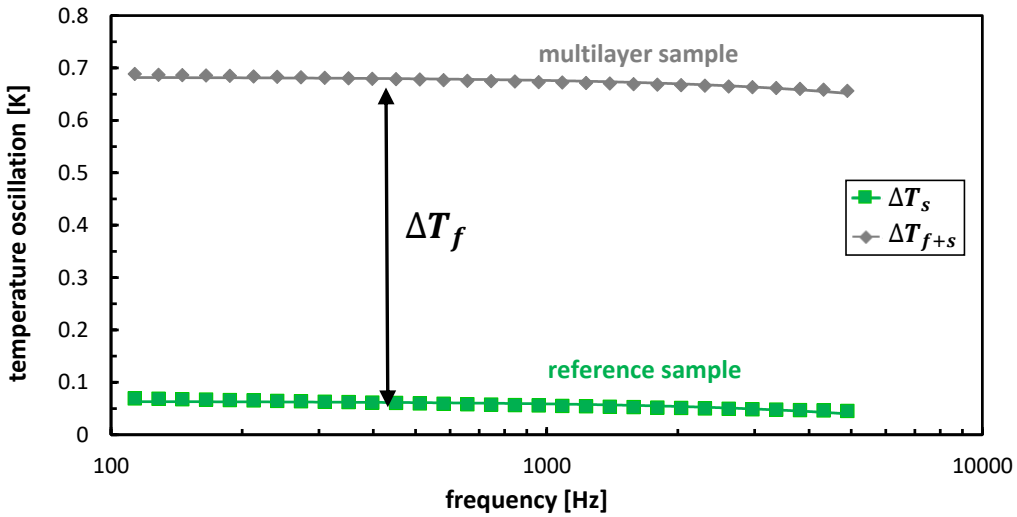

Figure 3.12: The amplitude of the heater's temperature oscillation $\Delta T_{2\omega}$ for both the reference (green line) and multilayer sample (grey line) as a function of excitation frequency f, showing that their difference ΔT_f is independent of the frequency. By removing the signal of the reference sample from that of the multilayer sample with the studied film, it is possible to subtract the common background contribution of the parasitic interfacial thermal resistance, such as the one between the metal heater and the underlying film, and the one between the substrate and the first deposited layer.

Although the differential 3ω method requires two sets of measurements, a detailed study performed by Borca-Tasciuc *et al.* [19] showed that it is advantageous compared to the slope method, because it can reduce the uncertainty in the determination of the thermal conductivity of the film of interest. The value of k_f obtained by Eq. (3.34) is insensitive to the substrate thermal conductivity, and the contributions from any additional layers are mostly eliminated by the measurement of the reference sample. Because of the mentioned advantages, the differential technique was used to perform the thickness-dependent experiments of the cross- and in-plane thermal conductivity of SiO_2, Si_3N_4, AlN and CuI thin films in this thesis. Additional details about the differential 3ω technique can be found from various references [18,19,21,26] and are therefore not discussed in detail here.

3.3.2.2. Determination of in-plane thermal conductivity

The techniques applied to obtain the thermal conductivity within the in-plane direction of thin films are considerably more diverse than those applied for cross-plane measurements [21]. In this section, the state-of-the-art of in-plane thermal conductivity measurements of thin films and their disadvantages are described. Furthermore, we will present our improved in-plane measurement technique for supported film structures, which we developed to overcome the disadvantages of common techniques and to enable the measurement of both cross- and in-plane thermal conductivities of thin films without changing the sample during the measurement. This novel concept allows a precise comparison of cross- and in-plane conductivities, compared to what is achievable with the standard in-plane methods.

In general, techniques for supported film structures have an easier sample fabrication, but have more restrictions about their domain of validity. The common suspended samples are much more vulnerable to convection and radiation losses, and must be measured in vacuum [21]. The experimental setup and equipment used to determine the in-plane thermal conductivity are similar to those of the cross-plane 3ω method and will be presented in Section 4.3.1.2.

a) State-of-the-art of in-plane thermal conductivity measurements: Suspended film method

A problem for in-plane thermal conductivity measurements of thin films is the parasitic heat loss through the substrate material [21,26]. In order to overcome this problem, a suspended film structure as shown in Figure 3.13 is needed. However, such a suspended structure drastically complicates the microfabrication and data evaluation of the thin film sample [21,26,34].

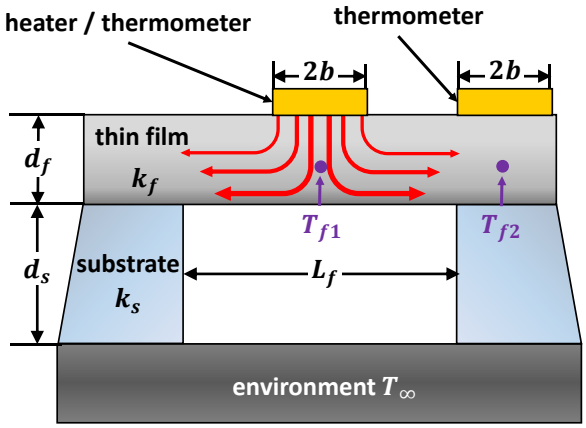

Figure 3.13: Schematic cross-section for determining the in-plane thermal conductivity of suspended thin films. The in-plane thermal conductivity can be deduced from the difference in heater/thermometer temperature rise of two measurements using two metal strips with all other parameters unchanged [21,35] (modified from Ref. [26]).

Figure 3.13 shows the schematic cross-section of a standard suspended film sample for determining the in-plane thermal conductivity of thin films. In order to obtain the thermal properties within the in-plane direction of the investigated film, two metal strips have to be deposited on the surface of the suspended specimen. Similar to the 3ω method, the first metal strip on top of the suspended film serves both as thermometer and electrical heater and the second strip only as thermometer. A DC current is applied to the first metal strip, in order to obtain the total temperature of the suspended film T_{f1} (heater 1) and of the film-on-substrate structure T_{f2} (heater 2), as illustrated in Figure 3.13. The in-plane thermal conductivity $k_{f\parallel}$ can then be given by [21,26]:

$$k_{f\parallel} = \frac{P_l\, L_f}{2d_f\left(T_{f1} - T_{f2}\right)} \tag{3.35}$$

where P_l is the dissipated heating power per unit length, $L_f/2$ is the length between heater 1 and the substrate, T_{f1} is the suspended thin film temperature and T_{f2} is the temperature of the film-on-substrate structure, detected by the metal strips.

Beside the complex microfabrication, the suspended methods have other major drawbacks including the radiation losses and thermal contact resistances, which will be discussed below:

- **Radiation losses**

The radiation losses from both top and bottom surfaces of the suspended film are critical for the accuracy of the measurement, even if the sample is put into a high vacuum chamber. Dames [21] provided an approximation that estimates the effect of the radiation losses as the heat flow ratio between the radiation and conduction Q_{rad}/Q_{cond} of the suspended sample:

$$\frac{Q_{rad}}{Q_{cond}} \approx \frac{2h_{rad}\left(L_f/2\right)^2\left[(1/2)\left(T_{f1}/T_{f2}\right)-T_\infty\right]}{k_f d_f\left(T_{f1}-T_{f2}\right)} \tag{3.36}$$

where h_{rad} is the linearized radiation coefficient, $L_f/2$ is the distance between heater 1 and the substrate, k_f thermal conductivity of the film, d_f film thickness, T_∞ temperature of the surroundings and $T_{f1/2}$ the temperatures of the sample corresponding to Figure 3.14(b), respectively. If the radiative surroundings T_∞ are assumed at nearly the same temperature as the film-on-substrate system T_{f2}, the approximation by Dames [21] can be re-written as:

$$\frac{Q_{rad}}{Q_{cond}} \approx \frac{h_{rad}\left(L_f/2\right)^2}{k_f d_f} \tag{3.37}$$

Unfortunately, the linearized radiation coefficient h_{rad} depends on the emissivity ε_f of the suspended film, which is usually unknown. Dames [21] demonstrated that the impact of the radiation losses, given by the heat flow ratio Q_{rad}/Q_{cond}, can reach acceptable values of about 1%, assuming the worst case of h_{rad} = 6.1 $Wm^{-2}K^{-1}$ at 300 K, a silicon film with d_f = 1 µm, $L_f/2$ = 500 µm, and $k_f \approx$ 150 $Wm^{-1}K^{-1}$. However, if the film is changed to a dielectric one such as SiO_2 with $k_f \approx$ 1.0 $Wm^{-1}K^{-1}$ [18], the radiation losses would be absolutely unacceptable. Therefore, the thin films which can be studied using the suspended method is limited to high thermal conductive materials.

- **Contact and substrate spreading resistance**

  Dames [21] demonstrated that the contact and spreading resistance reaching from the film edge to the environment can also drastically reduce the accuracy of the suspended in-plane measurement. In Figure 3.14(b), the contact and spreading resistance reaching from the film edge to the environment are illustrated as the thermal resistance $R_{f-\infty} \equiv R_{f-s} + R_s + R_{s-\infty}$. Song *et al*. [36] stated that it is a good practice to include a dedicated thermometer to measure the temperature of the film-on-substrate structure T_{f2}, as illustrated in Figure 3.14(b). If this thermometer is omitted and T_{f2} is approximated as environmental temperature T_∞, it is important to estimate the intervening resistances to ensure that they are negligible [21,37–39]. In order to neglect $T_{f2} - T_\infty$ in comparison with $T_{f1} - T_{f2}$, one should increase the distance between the metal strips $L_f/2$ to set R_f as large as possible. However, this will significantly increase the radiation losses and therefore reduce the accuracy of the measurement. One approach to prove that the temperature difference T_{f2} - T_∞ is negligible is to measure several samples with different distances of $L_f/2$ between heater and heat sink. This is comparable to the differential 3ω method, and a schematic analogous to Figure 3.14(b) can also be used to estimate the thermal resistance $R_{f-\infty}$ if it is not negligible.

Finally, we need to address that parasitic heat losses such as heat conduction loss along the heater, convection and radiation losses to the ambient, must be reduced to ensure a one-dimensional heat condition inside the in-plane direction of the suspended film. Dames [21] suggested that the heat conduction losses along the metal strips can be reduced by sophisticated microfabrication to reduce their cross-sectional area. In order to reduce the influence of the radiation losses, the suspended in-plane measurements have to be performed inside a high vacuum chamber [21]. Another approach to reduce the radiation losses is to coat the surface of the sample with a low emissivity material [21,26]. As mentioned in Section 2.4, the most efficient approach to handle with radiation heat loss and contact resistances of

additional dielectric layers would be using a transient heating (AC heating current) and temperature sensing technique such as the differential 3ω method [21,26]. Therefore, in the following section, we present our improved in-plane 3ω method which is called "multi-heater" 3ω method.

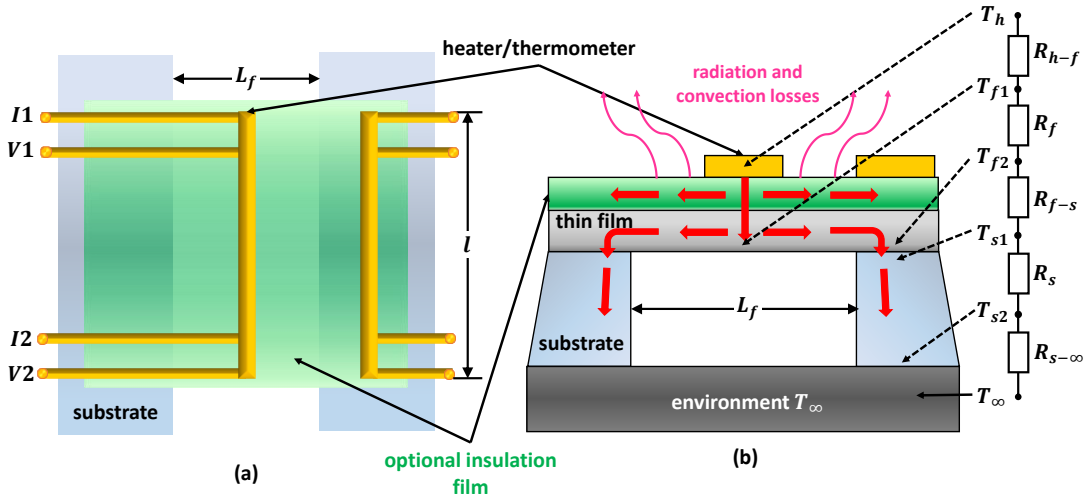

Figure 3.14: In-plane thermal conductivity measurement with two metal strips acting as a heater/thermometer and temperature sensor to measure the in-plane thermal conductivity of a suspended film: (a) top view of the suspended film sample (b) cross-section of the suspended film sample including the thermal boundary resistances of the heater, suspended film, substrate, environment, and the heat flow inside the sample, indicated by the red arrows (modified from Ref. [21]).

b) Improved in-plane measurements: Supported film method (multi-heater 3ω method)

As mentioned before, in-plane thermal conductivity measurements can be divided into those for suspended and supported films. In general, methods for the suspended films are only sensitive for the in-plane thermal conductivity and cannot properly detect the heat flow in the cross-plane direction [22]. Furthermore, the microfabrication to obtain a suspended film and the significant impact of radiation losses are serious challenges. Therefore, one of our main aims of this thesis is to develop a new approach to measure both cross- and in-plane thermal conductivities of thin films without changing the sample during the measurement process, in order to characterize the thickness dependency of the film's thermal conductivity. This improved measurement concept offers the advantage of using the same film-substrate

platform, which improves the reproducibility of the measurements, since the variation of contact conditions between heater, film and substrate are excluded. Therefore, our multi-heater 3ω method allows more precise comparisons of cross- and in-plane conductivities, compared to what is achievable with the standard in-plane methods such as the techniques for suspended films discussed above.

We used our multi-heater 3ω method for supported films because of two main reasons. Firstly, we want to focus on simultaneously determining the cross- and in-plane thermal conductivities of thin films without changing the sample during the measurement, which allows a precise comparison of cross- and in-plane conductivities. Secondly, compared to the other methods, the multi-heater technique is more sensitive for thin films with a small to moderate $k_{f\parallel}$value [22]. This characteristic is of great importance, since our multi-heater technique is appropriate for poorly thermal conductive thin films (e.g. CuI [24]), used for thermoelectric applications.

The basic measurement principle for the in-plane measurement is similar to that for the cross-plane 3ω measurement, presented in Section 3.3.2.1. As for the cross-plane technique, the surface of the thin film is heated over a finite region by a metal strip, and the lateral spreading of the heat inside the film modifies the temperature distribution, which is different from the one for a strictly one-dimensional case. The lateral heat spreading is governed by the thickness and thermal conductivity of the film and also by the dimensions of the metal heater. By comparing the temperature rises in four metal heaters with different widths, the cross- and in-plane thermal conductivities can be obtained.

If we use a heater with a width $2b$, which is much larger compared to the film thickness d_f ($2b \gg d_f$), this will lead to a one-dimensional heat flux vertical to the film surface (cross-plane) (Figure 3.10(a)). This behavior can be approximated as a one-dimensional heat conduction model, presented in Section 3.3.2.1. On the other hand, Kurabayashi *et al*. [22,33] and Borca-Tasciuc *et al*. [19] reported that working with a very narrow heater compared to

the cross-plane measurement will result in a divergent heat pattern that spreads along the in-plane direction, as shown in Figure 3.10(b) and Figure 3.15.

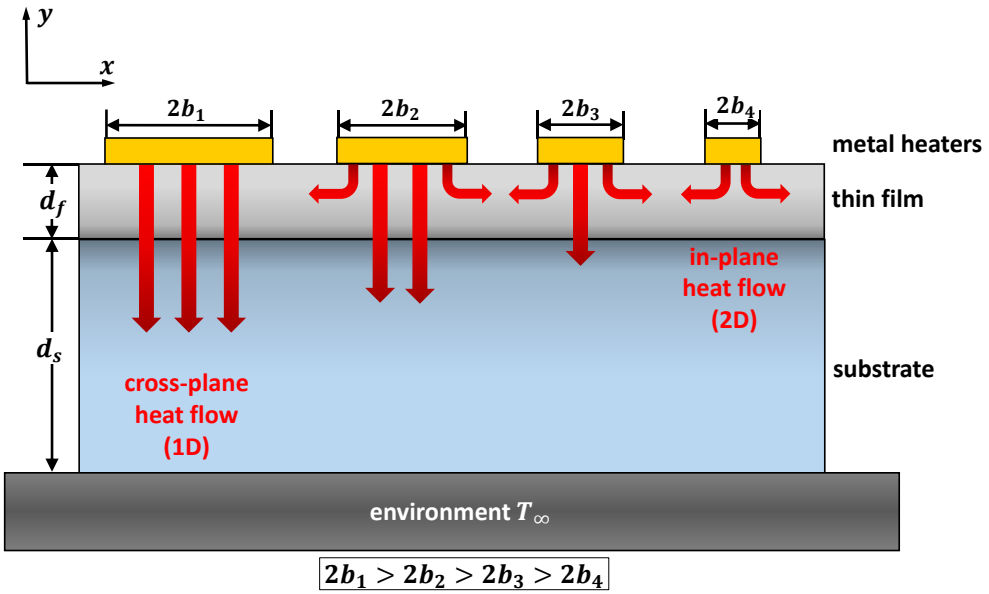

Figure 3.15: Cross-sectional schematic of the improved microstructure used for measuring both the cross- and the in-plane thermal conductivities in the same thin film. The line-width of the four heaters deposited on the thin film sample varies, in order to extract both the cross- and in-plane thermal conductivity. When the metal strip width is much larger than the thin film thickness, the thermal conduction is nearly one-dimensional in the direction normal to the film, and the cross-plane conductivity has a dominant influence on the temperature rise. On the other side, the sensitivity of the measurement to the in-plane conductivity increases with decreasing values of the ratio of the strip width to the film thickness.

Therefore, the half-width b of the metal heater must be small enough to comply with the following condition [21,26]:

$$\frac{b}{d_f}\left(\frac{k_{f\perp}}{k_{f\parallel}}\right)^{1/2} \leq 3 \tag{3.38}$$

where $k_{f\perp}$ and $k_{f\parallel}$ represent the cross- and in-plane thermal conductivity values of the thin film, and d_f the film thickness, respectively. In this case, the metal strip is sensitive to the in-plane thermal conductivity component (see Figure 3.16), and the in-plane thermal

conductivity can be determined by using Eq.(3.32) or (3.33) [19]. The approximations of the film thermal resistance R_f is then given by: [19,26]:

$$R_f = \frac{\Delta T_f}{P_l} = \frac{1}{\pi}\left(\frac{1}{k_{f\perp}\cdot k_{f\parallel}}\right)^{1/2}\int_0^{\infty}\frac{\sin^2 u}{u^3}\tanh\left[u\frac{b}{d_f}\left(\frac{k_{f\perp}}{k_{f\parallel}}\right)^{1/2}\right]du \qquad (3.39)$$

Generally, the cross-plane thermal conductivity $k_{f\perp}$ must be firstly determined using a metal strip that is only sensitive to heat flow perpendicular to the thin film, as mentioned before. Subsequently, the in-plane thermal conductivity $k_{f\parallel}$ can be obtained with a significantly narrowed-width heater (see Figure 3.15).

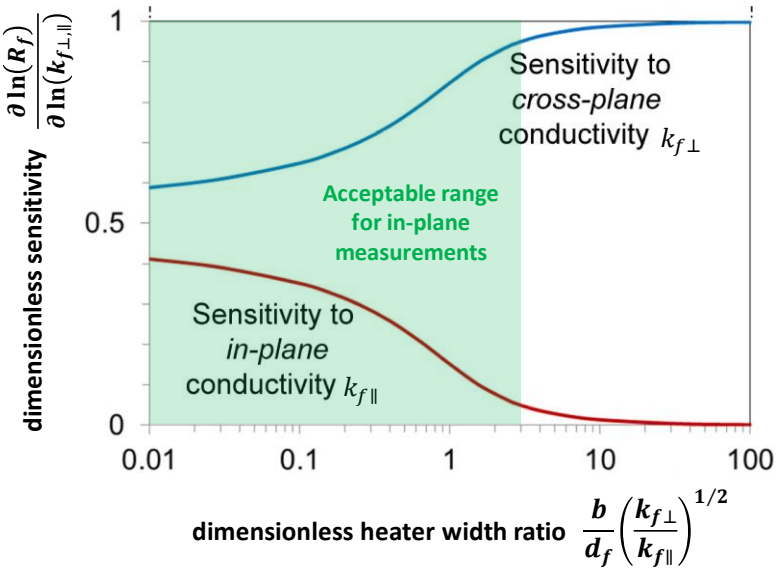

Figure 3.16: Sensitivity of the metal heaters used for our multi-heater 3ω method to simultaneously measure the cross- and in-plane thermal conductivity of amorphous thin films in dependence of the dimensionless heater width. For wide heaters, the thermal resistance of the film R_f is sensitive only to the cross-plane conductivity, while for narrow heaters, R_f is sensitive to the conductivities in both directions. The calculation is based on Eq. (3.39), and a perfectly isothermal substrate is assumed. The green shaded area represents the acceptable range for in-plane measurements by using the differential 3ω multi-heater method (adapted and modified from Ref. [21]).

Furthermore, to ensure that we obtain reliable in-plane thermal conductivity values from our multi-heater method, the thermal conductivity of the substrate must be large enough to be

approximated as isothermal ($k_s \to \infty$). In the case of an anisotropic film, Borca-Tasciuc *et al.* [19] and Dames [21] demonstrated that the error of this thermal design rule is given by:

$$\text{Error} \approx \frac{k_{f\perp} \cdot k_{f\parallel}}{k_s^2} \tag{3.40}$$

This thermal design rule implicates that the multi-heater 3ω method is basically not applicable to investigate materials with extremely high cross- and in-plane thermal conductivity values, such as graphene [21]. In this case, the suspended film method is more suitable. For every 3ω film-on-substrate sample investigated in this thesis, the error is always below 1.4% (see Table A.4 of Appendix B).

In this work, we improved the sensitivity and accuracy of in-plane measurement by measuring a series of multiple heaters with different widths $2b$ but a constant length l [21] and to distinguish between the heat flow in cross- and in-plane directions. Therefore, we deposited four metal heaters on top of the investigated thin film sample, as illustrated in Figure 3.15. The heater width was varied in order to be able to obtain both the cross- and in-plane thermal conductivities of thin films with a better accuracy. Section 4.3.1 provides detailed information about the structure and dimensions of the multi-heater samples used to study the heat conduction of AlN and CuI thin films.

3.4. Summary

In this chapter, the history, theoretical basics, experimental considerations, and several modifications of the 3ω method have been presented. We have concluded that the measured 3ω voltage $V_{3\omega}$ is directly related to the thermal wave amplitude $\Delta T_{2\omega}$, which is then compared to a thermal model depending on the excitation frequency ω to obtain the thermal conductivity of thin films, substrates and multilayer-structures. This process was presented in detail, providing the fundamentals for the thermal measurements performed in this thesis. We provided an expression for the thermal wave as a function of the experimental variables. Then,

an analytical expression of the thermal wave amplitude induced by a thin film deposited onto a substrate was given, and the differential approach was described in Section 3.3.2.1.

Furthermore, we introduced a new approach to measure both cross- and in-plane thermal conductivities of thin films without changing the sample during the measurement process, in order to characterize the thickness dependency of the film's thermal conductivity. This novel measurement concept offers the advantage of using the same film-substrate platform as support. This improves the reproducibility of the measurements, since the variation of contact conditions between heater, film and substrate is excluded. Therefore, our multi-heater 3ω method allows a more precise comparison of cross- and in-plane conductivities, compared to what is achievable with standard in-plane methods such as techniques for suspended films (Section 3.3.2.2).

The following chapter will thoroughly describe the experimental methodology used to characterize the cross- and in-plane thermal conductivity of SiO_2, Si_3N_4, AlN and CuI thin films. The experimental setup of the 3ω method as well as the sample preparation are introduced. It will also provide the description of SiO_2, Si_3N_4, AlN and CuI thin films and the experimental methodology used to synthesize them. Furthermore, we will apply the fundamental 3ω principle to the AFM and demonstrate the experimental setup of our 3ω Microscopy technique. This novel characterization technique is utilized to quantitatively study the local thermal properties of thin-film-on-substrate systems.

3.5. References

[1] O.M. Corbino, Thermal oscillations in lamps of thin fibers with alternating current flowing through them and the resulting effect on the rectifier as a result of the presence of even-numbered harmonics, Physikalische Zeitschrift (11) (1910) 413–417.

[2] L.R. Holland, Physical Properties of Titanium. III. The Specific Heat, Journal of Applied Physics 34 (8) (1963) 2350–2357.

[3] D. Gerlich, B. Abeles, R.E. Miller, High-Temperature Specific Heats of Ge, Si, and Ge-Si Alloys, Journal of Applied Physics 36 (1) (1965) 76–79.

[4] L.R. Holland, R.C. Smith, Analysis of Temperature Fluctuations in ac Heated Filaments, Journal of Applied Physics 37 (12) (1966) 4528–4536.

[5] N.O. Birge, S.R. Nagel, Specific-heat spectroscopy of the glass transition, Physical review letters 54 (25) (1985) 2674–2677.

[6] N.O. Birge, Specific-heat spectroscopy of glycerol and propylene glycol near the glass transition, Physical Review B 34 (3) (1986) 1631–1642.

[7] N.O. Birge, S.R. Nagel, Wide-frequency specific heat spectrometer, Review of Scientific Instruments 58 (8) (1987) 1464–1470.

[8] D.G. Cahill, R.O. Pohl, Thermal conductivity of amorphous solids above the plateau, Physical Review B 35 (8) (1987) 4067–4073.

[9] H.S. Carslaw, J.C. Jaeger, Conduction of heat in solids, 2nd ed., Clarendon, Oxford, (1959) 1-92.

[10] D.G. Cahill, H.E. Fischer, T. Klitsner, E.T. Swartz, R.O. Pohl, Thermal conductivity of thin films: Measurements and understanding, Journal of Vacuum Science & Technology A: Vacuum, Surfaces, and Films 7 (3) (1989) 1259–1266.

[11] D.G. Cahill, Thermal conductivity measurement from 30 to 750 K: The 3ω method, Review of Scientific Instruments 61 (2) (1990) 802–808.

[12] D.H. Jung, T.W. Kwon, D.J. Bae, I.K. Moon, Y.H. Jeong, Fully automated dynamic calorimeter, Measurement Science and Technology 3 (5) (1992) 475–484.

[13] R. Frank, V. Drach, J. Fricke, Determination of thermal conductivity and specific heat by a combined 3ω/decay technique, Review of Scientific Instruments 64 (3) (1993) 760–765.

[14] I.K. Moon, Y.H. Jeong, S.I. Kwun, The 3ω technique for measuring dynamic specific heat and thermal conductivity of a liquid or solid, Review of Scientific Instruments 67 (1) (1996) 29–35.

[15] D.G. Cahill, M. Katiyar, J.R. Abelson, Thermal conductivity of a-Si: H thin films, Physical Review B 50 (9) (1994) 6077–6081.

[16] D.G. Cahill, M. Katiyar, J.R. Abelson, Heat transport in micron thick a-Si: H films, Philosophical Magazine Part B 71 (4) (1995) 677–682.

[17] M. Bogner, A. Hofer, G. Benstetter, H. Gruber, R.Y. Fu, Differential 3ω method for measuring thermal conductivity of AlN and Si3N4 thin films, Thin Solid Films 591 (2015) 267–270.

[18] S.M. Lee, D.G. Cahill, Heat transport in thin dielectric films, Journal of Applied Physics 81 (6) (1997) 2590–2595.

[19] T. Borca-Tasciuc, A.R. Kumar, G. Chen, Data reduction in 3ω method for thin-film thermal conductivity determination, Review of Scientific Instruments 72 (4) (2001) 2139–2147.

[20] C.E. Raudzis, F. Schatz, D. Wharam, Extending the 3ω method for thin-film analysis to high frequencies, Journal of Applied Physics 93 (10) (2003) 6050–6055.

[21] C. Dames, Measuring the Thermal Conductivity of Thin Films: 3 Omega and related Electrothermal Methods, Annual Review of Heat Transfer 16 (1) (2013) 7–49.

[22] Y.S. Ju, K. Kurabayashi, K.E. Goodson, Thermal characterization of anisotropic thin dielectric films using harmonic Joule heating, Thin Solid Films 339 (1-2) (1999) 160–164.

[23] S.M. Lee, D.G. Cahill, R. Venkatasubramanian, Thermal conductivity of Si-Ge superlattices, Applied Physics Letters 70 (22) (1997) 2957–2959.

[24] C. Yang, D. Souchay, M. Kneiß, M. Bogner, H.M. Wei, M. Lorenz, O. Oeckler, G. Benstetter, Y.Q. Fu, M. Grundmann, Transparent flexible thermoelectric material based on non-toxic earth-abundant p-type copper iodide thin film, Nature communications 8 (2017) 16076.

[25] J.S. Dugdale, The electrical properties of metals and alloys, Dover Publications, Inc, Mineola, New York, (1977) 240-245.

[26] D. Zhao, X. Qian, X. Gu, S.A. Jajja, R. Yang, Measurement Techniques for Thermal Conductivity and Interfacial Thermal Conductance of Bulk and Thin Film Materials, Journal of Electronic Packaging 138 (4) (2016) 40802.

[27] D.G. Cahill, K. Goodson, A. Majumdar, Thermometry and Thermal Transport in Micro/Nanoscale Solid-State Devices and Structures, Journal of Heat Transfer 124 (2) (2002) 223.

[28] T. Borca-Tasciuc, G. Chen, Experimental Techniques for Thin-Film Thermal Conductivity Characterization, in: Tritt (Hg.) (2004) – Thermal Conductivity, pp. 205–237.

[29] D. Koninck, Thermal Conductivity Measurements using the 3-Omega Technique: Application to Power Harvesting Microsystems, McGill University, Montréal, Canada (2008) 2-1 - 2-18.

[30] A. Jacquot, B. Lenoir, A. Dauscher, M. Stölzer, J. Meusel, Numerical simulation of the 3ω method for measuring the thermal conductivity, Journal of Applied Physics 91 (7) (2002) 4733–4738.

[31] J. Jaramillo-Fernandez, J. Ordonez-Miranda, E. Ollier, S. Volz, Tunable thermal conductivity of thin films of polycrystalline AlN by structural inhomogeneity and interfacial oxidation, Physical chemistry chemical physics 17 (12) (2015) 8125–8137.

[32] H. Bateman, A. Erdélyi, Tables of integral transforms: Volume 1 (Chapter 1), McGraw-Hill, New York, (1954) 7-60.

[33] K. Kurabayashi, M. Asheghi, M. Touzelbaev, K.E. Goodson, Measurement of the thermal conductivity anisotropy in polyimide films, Journal of Microelectromechanical Systems 8 (2) (1999) 180–191.

[34] J. Lee, Z. Li, J.P. Reifenberg, S. Lee, R. Sinclair, M. Asheghi, K.E. Goodson, Thermal conductivity anisotropy and grain structure in Ge 2 Sb 2 Te 5 films, Journal of Applied Physics 109 (8) (2011) 84902.

[35] F. Völklein, H. Reith, A. Meier, Measuring methods for the investigation of in-plane and cross-plane thermal conductivity of thin films, Physica status solidi A 210 (1) (2013) 106–118.

[36] D. Song, G. Chen, Thermal conductivity of periodic microporous silicon films, Applied Physics Letters 84 (5) (2004) 687–689.

[37] Y.C. Tai, C.H. Mastrangelo, R.S. Muller, Thermal conductivity of heavily doped low pressure chemical vapor deposited polycrystalline silicon films, Journal of Applied Physics 63 (5) (1988) 1442–1447.

[38] F. Völklein, Thermal conductivity and diffusivity of a thin film SiO2-Si3N4 sandwich system, Thin Solid Films 188 (1) (1990) 27–33.

[39] J.E. Graebner, J.A. Mucha, L. Seibles, G.W. Kammlott, The thermal conductivity of chemical-vapor-deposited diamond films on silicon, Journal of Applied Physics 71 (7) (1992) 3143–3146.

Chapter 4: Materials and Characterization Techniques

Thermal properties of thin films are intricately related to their microstructures and therefore their accurate characterization is crucial to understand the thermal transport. This chapter provides the descriptions of experimental methodologies used to synthesize and characterize SiO_2, Si_3N_4, AlN and CuI films. The experimental techniques utilized to investigate the crystalline structure, surface morphology, electrical and thermal properties of the mentioned thin films are discussed in details. The experimental setups of the macro- and microscopic 3ω methods as well as the composition and preparation of thin film-on-substrate samples are also introduced.

4.1. Materials

4.1.1. Silicon dioxide and silicon nitride

SiO_2 and Si_3N_4 thin films have been widely used in micro- and nanoelectronics over the past decades [1]. The main reason is due to their excellent insulating properties, i.e., high dielectric constants of 3.8 to 3.9 (thermal SiO_2) and 7.0 to 7.5 (Si_3N_4), respectively [1]. SiO_2 films prepared by thermal oxidation of silicon are often utilized as primary gate dielectrics and therefore are one of the most important technological films in semiconductor manufacturing. They ensure low density of traps at the Si/SiO_2 interface, excellent dielectric properties, and high-temperature stability in fabrication processes. In addition, chemical vapor deposited (CVD) SiO_2 and Si_3N_4 thin films have also been widely employed in semiconductor manufacturing and devices. They function as dielectric layers (e.g. field oxides), sidewall spacers and passivation layers [1].

As the thermal conductivities of SiO_2 and Si_3N_4 thin films are well-reported [2–5], they can be used as reference films in order to verify the experimental results obtained from our modified 3ω techniques (i.e., multi-heater 3ω technique and 3ω Microscopy). Studies revealed that the thermal conductivities of these films are strongly dependent on their film thicknesses [2–7]. Lee *et al*. [2] and Griffin *et al*. [4,5] reported that the cross-plane thermal conductivity values of SiO_2 and Si_3N_4 thin films prepared by CVD increased with the increase in film thickness.

In this thesis, SiO_2 and Si_3N_4 thin films were deposited onto a Si (100) substrate using plasma enhanced chemical vapor deposition (PECVD). Different aspects of using PECVD for growth of thin films and the deposition parameters of the investigated SiO_2 and Si_3N_4 films are presented in the following section.

4.1.1.1. Deposition of SiO_2 and Si_3N_4 thin films

PECVD is widely used in semiconductor manufacturing to deposit SiO_2 and Si_3N_4 thin films onto wafers containing metal films or other temperature-sensitive structures [8]. In this thesis, PECVD has been employed to grow SiO_2 and Si_3N_4 thin films on p-type Si (100) substrates of 640 μm in thickness. In order to study the thickness-dependency of thermal conductivity, the thicknesses of the deposited SiO_2 and Si_3N_4 films were varied between 100 - 1000 nm and 300 - 1000 nm, respectively.

Table 4.1: Deposition parameters for PECVD of SiO_2 and Si_3N_4 thin films on Si (100) substrates, serving as reference samples for the 3ω method.

	Sources [sccm]	Total gas pressure [Torr]	RF power [W]	RF frequency [MHz]	Deposition temperature [°C]
SiO_2	5.3% SiH_4/N_2 → 30.9 N_2O → 120	1.0	17.0	13.56	300
Si_3N_4	5.3% SiH_4/N_2 → 60 NH_3 → 1.5	1.8	16.0	13.56	300

Prior to the film deposition, the substrates were ultrasonically cleaned in acetone, ethanol, and de-ionized water for five minutes sequentially. Then the Si substrates were submerged into RCA-1 ($NH_4OH:H_2O_2:H_2O$ = 1:1:5) at 75°C for five minutes. After being rinsed in de-ionized water, the Si substrates were dipped for two minutes in 2% hydrofluoric acid (HF) solution to remove the native oxide layers on their surfaces. Then, the Si substrates were rinsed using de-ionized water and dried using nitrogen (N_2) gas. Table 4.1 summarizes the deposition parameters of the investigated SiO_2 and Si_3N_4 thin films.

4.1.2. Aluminum nitride

AlN thin films have been widely used in SAW devices [9,10], LEDs [11], and MEMS because of their outstanding properties, such as high piezoelectric coupling factor, excellent dielectric properties, wide band gap and high thermal conductivity [12]. Single crystalline AlN is one of the promising candidates for effective heat conductors in microelectronic devices due to its high thermal conductivity (320 $Wm^{-1}K^{-1}$) at room temperature [13], which makes it an ideal material to solve the thermal management problem. However, thermal conductivities of thin film and coating materials could be substantially different from those of their bulk counterparts [2,14–18]. Therefore, precise measurement of the cross- ($k_{f\perp}$) and in-plane ($k_{f\parallel}$) thermal conductivities of polycrystalline AlN thin films is beneficial for developing micro- and nanoelectronic devices.

Therefore, a goal of this thesis is to provide an improved 3ω technique to measure both cross- and in-plane thermal conductivities of high-thermally conductive AlN thin films, in order to study the thickness-dependency of thermal conductivity. Experimental work and theoretical analysis have been performed to study the effects of crystallinity, grain/surface particle sizes, and interfacial structures of AlN thin films on their thermal conductivity. The experimental results of these investigations will be presented in Chapter 5.

4.1.2.1. Physical properties of AlN

AlN is an ionic binary compound that belongs to the III-V group [19]. In its wurtzite phase as illustrated in Figure 4.1(a), it is the largest bandgap nitride semiconductor with a bandgap of 6.28 eV at room temperature [19]. Wurtzite AlN crystallizes in a hexagonal structure with lattice parameters a_{AlN} = 3.11 Å and c_{AlN} = 4.98 Å. The ordered structure is described by the space group $P6_3mc$ and consists of two interpenetrating hexagonal close-packed sublattices, each one containing either Al- or N-atoms, as shown in Figure 4.1(b) [19]. There are four Al-atoms per unit cell located at (0, 0, 0), (1/3, 2/3, 1/2), (0, 0, 3/8) and (1/3, 2/3, 7/8). The N-lattice is separated from the Al-arrangement along the c-axis by an offset of 3/8 of the cell height [20]. In this structure, each Al-atom is tetrahedrally coordinated to form four equivalent bonds with N-atoms. Conversely, each N-atom is coordinated by four Al-atoms.

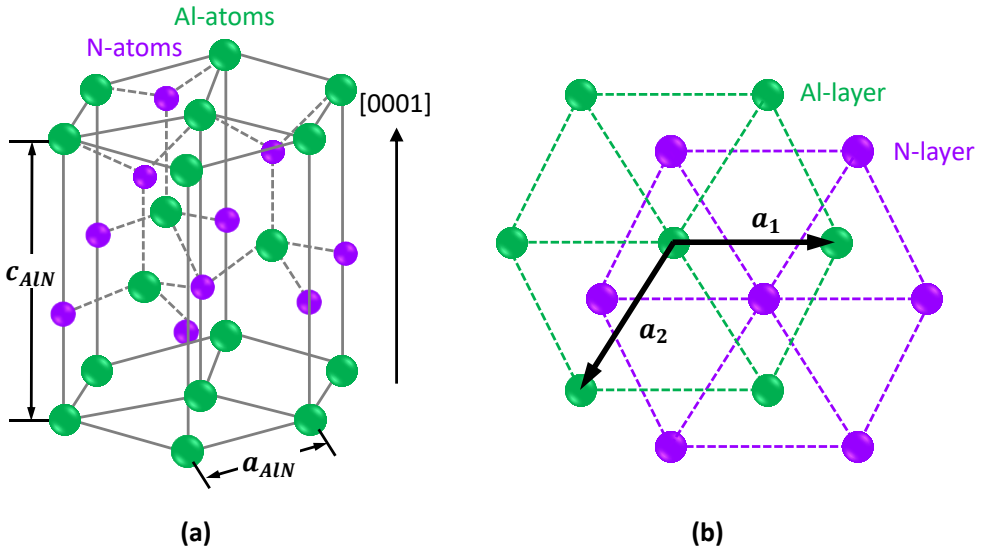

Figure 4.1: (a) Crystal structure of AlN in its wurtzite phase (space group $P6_3mc$). Aluminum and nitrogen bonds are illustrated by the dashed lines colored in grey (adapted and modified from Ref. [21]); (b) Stacking of aluminum and nitrogen in a hexagonal crystal of lattice constants $a = a_1 = a_2$ and c (adapted and modified from Ref. [20]).

In order to prepare AlN thin films, various deposition techniques, such as CVD [22,23], pulsed laser deposition (PLD) [24] molecular beam epitaxy (MBE) [25], and magnetron sputtering [26–28] have been utilized. Among them, magnetron reactive sputtering is one of

the most widely used deposition techniques [29]. The main parameters in magnetron reactive sputtering are growth temperature, pressure, and gaseous ratio of argon (Ar) and N_2, etc. In this thesis, the deposition of AlN thin films with a thickness varying from 99 to 1009 nm on Si (100) substrates were performed using RF reactive magnetron sputtering. Different aspects using RF magnetron sputtering for growth of AlN thin films are discussed in the following section.

4.1.2.2. Deposition of AlN thin films

Magnetron sputtering is one of the most versatile sputtering techniques, because it can be employed to deposit both insulating and non-insulating materials [29]. Due to the dielectric nature, direct evaporation of electrically insulating materials is difficult and inefficient. This issue can be overcome by sputtering the target with an RF power supply in a reactive mode. This approach is advantageous, because of its high deposition rate compared to other commonly used techniques [29].

In this thesis, AlN thin films were deposited onto p-type doped Si (100) substrates using an RF reactive magnetron sputtering process with an RF power of 5 kW and a DC power of 100 W. Before deposition, substrates were cleaned as described in Section 4.1.1.1 on page 99. The sputtering process was conducted in the reactor. The ambient pressure and temperature in the deposition chamber were controlled to be 9.5 mTorr and 25°C, respectively. An Al-target (99.9995% purity) of 5 inch (12.7 cm) in diameter was utilized for deposition of the thin film using a gas mixture of N_2 (50 sccm) and Ar (10 sccm). The purity of N_2 and Ar gases was 99.995%. The thicknesses of the deposited AlN films were between 99 to 1009 nm in order to study the film thickness-dependency of thermal conductivity.

4.1.3. Copper Iodide

CuI is a binary metal halide semiconductor with a wide direct bandgap of 3.1 eV and excellent thermoelectric properties [30,31]. Therefore, CuI films provide a great potential to improve

thermoelectric [31,32] and optoelectronic applications [30,33], such as microscale transparent flexible thermogenerators [31], transparent electrically conductive layers [34], LEDs [30,35] and solar cells [36,37].

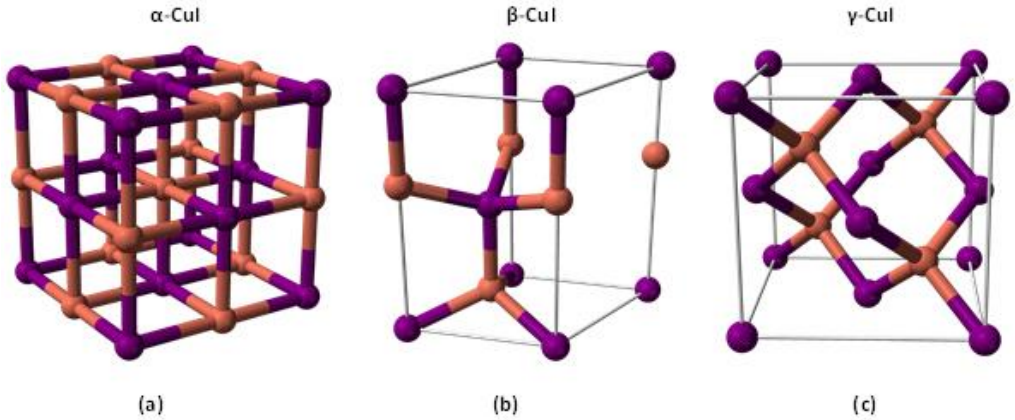

Figure 4.2: Crystal structure of CuI in its (a) rock salt structure (space group $Fm\bar{3}m$) (b) wurtzite structure (space group $P6_3mc$) (c) zincblende structure (space group $F\bar{4}3m$) (adapted and modified from Ref. [38]).

In this thesis, we focus on room temperature thermoelectric performances of CuI thin films, since CuI in its ground-state phase was recently reported as a high performance p-type transparent conductor [31–33,39]. CuI is an environment-friendly material composed of non-toxic and naturally abundant elements [31]. Interestingly, the presence of heavy elements like iodine (I) leads to a low thermal conductivity, which is necessary for a good thermoelectric performance [31]. CuI undergoes multiple polymorphic phase transitions during heating, i.e., γ (zincblende structure, space group $F\bar{4}3m$) → β (wurtzite structure, $P6_3mc$) → α (rock salt structure, $Fm\bar{3}m$) at 643 K and 673 K, respectively [31,40].

Figure 4.2 shows the α-, β-, and γ-structures of CuI. The α- or β-phase acts as a superionic conductor, which is regarded as a phonon-liquid material with a low thermal conductivity [41]. Whereas in its γ-phase at room temperature (or below 643 K), it is a wide direct bandgap (E_g = 3.1 eV) semiconductor with p-type conductivity [31]. The Cu-vacancy, which has a shallow acceptor level, is primarily responsible for p-type conductivity of γ-CuI [42]. Recently, Yang *et al*. [31] reported a record high room temperature hole conductivity

σ > 280 Scm^{-1} for CuI thin films. At 300 K, a large Seebeck coefficient of γ-CuI (S = 237 μVK^{-1} for a hole concentration p of 10^{20} cm^{-3}) was theoretically predicted [43]. Consequently, a high thermoelectric performance in the wide bandgap γ-CuI can be expected due to its high values of σ (with respect to the large bandgap) and S as well as the predicable low thermal conductivity value [31]. For the purpose of exploring transparent p-type thermoelectric materials, the thermoelectric properties of γ-CuI thin films have been investigated in this thesis. There are growing numbers of studies that investigated CuI films [30,32,33,39,44–49]. However, little research has been conducted to investigate the thermal properties of γ-CuI thin films, which are crucial to understand and develop thermoelectric applications. Therefore, a main goal of this thesis is to study the cross- and in-plane thermal conductivities of γ-CuI thin films as a function of film thickness, by using our modified 3ω methods.

4.1.3.1. Deposition of CuI thin films

Various synthesis techniques can be used to prepare CuI thin films, such as PLD [34,49], magnetron sputtering [32], iodination reaction [30,50], and hydrothermal evaporation [47]. In this thesis, γ-CuI thin films were deposited onto p-type doped Si (100) substrates using DC sputtering in a dynamically pumped chamber with a base pressure of about 1×10^{-5} mbar. Prior to the film deposition, the substrate was ultrasonically cleaned in acetone, ethanol and then dried with nitrogen gas. A high purity Cu-target (99.999% purity) of 4 inch in diameter was utilized for deposition of the γ-CuI thin films. A heated iodine source (iodine particles inside a cylinder of stainless steel) was connected with the deposition chamber in order to introduce iodine vapor for the γ-CuI deposition [31,39]. To maintain an acceptable iodine vapor pressure ($\approx 1 \times 10^{-3}$ mbar), the iodine source was kept at a temperature of 180 °C [39]. For adjustment of the iodine partial pressure, the throttle valve between the chamber and turbo molecular pump was partially closed. Ar-gas was added to set the overall pressure to 0.02 mbar [31]. Pre-sputtering was performed with a power of 30 W for 20 minutes with the shutter closed. The γ-CuI samples were sputtered at a power of 30 W at room temperature

[31]. The thicknesses of the deposited γ-CuI films were between 70 to 400 nm in order to study the thickness-dependency of the γ-CuI film thermal conductivity. The γ-CuI films were produced in the University of Leipzig as a joint research work [31], and part of the results were jointly obtained with Dr. Chang Yang in the University of Leipzig.

4.2. Material and nanostructure characterization

The crystalline structures of AlN and γ-CuI thin films were studied using a Rigaku SmartLab X-ray diffraction (XRD) spectrometer, with a Bragg-Brentano configuration and a Cu Kα line as an excitation source (40 kV/30 mA; λ_{wave} = 0.154 nm). The scan speed was set as 1 degree/min with 0.05 degree/step. The Bragg-Brentano (θ-2θ) configuration was used to identify the crystallographic phases and preferred orientations. The results of the XRD analysis were used to estimate the average grain sizes of the thin films by employing the Scherrer equation.

In this thesis, surface morphologies of AlN and γ-CuI thin films were investigated using a Bruker Dimension Icon AFM. For the AFM, typical scans were taken over an area of 1 μm × 1 μm (AlN films) or 5 μm × 5 μm (γ-CuI films) at a constant scan speed of 1 Hz. For γ-CuI films the scan-size was increased due to the larger surface particle sizes. The film's average surface particle/crystallite size distributions of the 3ω film samples as a function of film thickness were obtained based on analysis of the AFM images. The NanoScope Analysis software was used to determine the particle size distribution at the surface of the thin film samples. Furthermore, the AFM was used to measure the local thermal conductivity of thin films by combining the experimental setup of the AFM with the fundamental 3ω method. Details about this 3ω Microscopy technique are given in Section 4.3.2.

A scanning electron microscopy (SEM) with Energy Dispersive X-ray analysis (EDX) was employed to characterize the morphology, chemical composition and the interface region between the thin film and substrate, which is considered as an important factor for thermal performance. The SEM characterizations were performed using a Zeiss ULTRA 55 SEM and

an EDAX-EDX module. To analyze the cross-section, our AlN and γ-CuI samples were cleaned with acetone and ethanol, followed by high purity nitrogen drying.

The Seebeck coefficient S and the electrical conductivity σ of the γ-CuI were simultaneously determined under a helium atmosphere employing a Linseis LSR-3 measurement device [31]. The carrier type, density and mobility of our γ-CuI thin film samples were detected by Yang *et al*. [31] using an experimental Van-der-Pauw setup with a magnetic field of about 0.4 T.

The local thermal conductivity, cross- and in-plane thermal conductivities of thin film-on-substrate samples were obtained utilizing our 3ω Microscopy and differential multi-heater 3ω method as described in the following sections.

4.3. Thermal characterization and sample structure

4.3.1. Macroscopic 3ω method

In- and cross-plane thermal conductivity values of SiO_2, Si_3N_4, AlN and γ-CuI thin films were obtained utilizing both differential and multi-heater 3ω method, presented in Section 3.3.2.

4.3.1.1. Sample preparation

The sample preparation process of the macroscopic 3ω structures consists of three major steps:

1) surface cleaning of the film-on-substrate structure;

2) deposition of titanium (Ti) and Au for the 3ω heater/thermometer structures;

3) microfabrication of the 3ω heater/thermometer structures.

1) Surface cleaning

Since the above described methods assume a negligibly small interfacial thermal resistance between the heater and the sample, it is crucial to obtain a proper interface, where the heater

is in intimate contact with the sample surface. To eliminate possible particulate impurities, the sample used in the experiments were cleaned with acetone in an ultrasound bath for 5 minutes. The residual solvent was removed with ethanol, followed by drying with high purity nitrogen gas. To dehydrate the surface of the substrate, it was pre-baked at 200°C for 5 minutes on a hot-plate.

2) Deposition of Au and Ti

To fabricate the 3ω heater, a 20 nm thick Ti layer was first deposited using pulsed DC sputtering onto the surface of the film-on-substrate samples, followed by an Au layer between 250 and 500 nm in thickness. Au was used as the heater material because of its high temperature stability and high temperature coefficient of resistance α. The Ti layer was deposited to improve the adhesion strength of the Au-heater [51].

3) Microfabrication of the 3ω heater/thermometer structures

The deposited Au and Ti layers were patterned by a conventional microfabrication technique/lift-off process, as illustrated in Figure 4.3. The lithography mask used here was designed to yield four 3ω heater structures of line widths varied between about 1 and 25 μm and a length of 9 mm on the same thin film or substrate as shown in Figure 4.3.

Measured data obtained from the metal heaters with varied widths enable one to extract both the cross- and in-plane thermal conductivities of the same thin film sample (see Section 3.3.2.2). The heater widths and lengths were defined to satisfy the experimental design criteria of the 3ω method, which have been introduced in Section 3.3 (see Tables A.1 to A.3 of Appendix B).

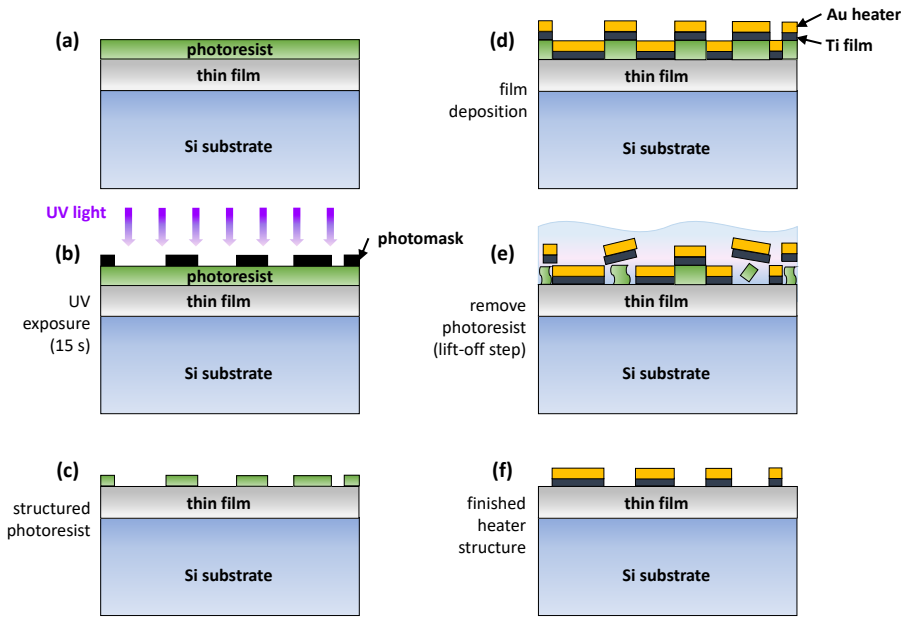

Figure 4.3: Microfabrication process steps for generating the 3ω line heater structure, which is necessary to obtain both cross- and in-plane thermal conductivity of thin films: (a) coat and prebake photoresist, (b) expose and develop photomask, (c) mask for 3ω structures, (d) deposition of Au/Ti films, (e) lift-off step, (f) finished 3ω line heater structure.

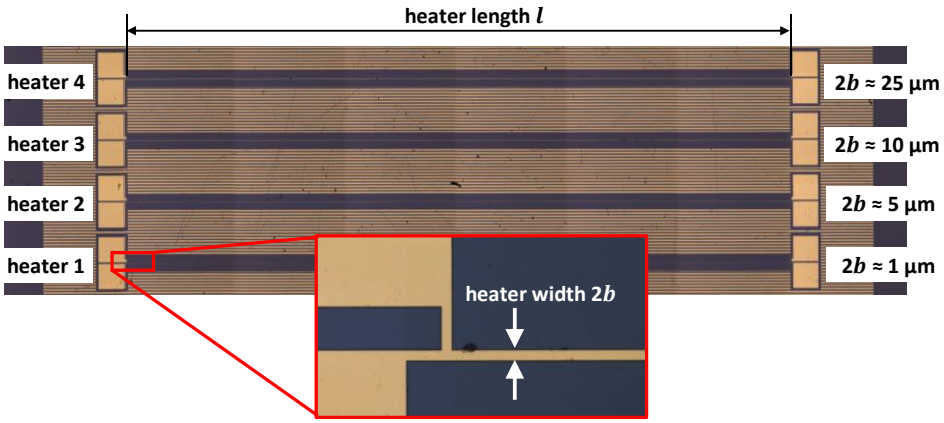

Figure 4.4: Top view of optical microscope image of the improved microstructure used for measuring both the cross- and the in-plane thermal conductivities in the same thin film. The Au heaters of line width $2b$ varying between around 1 and 25 µm and length of 9 mm are deposited on the same thin film sample. When the metal strip width is much larger than the thin film thickness, the thermal conduction is nearly one-dimensional in the direction normal to the film, and the cross-plane conductivity has a dominant influence on the temperature rise. On the other side, the sensitivity of the measurement to the in-plane conductivity increases with decreasing values of the ratio of the strip width to the film thickness (this figure is not in scale).

First, the film-on-substrate samples were covered with a Shipley 1827 photoresist for metal lift-off processing by spin coating at 5500 rpm (maximum coating uniformity) for 30 seconds, resulting in a homogenous resist layer of 1 µm, which was prebaked at 90 °C for 2 minutes on a hotplate to eliminate the remaining solvent concentration. The resist-coated samples were covered with a photomask containing the 3ω heater structures and then exposed to ultraviolet light for 15 seconds. After exposure, the photoresist of the film-on-substrate structures were developed in a developer bath of MF-319 for 45 seconds, followed by de-ionized water cleaning. After that, the Au/Ti layers were deposited at the entire surface of the sample (see Figure 4.3(d)). Then the photoresist was removed by sonication in acetone for 10 minutes. Finally, the sample surface was cleaned using ethanol, followed by high-purity nitrogen drying.

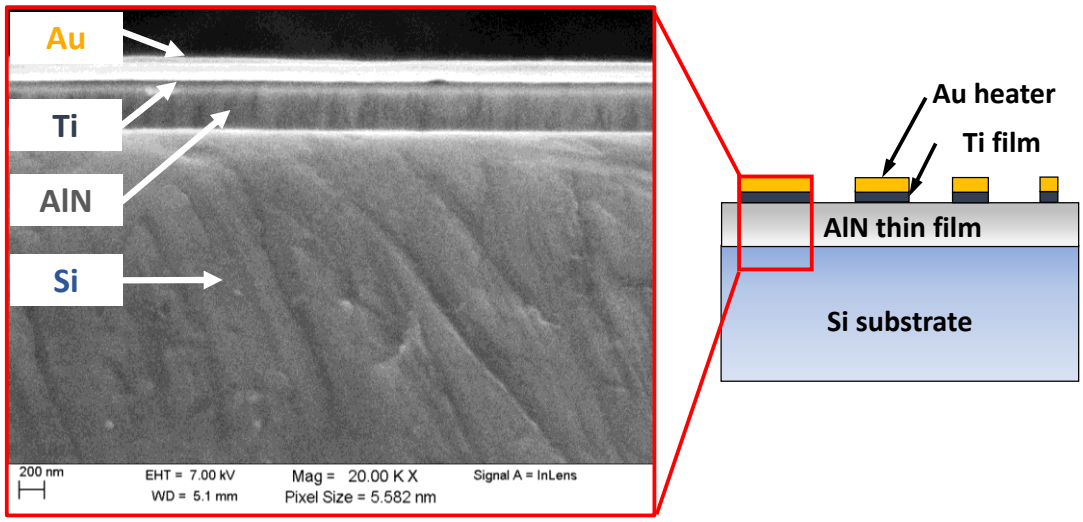

Figure 4.5: Cross-sectional SEM image of a 20 nm Ti film and a 250 nm Au layer deposited onto a 304 nm AlN film, studied in this thesis.

After the microfabrication of the 3ω heater structures, the heater length l and line width $2b$ were measured using a Nikon DS-Ri2 optical microscope. Figure 4.4 provides the microscope image of the four 3ω heater structures of line widths varied between 1 and 25 µm and a length of 9 mm, microfabricated on the same thin film, used for measuring the cross- and in-plane thermal conductivity of thin films. The resulting width of the 3ω heaters is uniform along the

length. Thus, to be as rigorous as possible when doing the 3ω measurements, the width of all heaters were measured separately for each sample.

Figure 4.5 shows a cross-sectional SEM image of the Ti (20 nm) and the Au (250 nm) films deposited by pulsed DC sputtering onto the surface of a 304 nm thick AlN thin film, investigated in this thesis. Both the Ti and Au layers are continuous and homogenous.

The schematic cross-sections of the investigated reference and thin film samples are illustrated in Figure 4.6. Table 4.2 summarized all details about the 3ω samples, which were investigated within this thesis to study the thickness-dependency of thermal conductivity.

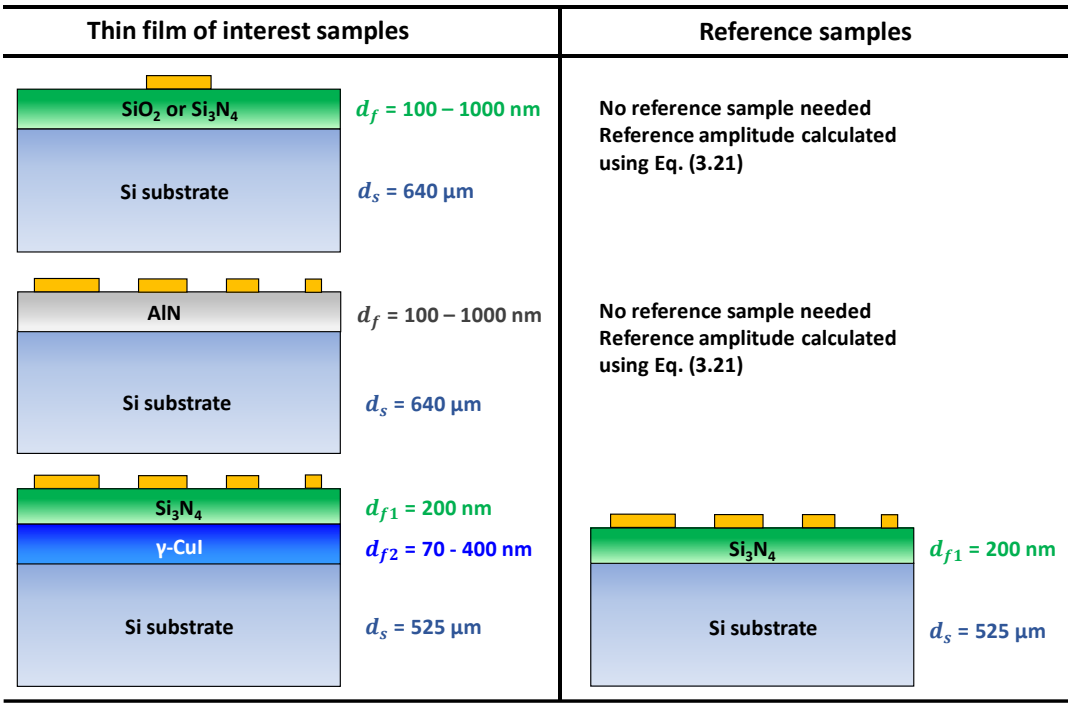

Figure 4.6: Schematic cross-sections of 3ω film-on-substrate samples required for the differential 3ω method: (right column) sample without the film of interest, (left column) multilayer samples including the film of interest and if necessary, the reference film-on-substrate structure. In such systems, the voltage drop across the metal strip depends on the temperature rise caused by the whole multilayer structure. The measured thermal transfer function is therefore the sum of the contributions of the thermal oscillations coming from different components of the system.

Table 4.2: Details about the 3ω thin film-on-substrate samples to study the thickness dependancy of the cross- and in-plane thermal conductivities of thin films.

No.	Direction	Thin film		Substrate		Other layers		3ω heaters			
		Material	d_f [nm]	Material	d_s [µm]	Material	d_f [nm]	Material	d_h [nm]	Width [µm]	TCR [K^{-1}]
1	Cross-plane	SiO_2	92	Si	640	None		Au	500	5-20	0.0031
2	Cross-plane	SiO_2	291	Si	640	None		Au	500	5-20	0.0031
3	Cross-plane	SiO_2	499	Si	640	None		Au	500	5-20	0.0031
4	Cross-plane	SiO_2	690	Si	640	None		Au	500	5-20	0.0031
5	Cross-plane	SiO_2	1002	Si	640	None		Au	500	5-20	0.0031
6	Cross-plane	Si_3N_4	298	Si	640	None		Au	500	5-20	0.0031
7	Cross-plane	Si_3N_4	500	Si	640	None		Au	500	5-20	0.0031
8	Cross-plane	Si_3N_4	601	Si	640	None		Au	500	5-20	0.0031
9	Cross-plane	Si_3N_4	698	Si	640	None		Au	500	5-20	0.0031
10	Cross-plane	Si_3N_4	1001	Si	640	None		Au	500	5-20	0.0031
11	Cross- and in-plane	AlN	99	Si	640	None		Au	250	1-25	0.0031
12	Cross- and in-plane	AlN	304	Si	640	None		Au	250	1-25	0.0031
13	Cross- and in-plane	AlN	511	Si	640	None		Au	250	1-25	0.0031
14	Cross- and in-plane	AlN	710	Si	640	None		Au	250	1-25	0.0031
15	Cross- and in-plane	AlN	1009	Si	640	None		Au	250	1-25	0.0031
16	Cross- and in-plane	γ-CuI	70	Si	525	Si_3N_4	200	Au	250	1-25	0.0043
17	Cross- and in-plane	γ-CuI	200	Si	525	Si_3N_4	200	Au	250	1-25	0.0043
18	Cross- and in-plane	γ-CuI	400	Si	525	Si_3N_4	200	Au	250	1-25	0.0043

4.3.1.2. 3ω experimental setup

The main challenge of the experimental setup is the reliable extraction of the 3ω voltage signals from the voltage oscillations of the thin film sample, since the amplitude of the 1ω voltage is typically 100 to 1000 times larger than that of the 3ω voltage [2,52]. Therefore, an appropriate electrical circuit, consisting of a differential lock-in amplifier and a bridge circuit, including two differential operational amplifiers (DA1/2, AD 620A), is needed. Figure 4.7 shows a schematic diagram of the experimental setup used to extract the 3ω voltage component along the metal heater.

An internal signal generator of the digital lock-in amplifier (Anfatec Instruments eLockIn204/2) produces the AC heating current. The generated heating current contains a low harmonic distortion of 0.0005%, because any third harmonic content in the signal generator can induce interfering signals during the thermal conductivity measurement. Both current ($I1$, $I2$) and voltage ($V1$, $V2$) pads (see Figure 3.2) of the 3ω heater structure are contacted with the lock-in amplifier using four micromanipulators as illustrated in Figure 4.8.

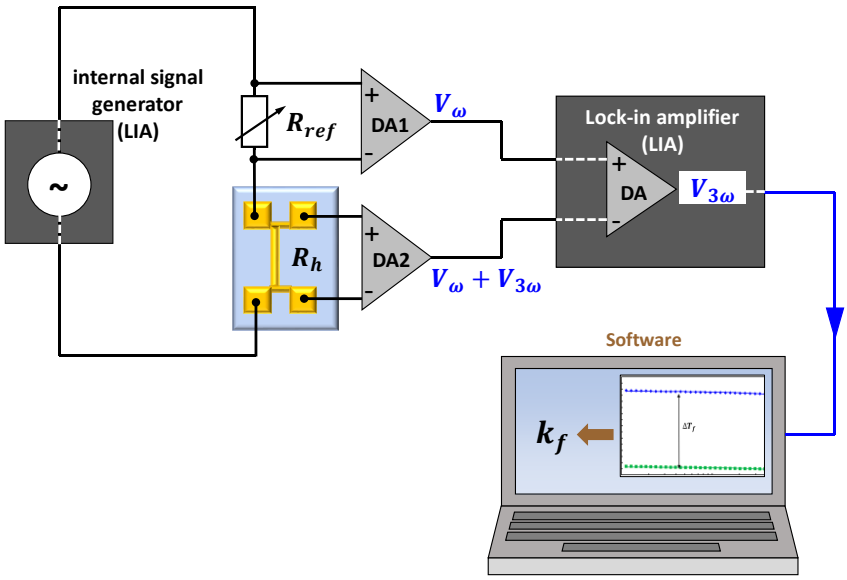

Figure 4.7: Schematic circuit diagram used to extract the 3ω voltage component from the voltage signal across the metal strip deposited on the sample and description of the operational amplifier-based electronic conditioning stage employed to perform the signal treatment (adapted and modified from Ref. [51]).

Due to the finite dynamic reserve of the lock-in amplifier of 135 dB, the suppression of the 1ω voltage from the 3ω signal is accomplished by a bridge circuit balanced by adjusting the series reference resistance R_{ref} [52]. The reference resistance R_{ref} needs a low temperature coefficient of resistance (≈15 ppm/K) and also a low thermal resistance to the environment to minimize any spurious 3ω artifacts, which could influence the measurement of the third harmonic voltage. To properly detect the 1ω and 3ω voltage signals, a differential lock-in amplifier with a bandwidth of 0.1 Hz up to 2 MHz was used. In order to reduce radiation and convection losses, the measurement was performed inside a vacuum chamber with a pressure less than 3.1 Pa using a Pfeiffer HiCub 80 turbo pumping station.

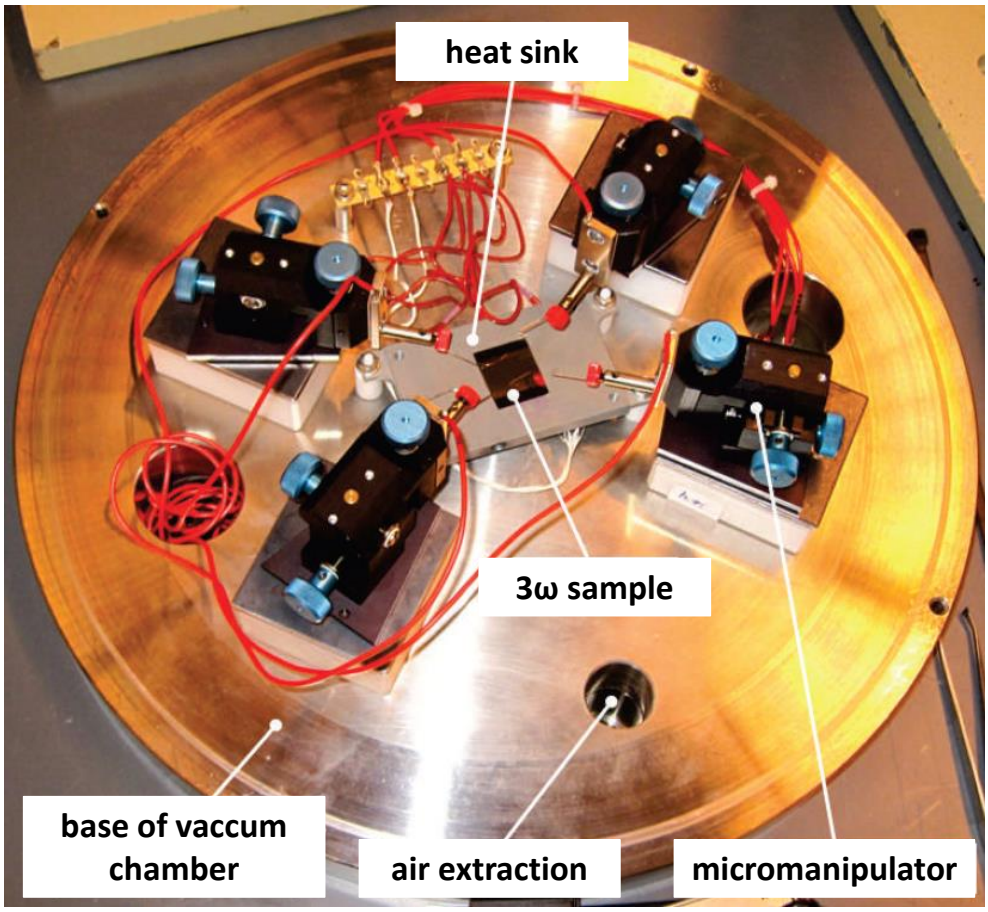

Figure 4.8: Setup of sample connection inside the vacuum chamber. Current and voltage pads (see Figure 3.2) of the 3ω heater structure are contacted with the lock-in amplifier, using four micromanipulators.

4.3.1.3. Thickness-dependent thermal conductivity measurements of thin films

Prior to the 3ω measurements, seven experimental variables have to be obtained for each sample, in order to calculate the thermal conductivity of SiO_2, Si_3N_4, AlN and γ-CuI thin films using Eq. (3.33) and Eq. (3.34):

- thin film thickness d_f;
- metal heater width $2b$ and length l;
- temperature coefficient of resistance of the metal heater α;
- heating power P of the metal heater;
- averaged amplitude of temperature oscillation of the substrate or reference sample ΔT_s;
- averaged amplitude of the temperature oscillation of the thin film-on-substrate or thin film-on-reference structure ΔT_f.

1) Thin film thickness d_f

The thicknesses of the investigated SiO_2, Si_3N_4, AlN and γ-CuI thin films d_f were measured using a surface profilometer. The reported values of the film thickness were obtained by averaging over at least five measurements. The measured film thickness values d_f of all the samples are listed in Table 4.2.

After the deposition of the thin films, the film thicknesses were once verified by performing film thickness measurements using a ZEISS laser-scanning microscope (LSM-800). Figure 4.9 shows the LSM image and line-scan evaluation of the film thickness measurement of a 1000 nm thick PECVD SiO_2 film deposited on a Si substrate. The LSM measurement is also capable to verify the thickness ($d_h \approx 500$ nm) of the metal heater used to perform the 3ω measurements. The thin film thicknesses obtained by the LSM were in good agreement with the results of the surface profilometer.

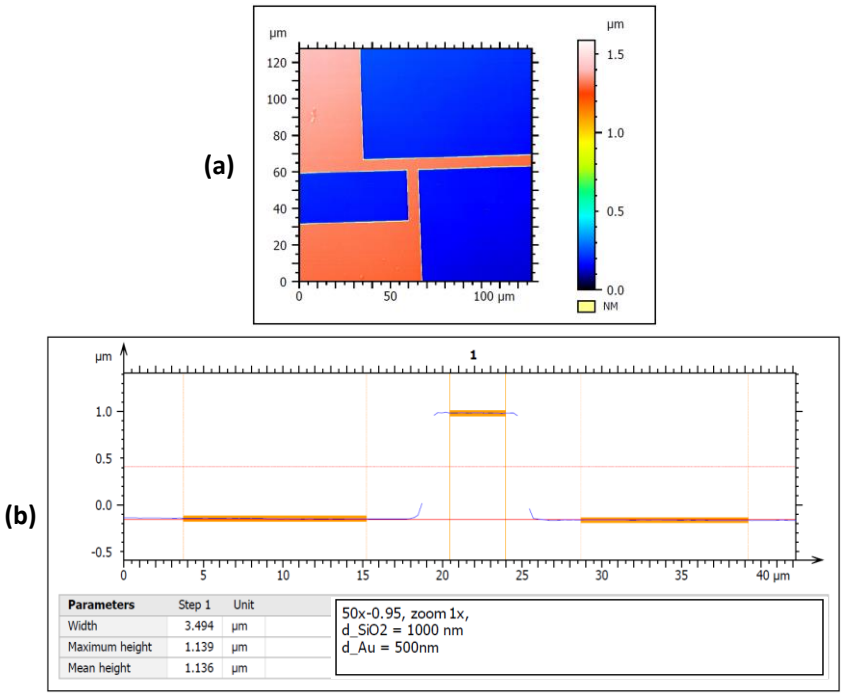

Figure 4.9: LSM image and line-scan of a 1000 nm thick PECVD SiO_2 film deposited on a Si substrate to verify the SiO_2 film thickness and 3ω line heater geometries: (a) topography image of the LSM (b) line-scan image of the evaluated LSM data to obtain the heater and film thickness.

2) Metal heater width $2b$ and length l

The line width $2b$ and length l of the metal heater were measured for each sample with a Nikon DS Ri2 optical microscope, calibrated for high precision measurements, as illustrated in Figure 4.10. To be as exact as possible for the data when executing the 3ω measurements, the line-width and length of all heaters were measured separately for each sample and the heater dimensions of all thin film samples are listed in Table 4.2. Figure 4.10 shows the optical microscope image of a 3ω line heater deposited on a 99 nm AlN thin film on a Si substrate. The heater width was measured to be 5.92 µm. As the heater width is much larger than the film thickness of 99 nm the heater was utilized to extract the cross-plane thermal conductivity of the AlN thin film, as introduced in Section 3.3.2.1.

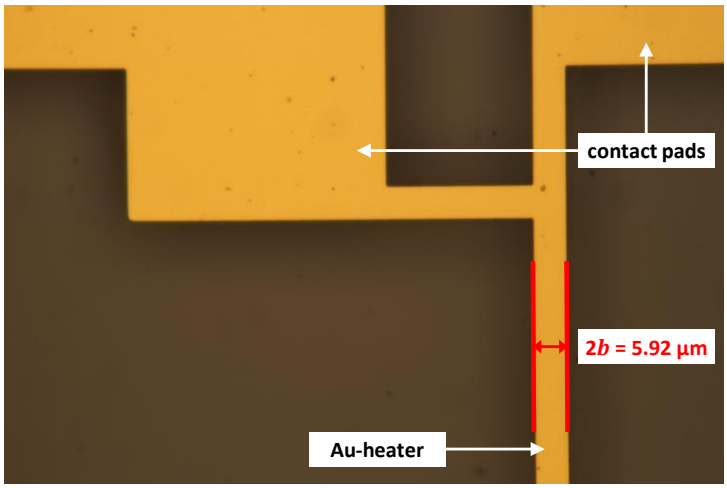

Figure 4.10: Top view of a microfabricated 3ω line heater structure on a 99 nm AlN thin film on a Si substrate with a width of 5.92 µm obtained by an optical microscope.

3) Temperature coefficient of resistance α of the metal heater

The temperature coefficient of resistance (TCR) α of the metal heaters were determined by measuring the electrical resistance of the metal heater $R_h(T)$ as a function of the heater temperature T_h, employing a four point probe method. Therefore, the 3ω samples were placed in a vacuum chamber and a step-wise temperature application was implemented, keeping the sample at a constant temperature until the thermal equilibrium was reached.

The electrical resistance of the heater was measured between 20 and 120°C with a temperature step of 10 K. Figure 4.11 shows the measurement results of the TCR measurements of the AlN and γ-CuI thin film heater structures. The coefficient α was then determined from the slope of the electrical resistance versus temperature curve, as given by Eq. (3.2). The slope of the experimental data was determined by a linear fitting curve. The reported TCR values were obtained by averaging over five measurements for each thin film sample. The average α-values of the AlN and γ-CuI thin film heater structures, depicted in Figure 4.11, are 0.00310 K^{-1} and 0.00434 K^{-1}, respectively. The maximum deviation of the calculated values of the five measurements was below 0.8% for each sample. The temperature coefficients of the metal heaters used in this thesis are listed in Table 4.2.

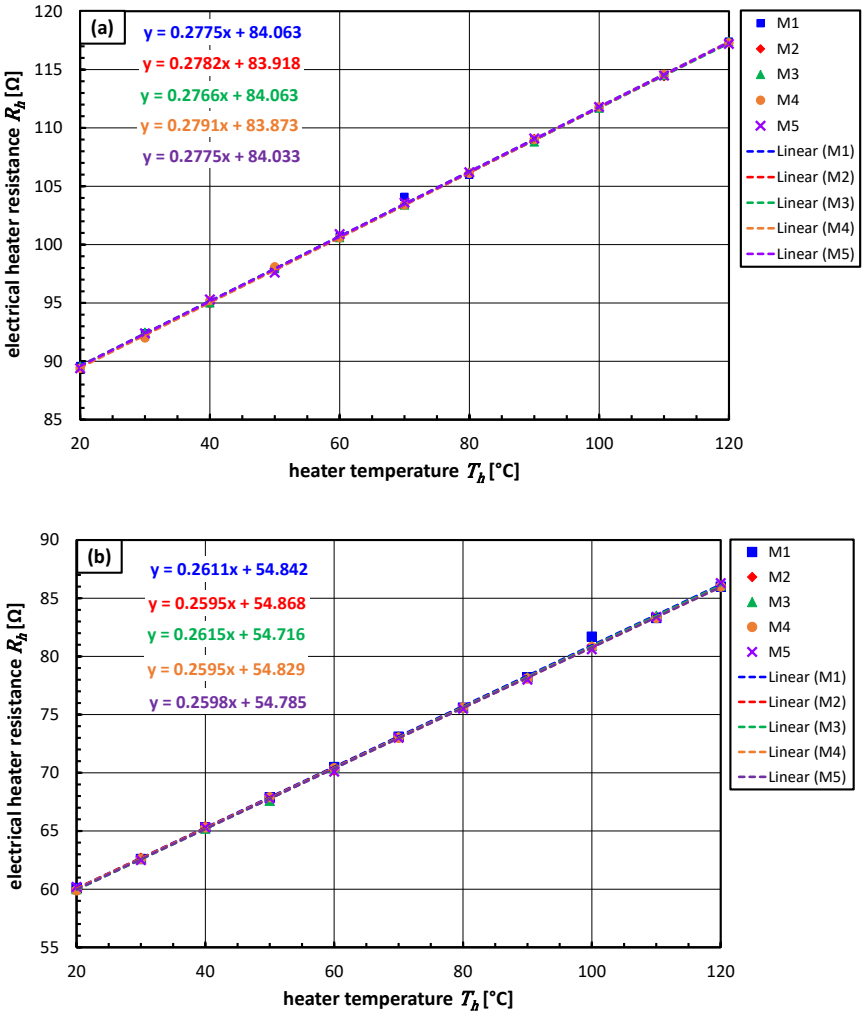

Figure 4.11: Electrical resistance of the metal heater $R_h(T)$ as a function of the heater temperature T_h to determine the metal heater's TCR α. The electrical resistance of the heater was measured between 20 and 120°C with a temperature step of 10 K. The coefficient α was then determined from the slope of the linear fitting curve (dashed lines), as given by Eq. (3.2). The average values out of five measurement of the (a) the AlN and (b) γ-CuI samples are 0.00310 and 0.00434 K^{-1}, respectively.

4) Heating power P of the metal heater

The rms value of the heating power P produced by the metal heater when heated by the heating current I_h was calculated using:

$$P = \frac{{V_h}^2}{R_h} \tag{4.1}$$

$$I_h = \frac{V_h}{R_h} \tag{4.2}$$

where V_h and R_h are the voltage drop at and the electrical resistance of the 3ω line heater, respectively. Both were measured using a digital multimeter. The dissipated heating power of the heater was determined before every 3ω measurement and ranged between 30 and 165 mW (rms), which is corresponding to a heating current of 10 up to 30 mA (rms).

5) Average amplitude of the temperature oscillation of the thin film-on-substrate or thin film-on-reference-structure ΔT_f:

In order to obtain the average amplitude of the temperature oscillation of the thin film-on-substrate or thin film-on-reference-structure, the samples were placed onto a chuck at room temperature and four microprobes were positioned onto the electrical pads of the metal heater, as depicted in Figure 4.8. Then 3ω measurements were performed by recording the amplitude of the 3ω voltage $V_{3\omega}(f)$ for heating frequencies, ranging from 100 to 1000 Hz. Thus, considering the typical values of the specific heat capacity $c_{p,Si}$ (711 $Jkg^{-1}K^{-1}$ [53]), the density ρ_{Si} (2330 kgm^{-3} [53]) and the thermal conductivity k_{Si} of Si (147 $Wm^{-1}K^{-1}$ [53]), the thermal wave propagates at a distance λ_{si} between 266 and 84 µm (using Eq. (3.13)) beneath the samples at frequencies between 100 and 1000 Hz. The amplitude of the thermal oscillation ΔT_f can be obtained from the 3ω voltage component using Eq. (3.10). For heating frequencies below 100 Hz, the thermal wave, which propagates into the sample, would be reflected from the backside/bottom of the substrate and could lead to a superposition of the thermal wave. This superposition causes an unstable 3ω voltage.

For heating frequencies above the 1000 Hz, the thermal wave can be disturbed and/or reflected at the interface between the thin film and substrate, also leading to serious interference issues during the 3ω voltage detection. As a result, the heating frequency and therefore the thermal penetration depth (see Eq. (3.13)) should be in the range of the linear regime (constant negative imaginary part of the 3ω voltage), introduced in Section 3.3.1.3, in

order to avoid reflections at the bottom of the substrate or the interface between the film and substrate. Within this frequency range, the experimental design criteria of the studied thin film samples for the 3ω method are satisfied, in order to achieve a low measurement error of 1% (see Appendix B) [52].

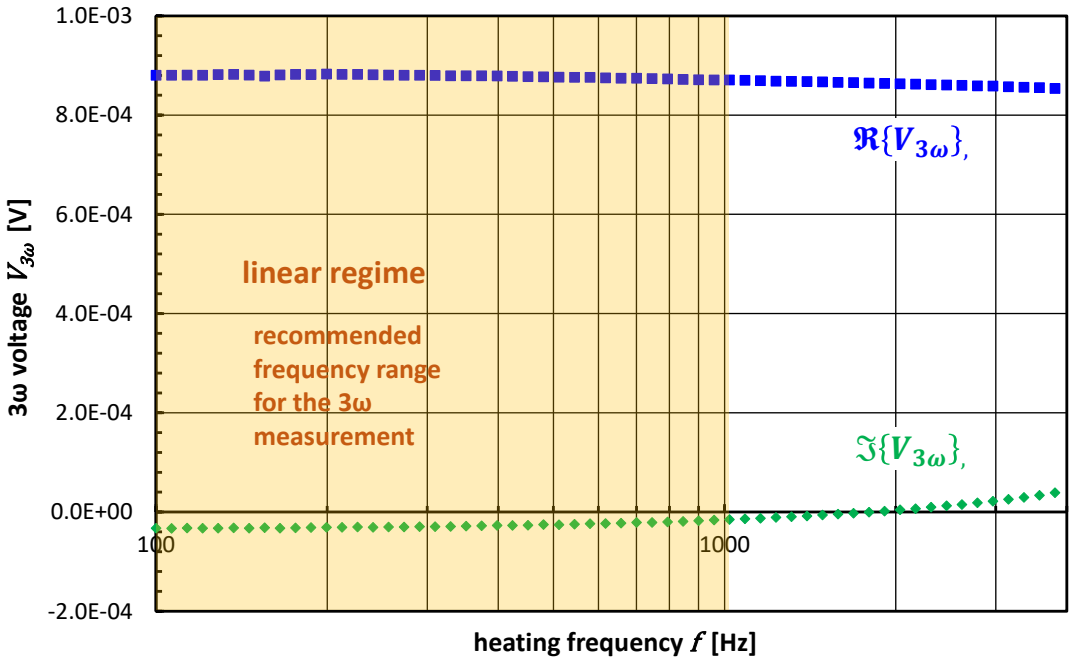

Figure 4.12: Real (blue colored squares) and imaginary (green colored diamonds) parts of the 3ω voltage of a 600 nm PECVD Si_3N_4 film deposited on a 640 µm thick Si substrate, to obtain the amplitude of the temperature oscillation of the film-on-substrate system ΔT_f. The orange colored area represents the recommended heating frequency range to perform 3ω measurements of the Si_3N_4 film, which is between 100 and 1000 Hz. This region is the so called linear regime, where the imaginary part of the 3ω voltage has an almost constant negative value.

To calculate the amplitude of the frequency-dependent thermal oscillation of the film-on-substrate structure, the thermal oscillations were averaged over the entire frequency range between 100 and 1000 Hz. Figure 4.12 shows an example of a 3ω measurement data to detect the frequency-dependent 3ω voltage component, in order to determine the amplitude of the temperature oscillation of the film-on-substrate system.

6) Average amplitude of temperature oscillation of the substrate or reference sample ΔT_s:

The average amplitude of the temperature oscillation of the substrate or reference sample ΔT_s can either be measured utilizing the 3ω method [52,54] or calculated using equations [2,55].

For analyzing complex systems composed of several films a reference sample is needed, because it enables the determination of the thermal conductivity of the specific film in a multilayer structure [12,52,56]. Furthermore, the differential approach is capable to obtain the thermal conductivity values of electrically conductive thin films, such as metals and semiconductors [52,56]. However, a dielectric thin film between the metal 3ω heater and the conductive thin film of interest is required. Therefore, the reference amplitude of temperature oscillation for the reference sample ΔT_s, can be obtained by performing a basic 3ω measurement as described in the paragraph above (see ΔT_f values). Due to the high electrical conductivity of γ-CuI thin films this approach was used to determine the reference amplitude of the temperature oscillations. The structure of the utilized reference sample is shown in Figure 4.6 and the experimental results are provided in Chapter 6.

As Cahill *et al*. [2,55] suggested, the amplitude of temperature oscillation of the substrate ΔT_s of a standard dielectric film-on-substrate system does not need to be measured and instead should be calculated using Eq. (3.22). Cahill *et al*. [2,55] and Borca-Tasciuc *et al*. [54] reported that the calculated values are in extremely good agreement with experimental results using Eq. (3.22) and is nowadays a standard procedure for the 3ω measurements [2,52,54,55,57]. In order to calculate the ΔT_s values, the specific heat capacity c_p, the density ρ and the thermal conductivity of the substrate k_s, in our case Si are needed. The thermal conductivity of the substrate is determined by Eq. (3.25) after performing a 3ω measurement over a frequency range between 100 and 1000 Hz, as demonstrated above. In this thesis we used literature values for the specific heat capacity c_p (711 $Jkg^{-1}K^{-1}$ [53]) and the density ρ (2330 kgm^{-3} [53]) for the Si substrate. In literature, these values always vary slightly, but this has no significant influence on the determined results of the thin film thermal conductivity as

a 10% deviation of one of these parameters would only result in a deviation below 1% of the calculated thin film thermal conductivity value. In this thesis, the amplitude of temperature oscillation of the substrate ΔT_s, was calculated for each of SiO_2, Si_3N_4 and AlN film-on-substrate samples and therefore no reference sample was needed. The experimental results are provided in Chapters 5 and 7.

Film thickness-dependent cross- and in-plane thermal conductivity measurements of AlN and γ-CuI thin film samples were performed by our differential multi-heater 3ω method. Due to the fact that the γ-CuI samples need a reference sample to obtain the thermal conductivity of the thermoelectric γ-CuI films, Eq. (3.34) was applied to determine the cross- and in-plane thermal conductivities. The thermal conductivity values of AlN thin films in cross- and in-plane direction were calculated by applying Eq. (3.33), as no reference sample was needed.

SiO_2 and Si_3N_4 thin films were served as reference samples, as their thermal conductivities are well-known [2]. Therefore, only the cross-plane thermal conductivity as a function of film thickness was studied. The thin film thermal conductivities of SiO_2 and Si_3N_4 were calculated using Eq. (3.33).

The film thicknesses of the investigated thin films were varied from:

- SiO_2 (92 to 1002 nm)
- Si_3N_4 (298 to 1001 nm)
- AlN (99 to 1009 nm)
- γ-CuI (70 to 400 nm)

The determined cross- and in-plane thermal conductivity values of SiO_2, Si_3N_4, AlN and γ-CuI thin films were obtained by averaging the thermal conductivity values over five 3ω measurements for each thin film sample. The maximum deviation of the calculated values of these five measurements was below 2.5% for each sample.

In order to reduce radiation and convection losses and simultaneously increase the reproducibility of our 3ω measurements, the measurements were performed inside a vacuum chamber with a pressure below 3.1 Pa. Figure 4.13 compares the reproducibility under vacuum conditions and in air without the cap of the vacuum chamber. For each condition five 3ω measurements were performed on the same 1000 nm thick PECVD SiO_2 film. Figure 4.13 clearly illustrates that the reproducibility of the 3ω measurements is drastically improved under vacuum conditions.

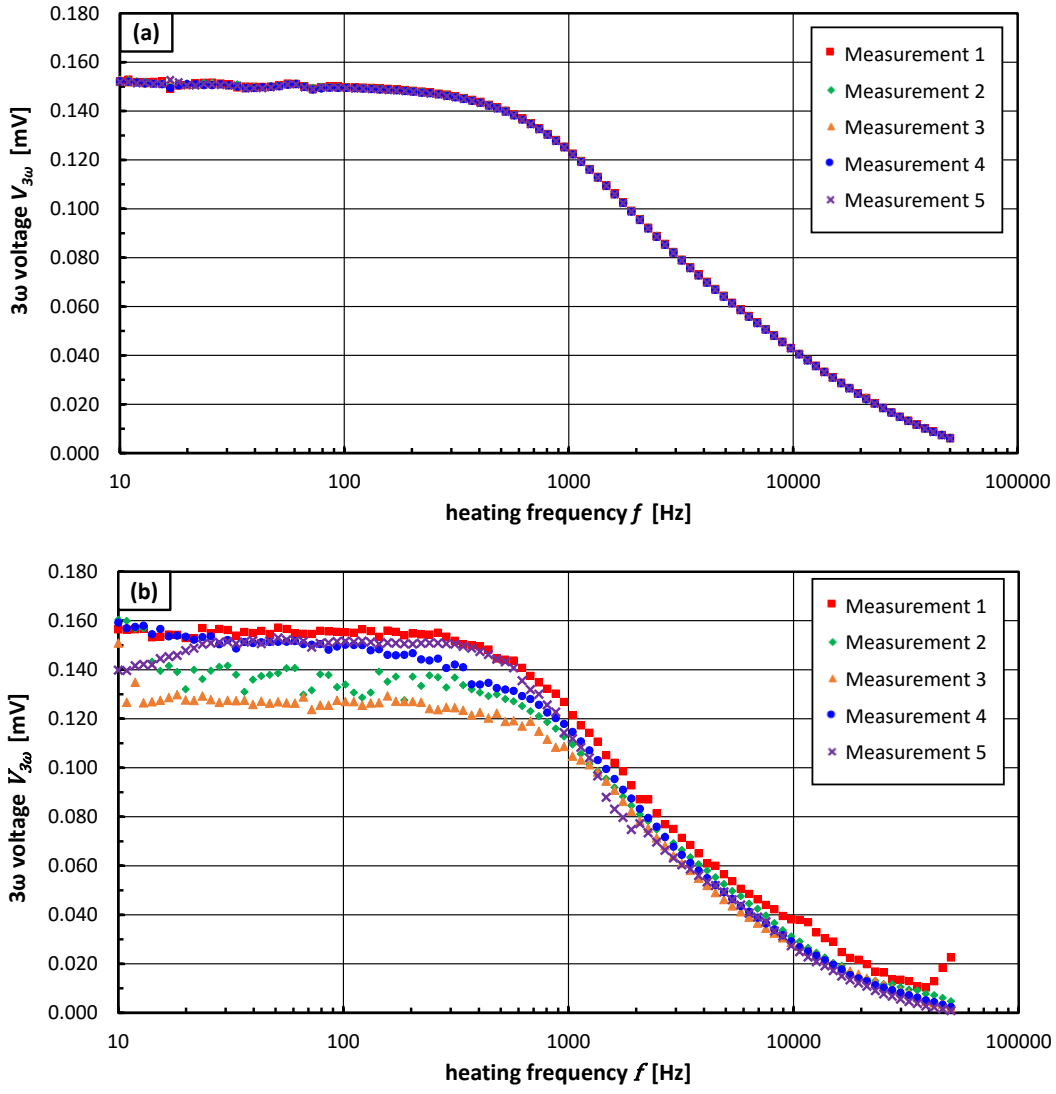

Figure 4.13: Experimental results of five 3ω measurements performed on the same 1000 nm thick PECVD SiO_2 film under (a) vacuum conditions (pressure in vacuum chamber below 3.1 Pa) and (b) in air without the protection of the vacuum chamber's cap.

The main sources of experimental uncertainties in the 3ω method measurements arise either from the fundamental assumptions used in the heat conduction models that are incorporated in the measurement procedure, or from the limited accuracy of the apparatus used to measure the variables, which are then employed to calculate the thermal conductivity. The detailed experimental uncertainty analysis of the macroscopic 3ω method is given in Appendix C.

The experimental parameters of the 3ω measurements corresponding to the SiO_2, Si_3N_4, AlN and γ-CuI thin films and the reference samples are summarized in Tables A7 to A.14 of Appendix D, respectively. The results of the thickness-dependent cross- and in-plane thermal conductivity measurements of the investigated SiO_2, Si_3N_4, AlN and γ-CuI are discussed in Chapters 5 to 7.

4.3.2. Local thermal properties of thin films (Microscopic 3ω method)

4.3.2.1. Principle of operation and experimental setup

Over the past decades, the 3ω measurements were performed utilizing various heater designs for studying thermal heat conduction of thin films and substrate materials [52]. The metal heater's width $2b$ and length l are in the range of several micrometers and millimeters, respectively (see Table 4.2) and the obtained thermal conductivity is the mean value over the heater area.

In our novel 3ω Microscopy setup, the metal heater is replaced by a thermo-resistive AFM probe, which is simultaneously operated as both a heater and thermometer. In order to investigate the local thermal properties, the thermo-resistive probe has to be in contact with the surface of the sample. If the AFM is operated in a contact mode (see Figure 4.14), the fundamental 3ω method can be applied to the resistive probe. In that case, an AC current $I(t)$ with an angular modulation frequency ω is driven through the thermo-resistive probe, and causes Joule heating and generates a temperature oscillation $\Delta T(\omega)$ at a frequency of 2ω. This results in a voltage oscillation $\Delta V(\omega)$ along the resistive probe with a frequency-dependent

third harmonic voltage component $V_{3\omega}(f)$, which depends on the temperature oscillation of the thermal probe [51]. As discussed in Section 3.2, temperature and voltage oscillations obtained by 3ω measurements are the key parameters for determining the local thermal properties of thin films and substrate materials.

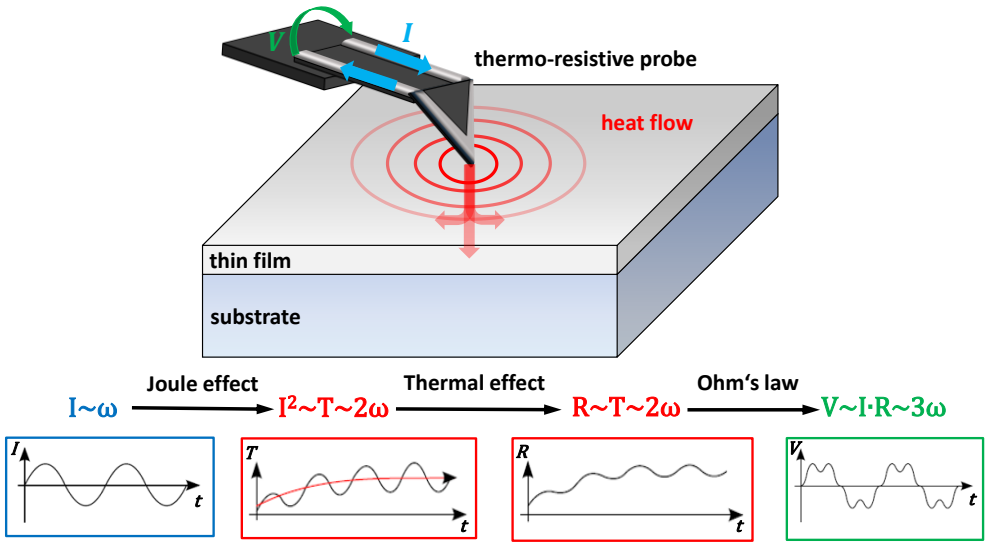

Figure 4.14: The 3ω Microscopy method uses a thermo-resistive AFM probe as both the heater and thermometer. An AC current at angular frequency ω heats the surface of the sample at a frequency of 2ω. Since the resistance of the thermo-resistive probe increases with temperature, temperature oscillations produce an oscillation of the electrical resistance at a frequency of 2ω. Consequently, the voltage drop across the thermo-resistive probe has a small component at a frequency of 3ω that can be used to measure the local temperature oscillations and the local thermal response of the film-on-substrate structure.

The temperature oscillation of the thermo-resistive probe at the surface of the investigated sample can be determined by an approximation of Eq. (3.19) and is given by Eq. (3.22), if the thermal penetration depth λ is much larger than the half-width b of the heat source ($\lambda \gg b$) [55]. With a contact area of several tens of nanometers of the thermo-resistive probe and a thermal penetration depth λ (see Section 4.3.1.3) of several micrometers, this condition should be satisfied [58,59]. As indicated by Eq. (3.25), the local thermal conductivity value of a bulk material can be obtained from the slope of the in-phase magnitude of the measured $\Delta T_{2\omega,avg}$ (real part from the temperature oscillation) as a function of $\ln(2\omega)$.

In order to obtain local thermal conductivity values of thin films, the classic 3ω method, presented in Section 3.3.2.1, has been utilized. Using the classic 3ω method, the thermal conductivity of a thin film can be obtained by comparing the average amplitude of the temperature oscillation of a film-on-substrate sample with the corresponding value of the substrate. The temperature variation of the film-on-substrate sample can be experimentally measured by detecting the voltage oscillation across the thermo-resistive AFM probe, which is proportional to the oscillating resistance value. The thermal response of the substrate ΔT_s can be calculated directly from Eq. (3.22) and subtracted from the measured amplitude of the temperature oscillation ($\Delta T_{2\omega|avg} = \Delta T_f + \Delta T_s$). Thermal conductivity of the substrate k_s can also be calculated from the slope of $\Delta T_{2\omega|avg}$ versus $\ln(2\omega)$ as shown by Eq. (3.25). Finally, Eq. (3.33) allows the direct measurement of the local thermal conductivity at any position of surface of the studied thin film.

4.3.2.2. Experimental setup

The thermo-resistive probe represents the heart of the experimental 3ω Microscopy setup, because accuracy, thermal and spatial resolution of the local thermal measurements are determined by the probe specifications such as TCR α_{tip}, thermal exchange radius r_{th} and cut-off frequency f_{cut}.

The thermal exchange radius r_{th} between the tip of the thermo-resistive probe and thin film sample is the most critical parameter of our 3ω Microscopy, because it defines the lateral spatial resolution of local thermal conductivity measurements. Therefore, an accurate value of the thermal exchange radius r_{th} is absolutely critical in order to precisely determine the local thermal properties of thin films [58,60,61]. So far, the thermal exchange radius is estimated to be equal to the tip-apex radius r_{tip} of the thermo-resistive probe, which can be obtained from the SEM images [58,59]. However, as this estimation is not accurate enough, an experimental technique to precisely evaluate the thermal exchange radius of thermo-resistive probes was provided by Puyoo *et al*. [58]. Detailed information about this

evaluation procedure can be found in reference [58]. Furthermore, Puyoo *et al*. [58] evaluated the thermal exchange radii of two thermo-resistive probes: the widely used Wollaston wire probe and a new thermo-resistive probe that consists of a palladium (Pd) film on a SiO_2 substrate, and they demonstrated that the thermal exchange radius is strongly dependent on the tip sharpness and the environmental conditions [58]. In the following, we will discuss the specifications of these two probes and discuss, which one is the most suitable for our 3ω Microscopy technique.

The most commonly used thermo-resistive probe for the scanning thermal microscopy (SThM) applications is the so-called "Wollaston wire" probe [58,62,63]. The Wollaston wire probe was the first thermo-resistive probe for SThM [62,64]. Figure 4.15 shows a schematic illustration and also an SEM image of the Wollaston wire probe.

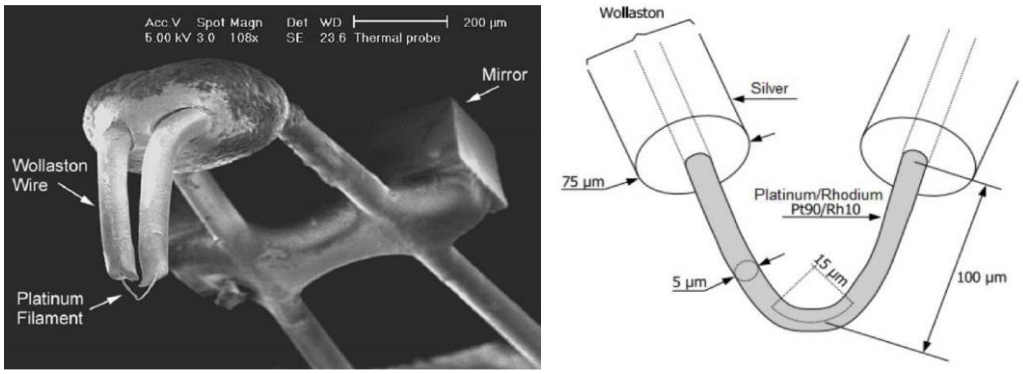

Figure 4.15: (a) SEM image and (b) schematic illustration of the thermo-resistive Wollaston wire probe (adapted and modified from Ref. [65]).

The cantilever is made of a Wollaston wire consisting of a silver shell of 250 µm in diameter and a core of an alloy of platinum (Pt) and rhodium (Rd) (Pt_{90}/Rd_{10}) of 5 µm in diameter [58,62]. At the extreme condition of the cantilever, the wire is bent into a V-shape and electrochemically etched to uncover the Pt_{90}/Rd_{10} part over a length of approximately 200 µm [58,62]. As mentioned above, the most important parameter of the Wollaston wire probe is its thermal exchange radius. Puyoo *et al*. [58] evaluated the thermal exchange radius and the cut-off frequency of the Wollaston probe, which are 820 nm and 240 Hz, respectively. As a

result, the large thermal exchange radius and low cut-off frequency limit the accuracy, speed and spatial resolution of local thermal analysis at nanoscale.

In this study, a novel commercial Pd/SiO_2 thermo-resistive probe from Bruker Instruments (VITA-GLA DM) is used as heater/thermometer in our 3ω Microscopy system. Figure 4.16 shows an SEM image of the thermo-resistive probe.

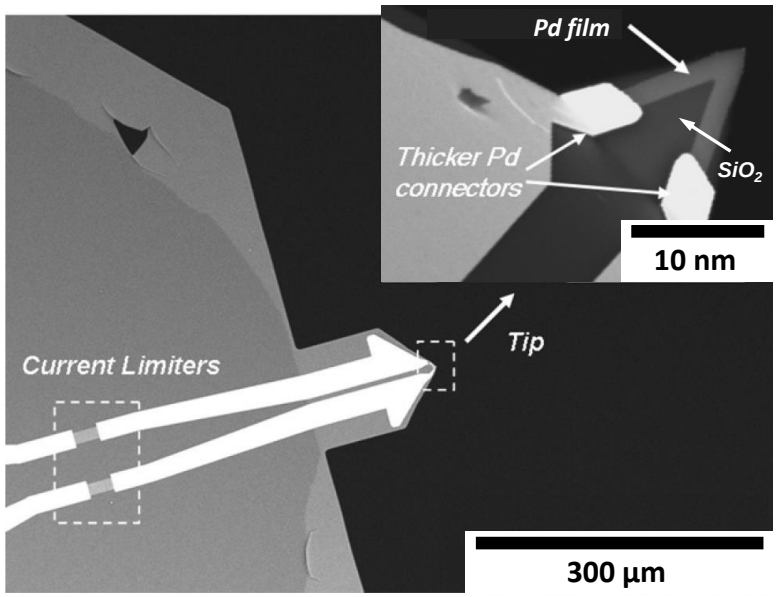

Figure 4.16: SEM image of the new thermo-resistive Pd/SiO_2 probe from Bruker Instruments (image from VITA-GLA DM) (adapted and modified from Ref. [57]).

It is a specially designed SiO_2 silica contact mode probe that incorporates a thin Pd ribbon near the apex of the tip. Two nickel chromium current (NiCr) limiters are located upstream from the tip, as shown in Figure 4.16. The thin Pd ribbon serves as the thermo-resistive module. Its temperature coefficient α has a value of 1.2×10^{-3} K^{-1} [58,66], which is large enough to generate a detectable 3ω voltage ($V_{3\omega}$). The electrical resistance $R_{h,0}$ of the resistive probe is 347 Ω at room temperature. The Pd tip resistance ($R_{h,Pd}$ = 179 Ω) and the resistance of the NiCr current limiters ($R_{h,NiCr}$ = 168 Ω) can be obtained by a two point probe measurement. The length l and width w of the Pd-strip are 10 µm and 1.4 µm, respectively. The tip height is about 10 µm and the total thickness of the tip's Pd and SiO_2 films is 1 µm. Both the length and width of the Pd tip were verified by SEM observation. This Pd tip has a

curvature radius of about 50 nm [62,67] and its time response has been estimated to be a few tens of microseconds [58,66]. Furthermore, the Pd/SiO_2 thermo-resistive provides a thermal cut-off frequency of 2750 Hz [58], which drastically reduces the image acquisition time compared to that from the Wollaston wire probe [58,62]. Another advantage of using the Pd/SiO_2 probe is the small thermal exchange radius of about 100 nm, which is roughly 8 times smaller than the exchange radius of the Wollaston wire [58]. Due to the small thermal exchange radius and the large cut-off frequency of the Pd/SiO_2 SThM probe, the spatial and thermal resolutions of local thermal measurements can be improved [58,67].

Figure 4.17 shows a schematic diagram of the experimental setup of the 3ω Microscopy utilized to measure the 3ω voltage and then obtain the local thermal properties of thin films and substrate materials. The experimental setup of the 3ω Microscopy is based on an AFM equipped with a thermo-resistive probe (Pd/SiO_2 probe), which records the local thermal properties of thin films while simultaneously measures the topography in contact mode configuration.

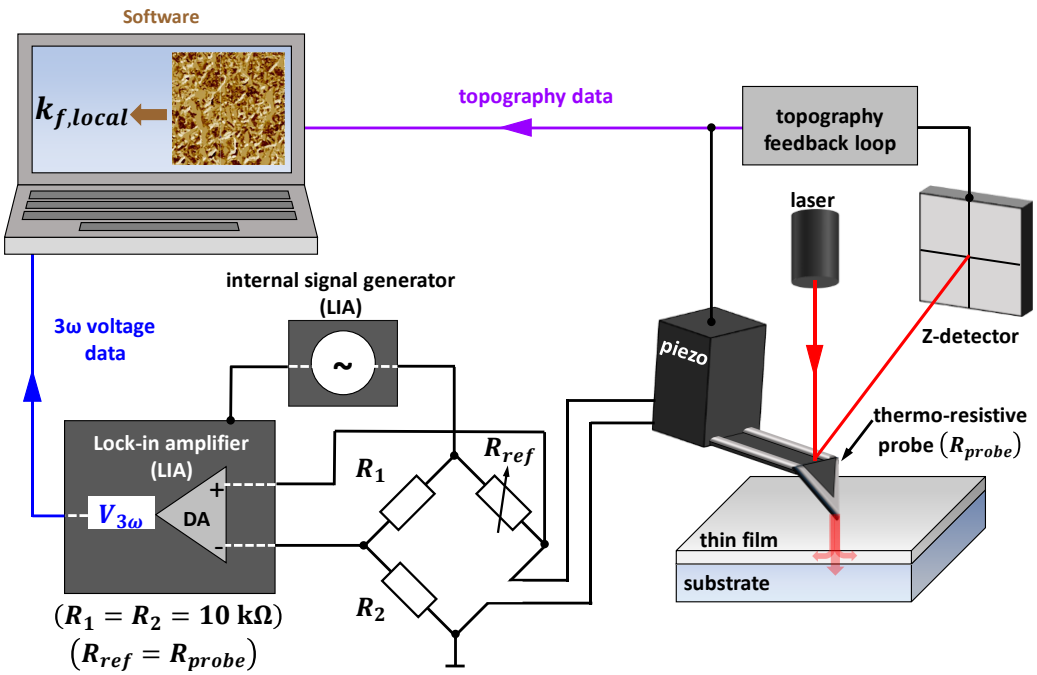

Figure 4.17: Schematic of the experimental setup and Wheatstone bridge circuit developed to measure the 3ω voltage from the voltage signal across the thermo-resistive AFM probe placed on top of the thin film's surface.

In this thesis, a Bruker Dimension Icon AFM with a VITA-SThM extension was used to implement the 3ω Microscopy technique to measure the local thermal properties of thin films. An internal signal generator of the digital lock-in amplifier (Anfatec Instruments eLockIn204/2) produces an AC heating current [51]. As discussed in Section 4.3.1.2, the generated heating current contains a low harmonic distortion, because any third harmonic content in the signal generator can induce interfering signals during the local thermal conductivity measurement. Due to the finite dynamic reserve of the lock-in amplifier (135 dB), the suppression of the 1ω voltage from the 3ω signal is accomplished by a Wheatstone bridge circuit [52], as illustrated in Figure 4.17. Therefore, the thermo-resistive probe and a variable reference resistor R_{ref} are both parts of the Wheatstone circuit. In order to effectively suppress the 1ω voltage from the 3ω voltage signal, the variable resistor R_{ref} has to be adjusted so that its electrical resistance is equal to the probes electrical resistance ($R_{ref} = R_{h,0}$). The reference resistor R_{ref} needs a low temperature coefficient of resistance (≈15 ppm/K) and also a low thermal resistance to the environment in order to minimize any spurious 3ω artifacts, which could influence the measurement of the third harmonic voltage [51].

The AC signal generator is responsible to drive the heating current through the resistive Pd/SiO_2 probe. Firstly, a small current is applied to determine the resistance $R_{h,0}$ of the thermo-resistive probe. Then, a significantly higher AC current between 1 and 3 mA is applied for heating the thermo-resistive tip. By scanning the Pd tip above the surface of the thin film, the temperature distribution of the probe-induced heat can be measured depending on the tip position at the surface of the sample, as it is depicted in Figure 4.14. As mentioned before, the thermo-resistive probe is simultaneously acted as a heater and a thermometer, and the periodical resistance variation $\Delta R(t)$ due to the varying thermal conductivity of the sample is very small, due to the minimal contact area between thin film and thermo-resistive probe.

By performing the 3ω Microscopy measurements inside a vacuum chamber with a pressure less than 4.0 Pa using the turbo pumping station of the Bruker AFM system, radiation and convection losses were reduced.

4.3.2.3. 3ω Microscopy calibration

Applying the standard 3ω heater layout as presented in Section 3.2, the thermal conductivity of the thin films can be determined by comparing the temperature oscillation in a film-on-substrate structure with the corresponding value of the substrate, with the condition that the thermal penetration depth λ is much larger than the half-width b of the heat source (see Section 3.3.1.2) [55]. The substrate must see the 3ω heater as a line source of heat, which can be accomplished if the ratio between the penetration depth of the thermal wave and the heater half-width is larger than five ($\lambda_s / b > 5$) to keep measurement errors of the 3ω method under 1% [54] .As the standard 3ω heater is replaced by a thermo-resistive probe, the heater half-width b is equivalent to thermal exchange radius r_{th} of the Pd tip [58,60]. With a thermal exchange radius of about 100 nm [58] and thermal penetration depth of several micrometers (between around 266 to 84 μm), these conditions are satisfied for the 3ω Microscopy technique and the local thermal conductivity of the thin films $k_{f,local}$ is then given by:

$$k_{f,local} = \frac{P_l \, d_f}{r_{th} \cdot \Delta T_f} \tag{4.3}$$

where r_{th} is the thermal exchange radius, ΔT_f the temperature rise caused by the thin film, d_f the thin film thickness and P_l the heating power per unit length. However, the amplitude of the heating power P_l applied in the thin film has to be determined for the Pd tips. Assy *et al*. [65] and Gomes *et al*. [62,68] recommended that an experimental calibration for quantitative local thermal conductivity measurements can be performed with reference measurements of a flat bulk sample of well-known thermal conductivity in a range that covers the expected thermal conductivity value of the investigated thin film material.

In this thesis, a commercial glass-ceramic reference material (BCR-724) was utilized as a calibration sample for the 3ω Microscopy technique. The thermal conductivity value of this reference sample was investigated by a hot wire technique, which is similar to the 3ω method and the results were certified by the Institute for Reference Materials and Measurements of the Joint Research Centre (European Commission) [69]. The thermal conductivity value for the BCR-724 bulk sample with a diameter of 26.9 mm and a height of 22.0 mm is (4.08 $\pm$ 0.002) $Wm^{-1}K^{-1}$ at room temperature [69]. The thermal conductivity of BCR-724 is in the range that mostly covers the expected cross-plane thermal conductivity value of the investigated AlN (3.2 - 13.2 $Wm^{-1}K^{-1}$), and γ-CuI (0.50 – 0.59 $Wm^{-1}K^{-1}$) thin films.

4.3.2.4. Applicability of the quantitative 3ω method to the AFM

The above sections introduce the necessary fundamentals of the 3ω Microscopy thermal characterization technique. Furthermore, the experimental 3ω Microscopy setup, variety of possible thermo-resistive probes and calibration procedure have been introduced above. Thus, it is appropriate at this point to question the applicability of the frequency-domain based 3ω method in combination with the AFM/SThM.

The frequency dependence of the 3ω voltage signal was derived in Section 3.3.1 and is based on the temperature distribution of an ideal line source (Eq. (3.19)). If the derivation of the ideal line source is considered, it becomes obvious that this approach is based on the extension of the source in just one direction. Since the width of the heater $2b$, which is equivalent to the thermal exchange radius of the Pd/SiO_2 probe ($r_{th} \approx 100$ nm), deviates from $2b \rightarrow 0$, a limitation of this approach to the actual geometry is reasonable. One possibility to quantify this limitation is to correlate the thermal penetration depth λ of the resulting cylindrical propagating thermal wave and the width $2b$ of the line heater (r_{th} of Pd/SiO_2 probe). The exact analytical description of the temperature distribution (Eq. (3.19)) can be approximated using Eq. (3.22). Cahill [55] demonstrated that a complete solution for the temperature oscillations in a line source of finite width is unnecessary, if the ratio between the penetration

depth of the thermal wave and the half-width of the line heater (Pd/SiO_2 probe) is larger than five ($\lambda_s/b > 5$) to keep measurement errors of the 3ω method under 1% [55]. As a result, the slope of the temperature oscillation versus $ln(\omega)$ curve is independent of the width of the line heater [55]. Therefore, for the 3ω Microscopy technique, the following precondition has to be satisfied:

$$\frac{\lambda}{r_{th}/2} > 5 \tag{4.4}$$

With a thermal exchange radius of about 100 nm and thermal penetration depth of several micrometers (between around 266 to 51 µm for frequencies between 100 and 2750 Hz), this condition is clearly satisfied for the 3ω Microscopy technique and the local thermal conductivity of the sample is then given by Eq. (4.3).

Apart from this theoretical condition, fundamental requirements, which determine the suitable frequency range of 3ω Microscopy measurements have to be defined. The lower and upper frequency limits are given by the thickness of the substrate d_s and the cut-off frequency f_{cut} of the thermo-resistive probe, respectively.

For low frequencies, the distance traveled by the thermal waves becomes comparable to the substrate thickness, thus inducing errors due to reflections of the thermal wave from the backside of the substrate and the poorly controlled thermal resistance between the substrate and the environment [52,70]. Therefore, the penetration depth of the thermal wave must be much smaller than the thickness of the substrate:

Lower frequency limit: $\lambda \ll d_s$ (4.5)

Jacquot *et al*. [70] suggested that the ratio between the substrate thickness d_s and the thermal penetration depth λ_s should be greater than 2. The γ-CuI and AlN films studied in this thesis were deposited onto 525 µm and 640 µm thick Si substrates, respectively. Thus, considering the typical values of the specific heat capacity $c_{p,Si}$ (711 $Jkg^{-1}K^{-1}$ [53]), the density ρ_{Si}

(2330 kgm^{-3} [53]) and the thermal conductivity k_{Si} of Si (147 $Wm^{-1}K^{-1}$ [53]), the thermal wave propagates at a distance λ_{Si} of 266 µm beneath the samples at a frequency of 100 Hz. Therefore, the minimum frequency should be higher than 100 Hz, to achieve a d_s/λ_{Si} ratio which is greater than 2.

The maximum frequency of the 3ω Microscopy method is defined by the cut-off frequency f_{cut} of the thermo-resistive Pd/SiO_2 probe (f_{cut} = 2750 Hz). The employed Pd/SiO_2 probe behaves like a low-pass filter [58,71]. In order not to attenuate the thermal signal of the thermo-resistive probe, the maximum heating frequency has to be chosen within the probe's bandwidth. Consequently, the f_{cut} limits the acquisition speed and the maximum heating frequency of the Pd/SiO_2 probe for 3ω Microscopy measurements [58].

Therefore, the upper frequency limit must be smaller than the cut-off frequency of the Pd/SiO_2 probe:

Upper frequency limit: $$f_{max} < f_{cut} \quad (4.6)$$

As a result, the suitable frequency range of our AFM/SThM combined 3ω technique, using the Pd/SiO_2 probe and a Si substrate between 525 and 640 µm in thickness is between 100 and 2750 Hz.

Apart from the problem of defining a suitable frequency range, another question which has to be answered is, if the assumption of a line source is justified when the line source is V-shaped. Moreover, since the thermal conductivity of the thin film in contact with the probe is of interest, there is the question if this interaction between tip and thin film is explainable by a line source although the contact seems to be a point.

The thermo-resistive-probe–sample system is obviously a combination of electrical and thermal field problems, since the material specific thermal characteristic of the thin film is to be determined from the amplitude of the periodical temperature oscillation and the resulting 3ω voltage component across the Pd/SiO_2 probe. In order to answer the above questions, Altes

et al. [63] studied the probe–sample system using FEM based simulation, with respect to the electrical–thermal combined fields. Altes *et al*. [63] demonstrated that the temperature distribution within the sample is hemispherical, as shown in Figure 4.18. Moreover, along the perpendicular direction to the thermo-resistive probe (line source), within the near field region, the logarithmic temperature decay of the line source is dominate [63], which fulfills the basic requirement of the 3ω method. For this reason, 3ω method should be applicable to the AFM/SThM system.

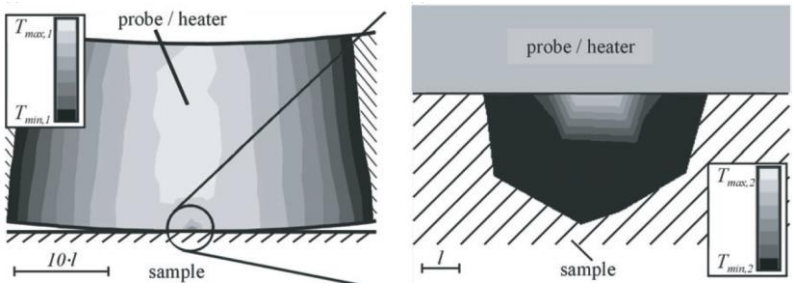

Figure 4.18: Cross-section images obtained by FEM analysis illustrating the temperature distribution at the contact area between a Wollaston wire probe and the studied sample: (a) temperature distribution within the tip of a Wollaston wire probe, (b) temperature distribution inside the studied sample (adapted from Ref. [63]).

4.3.2.5. Local thermal conductivity analysis

The AFM/SThM measurement based on the 3ω method has been theoretically verified to be applicable for the determination of local thermal conductivities of thin films and substrate materials [63]. However, it is still ambiguous whether the AFM/SThM method is practically feasible on thin film structures. For this reason, various thin films will be investigated by the 3ω Microscopy technique.

Since, the thermal properties of γ-CuI and AlN thin films are extensively studied in Chapters 5 and 6, they were used to verify the local thermal conductivity data obtained by the 3ω Microscopy method. Details about their sample structure are listed in Table 4.2. The

measurement procedures of the 3ω Microscopy are similar to those of the macroscopic 3ω method, presented in Section 4.3.1.3 and will therefore not be repeated here.

In order to obtain the local thermal properties, the samples were placed onto the AFM chuck at room temperature and the Pd/SiO_2 probe was positioned onto the surface of the thin film sample. After the probe positioning, the heating power per unit length P_l of the 3ω Microscopy measurements was set in the range of 0.4 Wm^{-1}.

To remove the fundamental voltage component at a frequency ω, the voltage amplitude between the contacts of the Pd/SiO_2 probe was balanced with the voltage of the reference resistor. The 3ω voltage amplitude $V_{3\omega}(f)$ was then recorded for different heating frequencies, ranging from 100 Hz to 2500 Hz, as discussed in Section 4.3.2.4. Within this frequency range, the penetration depth of the thermal wave was varied from 266 to 53 µm. Finally, the measured data obtained from the Pd/SiO_2 probe enable to determine the local thermal conductivities of the thin film samples by employing Eq. (4.3). Therefore, the thermal exchange radius r_{th} [58] of the Pd/SiO_2 is assumed as a constant value. The measurement time spent on each point is 5 ms, which is enough time to reach the thermal equilibrium (see Figure 2.13). By performing the measurements inside a vacuum chamber with a pressure less than 4.0 Pa using the turbo pumping station of the Bruker AFM system, radiation and convection losses were reduced.

The obtained local thermal conductivity values of AlN, and γ-CuI thin films were determined by averaging the thermal conductivity values over three 3ω Microscopy measurements for each thin film sample. The maximum deviation of the calculated values of these three measurements was below 3% for each sample.

The experimental parameters of the 3ω Microscopy measurements corresponding to the AlN and γ-CuI thin films are summarized in Tables A.15 and A.16 of Appendix D, respectively. The results of the local thermal conductivity measurements of the investigated γ-CuI and AlN films are discussed in Chapter 7.

4.4. Summary

In this chapter, the deposition parameters and conditions applied to prepare SiO_2, Si_3N_4; AlN and γ-CuI thin films with different film thicknesses are introduced. The experimental techniques used to characterize the crystalline structure and morphology of these thin films are also briefly introduced. Furthermore, the experimental methodology employed to measure the cross- and in-plane as well as the local thermal conductivities of thin films is thoroughly explained in this chapter. The experimental procedures and measurement conditions to perform thickness-dependent thermal conductivity measurements employing the macro- and microscopic 3ω method have been given. Additionally, the procedures used to implement the novel 3ω Microscopy technique, specially developed to quantitatively measure the local thermal properties of thin films are reported.

4.5. References

[1] M. Baklanov, M. Green, K. Maex, Dielectric films for advanced microelectronics, John Wiley & Sons, Chichester, England, (2007) 251-252.

[2] S.M. Lee, D.G. Cahill, Heat transport in thin dielectric films, Journal of Applied Physics 81 (6) (1997) 2590–2595.

[3] K.E. Goodson, M.I. Flik, L.T. Su, D.A. Antoniadis, Annealing-temperature dependence of the thermal conductivity of LPCVD silicon-dioxide layers, IEEE Electron Device Letters 14 (10) (1993) 490–492.

[4] A.J. Griffin, F.R. Brotzen, P.J. Loos, Effect of thickness on the transverse thermal conductivity of thin dielectric films, Journal of Applied Physics 75 (8) (1994) 3761–3764.

[5] A.J. Griffin, F.R. Brotzen, P.J. Loos, The effective transverse thermal conductivity of amorphous Si3N4 thin films, Journal of Applied Physics 76 (7) (1994) 4007–4011.

[6] J.C. Lambropoulos, M.R. Jolly, C.A. Amsden, S.E. Gilman, M.J. Sinicropi, D. Diakomihalis, S.D. Jacobs, Thermal conductivity of dielectric thin films, Journal of Applied Physics 66 (9) (1989) 4230–4242.

[7] D.G. Cahill, M. Katiyar, J.R. Abelson, Thermal conductivity of a-Si: H thin films, Physical Review B 50 (9) (1994) 6077–6081.

[8] D.M. Mattox, Handbook of physical vapor deposition (PVD) processing, 2nd ed., William Andrew; Elsevier Science, Oxford, (2010) 7-8.

[9] J. Zhou, H.F. Pang, L. Garcia-Gancedo, E. Iborra, M. Clement, M. de Miguel-Ramos, H. Jin, J.K. Luo, S. Smith, S.R. Dong, D.M. Wang, Y.Q. Fu, Discrete microfluidics based on aluminum nitride surface acoustic wave devices, Microfluid Nanofluid 18 (4) (2015) 537–548.

[10] M. Clement, L. Vergara, J. Sangrador, E. Iborra, A. Sanz-Hervas, SAW characteristics of AlN films sputtered on silicon substrates, Ultrasonics 42 (1-9) (2004) 403–407.

[11] H. Witte, A. Rohrbeck, K.M. Günther, P. Saengkaew, J. Bläsing, A. Dadgar, A. Krost, Electrical investigations of AlGaN/AlN structures for LEDs on Si(111), Physica status solidi A 208 (7) (2011) 1597–1599.

[12] J. Jaramillo-Fernandez, J. Ordonez-Miranda, E. Ollier, S. Volz, Tunable thermal conductivity of thin films of polycrystalline AlN by structural inhomogeneity and interfacial oxidation, Physical chemistry chemical physics 17 (12) (2015) 8125–8137.

[13] A. Jacquot, B. Lenoir, A. Dauscher, P. Verardi, F. Craciun, M. Stölzer, M. Gartner, M. Dinescu, Optical and thermal characterization of AlN thin films deposited by pulsed laser deposition, Applied Surface Science 186 (1-4) (2002) 507–512.

[14] Y. Zhao, C. Zhu, S. Wang, J.Z. Tian, D.J. Yang, C.K. Chen, H. Cheng, P. Hing, Pulsed photothermal reflectance measurement of the thermal conductivity of sputtered aluminum nitride thin films, Journal of Applied Physics 96 (8) (2004) 4563–4568.

[15] P.K. Kuo, G.W. Auner, Z.L. Wu, Microstructure and thermal conductivity of epitaxial AlN thin films, Thin Solid Films 253 (1-2) (1994) 223–227.

[16] T.S. Pan, Y. Zhang, J. Huang, B. Zeng, D.H. Hong, S.L. Wang, H.Z. Zeng, M. Gao, W. Huang, Y. Lin, Enhanced thermal conductivity of polycrystalline aluminum nitride thin films by optimizing the interface structure, Journal of Applied Physics 112 (4) (2012) 44905.

[17] D.G. Cahill, K. Goodson, A. Majumdar, Thermometry and Thermal Transport in Micro/Nanoscale Solid-State Devices and Structures, Journal of Heat Transfer 124 (2) (2002) 223.

[18] S.R. Choi, D. Kim, S.-H. Choa, S.-H. Lee, J.-K. Kim, Thermal Conductivity of AlN and SiC Thin Films, International Journal of Thermophysics 27 (3) (2006) 896–905.

[19] L.I. Berger, Semiconductor materials, CRC, Boca Raton, (1997) 123-124.

[20] J.J. Quinn, K.-S. Yi, Solid State Physics: Principles and Modern Applications, Springer Berlin Heidelberg, (2009) 25-28.

[21] T. Zhu, R.A. Oliver, Unintentional doping in GaN, Physical chemistry chemical physics 14 (27) (2012) 9558–9573.

[22] C. Ozgit, I. Donmez, M. Alevli, N. Biyikli, Self-limiting low-temperature growth of crystalline AlN thin films by plasma-enhanced atomic layer deposition, Thin Solid Films 520 (7) (2012) 2750–2755.

[23] S. Raghavan, J.M. Redwing, In situ stress measurements during the MOCVD growth of AlN buffer layers on (111) Si substrates, Journal of Crystal Growth 261 (2-3) (2004) 294–300.

[24] J. Keckes, S. Six, W. Tesch, R. Resel, B. Rauschenbach, Evaluation of thermal and growth stresses in heteroepitaxial AlN thin films formed on (0001) sapphire by pulsed laser ablation, Journal of Crystal Growth 240 (1-2) (2002) 80–86.

[25] N. Onojima, J. Suda, H. Matsunami, Lattice relaxation process of AlN growth on atomically flat 6H-SiC substrate in molecular beam epitaxy, Journal of Crystal Growth 237-239 (2002) 1012–1016.

[26] X. Song, R. Fu, H. He, Frequency effects on the dielectric properties of AlN film deposited by radio frequency reactive magnetron sputtering, Microelectronic Engineering 86 (11) (2009) 2217–2221.

[27] A. Belyanin, L. Bouilov, V. Zhirnov, A. Kamenev, K. Kovalskij, B. Spitsyn, Application of aluminum nitride films for electronic devices, Diamond and Related Materials 8 (2-5) (1999) 369–372.

[28] S.H. Lee, K. Hyun Yoon, D.S. Cheong, J.-K. Lee, Relationship between residual stress and structural properties of AlN films deposited by r.f. reactive sputtering, Thin Solid Films 435 (1-2) (2003) 193–198.

[29] P.M. Martin, Handbook of Deposition Technologies for Films and Coatings: Science, Applications and Technology, Elsevier Science, Burlington, (2009) 29-30.

[30] G. Lin, F. Zhao, Y. Zhao, D. Zhang, L. Yang, X. Xue, X. Wang, C. Qu, Q. Li, L. Zhang, Luminescence Properties and Mechanisms of CuI Thin Films Fabricated by Vapor Iodization of Copper Films, Materials 9 (12) (2016) 990.

[31] C. Yang, D. Souchay, M. Kneiß, M. Bogner, H.M. Wei, M. Lorenz, O. Oeckler, G. Benstetter, Y.Q. Fu, M. Grundmann, Transparent flexible thermoelectric material based on non-toxic earth-abundant p-type copper iodide thin film, Nature communications 8 (2017) 16076.

[32] C. Yang, M. Kneibeta, M. Lorenz, M. Grundmann, Room-temperature synthesized copper iodide thin film as degenerate p-type transparent conductor with a boosted figure of merit, Proceedings of the National Academy of Sciences of the United States of America 113 (46) (2016) 12929–12933.

[33] M. Grundmann, F.L. Schein, M. Lorenz, T. Böntgen, J. Lenzner, H. von Wenckstern, Cuprous iodide: A p-type transparent semiconductor, history, and novel applications, Physica status solidi A (2013) 1671–1703.

[34] B.L. Zhu, X.Z. Zhao, Transparent conductive CuI thin films prepared by pulsed laser deposition, Physica status solidi A 208 (1) (2011) 91–96.

[35] J.H. Lee, D.S. Leem, H.J. Kim, J.J. Kim, Effectiveness of p-dopants in an organic hole transporting material, Applied Physics Letters 94 (12) (2009) 123306.

[36] B.R. Sankapal, A. Ennaoui, T. Guminskaya, T. Dittrich, W. Bohne, J. Röhrich, E. Strub, M. Lux-Steiner, Characterization of p-CuI prepared by the SILAR technique on Cu-tape/n-CuInS2 for solar cells, Thin Solid Films 480-481 (2005) 142–146.

[37] C.H. Cheng, J. Wang, G.T. Du, S.H. Shi, Z.J. Du, Z.Q. Fan, J.M. Bian, M.S. Wang, Organic solar cells with remarkable enhanced efficiency by using a CuI buffer to control the molecular orientation and modify the anode, Applied Physics Letters 97 (8) (2010) 83305.

[38] Wikiwand, Copper(I) iodide, available at http://www.wikiwand.com/en/Copper(I) iodide (accessed on March 19, 2017).

[39] C. Yang, M. Kneiss, F.L. Schein, M. Lorenz, M. Grundmann, Room-temperature Domain-epitaxy of Copper Iodide Thin Films for Transparent CuI/ZnO Heterojunctions with High Rectification Ratios Larger than 10(9), Scientific reports 6 (2016) 21937.

[40] D.A. Keen, S. Hull, The high-temperature structural behaviour of copper(I) iodide, Journal of Physics: Condensed Matter 7 (29) (1995) 5793–5804.

[41] H. Liu, X. Shi, F. Xu, L. Zhang, W. Zhang, L. Chen, Q. Li, C. Uher, T. Day, G.J. Snyder, Copper ion liquid-like thermoelectrics, Nature materials 11 (5) (2012) 422–425.

[42] J. Wang, J. Li, S.S. Li, Native p-type transparent conductive CuI via intrinsic defects, Journal of Applied Physics 110 (5) (2011) 54907.

[43] M.K. Yadav, B. Sanyal, First-principles study of thermoelectric properties of CuI, Materials Research Express 1 (1) (2014) 15708.

[44] Z. Zheng, A. Liu, S. Wang, B. Huang, K.W. Wong, X. Zhang, S.K. Hark, W.M. Lau, Growth of highly oriented (110) γ-CuI film with sharp exciton band, Journal of Materials Chemistry 18 (8) (2008) 852.

[45] M. Xia, M. Gu, X. Liu, B. Liu, S. Huang, C. Ni, Luminescence characteristics of CuI film by iodine annealing, Journal of Materials Science: Materials in Electronics 26 (7) (2015) 5092–5096.

[46] I. Kosta, E. Azaceta, L. Yate, G. Cabañero, H. Grande, R. Tena-Zaera, Cathodic electrochemical deposition of CuI from room temperature ionic liquid-based electrolytes, Electrochemistry Communications 59 (2015) 20–23.

[47] B.A. Nejand, V. Ahmadi, H.R. Shahverdi, Growth of plate like γ-CuI nanostructure on copper substrate by hydrothermal evaporation of solution, Materials Letters 132 (2014) 138–140.

[48] Y. Ma, M. Gu, S. Huang, X. Liu, B. Liu, C. Ni, Colloidal synthesis of uniform CuI nanoparticles and their size dependent optical properties, Materials Letters 100 (2013) 166–169.

[49] P. Sirimanne, M. Rusop, T. Shirata, T. Soga, T. Jimbo, Characterization of CuI thin films prepared by different techniques, Materials Chemistry and Physics 80 (2) (2003) 461–465.

[50] N. Yamada, R. Ino, Y. Ninomiya, Truly Transparent p-Type γ-CuI Thin Films with High Hole Mobility, Chemistry of Materials 28 (14) (2016) 4971–4981.

[51] M. Bogner, A. Hofer, G. Benstetter, H. Gruber, R.Y. Fu, Differential 3ω method for measuring thermal conductivity of AlN and Si3N4 thin films, Thin Solid Films 591 (2015) 267–270.

[52] C. Dames, Measuring the Thermal Conductivity of Thin Films: 3 Omega and related Electrothermal Methods, Annual Review of Heat Transfer 16 (1) (2013) 7–49.

[53] R. Hull, Properties of crystalline silicon, INSPEC, London, (1999) p. 58, 98.

[54] T. Borca-Tasciuc, A.R. Kumar, G. Chen, Data reduction in 3ω method for thin-film thermal conductivity determination, Review of Scientific Instruments 72 (4) (2001) 2139–2147.

[55] D.G. Cahill, Thermal conductivity measurement from 30 to 750 K: The 3ω method, Review of Scientific Instruments 61 (2) (1990) 802–808.

[56] D. Zhao, X. Qian, X. Gu, S.A. Jajja, R. Yang, Measurement Techniques for Thermal Conductivity and Interfacial Thermal Conductance of Bulk and Thin Film Materials, Journal of Electronic Packaging 138 (4) (2016) 40802.

[57] M.K.L. Feuchter, Investigations on Joule heating applications by multiphysical continuum simulations in nanoscale systems, KIT Scientific Publishing, (2014).

[58] E. Puyoo, S. Grauby, J.M. Rampnoux, E. Rouviere, S. Dilhaire, Thermal exchange radius measurement: application to nanowire thermal imaging, The Review of scientific instruments 81 (7) (2010) 73701.

[59] M. Hinz, O. Marti, B. Gotsmann, M.A. Lantz, U. Dürig, High resolution vacuum scanning thermal microscopy of HfO2 and SiO2, Applied Physics Letters 92 (4) (2008) 43122.

[60] Y. Zhang, C.L. Hapenciuc, E.E. Castillo, T. Borca-Tasciuc, R.J. Mehta, C. Karthik, G. Ramanath, A microprobe technique for simultaneously measuring thermal conductivity and Seebeck coefficient of thin films, Applied Physics Letters 96 (6) (2010) 62107.

[61] S. Lefèvre, S. Volz, 3ω-scanning thermal microscope, Review of Scientific Instruments 76 (3) (2005) 33701.

[62] S. Gomès, A. Assy, P.O. Chapuis, Scanning thermal microscopy: A review, Physica status solidi A 212 (3) (2015) 477–494.

[63] A. Altes, R. Heiderhoff, L.J. Balk, Quantitative dynamic near-field microscopy of thermal conductivity, Journal of Physics D: Applied Physics 37 (6) (2004) 952–963.

[64] R.J. Pylkki, P.J. Moyer, P.E. West, Scanning Near-Field Optical Microscopy and Scanning Thermal Microscopy, Japanese Journal of Applied Physics 33 (Part 1, No. 6B) (1994) 3785–3790.

[65] A. Assy, S. Lefèvre, P.O. Chapuis, S. Gomès, Analysis of heat transfer in the water meniscus at the tip-sample contact in scanning thermal microscopy, Journal of Physics D: Applied Physics 47 (44) (2014) 442001.

[66] E. Puyoo, S. Grauby, J.M. Rampnoux, E. Rouvière, S. Dilhaire, Scanning thermal microscopy of individual silicon nanowires, Journal of Applied Physics 109 (2) (2011) 24302.

[67] P. Tovee, M. Pumarol, D. Zeze, K. Kjoller, O. Kolosov, Nanoscale spatial resolution probes for scanning thermal microscopy of solid state materials, Journal of Applied Physics 112 (11) (2012) 114317.

[68] S. Gomès, N. Trannoy, P. Grossel, DC thermal microscopy: Study of the thermal exchange between a probe and a sample, Measurement Science and Technology 10 (9) (1999) 805–811.

[69] D. Salmon, G. Roebben, A. Lamberty, R. Brandt, Certification of thermal conductivity and thermal diffusivity up to 1025 K of a glass-ceramic reference material BCR-724, European Commission: Directorate-General Joint Research Centre-Institute for Reference Materials and Measurements (2007) 66-67.

[70] A. Jacquot, B. Lenoir, A. Dauscher, M. Stölzer, J. Meusel, Numerical simulation of the 3ω method for measuring the thermal conductivity, Journal of Applied Physics 91 (7) (2002) 4733–4738.

[71] Y. Ezzahri, L.D. Patiño Lopez, O. Chapuis, S. Dilhaire, S. Grauby, W. Claeys, S. Volz, Dynamical behavior of the scanning thermal microscope (SThM) thermal resistive probe studied using Si/SiGe microcoolers, Superlattices and Microstructures 38 (1) (2005) 69–75.

Chapter 5: Cross- and in-plane Thermal Conductivity of AlN Thin Films

5.1. Introduction

As reported in Section 2.3.1, AlN thin films have been widely used in micro- and nanoelectronic applications, because of their outstanding physical properties, such as high piezoelectric coupling factor, excellent dielectric properties, wide band gap, and high thermal conductivity. Single crystalline AlN is one of the promising candidates for effective heat conductors in microelectronic devices due to its high thermal conductivity (320 $Wm^{-1}K^{-1}$) at room temperature [1], which makes it an ideal material to solve the thermal management problem.

However, as explained in Chapter 2 before, thermal conductivities of thin film and coating materials could be substantially different from those of their bulk counterparts [2–9], which are generally attributed to two main reasons. Firstly, compared with the bulk crystalline materials, many thin films prepared using deposition technologies have impurities, dislocations, and grain boundaries, all of which tend to reduce the thermal conductivity of the films [4,7,8,10]. Secondly, even though a film with less defects can be prepared, it is still expected to have reduced thermal conductivity due to grain boundary scattering and phonon leakage in these thin film materials. These two effects affect cross- and in-plane heat transport differently, so that the thermal conductivities of the thin films are generally anisotropic in these two directions, even though their bulk counterparts have the isotropic properties. Therefore, precise measurement of the cross- and in-plane thermal conductivities of polycrystalline AlN thin films is important for developing and improving microelectronic devices.

Therefore, in this chapter, experimental work and theoretical analysis have been conducted to understand the effects of crystallinity, grain/surface particle sizes, and interfacial structures of the AlN films on their thermal conductivities. It is for the first time that both the cross- and in-plane thermal conductivities of the AlN thin films were measured using an improved differential 3ω method (multi-heater 3ω approach). The fundamental theory, sample preparation method and experimental setup employed to perform multi-heater 3ω measurements have been previously introduced in Sections of 3.3.2.2, 4.3.1.1 and 4.3.1.2, respectively.

5.2. Results and Discussion

5.2.1. Thermal conductivity of SiO_2 and Si_3N_4 reference samples

During this investigation, the differential 3ω method (see Section 3.3.2.1) was employed to study the thickness dependency of the cross-plane thermal conductivities of SiO_2 and Si_3N_4 thin films with film thicknesses varied between 92 - 1002 nm and 298 - 1001 nm, respectively.

Figure 5.1 exhibits the temperature oscillation amplitudes $\Delta T_{2\omega}$ obtained from 3ω measurements of SiO_2 and Si_3N_4 thin films deposited on a p-type Si substrate. As the cross-plane thermal conductivity values of SiO_2 and Si_3N_4 thin films are well-reported [5,8,11], they can be used as reference values to verify the applied 3ω method. The reference temperature oscillation of the bare Si substrate (solid lines) was obtained using Eq. (3.22). The thermal conductivity of the Si substrate calculated by Eq. (3.25) is 141 $Wm^{-1}K^{-1}$, which is 5% below the literature values of the thermal conductivity of pure Si (≈ 147-148 $Wm^{-1}K^{-1}$) [5,12,13]. This deviation is mainly due to the impurity scattering by the doped boron in the Si substrate [7,8].

The frequency-independent temperature shift in the real part of the thermal oscillation amplitude ΔT_f between the dotted linear fitting curves (thin films) and the solid line (Si

substrate) is shown in Figure 5.1. The frequency-independent offsets are the temperature rises (ΔT_f) generated by the SiO_2 and Si_3N_4 films of different film thicknesses. The gradual increment of these offsets indicates that both thermal resistance and thermal conductivity of the SiO_2 and Si_3N_4 films increase as the film thickness increases.

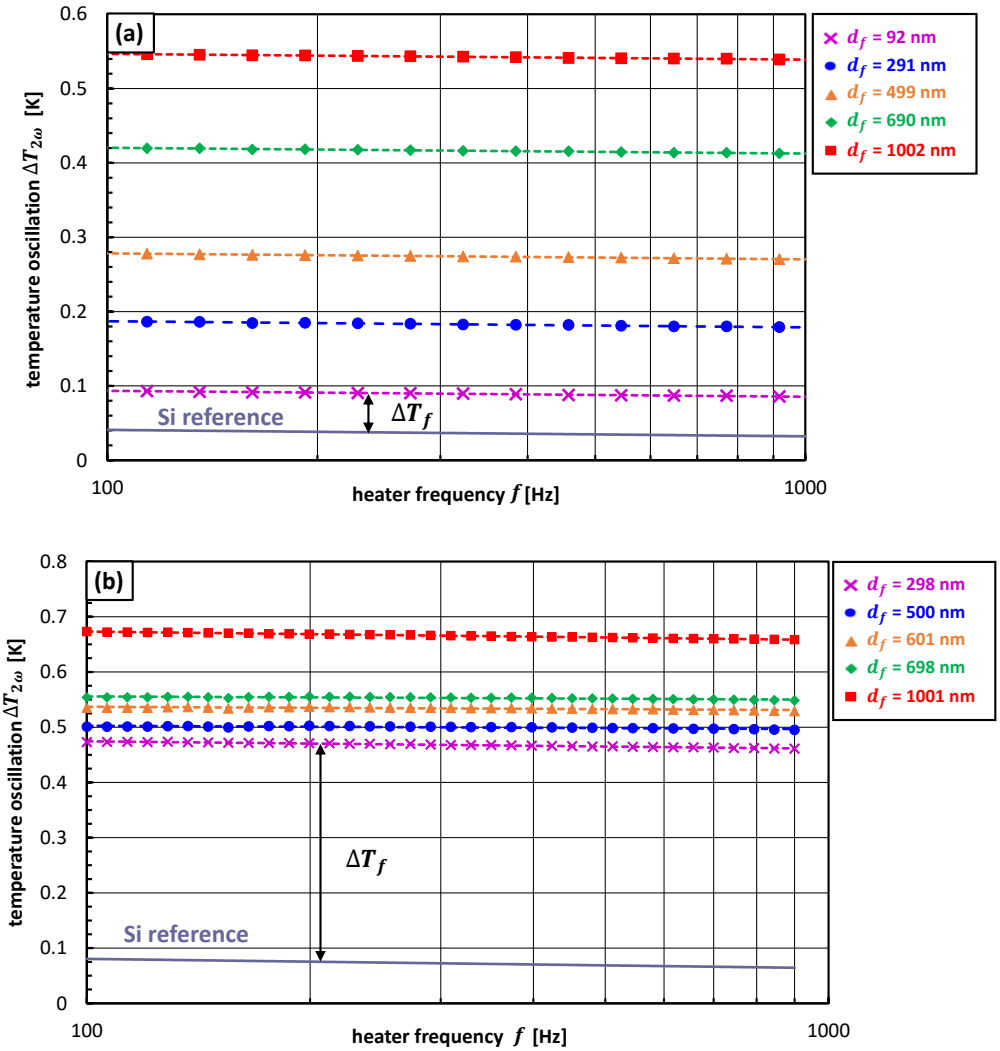

Figure 5.1: The temperature oscillation amplitudes $\Delta T_{2\omega}$ for the substrate and film-on-substrate structures: (a) SiO_2 thin films with film thickness d_f varied between 92 and 1002 nm (b) Si_3N_4 thin films with film thickness varied between 298 and 1001 nm. The dotted linear fitting curves represent the temperature oscillation amplitudes of the film-on-substrate structures, which were experimentally measured by detecting the 3ω voltage across the metal line heaters. The thermal conductivity of the SiO_2 and Si_3N_4 films were obtained by comparing the temperature amplitudes of the film-on-substrate structures with the corresponding value in the Si substrates. The solid lines represent the corresponding temperature amplitude of the Si substrates, calculated by Eq. (3.22).

Thermal conductivity data of the SiO_2 and Si_3N_4 thin films calculated using Eq. (3.33) are summarized in Table 5.1. The obtained thermal conductivity of the SiO_2 and Si_3N_4 films are 0.88 to 1.10 $Wm^{-1}K^{-1}$ and 0.80 to 1.70 $Wm^{-1}K^{-1}$, which are in good approximation with published values for SiO_2 and Si_3N_4 films fabricated by similar PECVD parameters [5,11]. The determined cross-plane thermal conductivity values of SiO_2 and Si_3N_4 thin films were obtained by averaging the thermal conductivity values over five 3ω measurements for each SiO_2 and Si_3N_4 film sample. The maximum deviation of the calculated values of these five measurements was below 2.5% for each sample.

Table 5.1: Experimental results of the cross-plane thermal conductivity measurements of SiO_2 and Si_3N_4 thin films using the differential 3ω method.

No.	Material	Film thickness d_f [nm]	Cross-plane thermal conductivity $k_{f\perp}$ [$Wm^{-1}K^{-1}$]
1	SiO_2	92	0.88 ± 0.026
2		291	1.01 ± 0.029
3		499	1.04 ± 0.031
4		690	1.05 ± 0.032
5		1002	1.10 ± 0.032
6	Si_3N_4	298	0.80 ± 0.019
7		500	1.21 ± 0.032
8		601	1.32 ± 0.038
9		698	1.51 ± 0.042
10		1001	1.70 ± 0.051

Table 5.1 lists the experimental results obtained for the cross-plane thermal conductivities of SiO_2 and Si_3N_4 thin films as a function of the film thickness d_f. The experimental values are considerably lower than those of the corresponding bulk materials which are about 1.4 $Wm^{-1}K^{-1}$ [11] and 30.0 $Wm^{-1}K^{-1}$ [5]. The measured thermal conductivity values of the SiO_2 and Si_3N_4 thin films were about 21% - 37% and 94% - 97% smaller than those of their bulk counterparts. Furthermore, the film thermal conductivity values of both SiO_2 and Si_3N_4 increase with film thickness, but the increase rate decreases gradually with increasing thickness, as illustrated in Figure 5.2. The obtained values are in a reasonable range, considering the reduced thickness of the measured thin films, and are in good agreement with

experimental data reported by Yamane *et al*. [11] and Lee *et al*. [5] for thin SiO_2 and Si_3N_4 films at room temperature. These investigations have experimentally demonstrated that a significantly decrease in the thermal conductivity of amorphous solids occurs as the film thickness decreases, which can explain the low values obtained in this thesis.

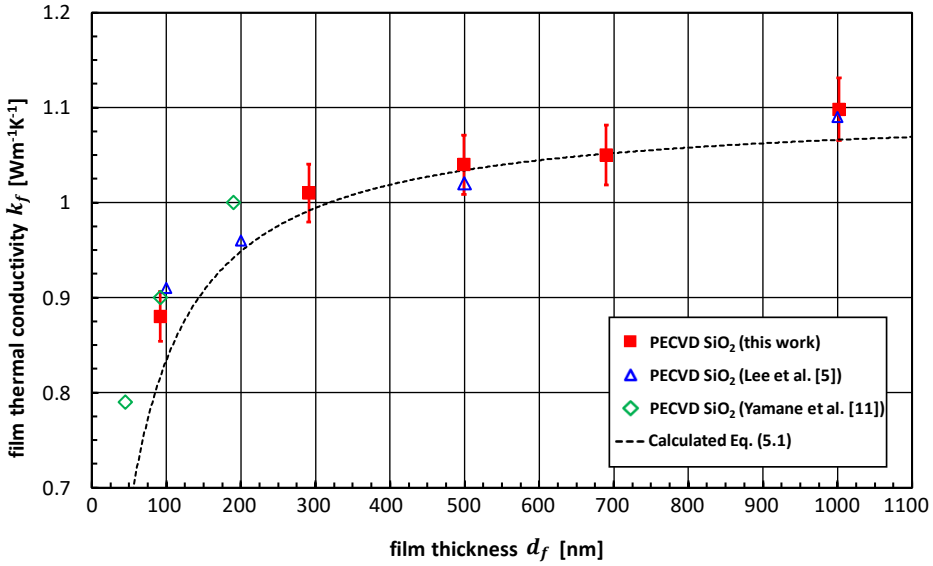

Figure 5.2: Cross-plane thermal conductivity of SiO_2 (PECVD) thin films as a function of film thickness d_f. Filled squares represent the experimental data obtained in this study by the differential 3ω method. The values are compared with other experimental results for PECVD SiO_2 thin films obtained by Lee *et al*. [5] (triangles), and Yamane *et al*. [11] (diamonds). The dotted line is a fit of Eq. (5.1) to calculate the cross-plane thermal conductivity of PECVD SiO_2 films, derived by Yamane *et al*. [11].

Film thickness dependence of SiO_2 and Si_3N_4 thermal conductivity values, measured by Yamane *et al*. [11] and Lee *et al*. [5], are also depicted in Figure 5.2 for a comparison with the values obtained in this study. The dashed line represents the theoretical cross-plane thermal conductivity values of PECVD SiO_2 films as a function of film thickness calculated by Yamane *et al*. [11]. The cross-plane conductivity values $k_{f\perp}$ are determined using [11]:

$$k_{f\perp} = \frac{k_i}{1 + k_i R_i / d_f} \tag{5.1}$$

where d_f is the film thickness, k_i the intrinsic thermal conductivity of PECVD SiO_2 films which is assumed to be a constant and independent of film thickness (k_i = 1.10 $Wm^{-1}K^{-1}$) [11], and R_i is the thermal resistance between the PECVD SiO_2 film and Si substrate (R_i = 2.9 × 10^{-8} m^2KW^{-1}) [11], respectively. Our results match remarkably well with the calculated thermal conductivity values for film thicknesses between 100 and 1000 nm. Therefore, our modified 3ω setup is capable to accurately measure the thermal conductivities of thin films with film thicknesses d_f between around 100 and 1000 nm. In the following section, we will present and discuss the results obtained for AlN thin films with film thicknesses varied between 99 and 1009 nm.

5.2.2. AlN thin film thermal conductivity

After the analysis of the reference samples given in the previous section, the discussion focuses on the in- and cross-plane thermal conductivity measurements of AlN thin films deposited on Si substrates. Yet, measurements of both cross- and in-plane thermal conductivities of AlN thin films deposited by RF magnetron sputtering as a function of film thickness have not been reported in literature.

In this section, the differential multi-heater 3ω method (see Section 3.3.2.2) was applied to study the thickness dependency of the cross- and in-plane thermal conductivities of the AlN thin films. This is achieved by subtracting the Si substrate contribution from the overall thermal response of the AlN film on Si substrate systems. Firstly, the thermal conductivity k_s of the Si substrate must be determined in order to set the ΔT_f reference for the differential multi-heater 3ω method, as introduced in Section 4.3.1.3. The thermal conductivity of the Si substrate calculated by Eq. (3.25) is 141 $Wm^{-1}K^{-1}$, which is approximately 5% smaller than the published values of pure Si (≈ 147-148 $Wm^{-1}K^{-1}$) [5,12,13] and about 5% higher than the literature value of p-doped Si (134 $Wm^{-1}K^{-1}$) [14]. This discrepancy is primarily caused by impurity scattering with the doped boron in the Si substrate [7,8], as also mentioned in Section 5.2.1.

The real parts of the in- and cross-plane amplitudes of the temperature oscillations $\Delta T_{2\omega}$, measured within the 3ω line heaters as a function of the AC heating current frequency f for the AlN thin films, are illustrated in Figure 5.3. The dotted lines represent the analytical linear fits performed based on the experimental data. The reference amplitudes of the temperature oscillations, associated with the bare Si substrate (solid line), are included as well for comparisons (calculated by Eq. (3.22)). For the thickness-dependent measurements, the heating frequency was limited to a range varied from 100 to 1000 Hz, confining the oscillation of the generated thermal wave well within the AlN/Si structure (see Section 4.3.1.3).

As can be observed in Figure 5.3, the diffusion of the thermal oscillation into the AlN films of different thickness produces a frequency-independent temperature rise ΔT_f through the metal heaters, which gradually increases with film thickness. The offsets between the temperatures corresponding to the determined Si substrate (solid line) and experimental data (dotted lines) are the temperature rises (ΔT_f) generated by the AlN films of different film thicknesses. The gradual increment of these offsets indicates that the AlN thermal resistance and thermal conductivities increase as the film thickness increases.

To obtain the $k_{f\perp}$ and $k_{f\parallel}$ values of the AlN films, their thermal properties have to be extracted from the AlN/Si structure. This was achieved by subtracting the reference signal of the Si substrate (solid line) from that of the sample including the AlN thin film (dotted lines), using Eq. (3.33) for the cross- and in-plane values. The experimental parameters corresponding to the AlN thin film samples, used to simultaneously determine the cross- and in-plane thermal conductivities, are listed in Tables A.9 and A.10 of Appendix D, respectively. The determined thermal conductivity values of the AlN thin films were obtained by averaging the thermal conductivity values over five 3ω measurements for each AlN sample. The maximum deviation of the obtained values of these five measurements was below 2.5% for each sample.

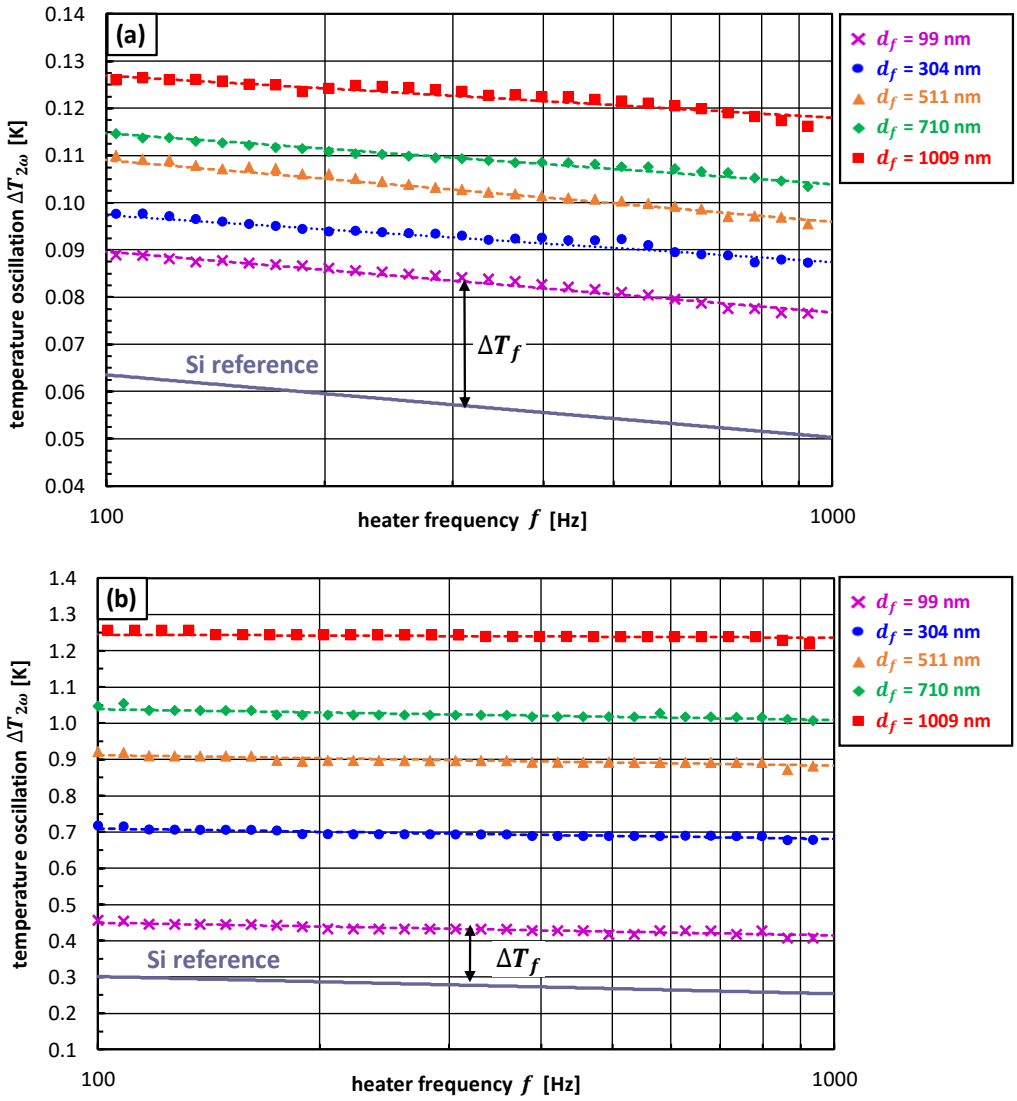

Figure 5.3: The temperature oscillation amplitudes $\Delta T_{2\omega}$ for the Si substrate and AlN film-on-substrate structures with film thickness d_f varied between 99 and 1009 nm for (a) the cross- (broad heater width, $2b \sim 25$ μm) and (b) in-plane (narrow heater, $2b \sim 1.0$ μm) case. The dashed lines represent the temperature oscillation amplitudes of the AlN film-on-substrate structures, which are experimentally measured using the 3ω multi-heater technique. The thermal conductivity of the AlN thin films are determined by comparing the temperature amplitudes of the AlN film-on-substrate structures with the corresponding value in the Si substrate. The solid line represents the corresponding temperature amplitude of the Si substrate, obtained by Eq. (3.22).

Table 5.2 lists the experimental results of the in- and cross-plane thermal conductivities of the AlN thin films as a function of the film thickness. The thermal conductivity values of the AlN film samples with thicknesses varied from 99 to 1009 nm are between 3.2 and 14.9 $Wm^{-1}K^{-1}$

for the cross-plane cases and between 10.2 and 18.6 $Wm^{-1}K^{-1}$ for the in-plane cases. Table 5.2 indicates that the in-plane thermal conductivities of the AlN thin films are approximately between 25% and 219% higher than the cross-plane ones.

The main reason to explain this result is that along the in-plane direction, phonons traveling along the directions parallel to the interface are not disturbed, whereas those along the cross-plane directions have a limited mean free path due to the film thickness and boundary scattering at the interfacial structures between the thin film and substrate [4,7,15,16] (see Section 5.2.3). The experimental values for both the cross- and in-plane directions are substantially lower (between about 94% and 99%) than that of the corresponding bulk material which is around 320 $Wm^{-1}K^{-1}$ [1]. Furthermore, the film thermal conductivity values of both the cross- and in-plane directions increase with the film thickness as shown in Figure 5.4. For relatively thick films, the increase of the cross-plane thermal conductivity appears to be gradually attenuated [8].

Table 5.2: Experimental results of the in- and cross-plane thermal conductivity of AlN thin films by the multi-heater 3ω method, and approximation of the average grain size of the investigated AlN thin films determined by the results of the XRD (Eq. (5.2)) measurements and the calculated thermal conductivity of the polycrystalline AlN films with different grain sizes by Eq. (5.3).

No.	Film thickness d_f [nm]	Thermal conductivity value [$Wm^{-1}K^{-1}$]		Average grain size value (XRD) D_P [nm]	Thermal conductivity values calculated by Slacks model $k_{p\perp}$ [$Wm^{-1}K^{-1}$]
		Cross-plane $k_{f\perp}$	In-plane $k_{f\parallel}$		
11	99	3.2 ± 0.09	10.2 ± 0.30	11	16
12	304	8.5 ± 0.22	12.5 ± 0.37	28	37
13	511	11.0 ± 0.33	13.9 ± 0.42	45	55
14	710	13.2 ± 0.40	16.4 ± 0.49	66	75
15	1009	14.9 ± 0.43	18.6 ± 0.57	119	114

The results obtained in this thesis are in good agreements with other experimental data reported by Zhao *et al*. [2], Choi *et al*. [7], Pan *et al*. [4] and Jaramillo-Fernandez *et al*. [16] for the cross-plane thermal conductivities of polycrystalline AlN films deposited by RF sputtering on Si substrates at room temperature. These investigations have reported values

that vary from 0.5 to 50 $Wm^{-1}K^{-1}$ (see Section 2.3.1), and have a strong dependence on film thickness (as in this thesis), as well as on deposition conditions and techniques. More recently, a similar trend has been observed by Belkerk *et al*. [9] and Duquenne *et al*. [17], who studied thermal transport properties AlN films deposited by balanced and unbalanced magnetron sputtering. Both studies found that the balanced magnetron process yielded cross-plane thermal conductivities of 2.5 to 50.0 $Wm^{-1}K^{-1}$ for 800 nm up to 3500 nm thick AlN films [9,17].

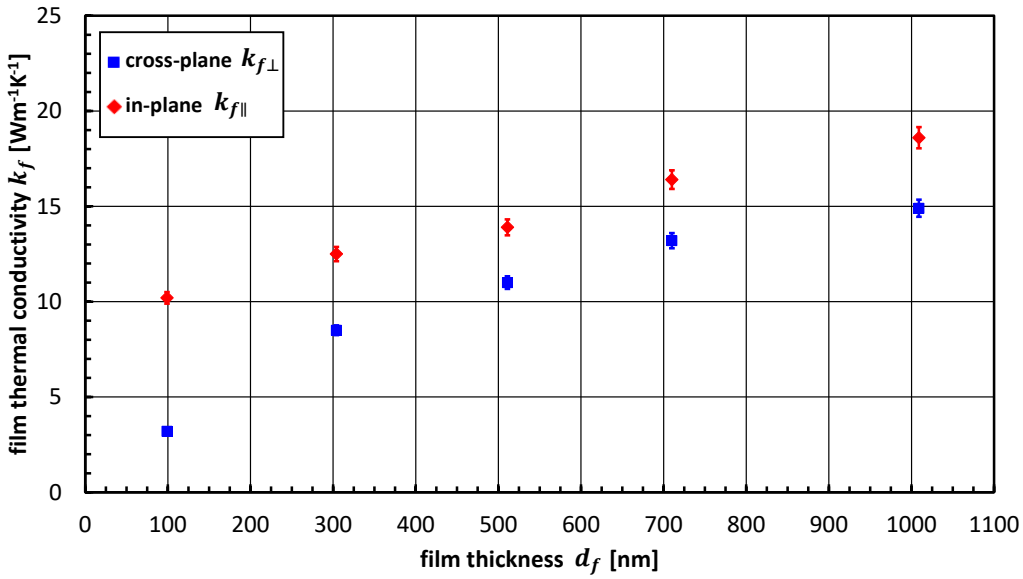

Figure 5.4: Cross- and in-plane thermal conductivity of AlN thin films as a function of film thickness. The squares represent the experimental data of the cross-plane conductivity and the diamonds the in-plane conductivity data obtained in this study by the multi-heater 3ω method.

On the other hand, unbalanced magnetron sputtering led to cross-plane thermal conductivities between 20 and 50 $Wm^{-1}K^{-1}$ for film thicknesses varied from 150 to 3500 nm [9,17]. These investigations addressed the thickness-dependence problem qualitatively, by attributing the decrease of the cross-plane thermal conductivity with film thickness to synthesis conditions, microstructure and average grain size, according to the Scherrer equation (XRD analysis).

Therefore, XRD analysis was utilized to get a qualitative approximation how strong the grain size D_P of the AlN changes as a function of film thickness d_f. The approximation of the grain

size was obtained by the Scherrer equation in this thesis. However, the effects of crystallinity, grain/surface particle sizes, and interfacial structures of AlN thin films on their cross- and in-plane thermal conductivities have not been investigated by other people so far. It is the first time that experimental work and theoretical analysis have been conducted to understand these effects. The results of these investigations are presented and discussed in the following section.

5.2.3. AlN thermal conductivity versus crystalline structure

Phonon transport in polycrystalline thin films has been proven to be strongly related to the structural features present within the thin films (see Sections 2.3). To investigate this correlation, the characterization of grain and surface particle sizes is mandatory. Therefore, experimental and theoretical analysis have been conducted to understand the effects of crystallinity, grain/surface particle sizes and interfacial structures of the AlN films on their cross- and in-plane thermal conductivities.

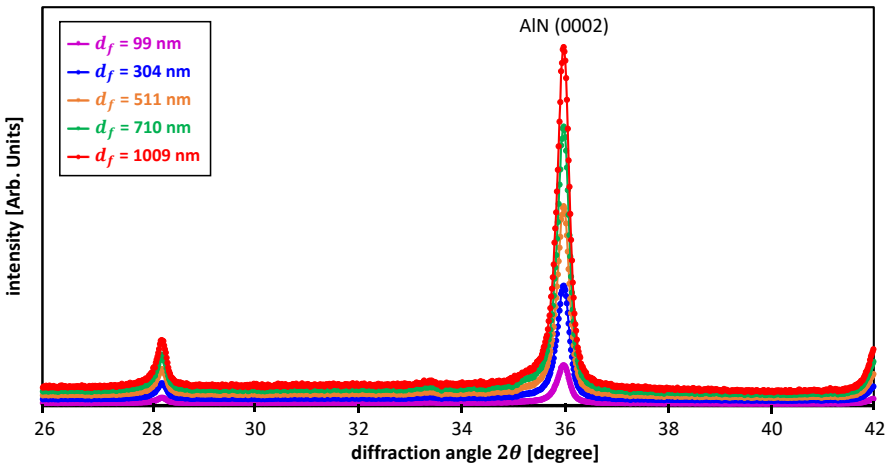

Figure 5.5: The XRD 2θ scan patterns (0002) of AlN thin films deposited on Si substrates. The thickness of the thin films varied between 99 and 1009 nm.

XRD patterns of AlN peaks have been recorded (see Figure 5.5) to investigate the influence of the AlN film's microstructure on their cross- and in-plane thermal conductivity values. XRD analysis reveals that the AlN thin films are of crystalline structure regardless of the thickness. According to the standard diffraction powder pattern of w-AlN (PDF 00-025-1133

of JCPDS-ICDD diffraction database), the polycrystalline hexagonal structure of wurtzite phase was detected in the films by XRD. In Figure 5.5, the $\theta - 2\theta$ spectra of the AlN thin films exhibit a single AlN peak near a Bragg angle θ of 36°, which is the characteristic of the (0002) orientation.

It was reported that the grain size significantly affected the thermal conductivity due to the grain boundary scattering effect and larger grain size enhanced the thermal conductivity, because of the longer phonon MFP [4,8,10]. According to this finding, the results of the XRD analysis in this study were used to determine the average grain sizes D_P of the AlN thin films. The average grain size of the thin film was calculated using the Scherrer equation [18]:

$$D_P = \frac{K \cdot \lambda_{wave}}{\beta \cdot \cos(\theta)} \tag{5.2}$$

where K is the dimensionless shape factor (K = 0.9 [18]), λ_{wave} the X-ray wavelength (λ_{wave} = 0.154 nm, see Section 4.2), β the line broadening at half the maximum intensity (FWHM) in radians, θ the Bragg angle, respectively. Table 5.2 lists the determined average grain size values as a function of the AlN film thickness. The values for the average grain size are between 11 and 119 nm for the AlN films with thicknesses varied from 99 to 1009 nm. The average grain size values increase with the film thickness.

To further support the grain size estimation by the Scherrer equation, the surface particle distribution and average size of the AlN films were investigated by AFM. Figure 5.6 presents the AFM images showing the surface morphologies (Figures 5.6(a) to (c)) and the surface particle size distribution (Figures 5.6(d) to (f)) of the 304, 511, and 710 nm AlN films with smooth surfaces and uniform grains. Surface particle distributions and average sizes of the AlN films were obtained by utilizing the NanoScope Analysis software. The evolution of the surface particle diameters of the 304, 511, and 710 nm AlN films is illustrated in Figure 5.7.

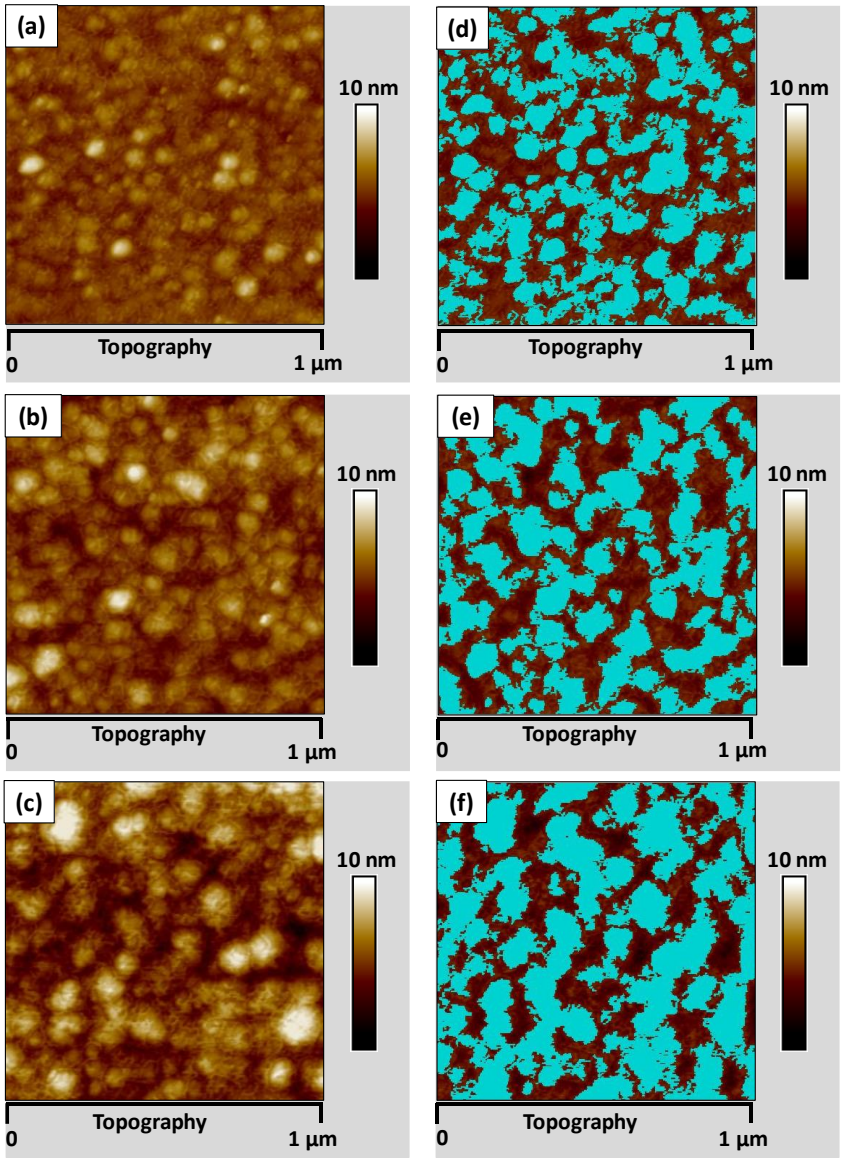

Figure 5.6: The AFM images of AlN films deposited on Si substrates with film thicknesses of (a) and (d) 304 nm, (b) and (e) 511 nm, (c) and (f) 710 nm to study the surface morphology and surface particle distribution and average particle size. The distribution of the surface particles in images (d) to (f) are highlighted in blue by the NanoScope Analysis software.

With the decrease of film thickness, obvious changes in surface particle size distributions were observed. In Figures 5.6(d) to (f), the surface particle size distribution is indicated by the blue areas, which cover the detected particles of the AlN films. It is clearly detectable that the particle size drastically decreases as the film thickness is decreased. The average surface particle sizes for AlN films with film thicknesses of 304, 511, and 710 nm are 44, 103, and 168 nm, respectively, suggesting that the average surface particle size decreases with

decreasing film thickness. Therefore, the surface particle size values for the AlN thin films measured by the AFM, qualitatively support the trend of the average grain size results obtained by the Scherrer model.

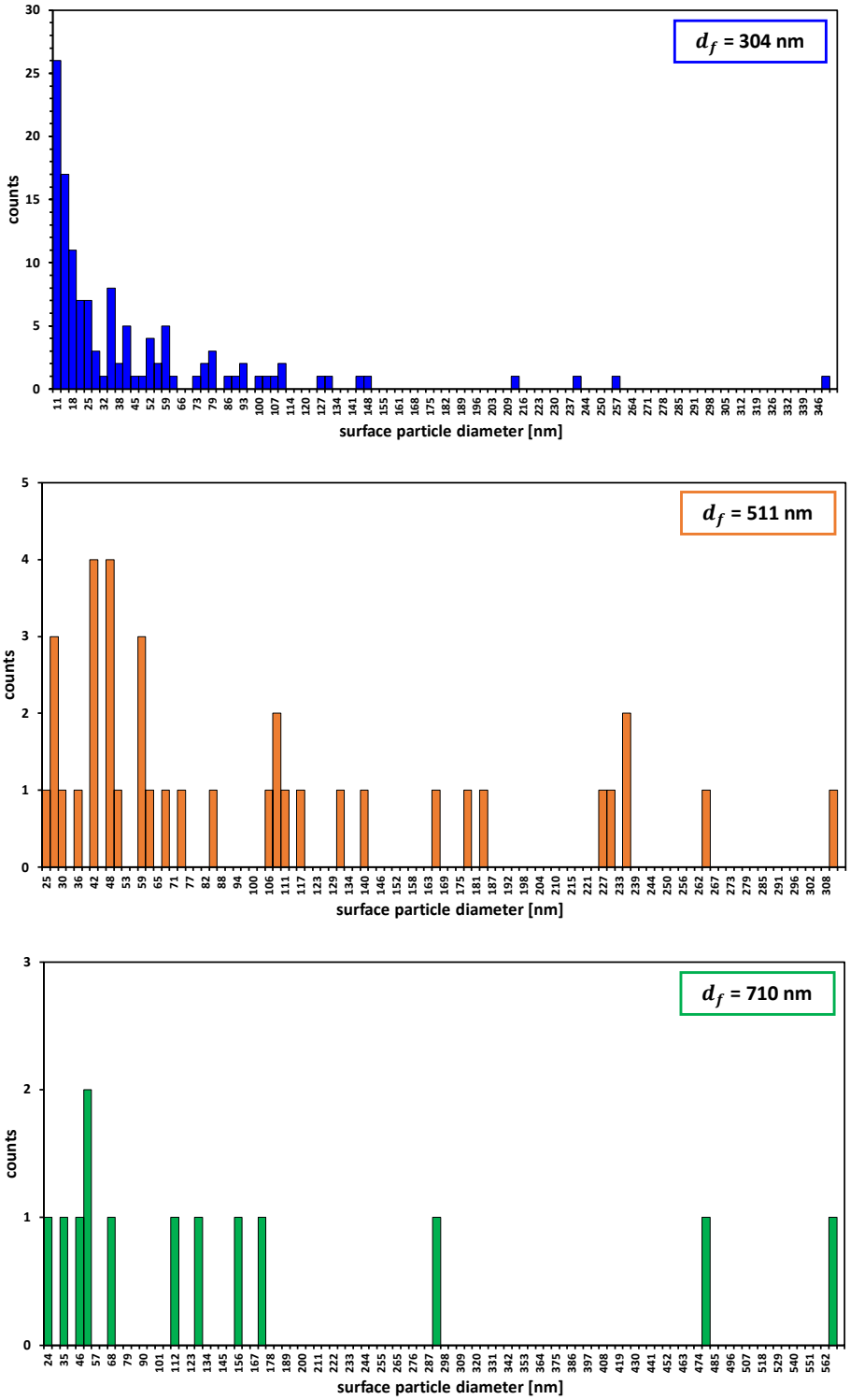

Figure 5.7: Film thickness dependency of the surface particle diameter distribution obtained by AFM images of AlN thin films with film thicknesses varied between 304, 511 and 710 nm.

According to these results, it can be derived that the reduced thermal conductivity for the thinner AlN thin films are mainly caused by the decrease in the grain and surface particle sizes. Additionally, the reduction of the thermal conductivity values in comparison to the bulk values can be attributed to the shorter MFP of phonons.

Slack *et al*. [10] reported that the grain size significantly affected the thermal conductivity of films due to the grain boundary scattering, because a smaller grain size could decrease the thermal conductivity of the film due to the shorter phonon MFP. Furthermore, Choi *et al*. [7], Pan *et al*. [4] and Jaramillo-Fernandez *et al*. [16] analyzed the XRD patterns of the AlN thin films in order to correlate the measured thermal conductivity with the microstructures of the films. They found that according to the XRD results, the increased thermal conductivity of thicker AlN thin films was primarily due to the increase in the average grain size [4,7,10]. The experimental work and results reported in this thesis support their observation.

Slack *et al*. [10] proposed a model for the grain size dependence of the cross-plane thermal conductivity of the polycrystalline AlN. In this model, the thermal conductivity $k_{p\perp}$ of the polycrystalline AlN with an average grain size of D_P can be determined by [10]:

$$k_{p\perp}{}^{-1} = \left(D_P \cdot v \cdot \frac{C}{3}\right)^{-1} + k_{pp}{}^{-1} \tag{5.3}$$

where v is the average sound velocity (6.98×10^3 ms^{-1}), C is the specific heat capacity per volume (6.4×10^5 Jm^{-3}K^{-1}), and k_{pp} is the thermal conductivity of the AlN single crystal (320 Wm^{-1}K^{-1} [1]) [10]. Using the average grain sizes obtained from the Eq. (5.2), the thermal conductivity of the polycrystalline AlN films with the grain sizes between 11 and 119 nm can be calculated using the Slack's model [10]. The calculated results are listed in Table 5.2, which suggest that the difference in the grain and surface particle sizes for different film thicknesses changes the thermal conductivity of the AlN films. However, the calculated thermal conductivity values are higher than the experimental data of our AlN films. This is reasonable since only the grain boundary scattering effect has been taken into account in

Slack's model [10]. In other words, the obtained data imply that there are other mechanisms besides the grain boundary scattering, which significantly affect the thermal conductivity in this study.

Therefore, EDX measurements were employed to analyze the chemical compositions of the deposited AlN films. Figure 5.8 presents the EDX results and the obtained atomic weight values of Al, N, O and Si elements of each AlN/Si film-on-substrate samples. As a common impurity of sputtered AlN films, the oxygen impurity was observed in the 99, 511 and 1009 nm AlN films in this study. The ratio of the atomic weight of AlN:O in the AlN/Si film-on-substrate samples, which were fluctuated without a clear dependence on film thickness, are in the range between 36.9:1 and 50.0:1. It cannot be clearly distinguished whether the oxygen comes from the Si substrates or the AlN films. Figures 5.8(a) to (c) show that atomic weight of the Si substrate is decreasing, which is caused by the increasing thickness of the AlN films. Finally, the EDX results revealed that the oxygen content does not significantly increase with film thickness and therefore does not show to cause the thickness-dependence of cross- and in-plane thermal conductivity values of AlN thin films.

Therefore, the difference between the data from Slack's model and experiment may be also caused by the phonon scattering induced by oxygen defects as supported by EDX results, and/or other mechanisms such as a lattice mismatch between the thin film and substrate material. Normally, the interface between the film and substrate material shows distorted or amorphous microstructures, because of the lattice mismatch and the existence of surface defects [4,7,16]. Furthermore, the oxygen content, which causes the phonon scattering of defects and leads to a reduction in thermal conductivity, shows no significant correlation with the film thickness, as indicated by the EDX data. In other words, the improvement of interfacial structure may be the main reason for the enhancement of thermal conductivity of the investigated AlN films in our study.

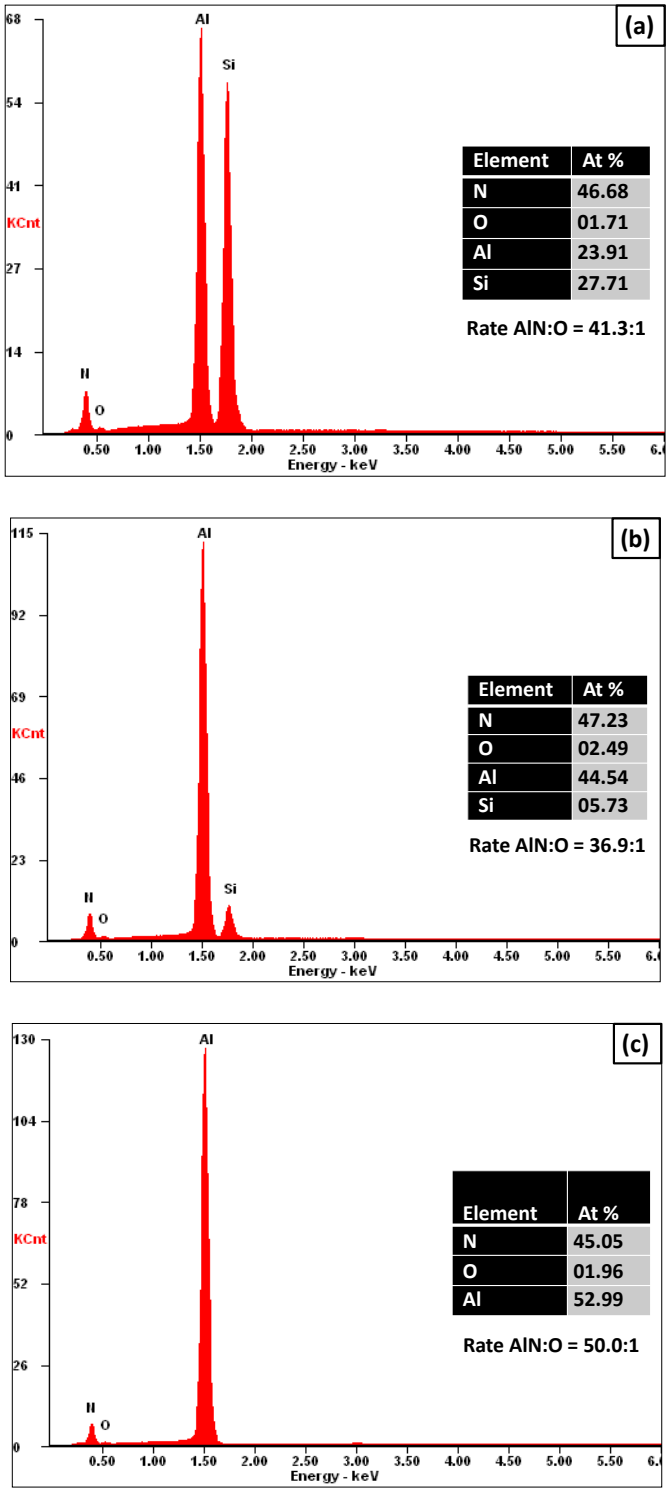

Figure 5.8: EDX results of AlN/Si film-on-substrate samples with film thicknesses of (a) 99 nm, (b) 511 nm, and (c) 1009 nm. The tables list the atomic weight in percent of Al, N, O and Si of the AlN/Si samples. The ratio of the atomic weight of AlN:O in the AlN films, which were fluctuant with no considerable dependence on film thickness, are in the range between 36.9:1 and 50.0:1. The atomic weight of the Si substrate is decreasing, which is caused by the increasing thickness of the AlN films.

In Figure 5.4, there is a decrease in the cross-plane thermal conductivity at around 304 nm, which is caused by the lattice mismatch between the AlN film and the Si substrate. It was reported that the interface between thin film and the substrate often has distorted or amorphous microstructures, because of the lattice mismatch and the existence of surface defects. [4,7,16].

As a result, it is supposed that the AlN thin film might have a graded changed interfacial layers, thus the cross-plane thermal conductivity of the 304 nm thick film in Figure 5.4 could be an average values of this graded changing structure, mainly caused by the differences of their lattice constants (Si (5.3 Å) [7], AlN (3.2 Å) [7]).

To support this theoretical statement, the structures of the AlN/Si interfaces were investigated using SEM. Figures 5.9(a) and (b) show the cross-sectional SEM images taken at the AlN/Si interfaces of the (a) 304 nm and (b) 1009 nm AlN film. A thin interfacial AlN layer with a thickness of about 40 to 50 nm can be observed at the interface of the films (see dotted red colored lines in Figure 5.9). The evolution of this AlN/Si interface region (which might be disordered) in the AlN thin film reveals that the interface scattering might be another important factor, which influences the thermal conductivity of the thin films, especially in the cross-plane direction.

The amorphous interface layers have also been observed by other groups in sputtered AlN films on Si substrates [4,7,16,19,20]. Therefore, it is reasonable to propose that the evolution of AlN regions with poor crystalline quality at the AlN/Si interface may have a significant influence on the differences between the cross- and in-plane thermal conductivity values of thin film samples.

Based on the work of Cahill *et al*. [13] and Jacquot *et al*. [1], amorphous and disordered AlN has a lower thermal conductivity than that of polycrystalline AlN since there is no coherence in the atomic vibration of amorphous AlN. Therefore, our AlN samples can be considered as a two-layered structure with a low thermal conductive amorphous/disordered interface layer

and a relatively high thermal conductive top polycrystalline AlN layer. Jaramillo-Fernandez *et al.* [16] and Pan *et al.* [4] did also experimentally verified these two layered structure between AlN thin film and Si substrates.

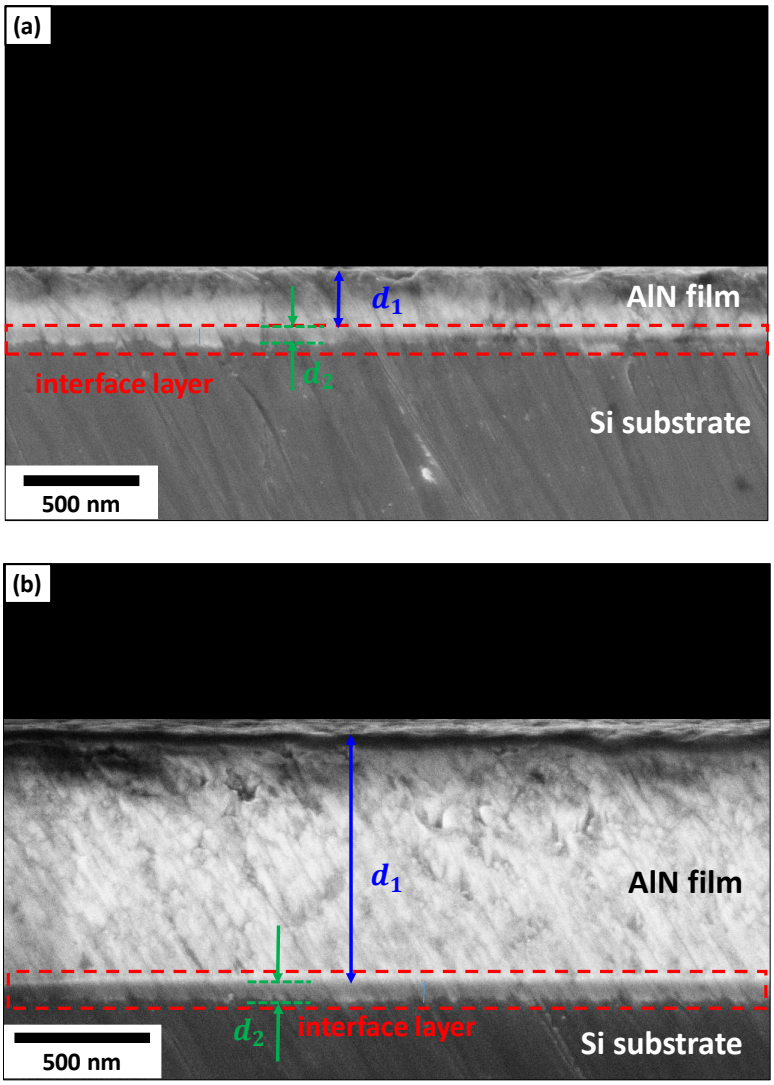

Figure 5.9: The cross-sectional SEM images of the (a) 304 nm and (b) 1009 nm thin AlN film deposited on Si substrate in order to investigate the structure of the AlN/Si interface. The SEM images show interfacial layers (red colored dashed lines) between the AlN films and the Si substrates, which affect the heat conduction in the cross-plane direction. The thickness of the AlN film and the interface layer are indicated by d_1 and d_2, respectively.

By simply assuming that the AlN film is composed of a two layered structure with thicknesses of d_1 and d_2, and thermal conductivity values of k_1 and k_2, the resulting thermal conductivity k_{eff} can be expressed by:

$$\frac{(d_1 + d_2)}{k_{eff}} = \frac{d_1}{k_1} + \frac{d_2}{k_2} \tag{5.4}$$

For example, if we insert the experimental data (Table 5.2) for the 304 nm AlN film obtained by the multi-heater 3ω technique in Eq. (5.4), we can determine the thermal conductivity of the disordered interface layer k_2 with thickness d_2.

Hereby, k_{eff}, k_1 and k_2 are the cross-plane, in-plane and disordered interface thermal conductivities, respectively. For the experimental data of the 304 nm AlN film we obtain a value of 3.0 $Wm^{-1}K^{-1}$ for the cross-plane thermal conductivity of the disordered interface layer (k_{eff} = 8.5 $Wm^{-1}K^{-1}$, k_1 = 12.5 $Wm^{-1}K^{-1}$, d_1 = 259 nm, d_2 = 45 nm).

According to Eq. (5.4) and the results of the cross-sectional SEM, it is evident that the reduced thermal conductivity value of the in the interface layer causes a significant decrease in the measured cross-plane thermal conductivity values at a film thickness of about 304 nm. The thinner the AlN film, the greater is the influence of the interface layer between the AlN film and the Si substrate on the cross-plane thermal conductivity value.

5.3. Summary

This chapter presents a modified measurement procedure to determine the cross- and in-plane thermal conductivities of the AlN thin films. In this study, the multi-heater 3ω method was applied to study the thickness dependency of the cross- and in-plane thermal conductivities of AlN thin films deposited using RF magnetron reactive sputtering.

The experimental results have shown that both cross- and in-plane thermal conductivities of the AlN thin films are significantly reduced compared to that of their bulk material counterparts. Furthermore, the film thermal conductivity values of both the cross- and in-plane ones decreases with the film thickness, but the decrease rate increases gradually with decreasing the film thickness for the cross-plane case. The XRD and AFM results indicated that the grain size and surface particle size of sputtered AlN films decreases with the decrease

in film thickness. According to these results, the decreased thermal conductivity of the AlN thin films with a smaller film thickness is mainly caused by the decrease in the average grain and surface particle sizes of the films. Theoretical analysis suggested that the difference of thermal conductivity values contributed by grain boundary scattering cannot fully explain the experimental data. It was considered that the amorphous and disordered interfacial regions at the AlN/Si interfaces, which have a much lower thermal conductivity than the polycrystalline AlN, played another important role in the differences in the thermal conductivity. This argument can be linked to the results of the cross-sectional SEM, which demonstrated that the amorphous and disordered layer at the interface obviously influences the heat transport in the cross-plane direction of the AlN film. The results indicated that improving the interfacial properties will significantly increase the thermal conductivity and promote the applications of AlN thin films in microelectronic devices.

Additionally, this chapter showed that the AlN thin films can be used in microelectronics and MEMS applications to replace traditional dielectric layers such as SiO_2 or Si_3N_4 as a heat-conducting layer owing to their significantly higher cross-plane thermal conductivities. Finally, it should be noted that the difference between the experimental data and theoretical calculation also implies that there are some other mechanisms influencing the thermal conductivity of the studied AlN thin films, which is worth further investigations.

5.4. References

[1] A. Jacquot, B. Lenoir, A. Dauscher, P. Verardi, F. Craciun, M. Stölzer, M. Gartner, M. Dinescu, Optical and thermal characterization of AlN thin films deposited by pulsed laser deposition, Applied Surface Science 186 (1-4) (2002) 507–512.

[2] Y. Zhao, C. Zhu, S. Wang, J.Z. Tian, D.J. Yang, C.K. Chen, H. Cheng, P. Hing, Pulsed photothermal reflectance measurement of the thermal conductivity of sputtered aluminum nitride thin films, Journal of Applied Physics 96 (8) (2004) 4563–4568.

[3] P.K. Kuo, G.W. Auner, Z.L. Wu, Microstructure and thermal conductivity of epitaxial AlN thin films, Thin Solid Films 253 (1-2) (1994) 223–227.

[4] T.S. Pan, Y. Zhang, J. Huang, B. Zeng, D.H. Hong, S.L. Wang, H.Z. Zeng, M. Gao, W. Huang, Y. Lin, Enhanced thermal conductivity of polycrystalline aluminum nitride thin films by optimizing the interface structure, Journal of Applied Physics 112 (4) (2012) 44905.

[5] S.M. Lee, D.G. Cahill, Heat transport in thin dielectric films, Journal of Applied Physics 81 (6) (1997) 2590–2595.

[6] D.G. Cahill, K. Goodson, A. Majumdar, Thermometry and Thermal Transport in Micro/Nanoscale Solid-State Devices and Structures, Journal of Heat Transfer 124 (2) (2002) 223.

[7] S.R. Choi, D. Kim, S.H. Choa, S.-H. Lee, J.-K. Kim, Thermal Conductivity of AlN and SiC Thin Films, International Journal of Thermophysics 27 (3) (2006) 896–905.

[8] M. Bogner, A. Hofer, G. Benstetter, H. Gruber, R.Y. Fu, Differential 3ω method for measuring thermal conductivity of AlN and Si3N4 thin films, Thin Solid Films 591 (2015) 267–270.

[9] B.E. Belkerk, A. Soussou, M. Carette, M.A. Djouadi, Y. Scudeller, Structural-dependent thermal conductivity of aluminium nitride produced by reactive direct current magnetron sputtering, Applied Physics Letters 101 (15) (2012) 151908.

[10] G.A. Slack, R.A. Tanzilli, R.O. Pohl, J.W. Vandersande, The intrinsic thermal conductivity of AIN, Journal of Physics and Chemistry of Solids 48 (7) (1987) 641–647.

[11] T. Yamane, N. Nagai, S.I. Katayama, M. Todoki, Measurement of thermal conductivity of silicon dioxide thin films using a 3ω method, Journal of Applied Physics 91 (12) (2002) 9772.

[12] R. Hull, Properties of crystalline silicon, INSPEC, London, (1999) p. 58, 98.

[13] D.G. Cahill, Thermal conductivity measurement from 30 to 750 K: The 3ω method, Review of Scientific Instruments 61 (2) (1990) 802–808.

[14] Y. Lee, G.S. Hwang, Mechanism of thermal conductivity suppression in doped silicon studied with nonequilibrium molecular dynamics, Physical Review B 86 (7) (2012).

[15] Y.S. Ju, K. Kurabayashi, K.E. Goodson, Thermal characterization of anisotropic thin dielectric films using harmonic Joule heating, Thin Solid Films 339 (1-2) (1999) 160–164.

[16] J. Jaramillo-Fernandez, J. Ordonez-Miranda, E. Ollier, S. Volz, Tunable thermal conductivity of thin films of polycrystalline AlN by structural inhomogeneity and interfacial oxidation, Physical chemistry chemical physics 17 (12) (2015) 8125–8137.

[17] C. Duquenne, M.P. Besland, P.Y. Tessier, E. Gautron, Y. Scudeller, D. Averty, Thermal conductivity of aluminium nitride thin films prepared by reactive magnetron sputtering, Journal of Physics D: Applied Physics 45 (1) (2012) 15301.

[18] A. Monshi, M.R. Foroughi, M.R. Monshi, Modified Scherrer Equation to Estimate More Accurately Nano-Crystallite Size Using XRD, World Journal of Nano Science and Engineering 02 (03) (2012) 154–160.

[19] A. Bourret, A. Barski, J.L. Rouvière, G. Renaud, A. Barbier, Growth of aluminum nitride on (111) silicon: Microstructure and interface structure, Journal of Applied Physics 83 (4) (1998) 2003–2009.

[20] G. Radtke, M. Couillard, G.A. Botton, D. Zhu, C.J. Humphreys, Structure and chemistry of the Si(111)/AlN interface, Applied Physics Letters 100 (1) (2012) 11910.

Chapter 6: Thermoelectric Properties of p-Type CuI Thin Films

6.1. Introduction

The increasing requirements for applications of advanced materials in electronics, energy storage and harvesting require a fundamental understanding of the underlying physical properties of the respective materials. Of particular relevance for a sustainable future are materials for energy harvesting. One approach to achieve this, which has been discussing intensely in recent years, is thermoelectric energy conversion. This discipline deals with the motionless solid-state conversion of temperature differences into electrical energy and vice versa. Thermoelectric energy recovery has gained a growing importance, especially near room temperature range, because of its wide applications such as consumer electronics and solar cells [1].

Efficient thermoelectric materials are usually highly-doped semiconductors with energy bandgaps of E_g given by [1,2]:

$$E_g \approx 10\ k_B T_O \tag{6.1}$$

in which the operating temperature and Boltzmann coefficient are represented by T_O and k_B, respectively. Due to their small energy bandgaps (E_g << 2 eV), most of the well-established thermoelectric materials, like $(Bi,Sb)_2Te_3$ films [3,4] are optically opaque, which limits their potential applications such as smart screens or windows. Currently, only a limited amount of optically transparent thermoelectric materials, with their energy bandgaps larger than 3 eV are available [1]. Development of these optically transparent thermoelectric materials and thin films opens new fields of promising applications, including smart screens or windows for energy harvesting, power recovery, and optoelectronics [1,5–7].

The applicability of certain materials to thermoelectrics can be assessed by their dimensionless figure of merit ZT, which only depends on material specific properties and should be maximized when the optimum efficiency is targeted at. The dimensionless figure of merit, ZT, is given by Eq. (1.1). As indicated by Eq. (1.1), high conversion efficiencies require materials with large Seebeck coefficient, large electrical and simultaneously low thermal conductivity values. Correspondingly, transparent thermoelectric materials originally should be belonged to the group of transparent conductor materials, which exhibit large ZT-values. Both p- and n-type transparent thermoelectric materials are needed to realize thermoelectric devices consisting of connected p- and n-type thermoelectric modules (see Figure 2.1(c)) [1]. Most studies investigated n-type transparent conductors [1]. Well-studied n-type transparent conductors are In_2O_3 [8], $SrTiO_3$ [9], and ZnO [10]. Among all of these n-type transparent conductors, Sn-doped In_2O_3 exhibits the largest figure of merit value ($ZT \sim 0.14$) at room temperature [8]. In contrast to n-type thermoelectric materials, p-type materials normally have low electrical conductivity values that are significantly below those of n-type transparent conductors, thus generally resulting in a reduced thermoelectric efficiency at room temperature, (e.g., $ZT \sim 0.001$ for $CuAlO_2$ [11], $ZT \sim 0.002$ for $CuCrO_2$ [12]). Therefore, transparent p-type thermoelectric thin films are the major challenge in the development of transparent thermoelectric modules [1].

In this chapter, thermal conduction and thermoelectric properties of γ-CuI thin films have been investigated, because studies, performed by Yang *et al*. [13–15], found the high room temperature efficiency of γ-CuI films, acting as p-type transparent conductor. Recently, Yang *et al*. [15] reported the highest measured hole conductivity value at room temperature that is larger than 280 S/cm. Further, Yadav *et al*. [16] theoretically determined a large S-value of γ-CuI ($S = 237\ \mu VK^{-1}$ for a hole concentration of $10^{20}\ cm^{-3}$) at 300 K. Therefore, a record-high ZT-value ($ZT \sim 0.21$ at 300 K) of γ-CuI thin films can be predicted due to their large values of electrical conductivity σ and Seebeck coefficient S as well as the expected low thermal conductivity k. This part of the report is a joint research work with the University of

Leipzig, and part of the results were jointly obtained with Dr. Chang Yang in the University of Leipzig.

However, in spite of these previous experimental and theoretical results, the in- and cross-plane thermal conductivities of the γ-CuI thin films, one of the most critical properties for high conversion efficiencies, still remain unknown and further investigations are desperately needed. Therefore, the main focus of this chapter is the investigation of cross-plane ($k_{f\perp}$) and in-plane ($k_{f\parallel}$) thermal conductivities of polycrystalline γ-CuI thin film, as these are critical for designing and analyzing thermoelectric devices at room temperature.

Experimental work and theoretical analysis have been conducted to understand the effects of crystallinity, grain/surface particle sizes, and interfacial structures of the γ-CuI films on their thermal conductivities. It is, for the first time, that both the in- and cross-plane thermal conductivities of γ-CuI thin films were measured as a function of film thickness. The thermal conductivities were obtained using our differential multi-heater 3ω method. The fundamental theory, sample preparation method and experimental setup employed to perform multi-heater 3ω measurements of γ-CuI thin films have been previously introduced in Sections of 3.3.2.2, 4.3.1.1 and 4.3.1.2, respectively.

6.2. Results and Discussion

6.2.1. Structural properties and chemical composition

As demonstrated in Chapter 5, phonon transport in polycrystalline thin films has been proven to be strongly related to structural features within thin films. To investigate this correlation, the accurate characterization of surface morphology and surface crystallite/particle size is mandatory. However, effects of surface morphology, crystallinity and crystallite/surface particle sizes of γ-CuI thin films on their cross- and in-plane thermal conductivities have not been investigated so far. Therefore, experimental and theoretical analysis have been performed to understand the effects of crystallinity and surface particle sizes of the γ-CuI thin

films on their cross- and in-plane thermal conductivities in order to improve the efficiency of thermoelectric devices based on γ-CuI films.

In order to correlate the measured thermal conductivity values with microstructures of the film, XRD pattern of the 200 nm γ-CuI thin film was obtained and the results are summarized in Figure 6.1.

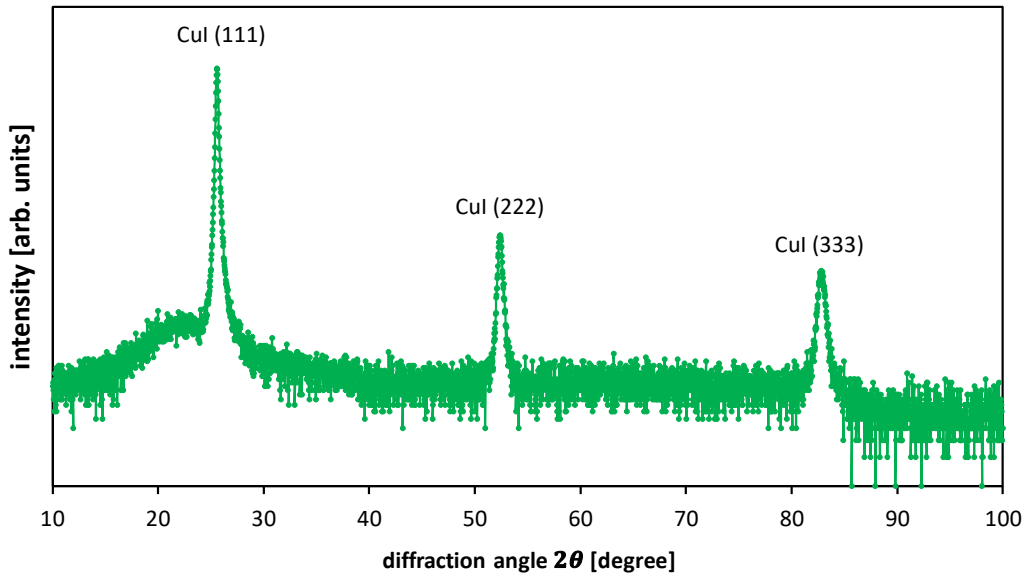

Figure 6.1: The XRD 2θ scan pattern of the 200 nm γ-CuI thin film deposited on Si (100) substrate. The XRD pattern exhibits three diffraction peaks at Bragg angles θ of 25°, 52° and 83°, which correspond to the (111), (222), (333) planes of CuI in a zinc-blende structure (adapted and modified from [1]).

XRD analysis reveals that the γ-CuI thin films grown on Si (100) substrates are of crystalline structure. According to the standard diffraction powder pattern of γ-CuI (PDF 060246 of JCPDS-ICDD diffraction database), the polycrystalline zinc-blende structure of CuI was detected in the film by XRD. In Figure 6.1, the θ-2θ spectra of the γ-CuI thin film exhibits three diffraction peaks at Bragg angles 2θ of 25°, 52° and 83°, which correspond to the (111), (222), (333) planes of CuI in a zinc-blende structure, suggesting the growth of γ-phase CuI is a bit preferred along the [111] direction [1].

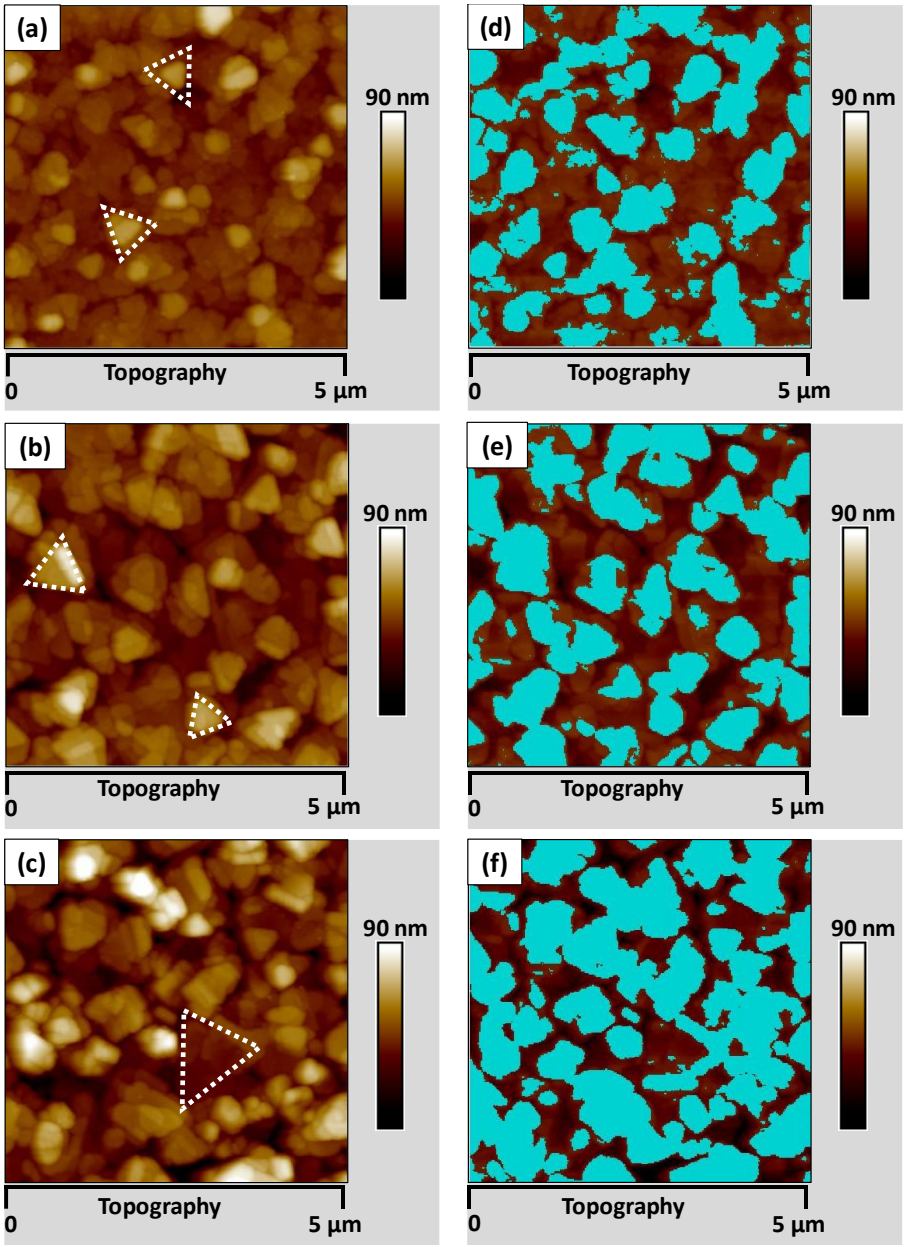

Figure 6.2: AFM images of γ-CuI films deposited on Si substrates with film thicknesses of (a) and (d) 70 nm, (b) and (e) 200 nm, (c) and (f) 400 nm to study the surface morphology and surface particle/crystallite distribution and average particle/crystallite diameter. The distribution of the surface particles/crystallites in images (d) to (f) are highlighted in blue by the NanoScope Analysis software. The dotted triangles indicate small triangular-like crystallites, which are linked with the (111) orientation of γ-CuI films.

The surface morphologies, surface particle size distribution and average surface particle size of γ-CuI films were investigated by AFM. Figures 6.2(a) to (c) present the AFM images showing the surface morphologies of the 70, 200, and 400 nm γ-CuI films. The investigated

γ-CuI films exhibit a very rough surface morphology, consisting of many small triangular-like crystallites, which are linked with the (111) orientation of γ-CuI films according to XRD patterns [1]. The random orientation of these grains indicates that the thin film has no in-plane epitaxial structures. Thus, we can conclude that the obtained γ-CuI thin films have a slightly preferred (111) orientation. These results are consistent with previous published results in literature [13–15].

Figures 6.2(d) to (f) illustrate the AFM images showing the surface particle/crystallite size distributions of the 70, 200, and 400 nm γ-CuI films. Surface particle distributions and average diameters of the γ-CuI films were obtained by utilizing the NanoScope Analysis software. In Figures 6.2(d) to (f), the surface particle/crystallite distribution is indicated by the blue areas, which cover the detected particles/crystallites of the γ-CuI films. With the decrease of film thickness, obvious changes in surface particle size distributions were observed. It is clearly detectable that the particle diameter decreases as the film thickness is decreased. The average surface particle/crystallite diameters for the γ-CuI thin films with film thicknesses of 70, 200, and 400 nm are 211, 267 and 341 nm, respectively. The evolution of the surface crystallite/particle diameter as a function of γ-CuI film thickness is summarized in Figure 6.3 and Table 6.1 on pages 171 and 180, respectively.

In Section 5.2, we have demonstrated that the grain size significantly affected both cross- and in-plane thermal conductivities of polycrystalline AlN thin films due to the grain boundary scattering, because a smaller grain and a smaller surface particle diameters decrease the thermal conductivity of the films due to the shorter phonon MFP. The average surface crystallite diameter values of the γ-CuI thin films measured by AFM support the trend of a reduced average grain size for thinner films. According to these results, a decreasing thermal conductivity for thinner γ-CuI films, which is primarily related to the decrease in average crystallite diameter, can be expected. Experimental results to verify this prediction will be provided in Section 6.2.2.1.

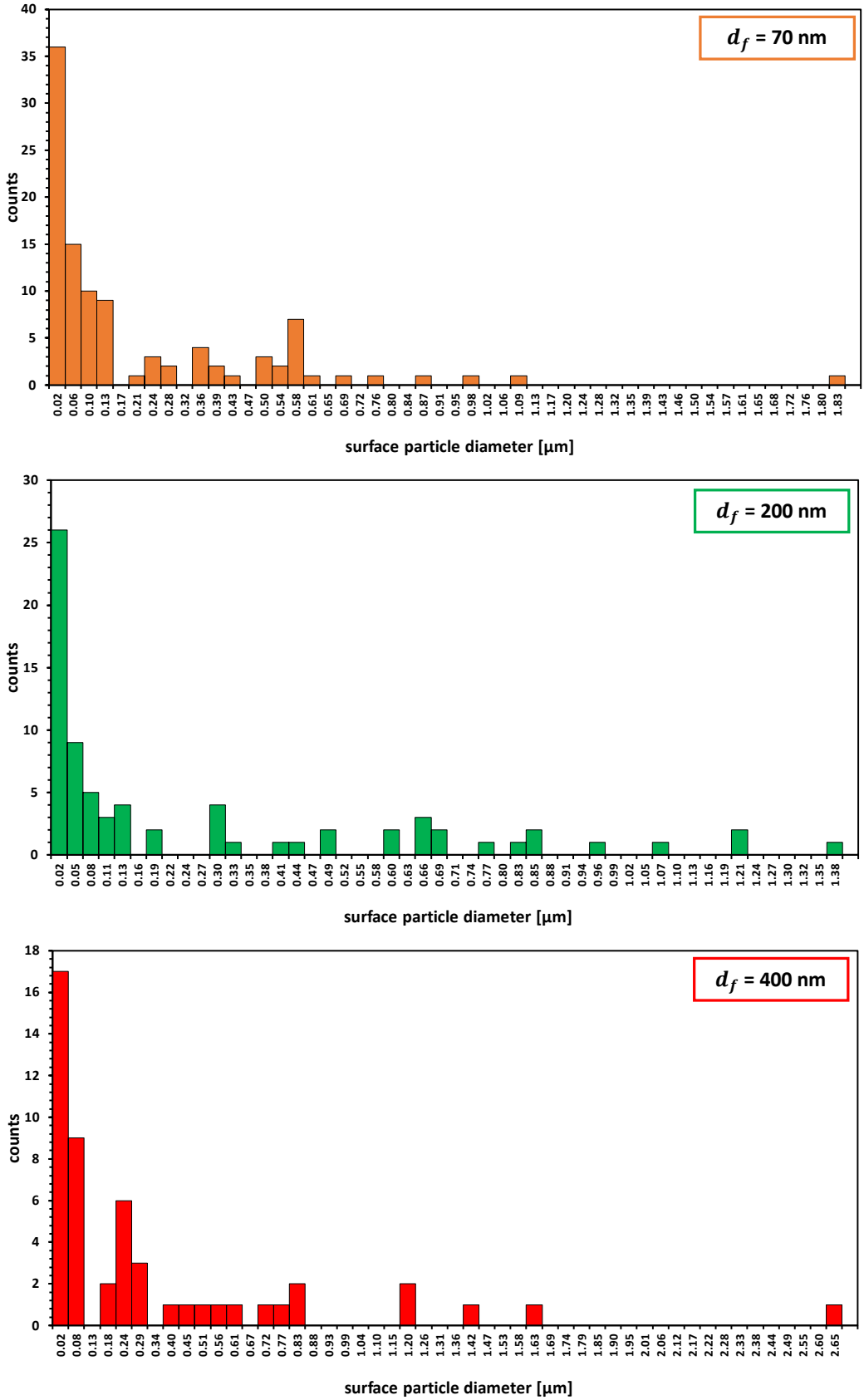

Figure 6.3: Film thickness dependency of the surface particle/crystallite diameter distributions obtained by AFM images of γ-CuI thin films with film thicknesses varied between 70 and 400 nm.

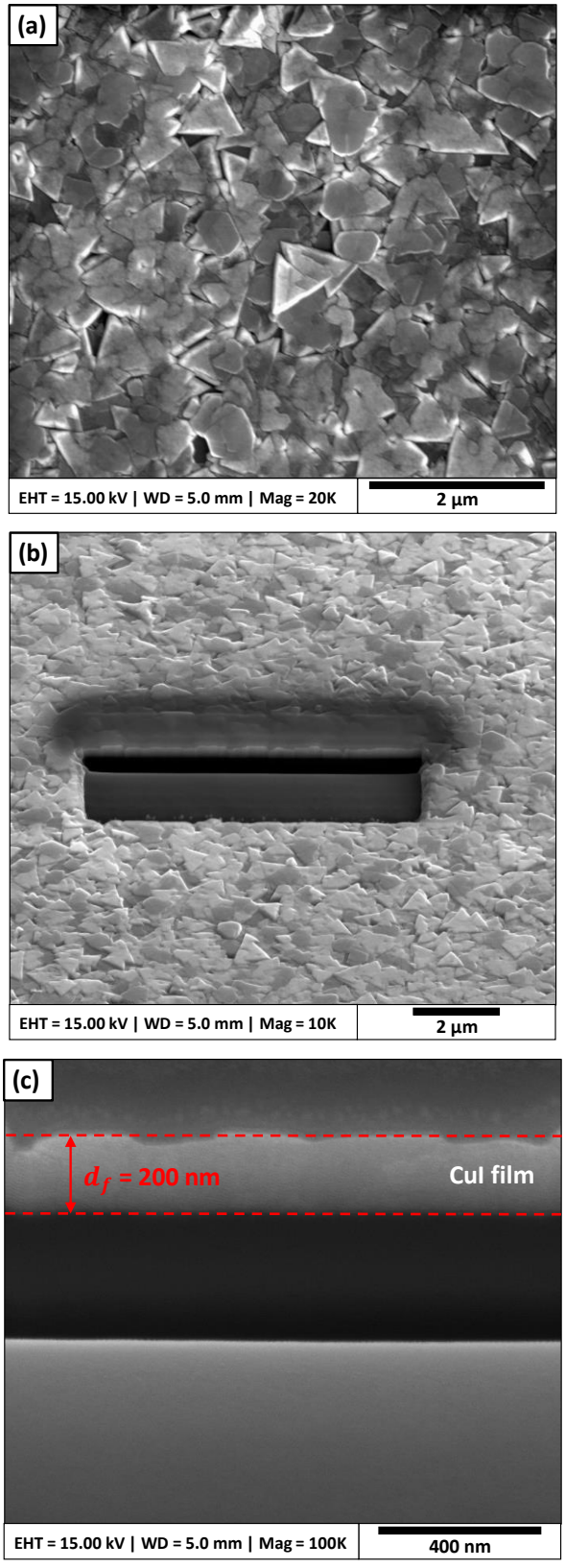

Figure 6.4: (a) and (b) surface and (c) cross-sectional SEM images of a γ-CuI thin film with 200 nm film thickness. In order to investigate the cross-section of the γ-CuI film, the surface of the thin film was FIB-modified at the center of the film (see image (b)). The γ-CuI sample was tilted inside the SEM chamber with an angle of 52°.

SEM and EDX were employed for studying cross-section and chemical composition of the 200 nm γ-CuI thin film used for the thermoelectric applications. Figure 6.4 shows the surface and cross-sectional SEM images of the γ-CuI thin film. Similar to the AFM images in Figures 6.2(a) to (c), Figures 6.4(a) and (b) show a very rough surface morphology, consisting of many small triangular-like crystallites, which are linked with the (111) orientation of γ-CuI films. In order to investigate the cross-section of the γ-CuI film, a small area of the cross-section of the film sample was obtained using focused ion beam (FIB) milling method. For the SEM image, the γ-CuI sample was tilted with an angle of 52°. The detailed microstructures could not be obtained from SEM analysis in Figure 6.4(c). However, the thickness of the 200 nm γ-CuI film corresponds well with the data evaluated by a surface profilometer.

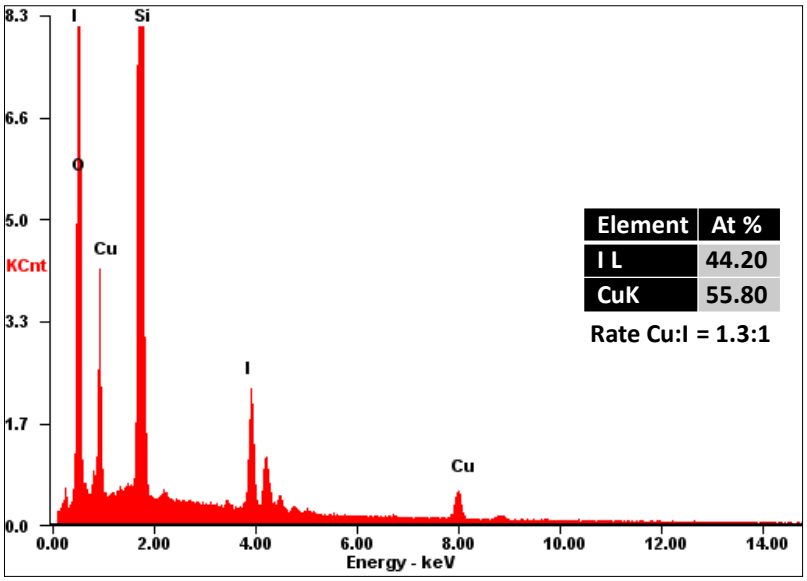

Figure 6.5: EDX results of γ-CuI/Si film-on-substrate samples with film thicknesses of 200 nm. The table lists the atomic weight in percentage of Cu(K) and I(L) of the γ-CuI/Si sample. The ratio of the atomic weight of Cu(K):I(L) in the γ-CuI film, is 1.3:1, indicating that the γ-CuI thin films are iodine deficient. Si and O are mainly attributed to the Si (100) substrate of the γ-CuI/Si samples.

Finally, quantitative analysis of the chemical compositions of γ-CuI thin films was determined by EDX analysis. The atomic ratio of Cu(K) to I(L) in the films determined by EDX was Cu(K):I(L) = 1.3:1, indicating that the γ-CuI thin films are iodine-deficient [1] and not

stoichiometric. Hence, appropriately introducing more iodine into γ-CuI thin film can increase the hole concentration and the electrical conductivity [1]. Additionally, other elements such as Si and O have been detected in the γ-CuI film. Silicon is mainly attributed to the Si (100) substrate of the γ-CuI film-on-substrate samples and oxygen is mostly from surface adsorption.

6.2.2. Thermoelectric properties

6.2.2.1. Cross- and in-plane thermal conductivity

In order to calculate the ZT-value, the thermal conductivity k of the γ-CuI thin film has to be known. A small thermal conductivity value would significantly increase the ZT-value, and therefore, the thermoelectric performance of the γ-CuI thin film. However, the thermal conductivity value of γ-CuI has never been reported in literature [1]. Generally, the thermal conductivity of semi-conductive materials depends on different heat conduction processes, which are [17]:

(1) k_e, heat conduction dominated by electrons and/or and holes;

(2) k_{ph}, heat conduction predominantly by phonon scattering.

The thermal conductivity k is given by the Wiedemann–Franz law [18]:

$$k = k_e + k_{ph} = \sigma L T_O + k_{ph} \tag{6.2}$$

with $\sigma = e\mu_p p$, L and T_o representing the electrical conductivity (μ_p = 8.3 $cm^2V^{-1}s^{-1}$ [1]), Lorenz factor (1.5×10^{-8} $W\Omega K^{-2}$ for ideal non-degenerate semiconductors) and the operating temperature, respectively [18]. The determined k_e-value for γ-CuI is between 0.02 and 0.06 $Wm^{-1}K^{-1}$ for hole concentrations p between 1.7×10^{19} and 1.0×10^{20} cm^{-3} [1]. However, the k_{ph}-value is independent on the film's electrical properties, and can be experimentally obtained using the multi-heater 3ω technique [1].

In this study, the differential multi-heater 3ω technique was employed to analyze the thickness dependency of the in- and cross-plane thermal conductivities of the γ-CuI thin films with film thicknesses varied between 70 and 400 nm.

For measuring the thermal conductivity of semiconducting films such as γ-CuI thin films, an additional electrical insulation layer between the electrical heater and γ-CuI thin film is needed (see Figure 4.6). In this work, a Si_3N_4 thin film (200 nm thick, deposited using PECVD) was deposited on top of the γ-CuI/Si film-on-substrate structure to serve as an electrical insulation layer. Si_3N_4 was used because of its well-known thermal properties [19,20], which have been discussed in Section 5.2.1. In multilayer systems, the voltage drop across 3ω heater depends on the temperature changes caused by the whole multilayer structure. The measured thermal transfer function is therefore the sum of the contributions of the thermal oscillations from different components of the system. To isolate the thermal signal changes caused exclusively by the investigated γ-CuI films, the differential multi-heater 3ω approach uses the average temperature difference measured between two similar sets of experiments, i.e., one involving the Si_3N_4/CuI/Si multilayer system and the other performed on a system without the studied γ-CuI film, which serves as a reference sample. The Si_3N_4/Si reference sample and the Si_3N_4/CuI/Si multilayer structure including the γ-CuI films of interest are illustrated in Figure 4.6 in Section 4.3.1.1.

Firstly, the amplitudes of the temperature oscillations $\Delta T_{2\omega}$, as a function of the AC heating current frequency of the Si_3N_4/Si reference sample must be measured in order to set the ΔT_f reference level for the differential multi-heater 3ω method. The real parts of the amplitudes of the temperature oscillations $\Delta T_{2\omega}$ for both in- and cross-plane thermal conductivities, measured within the 3ω heaters, as a function of the AC heating current frequency f for the Si_3N_4/Si reference sample, are illustrated in Figure 6.6.

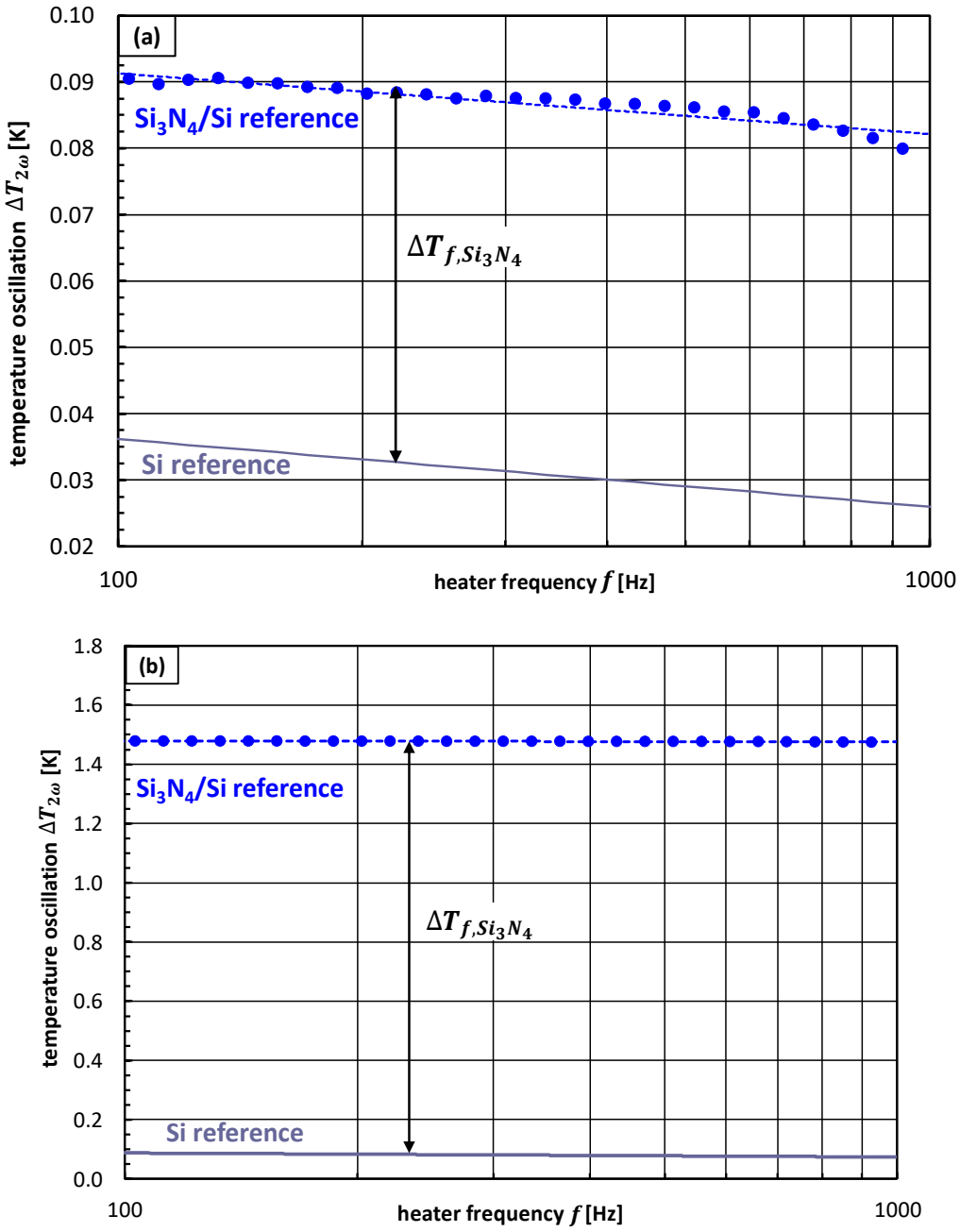

Figure 6.6: The temperature oscillation amplitudes $\Delta T_{2\omega}$ for the Si substrate and Si_3N_4/Si film-on-substrate structures with Si_3N_4 film thickness d_f of 200 nm for the (a) cross- (broad heater width, $2b \sim 25$ μm) and (b) in-plane (narrow heater width, $2b \sim 1.0$ μm) thermal conductivity determination of γ-CuI films. The dashed lines represent the temperature oscillation amplitudes of the Si_3N_4/Si film-on-substrate structures, which are experimentally measured using the 3ω multi-heater technique. The solid line represents the corresponding temperature amplitude of the Si substrate, obtained by Eq. (3.22).

For the 3ω measurements, the heating frequency f was limited to a range varied from 100 to 1000 Hz, in order to confine the oscillation of the generated thermal wave well within the Si_3N_4/Si structure (see Section 4.3.1.3). The dashed lines represent the analytical fit performed for the experimental data. The calculated (based on Eq. (3.22)) reference amplitude of the temperature oscillations, associated with that of the bare Si substrate (solid line), is included as well for a comparison. The slope of $\Delta T_{2\omega}$ as a function of the logarithm of the AC heating frequency yields the thermal conductivity of the Si substrate (k_{Si} = 141 $Wm^{-1}K^{-1}$), which is in a good agreement with results presented in Section 5.2.1. The presence of the 200 nm Si_3N_4 film produces a frequency-independent increase in the real part of the thermal oscillation amplitude $\Delta T_{f,Si_3N_4}$, as can be observed in Figure 6.6. The cross-plane thermal conductivity calculated using Eq. (3.33) for the Si_3N_4 reference films is 0.61 $Wm^{-1}K^{-1}$. The determined value is consistent with experimental data obtained in Section 5.2.1 and also with data in our previous paper [19] and Lee *et al*. [21]. The determined cross-plane thermal conductivity values of the Si_3N_4 reference films were obtained by averaging the thermal conductivity values over five 3ω measurements for each Si_3N_4 reference film. In each case, the maximum deviation of the determined values of these five measurements was below 1.7% for each sample.

After the analysis of the reference samples, the following discussion focuses on the in- and cross-plane thermal conductivity measurements of γ-CuI thin films included within the Si_3N_4/CuI/Si multilayer samples. The real parts of the amplitudes of the temperature oscillations $\Delta T_{2\omega}$ measured within the 3ω heaters for the cross- and in-plane directions, as a function of the AC heating current frequency for the Si_3N_4/CuI/Si multilayer samples, are illustrated in Figure 6.7. The dashed lines represent the analytical fits for the experimental data of the multilayer samples. The reference amplitudes of the temperature oscillations associated to the bare Si substrate (solid line) and to the reference sample including the 200 nm Si_3N_4 film (filled circles), are included as well for comparisons. For the thickness-dependent measurements, the heating frequency f was restricted to a range varied

from 100 to 1000 Hz, in order to confine the oscillation of the generated thermal wave well within the Si_3N_4/CuI/Si multilayer structure (see Section 4.3.1.3).

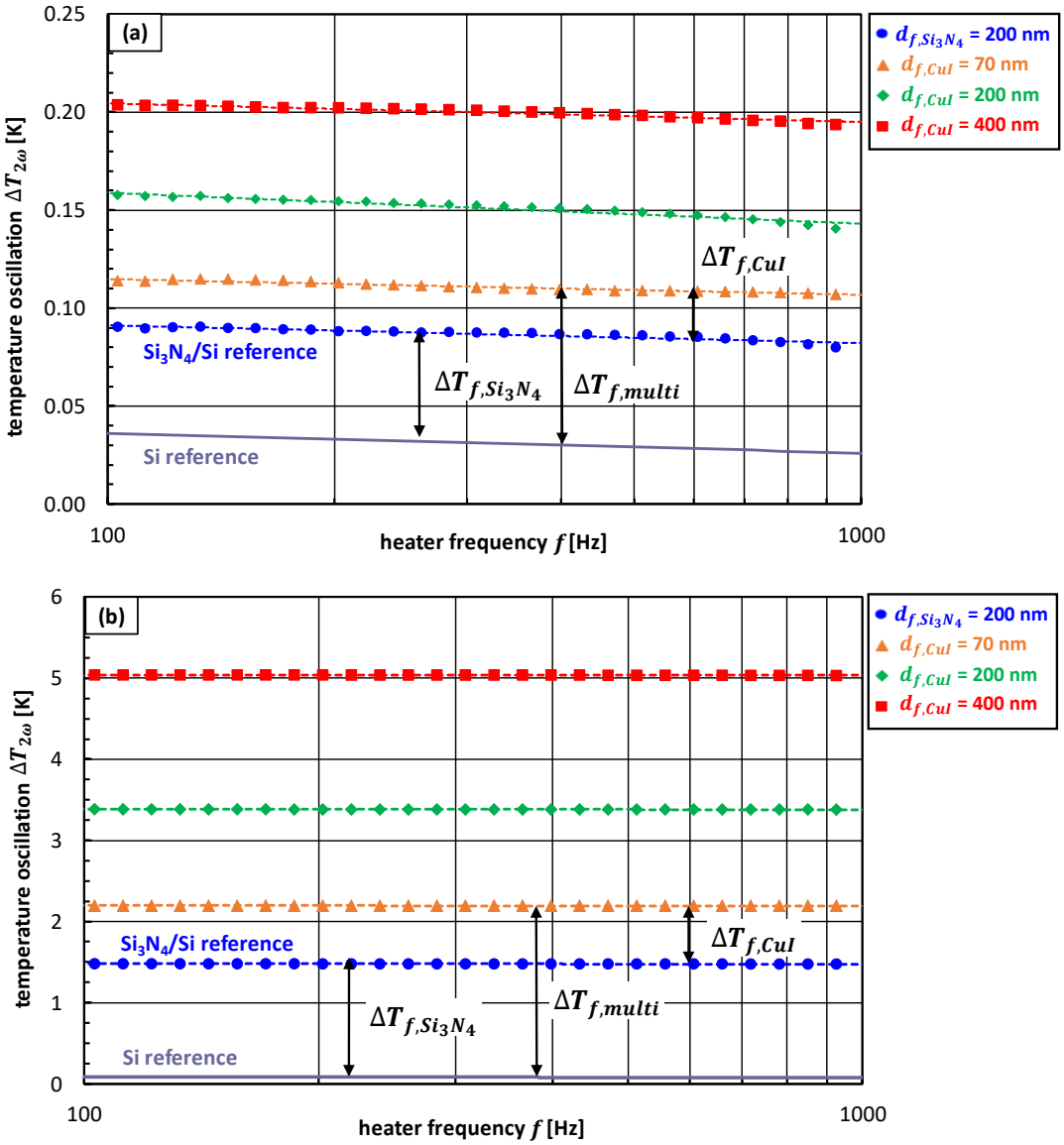

Figure 6.7: The temperature oscillation amplitudes $\Delta T_{2\omega}$ for the Si substrate, Si_3N_4/Si reference sample and Si_3N_4/CuI/Si multilayer sample with γ-CuI film thickness d_f varied between 70 and 400 nm for the (a) cross- (broad heater width, $2b \sim 25$ μm) and (b) in-plane (narrow heater width, $2b \sim 1.0$ μm) thermal conductivity determination of γ-CuI films. The dashed lines represent the temperature oscillation amplitudes of the Si_3N_4/CuI/Si multilayer samples (filled squares, diamonds, triangles) and the temperature oscillation amplitudes of the Si_3N_4/Si reference structure (filled circles), which are experimentally measured utilizing the 3ω multi-heater technique. The solid line represent the corresponding temperature amplitude of the Si substrate, determined by Eq. (3.22).

It must be noted that the amplitudes of the thermal oscillations as a function of heating frequency $\Delta T_{2\omega}(f)$ were obtained at comparable heating currents by similar heaters deposited on the Si_3N_4/CuI/Si multilayer samples and the Si_3N_4/Si reference structure.

As can be observed in Figure 6.7, the dissipation of the thermal oscillation into the γ-CuI films of different thicknesses produces a frequency-independent temperature rise $\Delta T_{f,CuI}$ through the 3ω heater, which gradually increases with film thickness. The offsets between the temperature readings corresponding to the determined Si substrate (solid line) and experimental data of the reference sample (dashed lines with filled circles) are the temperature rises ($\Delta T_{f.Si_3N_4}$) generated by the 200 nm Si_3N_4 film. The temperature offsets ($\Delta T_{f,CuI}$) between the temperature oscillations corresponding to the Si_3N_4/Si reference sample and the experimental data obtained from the Si_3N_4/CuI/Si multilayer samples are the temperature rises generated by the γ-CuI thin films of different thicknesses. The overall temperature rise $\Delta T_{f,multi}$ of the heater, presented in Figure 6.7 was generated by the whole underlying structure, i.e. the Si_3N_4 reference film and the γ-CuI thin film. The gradual increment of this offsets indicates that the γ-CuI thermal resistance as well as thermal conductivities increase as the film thickness increases.

To obtain the thermal conductivity values of γ-CuI films, their thermal properties have to be isolated. This was achieved by subtracting the signal of the Si_3N_4/Si reference sample (dashed lines with filled circles) from that of the Si_3N_4/CuI/Si multilayer sample (dashed lines with filled squares, diamonds, and triangles) including the γ-CuI thin film, using Eq. (3.34). The experimental variables corresponding to the Si_3N_4/Si reference and Si_3N_4/CuI/Si multilayer samples, used to simultaneously determine the cross- and in-plane thermal conductivities, are listed in Tables A.11 to A.14 of Appendix D, respectively. The maximum deviation of the obtained in- and cross-plane thermal conductivity values of γ-CuI thin film, based on five 3ω measurements for each sample, was found to be better than 2.3% in all cases.

Table 6.1 lists the experimental results of the in- and cross-plane thermal conductivities of the γ-CuI films as a function of the film thickness d_f. The thermal conductivity values of the γ-CuI thin films with thicknesses varied from 70 to 400 nm are between 0.45 and 0.56 $Wm^{-1}K^{-1}$ for the cross-plane cases and between 0.50 and 0.59 $Wm^{-1}K^{-1}$ for the in-plane cases. The experimental thermal conductivity values for γ-CuI films along both the cross- and in-plane directions are even lower than that of glass [22] or a phonon-liquid material like Cu_2Se [23] (which was reported to be about 1.0 $Wm^{-1}K^{-1}$ at room temperature) [1]. Such low cross- and in-plane thermal conductivity values can be associated with the heavy element iodine, which leads to strong phonon-scattering at grain boundaries due to the polycrystalline structure of the γ-CuI thin films [1].

Table 6.1: Experimental results of the cross- and in-plane thermal conductivities of γ-CuI thin films by the multi-heater 3ω method and average surface crystallite/particle diameters of the investigated γ-CuI thin films determined by AFM analysis.

No.	Film thickness d_f [nm]	Thermal conductivity value [$Wm^{-1}K^{-1}$]		Average surface particle diameter value (AFM) [nm]
		Cross-plane $k_{f\perp}$	In-plane $k_{f\parallel}$	
16	70	0.45 ± 0.011	0.50 ± 0.012	211
17	200	0.51 ± 0.013	0.55 ± 0.016	267
18	400	0.56 ± 0.016	0.59 ± 0.017	341

Furthermore, the film thermal conductivity values along both the cross- and in-plane directions decrease with the film thickness, but the decrease rate of the cross-plane conductivity gradually increases with decreasing film thickness as shown in Figure 6.8. It was reported that the grain size substantially affects the thermal conductivity due to the grain boundary scattering effect and smaller grain sizes reduce thermal conduction, because of the shorter phonon MFP [24,25]. According to experimental results of the 3ω method and the surface particle analysis of the AFM images, it can be assumed that the decreased thermal conductivity of the γ-CuI thin films for a thinner film thickness is primarily due to the decrease

in the surface particle size of the triangular shaped γ-CuI crystallites (see Table 6.1 and Figure 6.2) and therefore the grain size.

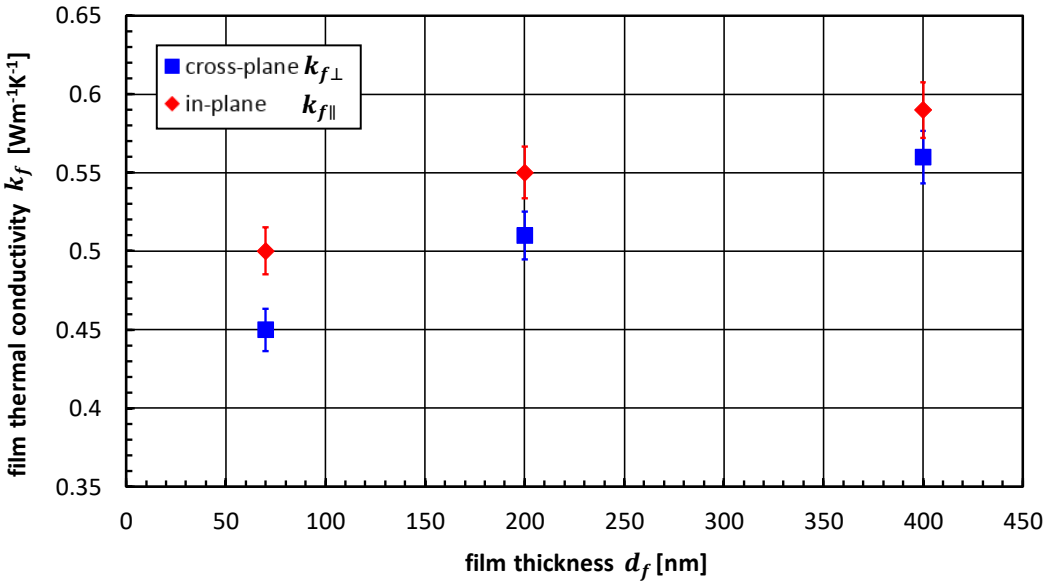

Figure 6.8: Cross- and in-plane thermal conductivity of γ-CuI thin films as a function of film thickness. The squares represent the experimental data of the cross-plane conductivity and the diamonds the in-plane conductivity data obtained in this study by the multi-heater 3ω method.

Table 6.1 also indicates that the in-plane thermal conductivities of the γ-CuI thin films are between 5.4% and 11.1% higher than the cross-plane ones. The main reason to explain this result is that along the in-plane direction, phonons traveling along directions parallel to the interface are less disturbed, whereas those along the cross-plane direction have a limited phonon MFP due to the film thickness and grain boundary scattering at the interfacial structures between the thin film and substrate [25,26], similar to the investigated AlN film-on-substrate samples (see Section 5.2). Lin *et al.* [7] studied the interface of γ-CuI thin films deposited at a Si (100) substrate using cross-sectional SEM. The cross-sectional SEM observed a thin amorphous γ-CuI layer with thickness of about 20 nm between the Si substrate and the γ-CuI films, which could limit heat transport in the cross-plane direction [7].

As demonstrated in Section 5.2.3, it can be further assumed that the interface of thin films near the substrate generally has distorted or amorphous microstructures, because of the lattice mismatch and the existence of surface defects [25,26]. Consequently, considering the

differences in the lattice constants of the γ-CuI (6.05 Å) [27] and Si (5.3 Å) [26], it is expected that γ-CuI thin films might have a graded changed interfacial layers, thus the cross-plane thermal conductivity of γ-CuI films could be an average value of this graded changing structure.

Finally, the total thermal conductivity values k_f of the γ-CuI thin films with different hole concentrations can be estimated by the Wiedemann–Franz law (see Eq. (6.2)) [1]. Figure 6.9 shows the room temperature (300 K) thermal conductivity values k_f obtained by Eq. (6.2) of γ-CuI thin films with d_f = 200 nm, in dependence on their hole concentration p.

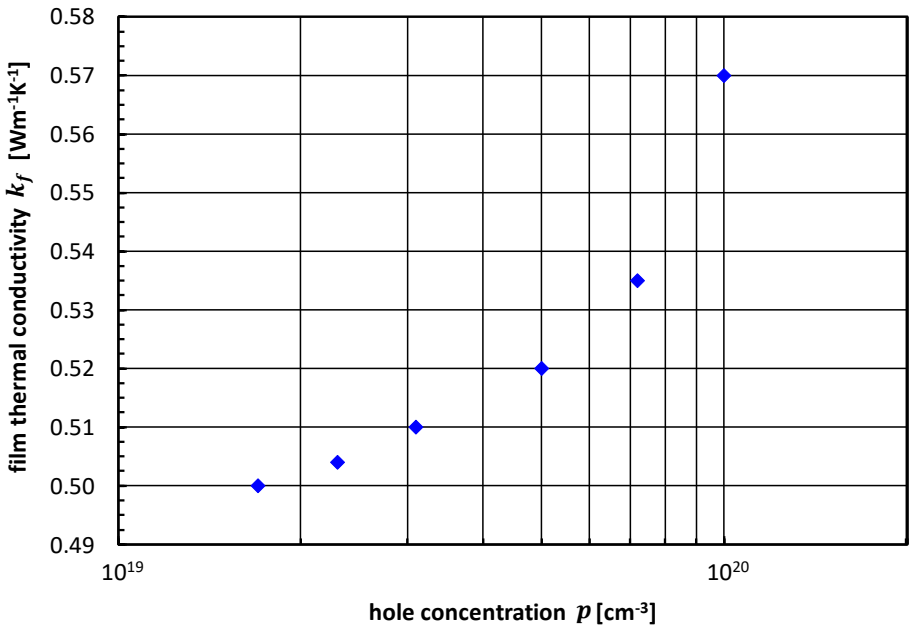

Figure 6.9: Total thermal conductivity values k_f of γ-CuI thin films with d_f = 200 nm, in dependence on their hole concentration p at room temperature (300 K). Based on experimentally obtained in-plane thermal conductivity values (3ω method) the total film thermal conductivities were determined using Eq. (6.2) (adapted and modified from Ref. [1]).

The hole concentrations p varied between 1.7×10^{19} and 1.0×10^{20} cm^{-3} [1]. The average hole mobility value μ_p = 8.3 cm^{2}V^{-1}s^{-1} was experimentally determined and reported by Yang *et al.* [1] and was assumed as constant value that does not change with hole concentration. Figure 6.9 illustrates that the total thermal conductivity values of γ-CuI thin films slightly

increase with increasing hole concentration, caused by the increased amount of energy carriers, which improve heat conduction in thin films, as introduced in Section 2.3.

It has to be mentioned that only the in-plane thermal conductivity values of γ-CuI thin films will be taken into account for further calculations of thermoelectric properties, as the thermal properties in in-plane direction are less influenced by the substrate material of thermoelectric devices based on γ-CuI thin films.

6.2.2.2. Thermoelectric figure of merit

The thermoelectric ZT-values of the investigated γ-CuI thin films (d_f = 200 nm) were calculated using Eq. (1.1), based on experimentally and theoretically obtained in-plane $k_{f\parallel}$ and total film k_f thermal conductivity , electrical conductivity σ and Seebeck coefficient S values, presented in Section 6.2.2.1. The experimental values of the electrical conductivity σ and Seebeck coefficient S were jointly obtained with Dr. Chang Yang in the University of Leipzig [1]. Figure 6.10 illustrates the obtained ZT-values using Eq. (1.1) in dependence of their hole concentration p at 300 K [1].

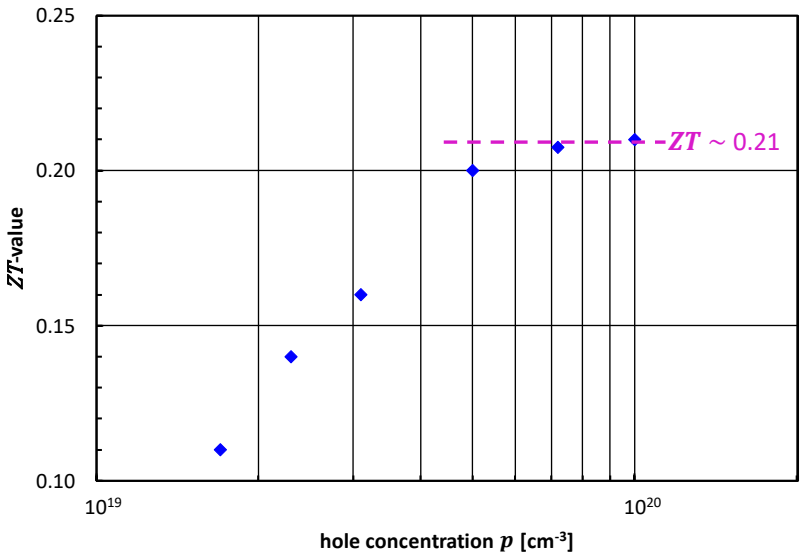

Figure 6.10: Thermoelectric figure of merit (ZT-values) of γ-CuI thin films with d_f = 200 nm, in dependence on their hole concentration p at room temperature (300 K). ZT-values were determined using Eq. (1.1). The dashed line indicates the saturation value of the thermoelectric figure of merit (adapted and modified from Ref. [1]).

The ZT-values increase as the hole concentration p increases, and reaches saturation values at concentrations higher than 5×10^{19} cm^{-3}. In this work, the highest ZT-value is 0.21 at 300 K, which is in the range of PbTe's (p-type) ZT-value in its bulk form (ZT = 0.3) [28]. The γ-CuI film's efficiency of thermoelectric energy conversion can also be improved when operated at temperatures higher than 300 K. However, higher operating temperatures (T_O > 350 K) often result in a degraded electrical conductivity of γ-CuI films [1,29]. Yamada *et al*. [29] presented that this reduced electrical conductivity is related to the diffusion of iodine in γ-CuI thin films throughout heat treatment. Therefore, thermal stability of the γ-CuI thin films should be investigated in future studies by developing concepts of suitable capping layers [1].

Table 6.2 lists the room temperature figures of merit ZT and energy band gaps E_g of common p- and n-type thermoelectric materials, as well as the experimental values of the investigated γ-CuI film [1], which are also illustrated in Figure 6.11.

Table 6.2: Carrier type, energy bandgap and room temperature thermoelectric performance of the γ-CuI thin film and other typical thermoelectric materials [1].

Carrier type	Material	Bandgap [eV]	$S^2\sigma$ [10^{-3}Wm^{-1}K^2]	$\boldsymbol{k}$ [Wm^{-1}K^{-1}]	$\boldsymbol{ZT}$ (300 K)	Reference
n	Bi_2Te_3	0.21	4.84	1.3	1.1	[30]
	$LaSrTiO_3$	2.3-3.2	2.3	9.1	0.08	[9,31]
	Al:ZnO	3.4	0.39	1.19	0.1	[10]
	In:SnO_2	> 3.5	1.8	4	0.14	[8]
p	PbTe	0.32	3	3	0.3	[28]
	CuSe	1.23	0.6 – 0.8	0.8	0.2	[23]
	$Ca_3Co_4O_9$	2.1	0.83	3.5	0.07	[32]
	$CuAlO_2$	3.5	0.01	3.5	0.001	[11]
	$CuCrO_2$	2.5-3.0	0.06	7.5	0.002	[12]
	γ-CuI	3.1	0.375	0.51	0.21	this work [1]

Figure 6.11 shows that p-type γ-CuI provides the largest ZT-value of the reported transparent conductor materials, which is about 50% higher than those of transparent n-type conductors

like Al:ZnO [10] and In:SnO_2 [8]. It is even 210 times larger than the ZT-value of $CuAlO_2$ [11], which also belongs to the group of p-type transparent conductors. Finally, Figure 6.11 clearly illustrates the great potential of using γ-CuI as transparent p-type thermoelectric material, due to its outstanding thermoelectric performance at room temperature.

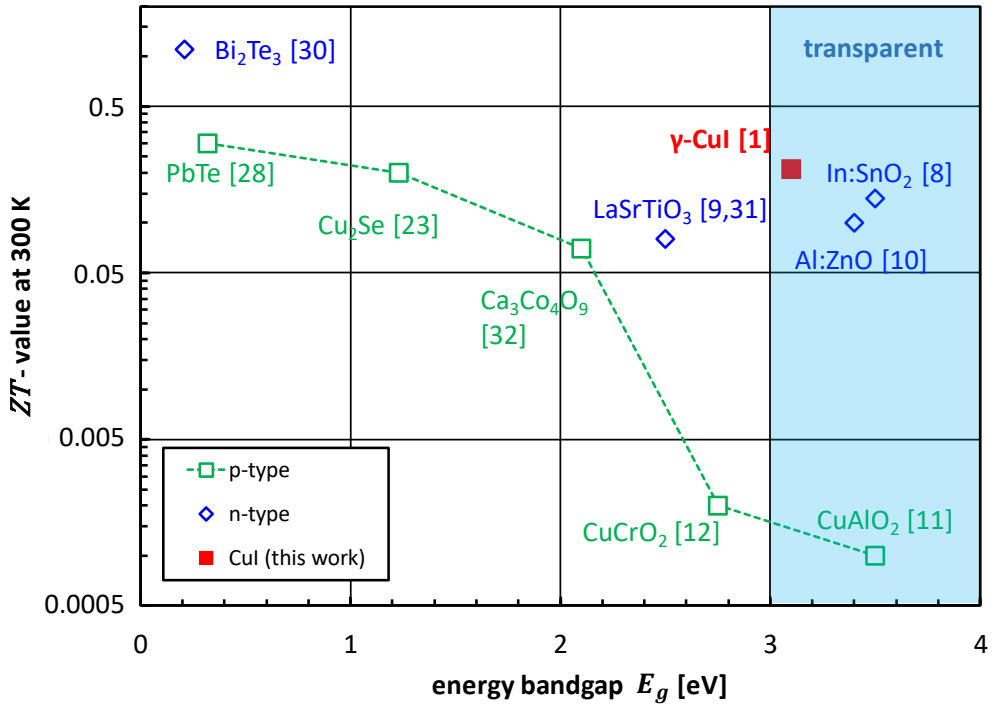

Figure 6.11: ZT-values of common p- and n-type thermoelectric materials and γ-CuI thin film (this thesis) versus energy bandgap E_g. The blue colored region highlights the bandgap values of transparent conductor materials. For detailed data see Table 6.2 (adapted and modified from Ref. [1]).

Regardless of γ-CuI's promising thermoelectric properties, there is still some room for improvement. Experimental data presented in Section 6.2.2.1 reveal that it is possible to slightly reduce the film thickness of γ-CuI without significantly changing both Seebeck coefficient and electrical conductivity, in order to obtain a lower in-plane thermal conductivity value, which leads to a higher ZT-value. In Section 6.2.2.1 we have demonstrated that the in-plane thermal conductivity decreases as the film thickness decreases, and the in-plane value of the 70 nm γ-CuI film is about 8% lower than the in-plane value of the 200 nm film. Thus, the ZT-value could be further enhanced by about 8% and results in a slightly improvement of γ-CuI's thermoelectric properties.

Furthermore, Yang *et al*. [1] stated that the ZT-value of γ-CuI films can be further increased by significantly raising its hole concentration p. Due to unintentional doping the highest hole concentration value of this work was 1×10^{20} cm^{-3} [1,16]. Therefore, Yang *et al*. [1] suggested to switch to an extrinsic doping technique, as they are commonly used to achieve highly degenerate semiconductor materials. Furthermore, Yang *et al*. [1] also stated that phosphor, nitrogen, sulfur and selenium might be suitable for the extrinsic doping process of γ-CuI films.

6.3. Summary

In brief, transparent and flexible p-type γ-CuI thin films exhibited an outstandingly high thermoelectric performance at room temperature. It is the first time that the in- and cross-plane thermal conductivity of γ-CuI thin films have been reported. The multi-heater 3ω method was utilized to study the thickness dependency of the in- and cross-plane thermal conductivity of γ-CuI thin films.

The experimental results have shown that both in- and cross-plane thermal conductivities of the γ-CuI thin films were even lower than that of glass. Such low cross- and in-plane thermal conductivity values at room temperature can be associated with the heavy element iodine, which leads to strong phonon-scattering at grain boundaries due to the polycrystalline structure of the γ-CuI thin films. Furthermore, the film thermal conductivity values of both the in- and cross-plane ones were found to decrease with decreasing film thickness, but the decrease rate increases slightly with decreasing the film thickness for the cross-plane direction case.

The AFM combined with the software-supported surface particle observation indicated that the average surface particle/crystallite sizes of sputtered γ-CuI films decreased with the decrease in film thickness. According to these results, the decreased thermal conductivity of the γ-CuI thin films at a low film thickness is mainly assumed due to the decrease in the average grain size of the films, which leads to an increased grain boundary scattering.

The observed low thermal conductivity values are extremely beneficial for the thermoelectric properties of γ-CuI thin films. Therefore, a high ZT-value of 0.21 at room temperature has been achieved for the 200 nm γ-CuI film, which is 1000 times higher compared to any other p-type transparent materials and almost twice compared to n-type materials [1].

6.4. References

[1] C. Yang, D. Souchay, M. Kneiß, M. Bogner, H.M. Wei, M. Lorenz, O. Oeckler, G. Benstetter, Y.Q. Fu, M. Grundmann, Transparent flexible thermoelectric material based on non-toxic earth-abundant p-type copper iodide thin film, Nature communications 8 (2017) 16076.

[2] A.F. Ioffe, Semiconductor Thermoelements, and Thermoelectric Cooling, Infosearch, ltd (1957).

[3] R. Venkatasubramanian, E. Siivola, T. Colpitts, B. O'Quinn, Thin-film thermoelectric devices with high room-temperature figures of merit, Nature 413 (6856) (2001) 597–602.

[4] T.C. Harman, P.J. Taylor, M.P. Walsh, B.E. LaForge, Quantum dot superlattice thermoelectric materials and devices, Science 297 (5590) (2002) 2229–2232.

[5] H. Kawazoe, M. Yasukawa, H. Hyodo, M. Kurita, H. Yanagi, H. Hosono, P-type electrical conduction in transparent thin films of CuAlO2, Nature 389 (6654) (1997) 939–942.

[6] I. Chowdhury, R. Prasher, K. Lofgreen, G. Chrysler, S. Narasimhan, R. Mahajan, D. Koester, R. Alley, R. Venkatasubramanian, On-chip cooling by superlattice-based thin-film thermoelectrics, Nature nanotechnology 4 (4) (2009) 235–238.

[7] G. Lin, F. Zhao, Y. Zhao, D. Zhang, L. Yang, X. Xue, X. Wang, C. Qu, Q. Li, L. Zhang, Luminescence Properties and Mechanisms of CuI Thin Films Fabricated by Vapor Iodization of Copper Films, Materials 9 (12) (2016) 990.

[8] V. Brinzari, I. Damaskin, L. Trakhtenberg, B.K. Cho, G. Korotcenkov, Thermoelectrical properties of spray pyrolyzed indium oxide thin films doped by tin, Thin Solid Films 552 (2014) 225–231.

[9] S. Ohta, T. Nomura, H. Ohta, K. Koumoto, High-temperature carrier transport and thermoelectric properties of heavily La- or Nb-doped SrTiO3 single crystals, Journal of Applied Physics 97 (3) (2005) 34106.

[10] J. Loureiro, N. Neves, R. Barros, T. Mateus, R. Santos, S. Filonovich, S. Reparaz, C.M. Sotomayor-Torres, F. Wyczisk, L. Divay, R. Martins, I. Ferreira, Transparent aluminium zinc oxide thin films with enhanced thermoelectric properties, Journal of Materials Chemistry A 2 (18) (2014) 6649.

[11] C. Ruttanapun, W. Kosalwat, C. Rudradawong, P. Jindajitawat, P. Buranasiri, D. Naenkieng, N. Boonyopakorn, A. Harnwunggmoung, W. Thowladda, W. Neeyakorn,

C. Thanachayanont, A. Charoenphakdee, A. Wichainchai, Reinvestigation Thermoelectric Properties of CuAlO2, Energy Procedia 56 (2014) 65–71.

[12] K. Hayashi, K. Sato, T. Nozaki, T. Kajitani, Effect of Doping on Thermoelectric Properties of Delafossite-Type Oxide CuCrO2, Japanese Journal of Applied Physics 47 (1) (2008) 59–63.

[13] M. Grundmann, F.L. Schein, M. Lorenz, T. Böntgen, J. Lenzner, H. von Wenckstern, Cuprous iodide: A p-type transparent semiconductor, history, and novel applications, Physica status solidi A (2013) 1671-1703.

[14] C. Yang, M. Kneiss, F.L. Schein, M. Lorenz, M. Grundmann, Room-temperature Domain-epitaxy of Copper Iodide Thin Films for Transparent CuI/ZnO Heterojunctions with High Rectification Ratios Larger than 10(9), Scientific reports 6 (2016) 21937.

[15] C. Yang, M. Kneibeta, M. Lorenz, M. Grundmann, Room-temperature synthesized copper iodide thin film as degenerate p-type transparent conductor with a boosted figure of merit, Proceedings of the National Academy of Sciences of the United States of America 113 (46) (2016) 12929–12933.

[16] M.K. Yadav, B. Sanyal, First-principles study of thermoelectric properties of CuI, Materials Research Express 1 (1) (2014) 15708.

[17] M. Kaviany, Essentials of heat transfer: Principles, materials, and applications, Cambridge University Press, Cambridge, New York, (2011) 1-722.

[18] H.S. Kim, Z.M. Gibbs, Y. Tang, H. Wang, G.J. Snyder, Characterization of Lorenz number with Seebeck coefficient measurement, APL Materials 3 (4) (2015) 41506.

[19] M. Bogner, A. Hofer, G. Benstetter, H. Gruber, R.Y. Fu, Differential 3ω method for measuring thermal conductivity of AlN and Si3N4 thin films, Thin Solid Films 591 (2015) 267–270.

[20] D.G. Cahill, Thermal conductivity measurement from 30 to 750 K: The 3ω method, Review of Scientific Instruments 61 (2) (1990) 802–808.

[21] S.M. Lee, D.G. Cahill, Heat transport in thin dielectric films, Journal of Applied Physics 81 (6) (1997) 2590–2595.

[22] R.W. Powell, C.Y. Ho, P.E. Liley, Thermal Conductivity of Selected Materials, National Standard Reference Data System-National Bureau of Standards 8 (1966) 89–91.

[23] H. Liu, X. Shi, F. Xu, L. Zhang, W. Zhang, L. Chen, Q. Li, C. Uher, T. Day, G.J. Snyder, Copper ion liquid-like thermoelectrics, Nature materials 11 (5) (2012) 422–425.

[24] G.A. Slack, R.A. Tanzilli, R.O. Pohl, J.W. Vandersande, The intrinsic thermal conductivity of AIN, Journal of Physics and Chemistry of Solids 48 (7) (1987) 641–647.

[25] T.S. Pan, Y. Zhang, J. Huang, B. Zeng, D.H. Hong, S.L. Wang, H.Z. Zeng, M. Gao, W. Huang, Y. Lin, Enhanced thermal conductivity of polycrystalline aluminum nitride thin films by optimizing the interface structure, Journal of Applied Physics 112 (4) (2012) 44905.

[26] S.R. Choi, D. Kim, S.-H. Choa, S.-H. Lee, J.-K. Kim, Thermal Conductivity of AlN and SiC Thin Films, International Journal of Thermophysics 27 (3) (2006) 896–905.

[27] O. Madelung, U. Rössler, M. Schulz, Cuprous iodide (gamma-CuI) lattice parameters, thermal expansion, Springer-Verlag, Berlin/Heidelberg (1999) 1–7.

[28] H. Beyer, J. Nurnus, H. Böttner, A. Lambrecht, E. Wagner, G. Bauer, High thermoelectric figure of merit ZT in PbTe and Bi2Te3-based superlattices by a reduction of the thermal conductivity, Physica E: Low-dimensional Systems and Nanostructures 13 (2-4) (2002) 965–968.

[29] N. Yamada, R. Ino, Y. Ninomiya, Truly Transparent p-Type γ-CuI Thin Films with High Hole Mobility, Chemistry of Materials 28 (14) (2016) 4971–4981.

[30] L.M. Goncalves, C. Couto, P. Alpuim, A.G. Rolo, F. Völklein, J.H. Correia, Optimization of thermoelectric properties on Bi2Te3 thin films deposited by thermal co-evaporation, Thin Solid Films 518 (10) (2010) 2816–2821.

[31] R.B. Comes, P.V. Sushko, S.M. Heald, R.J. Colby, M.E. Bowden, S.A. Chambers, Band-Gap Reduction and Dopant Interaction in Epitaxial La,Cr Co-doped SrTiO3 Thin Films, Chemistry of Materials 26 (24) (2014) 7073–7082.

[32] R. Funahashi, S. Urata, T. Sano, M. Kitawaki, Enhancement of thermoelectric figure of merit by incorporation of large single crystals in Ca3Co4O9 bulk materials, Journal of Materials Research 18 (07) (2003) 1646–1651.

Chapter 7: Characterization of local Thermal Properties of Thin Films using 3ω Microscopy

7.1. Introduction

Thin film technology has been developed rapidly in the past few years due to the advances in thin film preparation facilities and methods [1]. As a consequence, thin films have taken a prominent part in revolutionary development of micro- and nanoelectronic devices, MEMS and novel thermoelectric applications. Due to urgent requirements of a number of thermal management [1] and thermoelectric applications for energy harvesting [2], there is a significant demand for thermal conductivity characterization techniques of thin films [3], especially with high-spatially resolving techniques to analyze the local distribution of thermal characteristics, such as thermal conductivity. Therefore, a quantitative determination of the local thermal conductivity of thin films is mandatory within the fundamental characterizations.

Commonly used thermal characterization techniques such as IR thermography [4], TDTR [5], and macroscopic 3ω method [6,7] have restricted lateral spatial resolutions due to their optical diffraction limit or metal strips deposited on the surface of the thin film sample. These characterization methods are incapable to obtain the local thermal conductivity of thin films. SThM overcomes these limits and enables to qualitatively record local distributions of temperature [3] and thermal conductivity [3] with high resolutions for both thin films and bulk materials. The SThM utilizes a thermo-resistive AFM probe (see Section 4.3.2.1), acting as both heat source and temperature sensor.

Moreover, it has already been demonstrated that the SThM, combined with the fundamental 3ω principle, is capable to quantitatively measure the local thermal conductivity of bulk materials with a spatial resolution in nanometer ranges [8,9]. Based on these preliminary

studies, we develop a new experimental technique, which merges the basic AFM/SThM and differential 3ω method, introduced in Section 4.3.2, in order to quantitatively determine the local thermal conductivity of thin films. To realize this new "3ω Microscopy", the macroscopic 3ω method has been transferred to the microscopic level by combining the AFM with our extended differential 3ω method. Within this thesis, the 3ω Microscopy method is utilized to quantitatively measure the local thermal conductivities of thin-film-on-substrate systems, in order to demonstrate its potential as a promising and alternative thermal characterization technique.

The 3ω Microscopy method was employed in this chapter to study the thickness-dependency of local thermal conductivities of γ-CuI and AlN thin films with film thicknesses varied between 70 - 400 nm and 304 – 710 nm, respectively. It is for the first time that the local thermal conductivities of the γ-CuI and AlN thin films were quantitatively measured as a function of film thickness. The fundamental theory, experimental setup and sample preparation method to perform 3ω Microscopy measurements have been previously introduced in Sections of 3.3.2/4.3.2 and 4.3.1.1/4.3.2.5, respectively.

7.2. Results and Discussion

7.2.1. Calibration of the 3ω Microscopy setup

The SThM based on the 3ω method has been theoretically verified to be applicable for the determination of local thermal conductivities of thin films and substrate materials, which has been introduced in Section 4.3.2.4 [8]. However, it is still ambiguous whether the 3ω Microscopy is practically feasible on thin film structures or not. For this reason, γ-CuI and AlN thin films will be investigated using the 3ω Microscopy technique.

The quantitative local thermal conductivity $k_{f,local}$ of thin films can be determined from Eq. (4.3), if the amplitude of the heating power P_l applied in the thin film is known. Therefore, an experimental calibration for each thermo-resistive Pd/SiO_2 probe was performed and

utilized for quantitatively measuring local thermal conductivities. In Section 4.3.2.3, it has been demonstrated that an experimental calibration for quantitative local thermal conductivity measurements can be performed, if one can do reference measurements of a flat bulk sample with a well-known thermal conductivity in a range that covers the expected thermal conductivity values of the investigated thin films.

In this work, a commercial glass-ceramic reference material (BCR-724) was utilized as a calibration sample for the 3ω Microscopy technique. The thermal conductivity value of this reference sample was investigated by a hot wire technique, which is similar to 3ω method and the results were certified by the Institute for Reference Materials and Measurements of the Joint Research Centre (European Commission) [10]. The thermal conductivity value for the BCR-724 bulk sample with a diameter of 26.9 mm and a height of 22 mm is (4.08 $\pm$ 0.002) $Wm^{-1}K^{-1}$ at room temperature of 293 K [10]. The thermal conductivity of the BCR-724 is near to the range that covers the expected thermal conductivity values of the investigated γ-CuI (0.50 – 0.59 $Wm^{-1}K^{-1}$) [2] and AlN thin films (8.4 – 13.2 $Wm^{-1}K^{-1}$).

Figure 7.1 exhibits the temperature oscillation amplitudes $\Delta T_{2\omega}$ obtained from the 3ω Microscopy measurements of the BCR-724 reference sample. The amplitude of the heating power applied in the sample per unit length P_l of the BCR-724 reference sample was obtained using Eq. (3.22). The slope of the frequency-dependent temperature oscillation amplitudes $\Delta T_{2\omega}$ was recorded. The obtained slope of the fitted temperature oscillation amplitude $\Delta T_{2\omega}$ (dashed line) was measured to be -0.178 Ks. Thus, the amplitude of the heating power applied in the sample per unit length is 0.4 Wm^{-1}, with a slope of -0.178 Ks and a thermal conductivity of 4.08 $Wm^{-1}K^{-1}$. The theoretical approach of the 3ω Microscopy is applicable, as the measured temperature oscillation amplitudes $\Delta T_{2\omega}(f)$ and the fitting curve calculated by Eq. (3.22) are in good agreements.

For the 3ω Microscopy measurements, the heating frequency of the Pd/SiO_2 probe was limited to a range varied from 100 to 2500 Hz, in order to confine the oscillation of the generated

thermal wave well within the reference sample (see Section 4.3.2.4). Moreover, the heating frequency lies within the theoretically permissible frequency range (100 - 2750 Hz) of the 3ω Microscopy technique (derived in Section 4.3.2.4), using the Pd/SiO_2 probe and a 525 or 640 µm thick Si substrate.

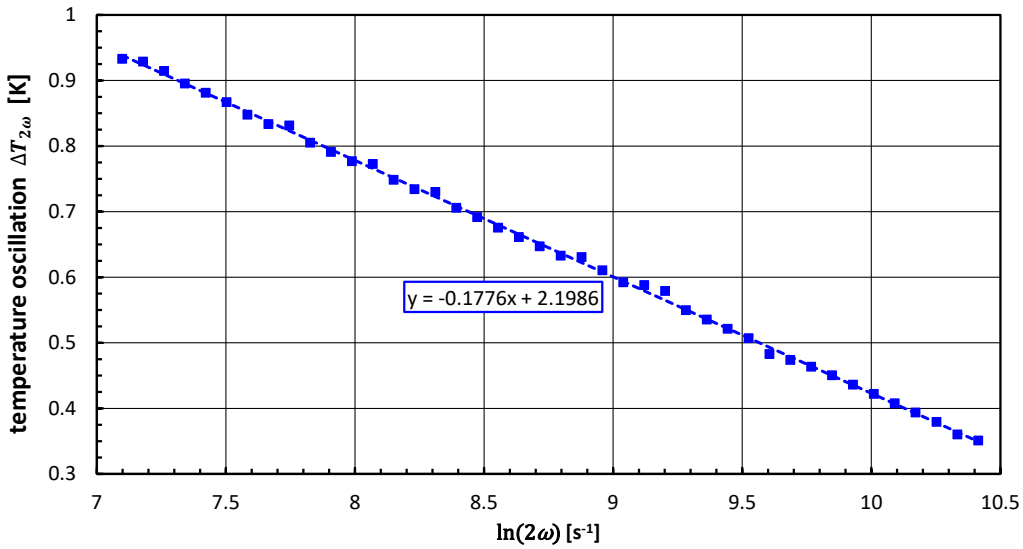

Figure 7.1: Experimental determination of heating power dissipated into the thin film sample by a reference measurement. Dashed line shows the linear fit of temperature oscillation amplitudes $\Delta T_{2\omega}(f)$ obtained from a 3ω Microscopy measurements of the BCR-724 reference sample (k_s = 4.08 $Wm^{-1}K^{-1}$ at room temperature [10]). The amplitude of the heating power applied in the sample per unit length P_l of the BCR-724 reference sample was obtained using Eq. (3.22). The obtained slope of the fitted temperature oscillation amplitudes $\Delta T_{2\omega}(f)$ (dashed line) is -0.178 Ks.

The determined rms values of the dissipated heating power of the BCR-724 reference sample were obtained by averaging the power values over five 3ω measurements at different positions on the surface of the reference sample. In each case, the maximum deviation of the determined values of these five measurements was below 1.2% for each measurement.

Previously reported theoretical and experimental investigations have assumed that the dissipated power into the specimen per unit length is a constant [3,9]. However, a simplified two-dimensional FEM model of our 3ω Microscopy setup (see Figure 7.2), including the thin film-on-substrate structure and the thermo-resistive Pd-tip, demonstrated that this assumption

is only valid for extremely high ($\approx k > 1000$ $Wm^{-1}K^{-1}$) and low ($\approx k < 10$ $Wm^{-1}K^{-1}$) thermal conductivity values (see Figure 7.3). Detailed information about the design and boundary conditions of the two-dimensional FEM simulation are listed in Appendix E.

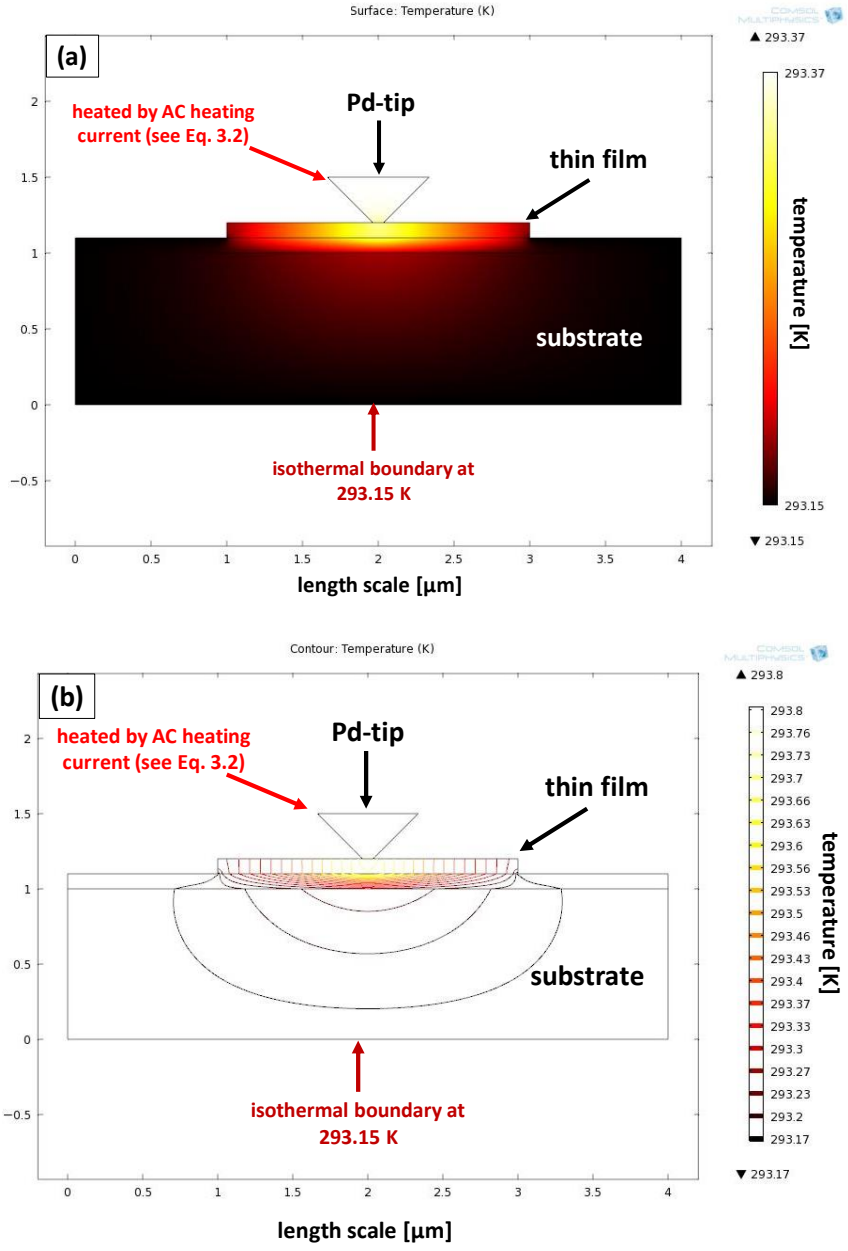

Figure 7.2: Simplified two-dimensional FEM simulation of the 3ω Microscopy setup, including the thermo-resistive Pd-tip and the investigated film-on-substrate structure. The FEM results of (a) surface temperature and (b) temperature contour of a film-on-substrate structure with thermal conductivity values 1.0 and 147.0 $Wm^{-1}K^{-1}$ of the film and the substrate were obtained by COMSOL Multiphysics. The Pd-tip was heated by an AC heating current of 10 mA (rms value) and both sides and the bottom of the FEM model were assumed as isothermal (293.15 K).

In Figure 7.3, the thermal FEM data obtained from COMSOL Multiphysics analysis indicate that the dissipated heating power was strongly dependent on the thermal conductivity of the investigated thin film material in the range between 10 up to 1000 $Wm^{-1}K^{-1}$. As the thermal conductivity values of the investigated γ-CuI thin films and the BCR-724 reference sample are clearly below 10 $Wm^{-1}K^{-1}$ [2] (see Table 6.1), we can assume that the dissipated heating is independent from the thermal conductivity of the γ-CuI films in this study. As the expected thermal conductivity values of AlN are at the beginning of the transition region between a constant or a thermal conductivity-dependent heating power value (see Figure 7.3), we also assume that the dissipated heating power of AlN is a constant value.

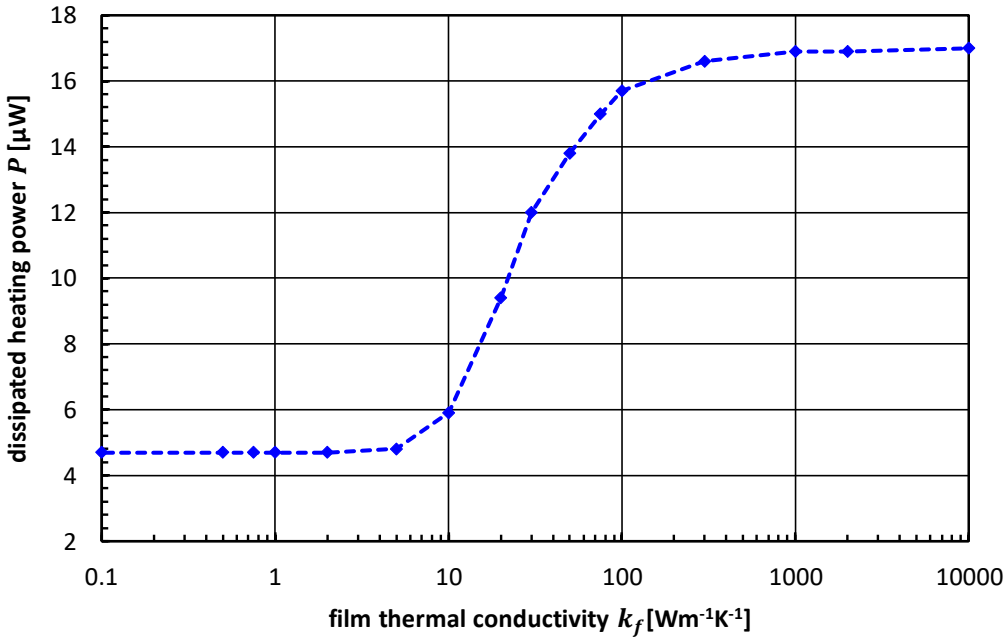

Figure 7.3: Heating power *P* (rms value) dissipated into the thin film sample depending on the thermal conductivity of the thin film material k_f obtained from a simplified two-dimensional FEM simulations of the 3ω Microscopy setup, illustrated in Figure 7.2.

FEM results obtained by Altes *et al.* [8] also showed that the amount of dissipated heat is a constant for materials with low and extremely high thermal conductivity values. Furthermore, FEM results from Altes *et al.* [8] demonstrated that the rms value of the dissipated heating power is frequency-independent within the permissible frequency range of 100 up to 2750 Hz.

7.2.2. Quantitative local thermal conductivity of γ-CuI thin films

In Chapter 6, γ-CuI thin films with different film thicknesses have been systematically investigated using the conventional differential 3ω method. Normally, for a conventional thermal measurement, a metal strip is required to be evaporated on top of the thin film sample [5], however, the metal strip cannot be evaporated with an infinitesimally small width due to the limitation of process. Besides these fabrication limitations, it is intricate to produce various thin films to investigate the thermal conductivity influenced by film thickness. The 3ω Microscopy overcomes this limitation by simultaneously recording the local thermal properties as well as the topography of the investigated thin films.

In this study, 3ω Microscopy measurements to quantitatively obtain the local thermal conductivity of thin films were conducted in five consecutive steps:

(1) Recording the topography of the thin film-on-substrate sample;

(2) Measuring the local 3ω voltage of the thermo-resistive probe in contact with the surface of the thin film sample at an AC heating current frequency of 1000 Hz, which lies well within the theoretically permissible range of 100 to 2750 Hz;

(3) Converting the local 3ω voltage $V_{3\omega}$ data into the local thermal oscillation amplitudes $\Delta T_{2\omega}$ using Eq. (3.10);

(4) Performing frequency-dependent 3ω measurements on the BCR-724 reference sample, in order to obtain the amplitude of the dissipated power per unit length P_l, as described in Section 7.2.1;

(5) Performing selective differential 3ω measurements on two specific points (minimum $\Delta T_{2\omega,min}$ and maximum $\Delta T_{2\omega,max}$ temperature oscillation values) on the surface of the thin film sample in the frequency range between 100 and 2500 Hz, in order to determine the absolute local thermal conductivity $k_{f,local}$ value for every position within the corresponding 3ω Microscopy image.

After the analysis of the BCR-724 reference samples given in the previous section, the following discussion will be focused on the local cross-plane thermal conductivity measurements of the γ-CuI thin films deposited on Si substrates. In this section, the 3ω Microscopy technique was employed to quantitatively investigate the thickness-dependency of local thermal conductivities of γ-CuI thin films with film thicknesses varied between 70 and 400 nm.

Figure 7.4 illustrates the images of spatially-resolved topography (a-c) and local thermal conductivity (d-f) of γ-CuI thin films with film thicknesses varied between 70 and 400 nm. The 3ω Microscopy measurements were performed with a scan area of 5 μm × 5 μm (with 512 lines) at a scan rate of 1 Hz.

Figures 7.4(a) to (c) present the AFM images showing the surface morphologies of the γ-CuI films with various thicknesses of (a) 70, (b) 200, and (c) 400 nm. The investigated γ-CuI films exhibit a very rough surface morphology, consisting of many small triangular-like crystallites (see dotted triangles in Figures 7.4(a) to (c)), which are linked to the (111) orientation of γ-CuI films according to XRD patterns [2], reported in Section 6.2.1. The random orientation of these grains indicates that the film has no apparent in-plane epitaxial structures. These results are consistent with experimental data in Section 6.2.1 and those previously published in literature [11–13].

Furthermore, Figures 7.5(a) to (c) illustrate the AFM images showing the surface particle/crystallite size distributions of the 70, 200, and 400 nm γ-CuI films. Surface particle distributions and average diameters of the γ-CuI films were obtained by utilizing the NanoScope Analysis software.

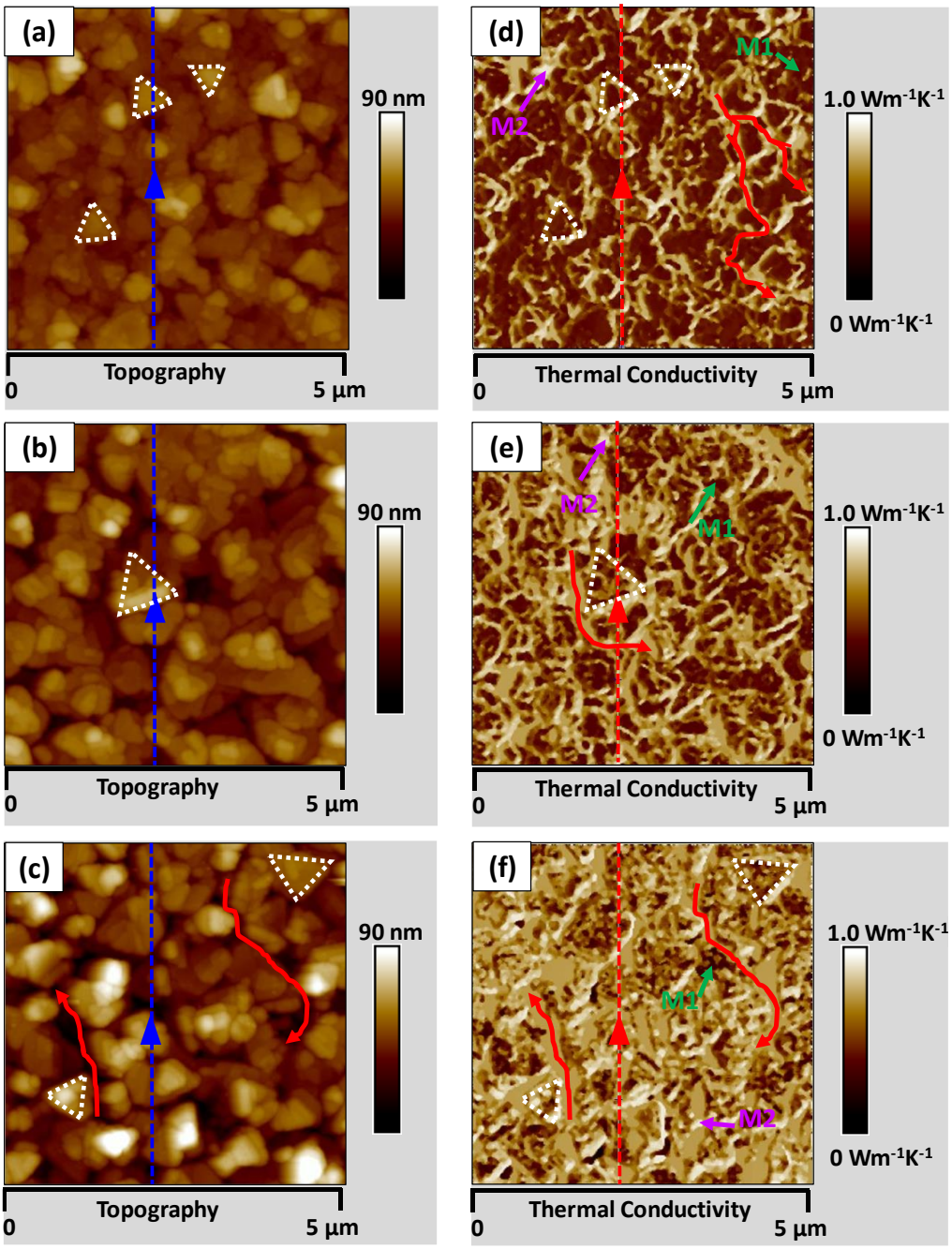

Figure 7.4: (a-c) Topography AFM and (d-f) local thermal conductivity images of γ-CuI thin films with different thicknesses of (a) and (d) 70 nm; (b) and (e) 200 nm; (c) and (f) 400 nm deposited on Si (100) substrates, revealing the surface morphology and local cross-plane thermal conductivity values of the γ-CuI thin films. The 3ω Microscopy measurements were carried out at heating frequency of 1000 Hz with scan area of 5 µm × 5 µm by 512 lines at a scan rate of 1 Hz, under vacuum conditions (pressure < 4.0 Pa). The γ-CuI films exhibit a very rough surface morphology, consisting of many small triangular-shaped crystallites, which are indicated by the dotted triangles.

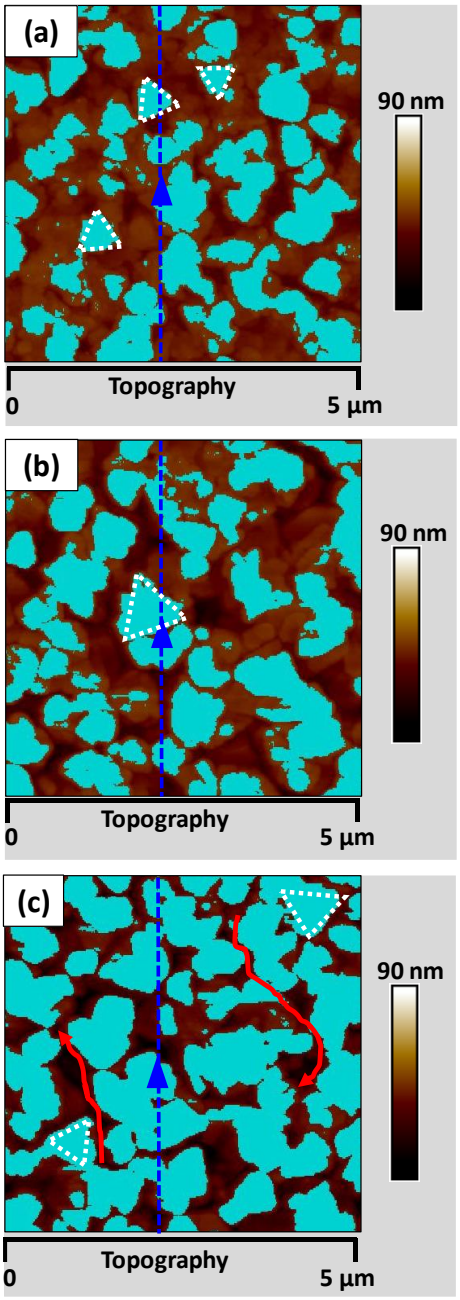

Figure 7.5: AFM images of γ-CuI films deposited on Si substrates with film thicknesses of (a) 70 nm, (b) 200 nm and (c) 400 nm to study the surface particle/crystallite distribution and average particle/crystallite diameter. The distribution of the surface particles/crystallites are highlighted in blue by the NanoScope Analysis software.

In Figures 7.5(a) to (c), the surface particle/crystallite distribution is indicated by the blue areas, which cover the detected particles/crystallites of the γ-CuI films. With the decrease of film thickness, obvious changes in surface particle size distributions were observed. Similar to experimental results of Section 6.2.1, it is clearly detectable that the particle diameter

decreases as the film thickness is decreased. The average surface particle/crystallite diameter for the γ-CuI thin films with film thicknesses of 70, 200, and 400 nm are 217, 251 and 395 nm, respectively. The average surface crystallite/particle size values are in good agreements with values presented in Table 6.1 of Chapter 6. At a different scanning position but equal scanning size (5 μm × 5 μm) on the surface of the same γ-CuI films, the corresponding values vary around 2.8% and 15.8% (see Table 6.1 of Chapter 6). The evolution of the surface crystallite/particle diameters as a function of γ-CuI film thickness is summarized in Figure 7.6 and Table 7.1. According to these result, a decreasing thermal conductivity for thinner films can be derived, which is mainly caused by the decrease in average crystallite/grain sizes of the γ-CuI films and simultaneously increase in grain boundary scattering [2].

Figures 7.4(d) to (f) show spatially-resolved thermal conductivity images of the γ-CuI thin films with film thicknesses varied between 70 and 400 nm. Areas with low thermal conductivity values appear dark, whereas those with higher thermal conductivity values are bright in the 3ω Microscopy images. In order to determine the absolute local thermal conductivity $k_{f,local}$ value for every position within the corresponding 3ω Microscopy image, frequency-dependent differential 3ω measurements on two specific points (minimum $\Delta T_{2\omega,min}$ and maximum $\Delta T_{2\omega,max}$ temperature oscillation amplitudes) of the γ-CuI thin films were performed, as introduced above. In Figures 7.4(d) to (f), M1 and M2 indicate the positions where the frequency-dependent 3ω measurements have been performed. Measurement positions M1 and M2 are highlighted by green and violet arrows, respectively (see Figures 7.4(d) to (f)). At measurement positions M1 and M2, the absolute values of minimum and maximum local thermal conductivity of each γ-CuI film have been obtained, respectively.

The local thermal conductivity values of both the positions M1 and M2 of the thermal images were determined from two frequency-dependent temperature oscillation curves $\Delta T_{2\omega}(f)$, obtained from two selective differential 3ω measurements. The real parts of the amplitudes of the temperature oscillations $\Delta T_{2\omega}(f)$ measured using the thermo-resistive Pd/SiO_2 probe, as

a function of the AC heating current frequency f for the γ-CuI-film-on-Si-substrate samples, are illustrated in Figures 7.7(a) to (c).

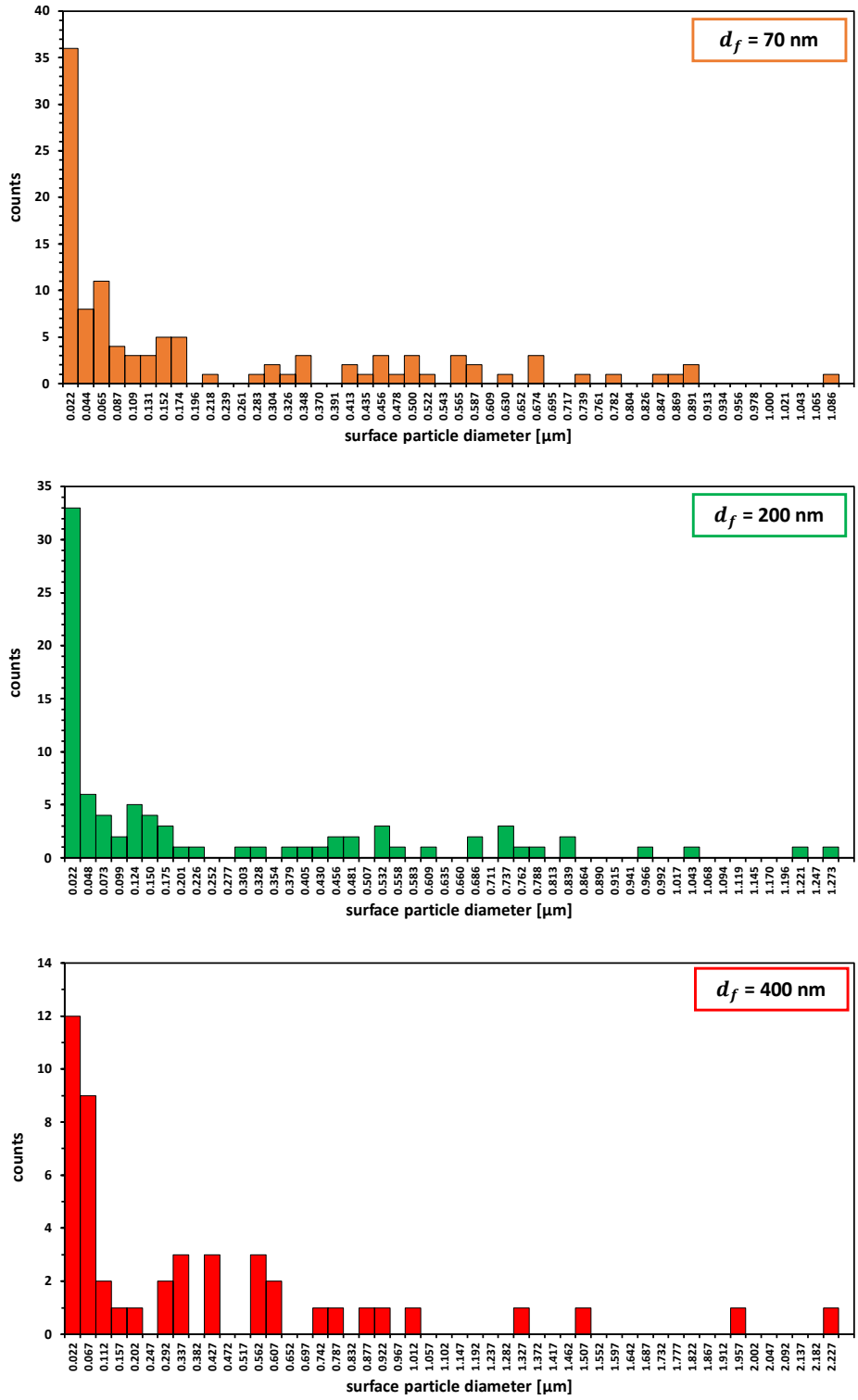

Figure 7.6: Film thickness dependency of the surface particle/crystallite diameter distributions obtained by AFM images of γ-CuI thin films with film thicknesses varied between 70 and 400 nm using the NanoScope Analysis software.

The dashed lines represent the analytical fits performed based on the experimental data of measurement positions M1 (minimal thermal conductivity: filled green diamonds) and M2 (maximum thermal conductivity: filled violet squares). For the thickness-dependent measurements, the heating frequency of the Pd/SiO_2 probe was limited to a range from 100 to 2500 Hz, to confine the oscillation of the generated thermal wave well within the γ-CuI/Si structure (see Section 4.3.2.4).

Firstly, the k_s-value of the Si substrate must be calculated, in order to set the ΔT_f reference for the differential 3ω method. The thermal conductivity of the Si substrate obtained by Eq. (3.25) is 141 $Wm^{-1}K^{-1}$, which is in a good agreement with experimental values obtained by the conventional macroscopic 3ω method (see Sections 5.2.1 and 6.2.2.1). The determined reference amplitudes of the temperature oscillations (using Eq. (3.22)), are associated with the bare Si substrate (solid line). As can be observed in Figures 7.7(a) to (c), the diffusion of thermal oscillation into the γ-CuI films at positions M1 and M2 produces a frequency-independent temperature rise $\Delta T_{f,M1}$ and $\Delta T_{f,M2}$ through the Pd/SiO_2 probe, which decreases with the thermal conductivity of the γ-CuI films. The offsets between the temperatures corresponding to the determined Si substrate (solid line) and experimental data (dashed lines) are the temperature rises ($\Delta T_{f,M1}$ and $\Delta T_{f,M2}$) generated by the γ-CuI thin films with different film thicknesses. The gradual increment of these offsets indicates that thermal resistance and maximum local thermal conductivities $k_{f,M2}$ of the γ-CuI increase as the film thickness d_f increases.

To obtain the local cross-plane thermal conductivities of the γ-CuI thin film at measurement positions M1 and M2, their thermal properties have to be extracted by the differential 3ω approach, as demonstrated in Section 3.3.2.1.

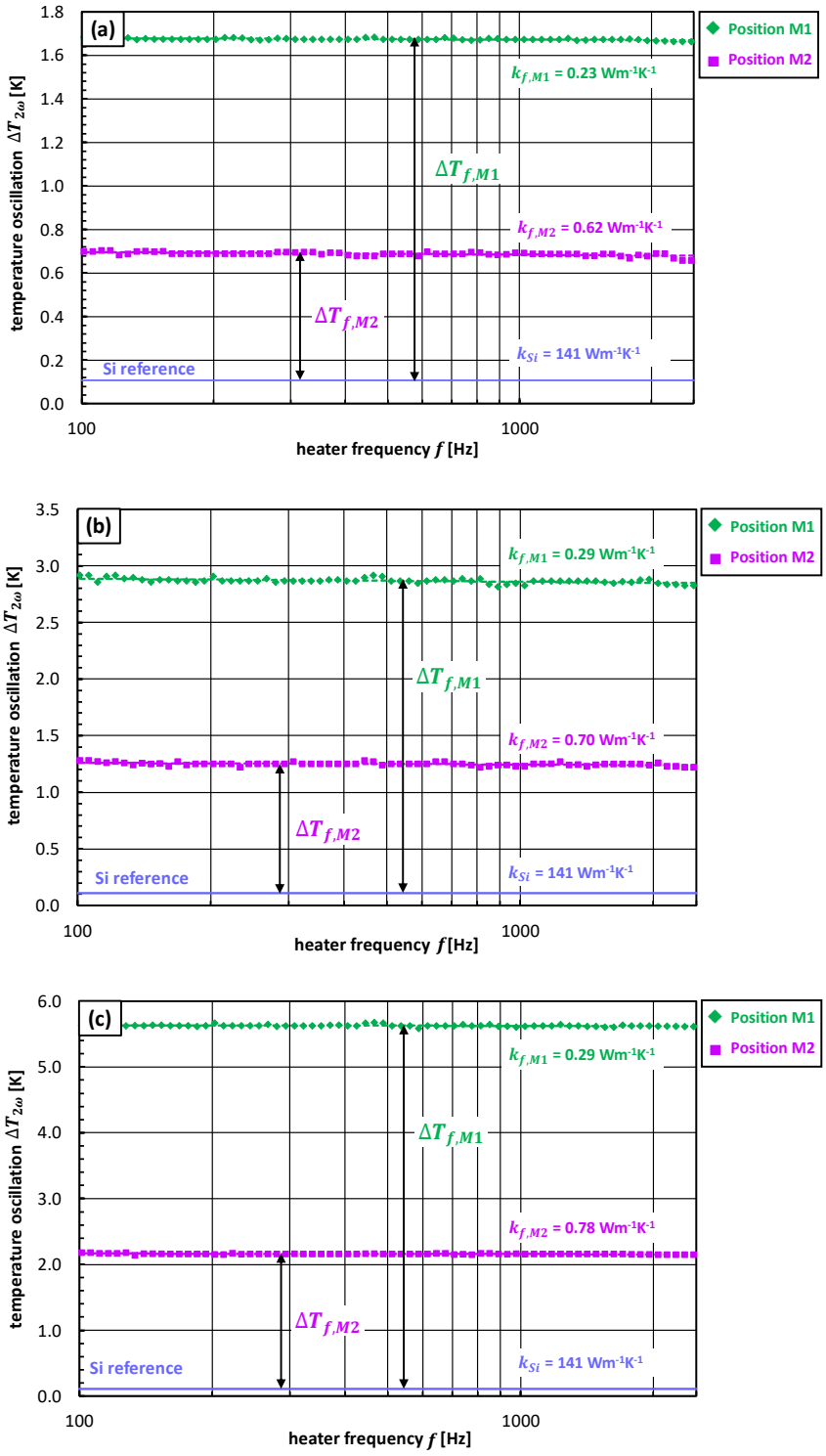

Figure 7.7: The temperature oscillation amplitudes $\Delta T_{2\omega}$ for the Si substrate and γ-CuI film-on-substrate structures with γ-CuI film thicknesses d_f of (a) 70 nm, (b) 200 nm and (c) 400 nm. The dashed lines represent the temperature oscillation amplitudes at positions M1 and M2, indicating the absolute minimum and maximum thermal conductivity of the γ-CuI/Si film-on-substrate structures, which are experimentally measured by the 3ω Microscopy technique. The solid line represents the corresponding temperature amplitude of the Si substrate, obtained by Eq. (3.22).

These results have been used to co-relate every position in the thermal 3ω Microscopy images with an absolute local thermal conductivity value, as depicted in Figures 7.4(d) to (f). The values at positions M1 and M2 represent minimum and maximum local thermal conductivity values of the γ-CuI films with the film thicknesses varied between 70 and 400 nm, respectively.

Table 7.1: Experimental results of minimum and maximum local cross-plane thermal conductivity $k_{f,M1/2}$ values of γ-CuI thin films obtained by selective differential 3ω Microscopy measurements to enable the quantitative analysis of local thermal conductivity distributions. Average surface particle/crystallite diameter values of γ-CuI films determined by AFM analysis as a function of film thickness.

No.	Film thickness d_f [nm]	Absolute local thermal conductivity value [$Wm^{-1}K^{-1}$]		Average surface particle diameter value (AFM) [nm]
		minimum $k_{f,M1}$	maximum $k_{f,M2}$	
16	70	0.23	0.62	217
17	200	0.29	0.70	251
18	400	0.29	0.78	395

The determined local minimum and maximum cross-plane thermal conductivity values of γ-CuI thin films were obtained by averaging the thermal conductivity values over three 3ω Microscopy measurements for each γ-CuI film. The maximum deviation of the determined values of these three measurements was below 3.1% for each sample. The random errors of the 3ω Microscopy measurements for a given γ-CuI film, based on the assumptions mentioned in Section 4.3.2.4, were found to be better than 3% in all cases. About 15% of the performed 3ω Microscopy measurements could not be utilized for the evaluation of the local thermal conductivity data due to tip-wearing and contact problems between the thermo-resistive Pd/SiO_2 probe and the thin film samples.

In order to compare the local thermal conductivity results obtained by the 3ω Microscopy method with the experimental cross-plane thermal conductivity data determined by the conventional macroscopic 3ω method presented in Section 6.2.2.1, the local conductivity

values have been averaged over the whole investigated scan-area (5 µm × 5 µm) for the γ-CuI thin films. Table 7.2 lists the experimental results of the averaged values of thermal conductivities for the γ-CuI films, obtained by the 3ω Microscopy method ($\bar{k}_{f,local}$) and the macroscopic 3ω method ($k_{f.macro}$), as a function of the film thickness d_f at room temperature.

The average cross-plane thermal conductivity values of the γ-CuI films with thicknesses varied from 70 to 400 nm are between 0.38 and 0.50 $Wm^{-1}K^{-1}$ obtained from the 3ω Microscopy method, and between 0.45 and 0.56 $Wm^{-1}K^{-1}$ obtained from the macroscopic 3ω method. Results listed in Table 7.2 indicate that the macroscopic thermal conductivity values of the γ-CuI thin films are in good agreements with those from the 3ω Microscopy ones. The average thermal conductivities obtained by the 3ω Microscopy method are between 5.9% and 15.5% below the values measured from the macroscopic 3ω method but have an almost identical data progression. These minor variations are still good enough for the first approach of quantitative measurements of the local thin film thermal conductivity.

Table 7.2: Experimental results of the cross-plane thermal conductivity of γ-CuI thin films obtained by the 3ω Microscopy and macroscopic 3ω method, as a function of film thickness.

No.	Film thickness d_f [nm]	Cross-plane thermal conductivity value [$Wm^{-1}K^{-1}$]	
		3ω Microscopy $\bar{k}_{f,local}$	Macroscopic 3ω method $k_{f\perp}$
16	70	0.38 ± 0.011	0.45 ± 0.011
17	200	0.48 ± 0.014	0.51 ± 0.013
18	400	0.50 ± 0.015	0.56 ± 0.016

Moreover, the experimental thermal conductivity values are lower than that of glass [14] or a phonon-liquid material like Cu_2Se [15] (which was reported to be about 1.0 $Wm^{-1}K^{-1}$ at room temperature). As mentioned in Section 6.2.2.1, such a low thermal conductivity value is associated with heavy element iodine, which leads to a strong phonon-scattering at grain boundaries due to the polycrystalline structure of the γ-CuI thin films [2].

Figure 7.8 illustrates that a change of the local thermal conductivity $k_{f,local}$ is dependent on the film thickness d_f of the γ-CuI film, which confirms the experimental results obtained by the macroscopic 3ω method in Section 6.2.2.1. Therefore, we can conclude that our new 3ω Microscopy approach is applicable to quantitatively determine the topography and local thermal conductivity of thin film materials, such as γ-CuI with a spatial resolution in the sub-micrometer range.

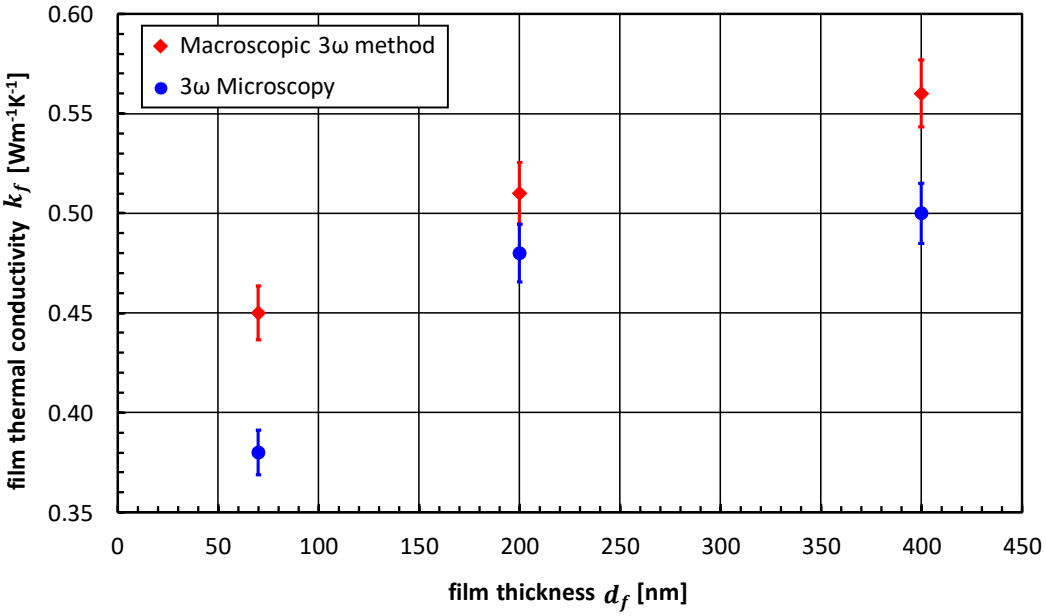

Figure 7.8: Local thermal conductivity results obtained by 3ω Microscopy and the experimental cross-plane thermal conductivity values determined by the conventional macroscopic 3ω method of γ-CuI thin films as a function of film thickness. The diamonds represent the experimental data of the macroscopic 3ω method and the circles the 3ω Microscopy data at room temperature.

In the following we will discuss experimentally obtained local thermal conductivity data shown in Figures 7.4(d) to (f). Figures 7.4(d) to (f) illustrate that the local thermal properties of thermoelectric γ-CuI thin films are strongly related to the film thickness, which supports the experimental data and discussions above. The areas of regions with higher thermal conductivity values are significantly larger as the film thickness increases, which can be verified by the average film thermal conductivity values $\bar{k}_{f,local}$ listed in Table 7.2 as function of film thickness d_f.

Furthermore, the triangular-shaped crystallite structures, identified in the topography images (see Figures 7.4(a) to (c)) have also been detected from the thermal images. The triangular-shaped structures are highlighted by dashed triangles in both topography and thermal images. Figures 7.4(d) to (f) illustrate that heat transport takes place predominantly at the boundaries of these triangular structures and changes considerably as the film thickness increases. The 70 nm thick γ-CuI film shows very narrow and contorted paths of high thermal conductivity, whereas the 400 nm thick γ-CuI film offers extremely broad and straight paths of high thermal conduction, leading to a higher average film thermal conductivity, as illustrated in Figure 7.8. In Figures 7.4(d) to (f), the high thermal conductive paths are indicated by the devious red lines. The narrow and contorted highly thermal conductive paths show an increased potential in phonon-scattering, compared to wide and straight high conductive paths, which could result in an impaired and reduced thermal conduction.

Furthermore, Figures 7.9(a) to (c) compare the local thermal conductivity and topography data obtained by vertical line measurements (see dashed blue and red colored lines in the topography and thermal images, respectively). Figures 7.9(a) to (c) show that the local thermal conductivities are normally higher at positions with small heights, which are the boundaries between triangular crystallites. Some of these regions have been highlighted by arrows in Figures 7.9(a) to (c). Moreover, the average local thermal conductivity values of $\bar{k}_{f,line}$ along the vertical line measurements (see red colored dashed lines in Figures 7.9(a) to (c)) are in good agreements with the average film conductivity values $\bar{k}_{f,local}$, listed in Table 7.2. On the basis of the experimental results of the 3ω Microscopy technique, it can be concluded that the decreased thermal conductivity of the γ-CuI thin films with decreased film thickness is mainly caused by the decreases in both the average surface crystallite (see AFM surface particle analysis in Figure 7.5 and Figure 7.6) and grain size. The grain size significantly affects the thermal conductivity due to the grain boundary scattering, because a smaller grain size could decrease the thermal conductivity of the film due to the shorter phonon MFP [2,16–18].

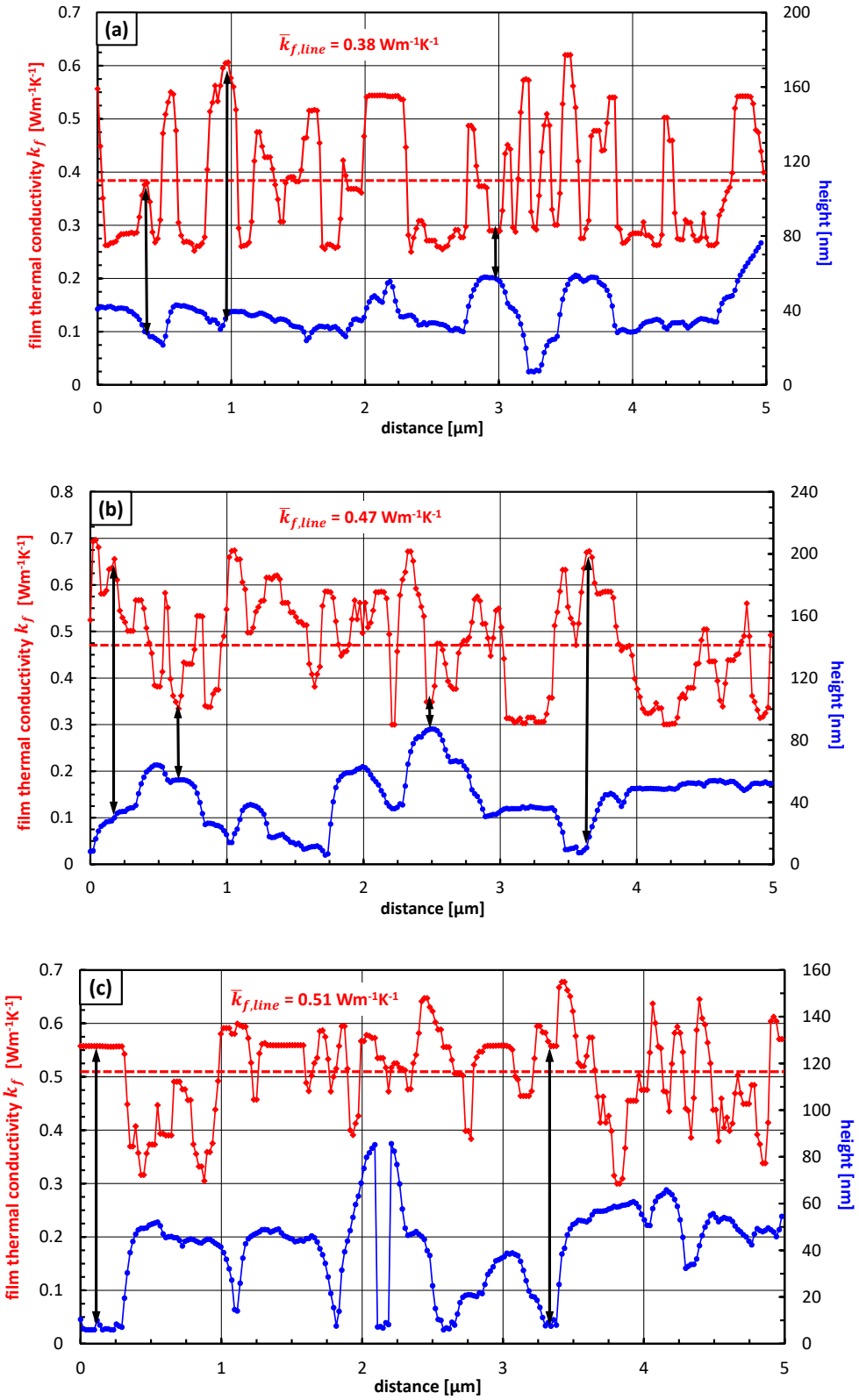

Figure 7.9: Vertical line scans, indicated by blue and red colored dashed lines in Figures 7.4(a) to (f) representing the topography data and local thermal conductivity values of (a) 70 nm, (b) 200 nm and (c) 400 nm thin γ-CuI films, respectively. The red colored dashed line represent the film thermal conductivity value $\bar{k}_{f,line}$ averaged of the line scan in Figures 7.4(d) to (f).

7.2.3. Quantitative local thermal conductivity of AlN thin films

After the investigation of the γ-CuI thin films provided in the previous section, the following discussions will be focused on the local cross-plane thermal conductivity measurements of AlN thin films deposited on Si substrates. Figure 7.10 shows the images of spatially-resolved topography (a-c) and local thermal conductivity (d-f) of AlN thin films with film thickness varied between 304 and 710 nm. The 3ω Microscopy measurements were performed with a scan area of 1 μm × 1 μm (with 512 lines) at a scan rate of 1 Hz and under vacuum conditions (pressure < 4.0 Pa), in order to reduce convection losses of the thermo-resistive probe.

Figures 7.10(a) to (c) present the AFM images showing the surface morphologies of the AlN films with various thicknesses of (a) 304, (b) 511, and (c) 710 nm. The studied AlN films have smooth surfaces and uniform round-shaped surface particle (see dotted circles in Figures 7.10(a) to (c). Figures 7.11(a) to (c) also illustrate the AFM images showing the surface particle/crystallite size distributions of the 304, 511, and 710 nm AlN films. Similar to experimental results of the γ-CuI films, it is observable that the particle diameter decreases as the film thickness is decreased. The average surface particle/crystallite diameters for the AlN films with film thicknesses of 304, 511, and 710 nm are 73, 100 and 108 nm, respectively. The average surface particle diameter value of the 511 nm film is in good agreement (3% higher) with the value presented in Section 5.2.3 of Chapter 5. At a different scanning position but equal scanning size (1 μm × 1 μm) on the surface of the same AlN films, the corresponding values of the 304 and 710 nm vary between 56% and 65%.

The evolution of the surface crystallite/particle diameters as a function of AlN film thickness is summarized in Figure 7.12 and Table 7.3. According to these results, a decreasing thermal conductivity for thinner films can be derived, which is mainly caused by the decrease in average crystallite/grain sizes of the AlN films and simultaneously increase in grain boundary scattering [1,16–18].

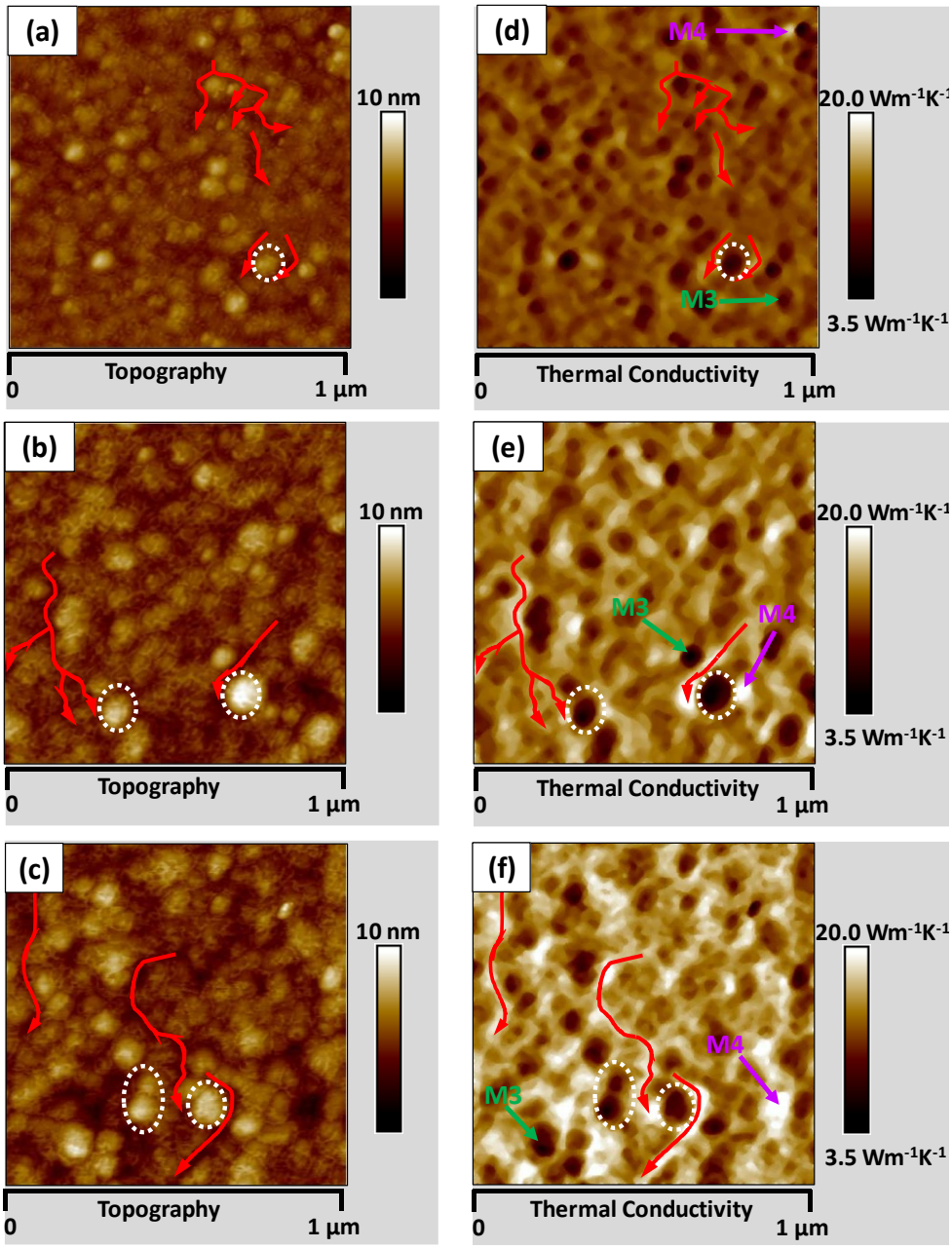

Figure 7.10: (a-c) Topography AFM and (d-f) local thermal conductivity images of AlN thin films with different thicknesses of (a) and (d) 304 nm; (b) and (e) 511 nm; (c) and (f) 710 nm deposited on a Si (100) substrate, revealing the surface morphology and local cross-plane thermal conductivity values of the AlN thin films. The 3ω Microscopy measurements were carried out at heating frequency of 1000 Hz with scan area of 1 µm × 1 µm by 512 lines at a scan rate of 1 Hz, under vacuum conditions (pressure < 4.0 Pa). The studied AlN films have uniform round-shaped surface particles, which are indicated by the dotted lines.

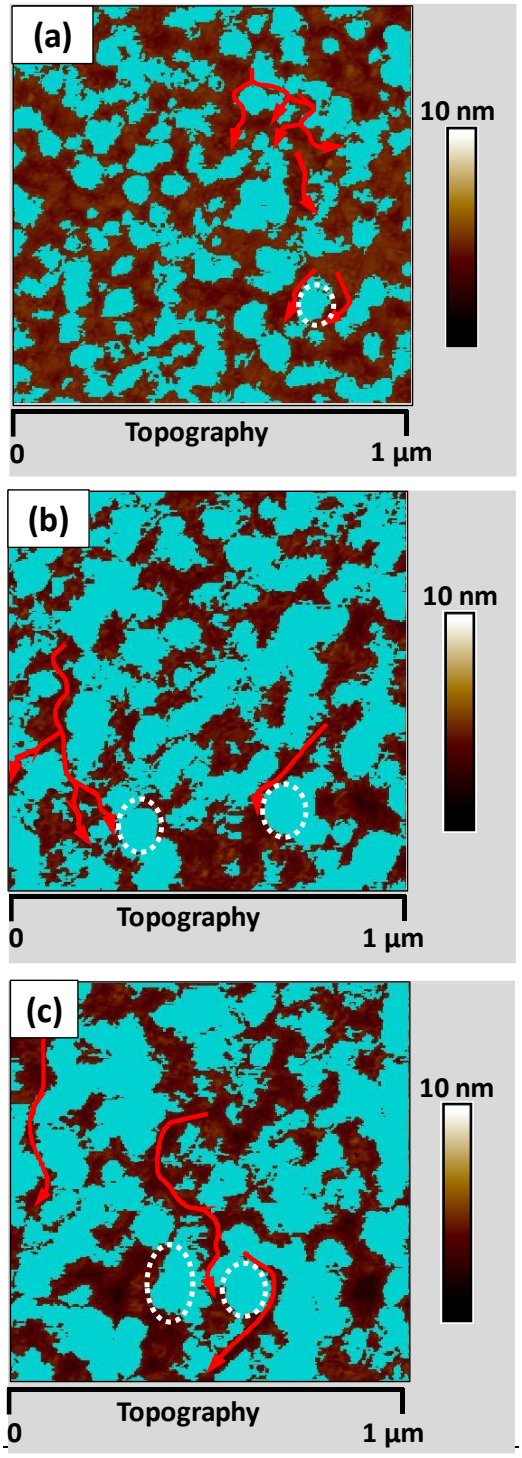

Figure 7.11: AFM images of AlN films deposited on Si substrates with film thicknesses of (a) 304 nm, (b) 511 nm and (c) 710 nm to study the surface particle/crystallite distribution and average particle/crystallite diameter. The distribution of the surface particles/crystallites are highlighted in blue by the NanoScope Analysis software.

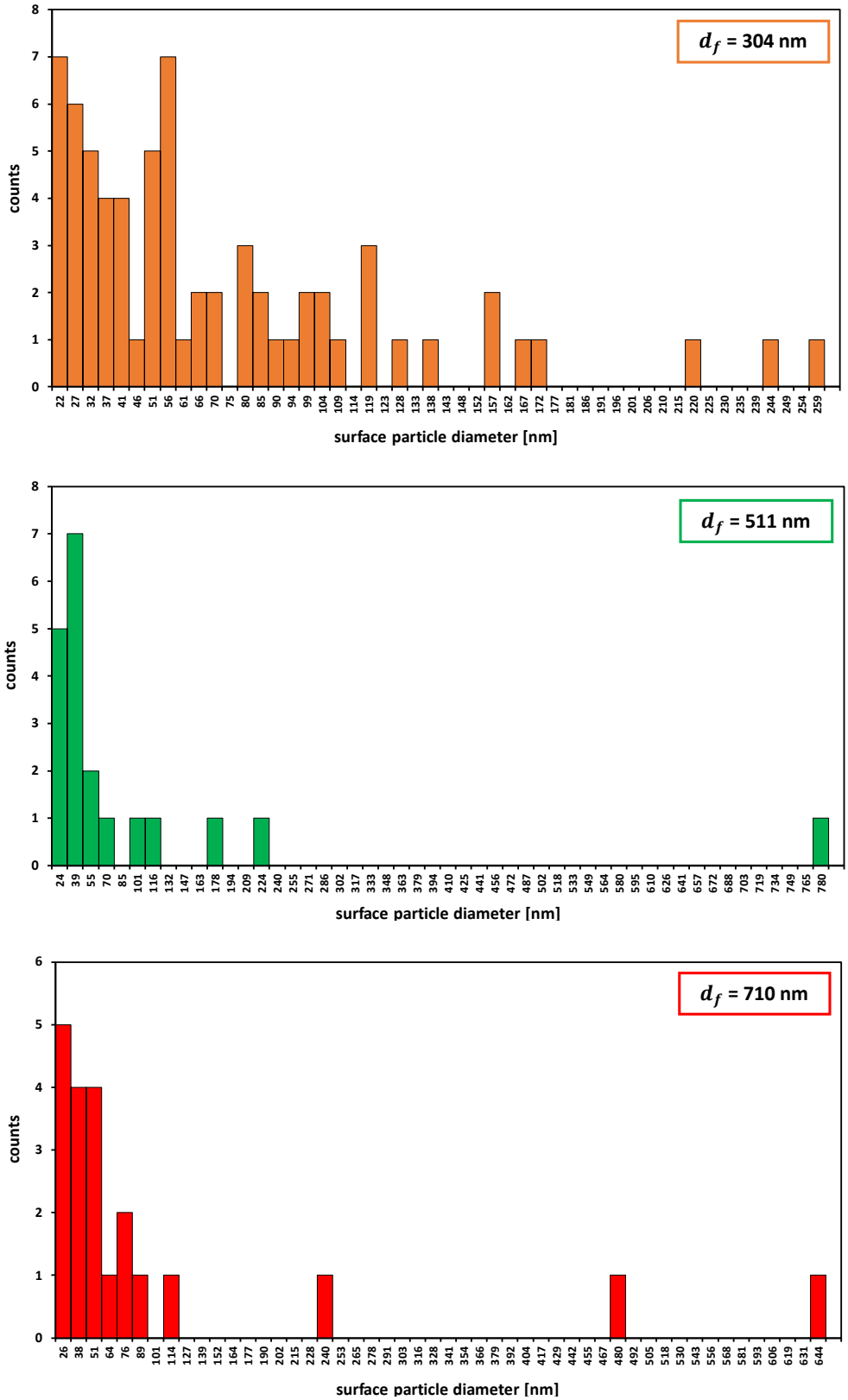

Figure 7.12: Film thickness dependency of the surface particle/crystallite diameter distributions obtained by AFM images of AlN thin films with film thicknesses varied between 304 and 710 nm using the NanoScope Analysis software.

Figures 7.10(d) to (f) illustrate spatially-resolved thermal conductivity images of the AlN thin films with film thickness varied between 304 and 710 nm. The real parts of the amplitudes of the temperature oscillations $\Delta T_{2\omega}(f)$, measured using the thermo-resistive Pd/SiO_2 probe, as a function of the AC heating current frequency f for the AlN-film-on-Si-substrate samples, are illustrated in Figures 7.13(a) to (c). As can be seen in Figures 7.13(a) to (c), the diffusion of thermal oscillation into the AlN films at positions M3 and M4 produces a frequency-independent temperature rise $\Delta T_{f,M3}$ and $\Delta T_{f,M4}$ through the Pd/SiO_2 probe, which decreases with increasing thermal conductivity. The offsets between the temperatures corresponding to the determined Si substrate (solid line) and experimental data (dashed lines) are the temperature rises ($\Delta T_{f,M3}$ and $\Delta T_{f,M4}$) generated by the AlN thin films with different film thicknesses. The gradual increment of these offsets indicates that both minimum $k_{f,M3}$ and maximum $k_{f,M4}$ local thermal conductivities of the AlN increase as the film thickness d_f increases.

To obtain the local cross-plane thermal conductivities of the γ-CuI thin film at measurement positions M3 and M4 their thermal properties have to be extracted by the differential 3ω approach, as demonstrated in Section 7.2.2. The obtained thermal conductivity values $k_{f,M3}/k_{f,M4}$ at positions M3 and M4 of the AlN thin films are listed in Table 7.3 and are between 4.4 $Wm^{-1}K^{-1}$ and 19.7 $Wm^{-1}K^{-1}$, respectively. These results have been used to co-relate every position in the thermal 3ω Microscopy images with an absolute local thermal conductivity value, as depicted in Figures 7.10(d) to (f).

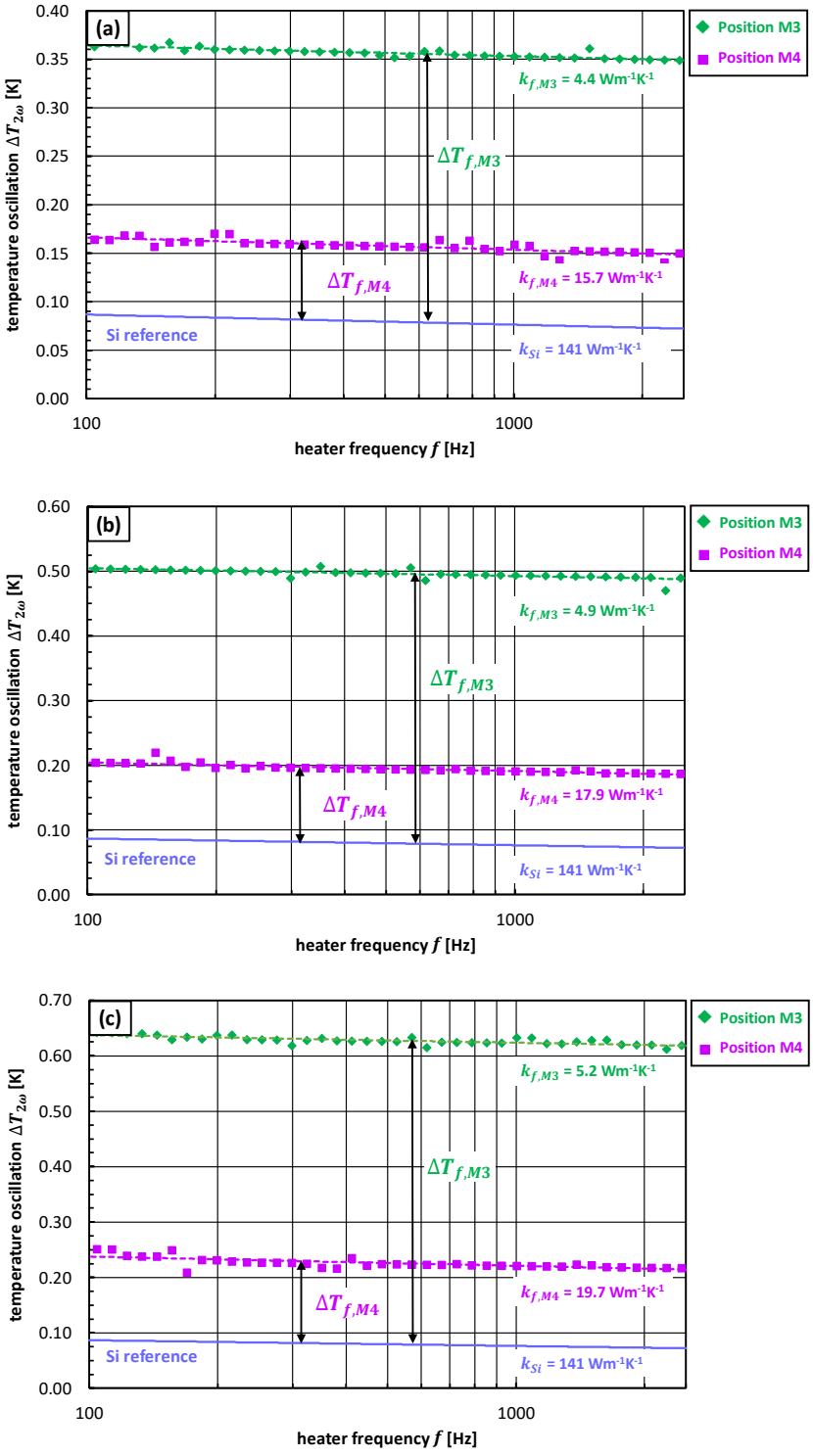

Figure 7.13: The temperature oscillation amplitudes $\Delta T_{2\omega}$ for the Si substrate and AlN film-on-substrate structures with AlN film thicknesses d_f of (a) 304 nm, (b) 511 nm and (c) 710 nm. The dashed lines represent the temperature oscillation amplitudes at positions M3 and M4, indicating the absolute minimum and maximum thermal conductivity of the AlN/Si film-on-substrate structures, which are experimentally measured by the 3ω Microscopy technique. The solid line represents the corresponding temperature amplitude of the Si substrate, obtained by Eq. (3.22).

Table 7.3: Experimental results of minimum and maximum local cross-plane thermal conductivity $k_{f,M3/4}$ values of AlN thin films obtained by selective differential 3ω Microscopy measurements to enable the quantitative analysis of local thermal conductivity distributions. Average surface particle/crystallite diameter values of AlN films determined by AFM analysis as a function of film thickness.

No.	Film thickness d_f [nm]	Absolute local thermal conductivity value [$Wm^{-1}K^{-1}$]		Average surface particle diameter value (AFM) [nm]
		minimum $k_{f,M3}$	maximum $k_{f,M4}$	
12	304	4.4	15.7	73
13	511	4.9	17.9	100
14	710	5.2	19.7	108

The determined local minimum and maximum cross-plane thermal conductivity values of AlN thin films were obtained by averaging the thermal conductivity values over three 3ω Microscopy measurements for each AlN film. The maximum deviation of the determined values of these three measurements was below 3.8% for each sample. The random errors of the 3ω Microscopy measurements for a given AlN film, based on the assumptions mentioned in Section 4.3.2.4, were found to be better than 3% in all cases.

In order to compare the local thermal conductivity results obtained by the 3ω Microscopy method with the experimental cross-plane thermal conductivity data determined by the conventional macroscopic 3ω method presented in Section 5.2.2, the local conductivity values have been averaged over the whole investigated scan-area (1 μm × 1 μm) for the AlN thin films. Table 7.4 lists the experimental results of the averaged values of thermal conductivities for the AlN films, obtained by the 3ω Microscopy method ($\bar{k}_{f,local}$) and the macroscopic 3ω method ($k_{f.macro}$), as a function of the film thickness d_f at room temperature.

Table 7.4 shows that average cross-plane thermal conductivity values of the AlN films with thicknesses varied from 304 to 710 nm are between 8.1 and 11.1 $Wm^{-1}K^{-1}$ obtained from the 3ω Microscopy method, and between 8.5 and 13.2 $Wm^{-1}K^{-1}$ obtained from the macroscopic 3ω method. The average film thermal conductivities obtained by the 3ω Microscopy method

are between 4.7% and 15.9% smaller than values measured from the macroscopic 3ω method. Figure 7.14 demonstrates that the average thermal conductivity values of both 3ω techniques have an almost identical data progression. This difference is mainly caused by the value of the dissipated heating power, which was assumed to be slightly to low, as the thermal conductivity of the AlN film is directly at the transition region between a constant and a thermal conductivity-dependent heating power value (see Figure 7.3). However, theses minor variations are still good enough for the first approach of quantitative measurements of the local thermal conductivity of AlN films.

Table 7.4: Experimental results of the cross-plane thermal conductivity of AlN thin films obtained by the 3ω Microscopy and macroscopic 3ω method, as a function of film thickness.

No.	Film thickness d_f [nm]	Cross-plane thermal conductivity value [$Wm^{-1}K^{-1}$]	
		3ω Microscopy $\bar{k}_{f,local}$	Macroscopic 3ω method $k_{f\perp}$
12	304	8.1 ± 0.24	8.5 ± 0.22
13	511	9.4 ± 0.28	11.0 ± 0.33
14	710	11.1 ± 0.33	13.2 ± 0.40

Figure 7.14 illustrates that a change of the local thermal conductivity $k_{f,local}$ is dependent on the film thickness d_f of the AlN film, which confirms the experimental results obtained by the macroscopic 3ω method within Section 5.2.2. Finally, we can conclude that our new 3ω Microscopy approach is applicable to quantitatively map the topography and local thermal conductivity of thin film materials, such as AlN with a spatial resolution in the sub-micrometer range. However, the 3ω Microscopy technique is limited to the assumption of a constant dissipated heating power, which is independent from the thin film's thermal conductivity value. For future work the thermal conductivity-dependent heating power function $P_l(k_f)$ has to be analyzed more extensively and then included in the data evaluation of the 3ω Microscopy method.

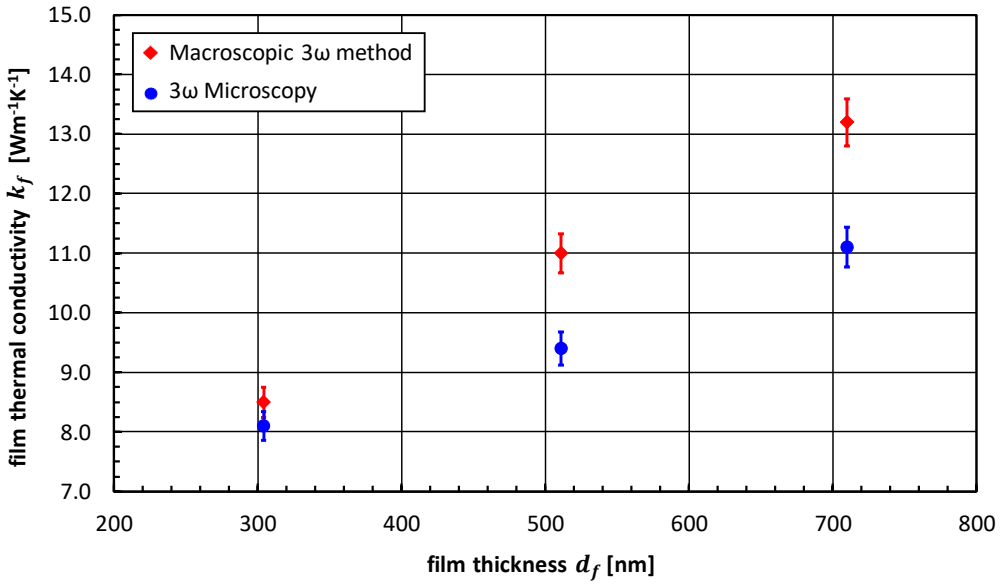

Figure 7.14: Local thermal conductivity results obtained by 3ω Microscopy and the experimental cross-plane thermal conductivity values determined by the conventional macroscopic 3ω method of AlN thin films as a function of film thickness. The diamonds represent the experimental data of the macroscopic 3ω method and the circles the 3ω Microscopy data at room temperature.

In the following we will discuss experimentally obtained local thermal conductivity data shown in Figures 7.10(d) to (f). Figures 7.10(d) to (f) illustrate that the local thermal properties of AlN thin films are strongly related to the film thickness, which supports the experimental data and discussions for γ-CuI films above. The areas of regions with higher thermal conductivity values are significantly larger as the film thickness increases, which can be verified by the average film thermal conductivity values $\bar{k}_{f,local}$ listed in Table 7.4 as function of film thickness d_f.

Furthermore, the round-shaped crystallite structures at the surface, identified in the topography images (see Figures 7.10(a) to (c)), have also been detected from the thermal images. These structures are highlighted by dashed circles in both topography and thermal images. Figures 7.10(d) to (f) illustrate that heat transport takes place predominantly between the boundaries of these surface structures and changes considerably as the film thickness increases. The 304 nm thick AlN film shows narrow and short contorted paths of high thermal conductivity, whereas the 511 and 710 nm thin AlN films show wide, long and straight paths

of high thermal conduction, leading to a significantly higher average film thermal conductivity, as illustrated in Figure 7.14. In Figures 7.10(d) to (f), the high thermal conductive paths are indicated by the devious red lines. The narrow and contorted highly thermal conductive paths show an increased potential in phonon-particle and phonon-boundary scattering, compared to wide and straight high conductive paths, which could result in an impaired and reduced thermal conduction, similar to experimental results obtained for γ-CuI films.

7.3. Summary

This chapter presents a novel 3ω Microscopy technique to quantitatively determine the local cross-plane thermal conductivities of thin-film-on-substrate systems. In order to satisfy the demand for high-spatially resolving techniques to quantitatively analyze thin film materials concerning their local thermal characteristic, the macroscopic 3ω method has been transferred to the microscopic level by combining the AFM with our extended differential 3ω method, which has never been reported in literature before.

The key parameter for the quantitative thermal conductivity determination is the heating power which is dissipated into the thin film sample. It is crucial to determine the absolute local thermal conductivity $k_{f,local}$ value for every position within the corresponding 3ω Microscopy image and thereby enable the quantitative thermal conductivity analysis. An experimental method was demonstrated to obtain the rms value of the heating power. This experimental approach has been verified by the 3ω Microscopy measurement performed on BCR-724 reference samples. The experimental results were in good agreements with values obtained by the macroscopic 3ω method within this thesis.

The main focus of this study was to investigate the thickness-dependency of local thermal conductivities of novel thermoelectric γ-CuI and AlN thin films with film thicknesses varied between 70 - 400 nm and 304 - 710 nm using the 3ω Microscopy technique. It is the first time that the local thermal conductivities of γ-CuI and AlN thin films were quantitatively measured

as a function of film thickness. The spatially-resolved 3ω Microscopy images demonstrated that heat transport predominantly takes place at the boundaries of triangular-shaped γ-CuI and round-shaped AlN structures and considerably changes as the film thickness increases. The thinnest γ-CuI and AlN films showed narrow and contorted paths of high thermal conductivity, whereas the thicker γ-CuI and AlN films showed very broad and straight paths of high thermal conduction, leading to higher average film thermal conductivity values. The narrow and contorted high thermal conductive paths show an increased potential in phonon-scattering, compared to wide and straight high conductive paths, which resulted in an impaired and reduced thermal conduction.

Furthermore, the average film thermal conductivity values obtained by 3ω Microscopy are in good agreements with cross-plane values, measured using the macroscopic 3ω technique (presented in Chapter 5 and 6). Moreover, the experimental results have shown that the local thermal conductivity values of the γ-CuI thin films were lower than that of glass. Such low cross- and in-plane thermal conductivity values at room temperature can be associated with heavy element iodine, which leads to a strong phonon-scattering at grain boundaries due to the polycrystalline structure of the γ-CuI thin films. These low thermal conductivity values are also extremely beneficial for the thermoelectric properties of γ-CuI thin films, which are leading to a high thermoelectric figure of merit. Additionally, the film thermal conductivity values of both the 3ω Microscopy and macroscopic 3ω method decrease with decreasing film thickness d_f. According to these results, it can be concluded that the novel 3ω Microscopy is capable to simultaneously determine the topography and absolute local thermal conductivity of low and medium thermal conductive thin films, such as γ-CuI and AlN within a spatial resolution in the sub-micrometer range.

Finally, this chapter shows that the 3ω Microscopy extends the research field of thin film thermal characterization techniques. It combines the advantageous of both conventional 3ω method and AFM technology to quantitatively study the heat transport of thin film materials. The 3ω Microscopy has been proven to provide additional experimental findings, which

cannot be identified or detected by conventional thermal characterization methods like SThM or the macroscopic 3ω technique. Furthermore, not only its spatially-resolved quantitative local thermal characterization, but also its nondestructive characteristic and the fact that a preliminary sample preparation is not needed, making the 3ω Microscopy a promising and alternative thermal characterization method.

Future investigations could consist of mapping both local cross- and in-plane thermal conductivity values as a function of film thickness using suspended thin film samples. Another interesting point would to quantitatively study both local electrical and thermal properties of thermoelectric γ-CuI, in order to provide local thermoelectric properties or ZT-values that could help to improve the properties of innovative thermoelectric devices at room temperature.

7.4. References

[1] M. Bogner, A. Hofer, G. Benstetter, H. Gruber, R.Y. Fu, Differential 3ω method for measuring thermal conductivity of AlN and Si3N4 thin films, Thin Solid Films 591 (2015) 267–270.

[2] C. Yang, D. Souchay, M. Kneiß, M. Bogner, H.M. Wei, M. Lorenz, O. Oeckler, G. Benstetter, Y.Q. Fu, M. Grundmann, Transparent flexible thermoelectric material based on non-toxic earth-abundant p-type copper iodide thin film, Nature communications 8 (2017) 16076.

[3] S. Gomès, A. Assy, P.O. Chapuis, Scanning thermal microscopy: A review, Physica status solidi A 212 (3) (2015) 477–494.

[4] M. Grecki, J. Pacholik, B. Wiecek, A. Napieralski, Application of computer-based thermography to thermal measurements of integrated circuits and power devices, Microelectronics Journal 28 (3) (1997) 337–347.

[5] D. Zhao, X. Qian, X. Gu, S.A. Jajja, R. Yang, Measurement Techniques for Thermal Conductivity and Interfacial Thermal Conductance of Bulk and Thin Film Materials, Journal of Electronic Packaging 138 (4) (2016) 40802.

[6] D.G. Cahill, Thermal conductivity measurement from 30 to 750 K: The 3ω method, Review of Scientific Instruments 61 (2) (1990) 802–808.

[7] S.M. Lee, D.G. Cahill, Heat transport in thin dielectric films, Journal of Applied Physics 81 (6) (1997) 2590–2595.

[8] A. Altes, R. Heiderhoff, L.J. Balk, Quantitative dynamic near-field microscopy of thermal conductivity, Journal of Physics D: Applied Physics 37 (6) (2004) 952–963.

[9] G.B.M. Fiege, A. Altes, R. Heiderhoff, L.J. Balk, Quantitative thermal conductivity measurements with nanometre resolution, Journal of Physics D: Applied Physics 32 (5) (1999) 13-17.

[10] D. Salmon, G. Roebben, A. Lamberty, R. Brandt, Certification of thermal conductivity and thermal diffusivity up to 1025 K of a glass-ceramic reference material BCR-724, European Commission: Directorate-General Joint Research Centre-Institute for Reference Materials and Measurements (2007) 66-67.

[11] M. Grundmann, F.L. Schein, M. Lorenz, T. Böntgen, J. Lenzner, H. von Wenckstern, Cuprous iodide: A p-type transparent semiconductor, history, and novel applications, Physica status solidi A (2013) 1671-1703.

[12] C. Yang, M. Kneiss, F.L. Schein, M. Lorenz, M. Grundmann, Room-temperature Domain-epitaxy of Copper Iodide Thin Films for Transparent CuI/ZnO Heterojunctions with High Rectification Ratios Larger than 10(9), Scientific reports 6 (2016) 21937.

[13] C. Yang, M. Kneibeta, M. Lorenz, M. Grundmann, Room-temperature synthesized copper iodide thin film as degenerate p-type transparent conductor with a boosted figure of merit, Proceedings of the National Academy of Sciences of the United States of America 113 (46) (2016) 12929–12933.

[14] R.W. Powell, C.Y. Ho, P.E. Liley, Thermal Conductivity of Selected Materials, National Standard Reference Data System-National Bureau of Standards 8 (1966) 89–91.

[15] H. Liu, X. Shi, F. Xu, L. Zhang, W. Zhang, L. Chen, Q. Li, C. Uher, T. Day, G.J. Snyder, Copper ion liquid-like thermoelectrics, Nature materials 11 (5) (2012) 422–425.

[16] S.R. Choi, D. Kim, S.-H. Choa, S.-H. Lee, J.-K. Kim, Thermal Conductivity of AlN and SiC Thin Films, International Journal of Thermophysics 27 (3) (2006) 896–905.

[17] T.S. Pan, Y. Zhang, J. Huang, B. Zeng, D.H. Hong, S.L. Wang, H.Z. Zeng, M. Gao, W. Huang, Y. Lin, Enhanced thermal conductivity of polycrystalline aluminum nitride thin films by optimizing the interface structure, Journal of Applied Physics 112 (4) (2012) 44905.

[18] J. Jaramillo-Fernandez, J. Ordonez-Miranda, E. Ollier, S. Volz, Tunable thermal conductivity of thin films of polycrystalline AlN by structural inhomogeneity and interfacial oxidation, Physical chemistry chemical physics 17 (12) (2015) 8125–8137.

Chapter 8: Conclusions and Future Work

8.1. Conclusions

For most micro- and nanoelectronic devices based on thin films applied in effective heat dissipation and thermoelectric devices for energy harvesting, thermal management is a critical topic for their performance and reliability. Therefore, this thesis focused on the investigations of cross- and in-plane thermal conductivities of both high- and low-thermal conductive thin film materials, i.e. AlN and γ-CuI. Highly thermal conductive AlN films, have been chosen for investigation as they are promising candidates for effective heat conductors in microelectronic devices. CuI films in their γ-phase, which exhibit low thermal conductivity values, have also been studied, because of their great interest in the field of novel thermoelectric applications.

The literature survey pointed out that thermal conductivities of thin films can be substantially different from those of their bulk counterparts, which is generally caused by oxygen impurities, dislocations, and grain boundary scattering. All these could affect the thermal conductivity of the films. These effects also influence cross- and in-plane heat conduction differently, so that the thermal conductivities of the thin films are generally anisotropic in these two directions. Therefore, in this thesis, experimental and theoretical analysis have been conducted to understand the effects of crystallinity, grain/surface crystallite sizes, and interfacial structures of AlN and γ-CuI films on their thermal conductivities as a function of film thickness. An improved differential multi-heater 3ω method was established and used to study the thickness-dependency of cross- and in-plane thermal conductivities of γ-CuI and AlN thin films sputtered on p-type doped Si substrates with film thicknesses varied between 70 – 400 nm and 100 – 1000 nm, respectively.

The thesis was also focused on thermal conductivity characterization techniques of thin films, especially for high-spatially resolving techniques to study the locally quantitative thermal characteristics, such as thermal conductivity. In order to meet this demand, our newly proposed 3ω Microscopy method, which combines the advantages of both the 3ω method and AFM technology, was applied to quantitatively measure the local thermal conductivities of γ-CuI and AlN thin films, with a spatial resolution in sub-micrometer range.

The main conclusions obtained from these investigations are summarized as follows:

(1) Cross- and in-plane thermal conductivities of film-on-substrate structures

Experimental results obtained by the improved multi-heater 3ω method revealed that both the cross- and in-plane thermal conductivities of AlN and γ-CuI thin films were drastically reduced compared to their bulk materials. The measured thermal conductivity values of the AlN and γ-CuI thin films were about 94% – 99% and 65% – 74% smaller than those of their bulk counterparts. Furthermore, the cross- and in-plane thermal conductivities of the AlN and γ-CuI thin films were strongly dependent on the film thickness, as film thermal conductivity values of both the cross- and in-plane directions decreased with the decrease in film thickness.

Both the XRD and AFM combined with the software-supported surface particle observation indicated that the average surface crystallite size of sputtered AlN and γ-CuI films decreased with the decrease in film thickness. According to these findings, the reduced thermal conductivity of the AlN and γ-CuI thin films with a smaller film thickness were primarily caused by the decrease in both average grain and surface crystallite size of the films.

However, theoretical analysis suggested that the difference of thermal conductivity values contributed by grain boundary scattering cannot fully describe the experimental data. It was considered that amorphous and disordered interfacial regions at the film-substrate interfaces, which have a much lower thermal conductivity than those of the

polycrystalline AlN and γ-CuI films, significantly influenced the heat conduction perpendicular to the thin films. The amorphous and disordered layer at the interface influenced the heat transport in the cross-plane direction of the investigated thin films. The results suggested that improving the interfacial properties could increase the heat conduction in the cross-plane direction and support the applications of AlN and γ-CuI thin films as effective heat conductor and thermoelectric layer in microelectronic devices, respectively.

- Additionally, this thesis showed that the AlN thin films can be utilized in micro- and nanoelectronic devices to replace traditional dielectric layers such as SiO_2 or Si_3N_4, and as an effective heat-conducting film owing to their significantly higher cross- and in-plane thermal conductivities (about 264% to 1255% higher for the same film thickness).

- One of the most critical properties for high thermoelectric conversion efficiencies of γ-CuI thin films, are their in- and cross-plane thermal conductivity values. Therefore, one main goal of this thesis was to study the in- and cross-plane thermal conductivities of polycrystalline γ-CuI thin film at room temperature. It was the first time that the in- and cross-plane thermal conductivity of γ-CuI thin films have been reported. The experimental results have shown that both in- and cross-plane thermal conductivities of the γ-CuI thin films were even lower than that of glass. Such low cross- and in-plane thermal conductivity values at room temperature have been associated with heavy element iodine, which leads to an increased phonon-scattering at grain boundaries due to the polycrystalline structure of the γ-CuI thin films. The observed low thermal conductivity values are extremely beneficial for the thermoelectric properties of γ-CuI thin films, which by far makes γ-CuI the most efficient, transparent and flexible p-type material for thermoelectric energy conversion at room temperature.

(2) Local thermal conductivity distribution of film-on-substrate structures

This thesis presents a novel 3ω Microscopy technique to quantitatively determine the local cross-plane thermal conductivities of thin-film-on-substrate systems. In order to satisfy the demand for high-spatially resolving techniques to quantitatively analyze thin film materials concerning their local thermal characteristic, the macroscopic 3ω method has been transferred to the microscopic level by combining the AFM with our extended differential 3ω method, which has never been reported in literature before.

It has been shown that the key parameter for the quantitative thermal conductivity determination is the heating power, which is dissipated into the thin film sample. It is crucial to determine the absolute local thermal conductivity $k_{f,local}$ value for every position within the corresponding 3ω Microscopy image and thereby enable the quantitative thermal conductivity analysis. An experimental method and a simplified two-dimensional FEM model were demonstrated to obtain the rms value of the heating power. For the 3ω Microscopy measurements, the heating power was assumed as a constant value that does not change with the thermal conductivity of the investigated materials.

It was the first time that the local thermal conductivities of γ-CuI and AlN thin films were quantitatively measured as a function of film thickness. The spatially-resolved 3ω Microscopy images demonstrated that heat transport predominantly takes place at the crystallite boundaries at the surface of γ-CuI and AlN films and significantly changes as the film thickness increases. The thinnest γ-CuI and AlN films exhibited short, narrow and contorted paths of high thermal conductivity, whereas the thicker γ-CuI and AlN films showed broad and straight paths of high thermal conduction, leading to considerably higher average film thermal conductivity values. The narrow and contorted high thermal conductive paths showed an increased potential in phonon-scattering, compared to wide

and straight high conductive paths, which resulted in an impaired and reduced thermal conduction.

Furthermore, the average film thermal conductivity values obtained by 3ω Microscopy are in good agreements with cross-plane values, obtained by the macroscopic 3ω technique. According to these results, it can be concluded that the novel 3ω Microscopy is capable to simultaneously map the topography and absolute local thermal conductivity of low and medium thermal conductive thin films, such as γ-CuI and AlN within a spatial resolution in the sub-micrometer range.

To summary, this thesis made good progress and improvements towards the thermal characterization and understanding of heat conduction in the cross- and in-plane direction of polycrystalline thin films by:

- Modifying and implementing the differential multi-heater 3ω technique to measure both cross- and in-plane thermal conductivities of thin films simultaneously, without changing the sample during the measurement process, in order to investigate the thickness-dependency of their thermal conductivity values.

- Studying the effects of crystallinity, grain/surface crystallite sizes, and interfacial structures of AlN and γ-CuI films on their cross- and in-plane thermal conductivities as a function of film thickness.

- Developing and improving the 3ω Microscopy for thin films to extend the research field of thin film thermal characterization techniques. It combined the advantageous of both conventional 3ω method and AFM technology to quantitatively study the heat transport of thin film materials. The 3ω Microscopy has been proven to provide additional experimental findings, which cannot be detected by conventional thermal characterization methods like SThM or the macroscopic 3ω technique. Finally, not only its spatially-resolved quantitative local thermal characterization, but also its

nondestructive characteristic and the fact that a preliminary sample preparation is not needed, making the 3ω Microscopy an alternative thermal characterization technique.

8.2. Future Work

Although this thesis provides new approaches for thermal measurement techniques and useful insights about the heat conduction in both cross- and in-plane directions of thin films, there are still a number of improvements and future work that could be pursued. The recommended fields of future work are listed below:

- Development of an analytical solution for measuring the thermal conductivity of multilayer structures with a bottom-heater-configuration, where the heater is placed between two films, by applying the differential 3ω approach. These bottom-heater-configurations are extremely useful, especially if the 3ω heater structure cannot be deposited on top of the investigated thin film. Additionally, this configuration is also beneficial for studying the influence of different capping or protective layers on top of thermoelectric or heat conductor films on their thermal conductivity, as the underlying heater structure does not change. Therefore, reproducibility and accuracy of the 3ω measurements can be enhanced as the boundary resistance between the metal heater, film and substrate is negligible. However, the 3ω bottom-heater-geometry has only been studied numerical using FEM simulations and suitable analytical heat conduction models would be beneficial, in order to implement a 3ω bottom-heater-measurement technique [1].

- Temperature-dependent 3ω measurements of thin films would be useful to analyze the cross- and in-plane thermal conductivities as a function of ambient temperature. These investigations are extremely interesting for thermoelectric γ-CuI thin films, in order to further increase its thermoelectric ZT-value. However, Yang *et al*. [2] reported that it is not simple to increase the ZT-value of γ-CuI films immediately by increasing the operation temperature due to its insufficient thermal stability at temperatures above

350 K, because higher temperatures can result in degraded electrical conductivity of γ-CuI [2].

- In order to expand the amount of high-spatially resolving techniques to study the locally quantitative thermoelectric properties, such as electrical and thermal conductivity, the 3ω Microscopy technique should be combined with electrical AFM methods, such as a conductive atomic force microscopy (C-AFM). Similar to the 3ω Microscopy method, this combined measurement technique could be helpful to further improve the efficiency of thermoelectric devices based on thin film materials.

- Advanced FEM simulations of the 3ω Microscopy setup are needed to further study the interaction between thermo-resistive AFM probe and the investigated thin film sample (e.g. interface resistance, effective contact area, tip wear). FEM simulations are also easy and cheap to design and test suitable geometries and materials for new thermo-resistive AFM probes (FIB modified probes), in order to improve the thermal resolution and reduce tip-wear of the 3ω Microscopy method. Furthermore, the 3ω Microscopy measurements assumed the dissipated heating power as a constant value. To further increase the accuracy of this thermal measurement technique, the heating power must be considered as function of the samples' thermal conductivity value. Therefore, the dissipated heating power as a function of the samples' thermal conductivity should be continued by using advanced FEM models.

8.3. References

[1] M. Feuchter, C. Jooss, M. Kamlah, The 3ω-method for thermal conductivity measurements in a bottom heater geometry, Physica status solidi A 213 (3) (2016) 649–661.

[2] C. Yang, D. Souchay, M. Kneiß, M. Bogner, H.M. Wei, M. Lorenz, O. Oeckler, G. Benstetter, Y.Q. Fu, M. Grundmann, Transparent flexible thermoelectric material based on non-toxic earth-abundant p-type copper iodide thin film, Nature communications 8 (2017) 16076.

Appendix

A. Modified Besselfunction

Modified Besselfunction of order zero K_0:

Detailed description in Ref. [1] (Appendix 3, page 109)

$$K_0(z) = -\left(\ln\left(\frac{1}{2}z\right) + \varrho\right)\cdot I_0(z) + \left(\frac{1}{2}z\right)^2 + \left(1+\frac{1}{2}\right)\cdot\frac{\left(\frac{1}{2}z\right)^4}{(2!)^2} + \left(1+\frac{1}{2}+\frac{1}{3}\right) \cdot\frac{\left(\frac{1}{2}z\right)^6}{(3!)^2} + \cdots \tag{A.1}$$

Where $\varrho \approx 0.57722$ is the Euler-Mascheroni constant [2] and $I_0(z)$ is given by:

$$I_0(z) = \sum_{r=0}^{\infty}\frac{\left(\frac{1}{2}z\right)^{2r}}{r!\,\Gamma(r+1)} \tag{A.2}$$

$$\Gamma(x) = \lim_{n\to\infty}\frac{n!\,n^{x-1}}{x\cdot(x+1)\cdot(x+2)\cdot\cdots\cdot(x+n-1)} \tag{A.3}$$

Details about approximate solution:

The integral in Eq. (3.19) has no direct analytical closed form. To obtain an approximate solution, Cahill [3] proposed to analyze its limits, when the thermal penetration depth λ is much larger than the metal strip's half-width b ($\lambda \gg b$) and when the thermal penetration depth is much smaller than the half-width b of the metal strip ($\lambda \ll b$). Therefore, the average amplitude of the heater's thermal oscillation $\Delta T_{2\omega|avg}$ as a function of heating frequency f can be divided into a linear regime ($\lambda \gg b$) at low frequencies and a planar regime ($\lambda \ll b$) at high frequencies [3]. The transition regime can be defined between these two cases.

For the linear regime, Borca-Tasciuc *et al.* [4] suggested that $\lambda/b > 5$ in order to keep measurement errors of the 3ω method under 1%. As presented in Figure 3.7, the linear regime is that part where the in-phase (real part) temperature oscillation $\Delta T_{2\omega}$ decreases linearly as a function of thermal excitation frequency 2ω and where the out-of-phase (imaginary part) temperature oscillations component has a constant negative value. This regime is defined within the range of low frequencies, if the thermal penetration depth is much larger compared to the half-width of the heater ($\lambda \gg b$) [3]. In this case, the wave number of the thermal oscillation is defined over a domain such that $1/\lambda < \eta < 1/b$ [5]. Then the upper limit of the integral in Eq. (3.19) can be replaced by $1/b$. Additionally, $\sin(\eta b)/\eta b$ can be evaluated at the limit where b tends towards 0 [3]:

$$\lim_{b\to 0} \frac{\sin(\eta b)}{\eta b} = 1 \qquad \text{(A.4)}$$

After these, the approximated solution of Eq. (3.19) is given by

$$\Delta T_{2\omega|avg} = \frac{P_l}{\pi k}\int_0^{1/b} \frac{1}{\sqrt{\eta^2+q^2}}\cdot d\eta \tag{A.5}$$

$$= \frac{P_l}{\pi k}\cdot \ln\left|\eta+\sqrt{\eta^2+q^2}\right|_0^{1/b} = \frac{P_l}{\pi k}\left[\ln\left|\frac{1}{b}+\sqrt{\frac{1}{b^2}+q^2}\right| - \ln|q|\right]$$

$$= \frac{P_l}{\pi k}\left[\ln\left(\frac{1}{bq}+\sqrt{\frac{1}{(bq)^2}+1}\right)\right] = \frac{P_l}{\pi k}\left[\ln\left(\frac{1+\sqrt{1+bq^2}}{bq}\right)\right]$$

$$= \frac{P_l}{\pi k}[-\ln(bq)+\ln(2)] = \frac{P_l}{\pi k}\left[-\ln\left(b\left(\frac{a}{\mathrm{i}2\omega}\right)^{-1/2}\right)+\ln(2)\right]$$

$$= \frac{P_l}{\pi k}\left[-\frac{1}{2}\ln\left(b^2\left(\frac{a}{\mathrm{i}2\omega}\right)^{-1}\right)+\ln(2)\right]$$

$$= \frac{P_l}{\pi k}\left[-\frac{1}{2}\ln\left(b^2\frac{\mathrm{i}2\omega}{a}\right)+\ln(2)\right]$$

$$= \frac{P_l}{\pi k}\left[-\frac{1}{2}\ln(2\omega)-\frac{1}{2}\ln\left(\frac{\mathrm{i}b^2}{a}\right)+\ln(2)\right]$$

$$= \frac{P_l}{\pi k}\left[-\frac{1}{2}\ln(\omega)-\frac{1}{2}\ln\left(\frac{\mathrm{i}b^2}{a}\right)+-\frac{1}{2}\ln(2)+\ln(2)\right]$$

$$= \frac{P_l}{\pi k}\left[-\frac{1}{2}\ln(\omega)-\frac{1}{2}\ln\left(\frac{\mathrm{i}b^2}{a}\right)+\mathrm{const}\right]$$

Where the constant can be written as:

$$\mathrm{const} = -\frac{1}{2}\ln(2)+\ln(2) = \frac{1}{2}\ln(2) \tag{A.6}$$

Detailed solution for the spatial and temporal temperature distribution of a line-heater is given by [3]:

$$T(r,t) = \frac{P_l}{k\pi}K_0(qr)\cdot e^{i2\omega t} \tag{A.7}$$

where K_0 is the zeroth-order-modified Bessel function. For very small arguments of the modified Bessel function the exact analytical description can be approximated as

demonstrated by Cahill *et al*. [1]. If the thermal penetration depth is much larger compared to the half-width of the heater or the distance from the heater r ($\lambda \gg r$) [3], K_0 can be approximated by neglecting terms of higher order. Finally, the amplitude of the line heater's temperature oscillation can be approximated by [3,6]:

$$\Delta T_{2\omega|avg} = \frac{P_l}{\pi k}\left[-\ln\left[\left(\frac{a}{\mathrm{i}2\omega}\right)^{-1/2}\cdot r\right] + \ln(2) - \varrho\right] \tag{A.8}$$

$$= \frac{P_l}{\pi k}\left[-\frac{1}{2}\ln\left[\left(\frac{a}{\mathrm{i}2\omega}\right)^{-1}\cdot r^2\right] + \ln(2) - \varrho\right]$$

$$= \frac{P_l}{\pi k}\left[-\frac{1}{2}\left[\ln\left(\frac{r^2}{a}\right) + \ln(\mathrm{i}2\omega)\right] + \ln(2) - \varrho\right]$$

$$= \frac{P_l}{\pi k}\left[-\frac{1}{2}[\ln(r^2) - \ln(a)] - \frac{1}{2}\ln(\mathrm{i}2\omega) + \ln(2) - \varrho\right]$$

$$= \frac{P_l}{\pi k}\left[\frac{1}{2}[\ln(a) - \ln(r^2)] - \frac{1}{2}\ln(\mathrm{i}2\omega) + \ln(2) - \varrho\right] =$$

$$= \frac{P_l}{\pi k}\left[\frac{1}{2}\ln\left(\frac{a}{r^2}\right) - \frac{1}{2}\ln(2\omega) - \frac{1}{2}\ln(\mathrm{i}) + \ln(2) - \varrho\right]$$

$$= \frac{P_l}{\pi k}\left[\frac{1}{2}\ln\left(\frac{a}{r^2}\right) - \frac{1}{2}\ln(2\omega) - \frac{1}{2}\frac{\pi\mathrm{i}}{2} + \ln(2) - \varrho\right]$$

$$= \frac{P_l}{\pi k}\left[\frac{1}{2}\ln\left(\frac{a}{r^2}\right) - \frac{1}{2}\ln(2\omega) + \ln(2) - \varrho - \frac{\pi\mathrm{i}}{4}\right]$$

$$= \frac{P_l}{\pi k}\left[\frac{1}{2}\ln\left(\frac{k}{\rho c_p b^2}\right) - \frac{1}{2}\ln(2\omega) + \gamma\right] - \mathrm{i}\frac{P_l}{4k}$$

B. Thermal design rules

Tables A.1 to A.4 summarize the main approximations and design rules introduced in Chapters 3 and 4, which have been applied to measure the thermal conductivity of thin films using the differential 3ω method. The experimental design rules applied to keep measurement errors of the 3ω method below 1% and to perform thin film thermal conductivity measurements within the acceptable range of the various approximations are briefly discussed.

The 3ω measurements were performed by recording the amplitude of the 3ω voltage $V_{3\omega}(f)$ for heating frequencies, ranging from 100 to 1000 Hz. Thus, considering the typical values of the specific heat capacity $c_{p,Si}$ (711 $Jkg^{-1}K^{-1}$ [7]), the density ρ_{Si} (2330 kgm^{-3} [7]) and the thermal conductivity k_{Si} of Si (147 $Wm^{-1}K^{-1}$ [7]), the thermal wave propagates at a distance λ_s between 266 and 84 µm (using Eq. (3.13)) beneath the sample surface at frequencies between 100 and 1000 Hz.

In this thesis the thickness d_s of the Si substrate varies between 525 and 640 µm. For the cross- and in-plane measurements the heater-half width b was in the range between about 0.5 and 12.5 µm. The length of the metal heaters was constant with a value of 9 mm. The substrate thickness, penetration depth of the thermal wave, the heater-half width and length are the most critical parameters for the applied 3ω approximations.

Table A.1: Approximations and design rules of the 3ω film-on-substrate samples to study the cross- and in-plane thermal conductivities of thin films using the differential 3ω method. The design rules have been chosen to keep measurement errors at about 1%. In this thesis the frequency range of the heating current was defined to keep measurement errors at about 1% [3,4,8].

Approximation	**Design criteria**	d_s **[µm]**	l **[mm]**	b **[µm]**	**Heating current frequency f [Hz]**	
					100 (λ_s = 266 µm)	**1000 (λ_s = 84 µm)**
Substrate is semi-infinite	$\frac{d_s}{\lambda_s} > 2$	525	-	-	2.0	6.3
		640	-	-	2.4	7.6
Heater is infinitely long	$\frac{l}{d_s} > 4.7$	525	9	-	17.1	17.1
		640	9	-	14.1	14.1
Substrate sees heater as line-source	$\frac{\lambda_s}{b} > 5$	-	-	0.5	532	168
		-	-	12.5	21.3	6.7

One of the most important conditions required to use the one-dimensional heat conduction model is that the heater width must be wide (cross-plane) or narrow (in-plane) compared to the investigated film thickness, in order to study both the cross- and in-plane thermal

conductivity (see Section 3.3.2). Eq. (3.30) and Eq. (3.38) provide the design rules for the cross- and in-plane thermal conductivity, respectively. Tables A.2 and A.3 show that in both cases most of the values are in an acceptable range of the one-dimensional heat flow approximation. However, only one value for the 70 nm γ-CuI is slightly higher than the design criteria, but is still in a tolerable range for the in-plane measurement, as the experimental data did not show any noticeable deviations or errors.

Table A.2: Design criteria (see Eq. 3.30) of the AlN and γ-CuI film-on-substrate samples to determine the cross-plane thermal conductivities using the differential 3ω method [3,4,8].

Thin film material	$\boldsymbol{b}$ **[µm]**	$\boldsymbol{d_f}$ **[nm]**	$\boldsymbol{k_{f\perp}}$ **[Wm^{-1}K^{-1}]**	$\boldsymbol{k_{f\parallel}}$ **[Wm^{-1}K^{-1}]**	$\boldsymbol{\frac{b}{d_f}\left(\frac{k_{f\perp}}{k_{f\parallel}}\right)^{1/2}}$ **[ ]**
AlN	12.5	99	3.2	10.2	70.7
	12.5	304	8.5	12.5	33.9
	12.5	511	11	13.9	21.7
	12.5	710	13.2	16.4	15.7
	12.5	1009	14.9	18.6	11.0
γ-CuI	12.5	70	0.45	0.5	169.4
	12.5	200	0.51	0.55	60.1
	12.5	400	0.56	0.59	30.4

Table A.3: Design criteria (see Eq. 3.38) of the AlN and γ-CuI film-on-substrate samples to determine the in-plane thermal conductivities using the differential 3ω method [4].

Thin film material	$\boldsymbol{b}$ **[µm]**	$\boldsymbol{d_f}$ **[nm]**	$\boldsymbol{k_{f\perp}}$ **[Wm^{-1}K^{-1}]**	$\boldsymbol{k_{f\parallel}}$ **[Wm^{-1}K^{-1}]**	$\boldsymbol{\frac{b}{d_f}\left(\frac{k_{f\perp}}{k_{f\parallel}}\right)^{1/2}}$ **[ ]**
AlN	0.5	99	3.2	10.2	2.8
	0.5	304	8.5	12.5	1.3
	0.5	511	11	13.9	0.8
	0.5	710	13.2	16.4	0.6
	0.5	1009	14.9	18.6	0.4
γ-CuI	0.5	70	0.45	0.5	6.7
	0.5	200	0.51	0.55	2.4
	0.5	400	0.56	0.59	1.2

Table A.4: Design criteria (see Eq. 3.40) of the AlN and γ-CuI film-on-substrate samples to determine the cross- and in-plane thermal conductivities using the differential 3ω method and to approximate the Si substrate as isothermal ($k_s \rightarrow \infty$) [4,8].

	d_s [nm]	$k_{f\perp}$ [$Wm^{-1}K^{-1}$]	$k_{f\parallel}$ [$Wm^{-1}K^{-1}$]	k_s [$Wm^{-1}K^{-1}$]	Error $\approx \frac{k_{f\perp} \cdot k_{f\parallel}}{k_s^2}$ [%]
AlN	99	3.2	10.2	141	0.1641
	304	8.5	12.5	141	0.5344
	511	11	13.9	141	0.7690
	710	13.2	16.4	141	1.0888
	1009	14.9	18.6	141	1.3939
γ-CuI	70	0.45	0.5	141	0.0011
	200	0.51	0.55	141	0.0014
	400	0.56	0.59	141	0.0016

C. Experimental uncertainty analysis

In order to determine the thermal conductivity of thin films using the 3ω method, several experimental parameters such as the 3ω voltage, film thickness and heating power must be individually measured by different methods and equipment. Each of these experimental methods and measurement devices possess a limited measurement accuracy. When mathematical operations are performed on these measured parameters to obtain the thermal conductivity of the investigated thin film, the uncertainties due to accuracy limitations of the measurement device or method propagates, which can influence the measured thermal conductivity results.

For a given function F defined in terms of uncorrelated parameters $\{x, y, \dots\}$ by a general equation $f\{x, y, \dots\}$, the contribution of the uncertainties related to parameters $\{x, y, \dots\}$ to the combined standard uncertainty, can be determined by partial derivatives of each of these experimental parameters [9].

If the variation in the measured parameters $\{x, y, ...\}$ are small, a first order approximation of the Taylor expansion can be used to obtain a reasonable estimation of the propagation of uncertainty from the experimental data. Therefore, the uncertainties of the 3ω measurements $\pm\Delta f$ are given by [10]:

$$\Delta f = \sqrt{\left(\frac{\partial f}{\partial x}\Delta x\right)^2 + \left(\frac{\partial f}{\partial y}\Delta y\right)^2 + \cdots} \tag{A.9}$$

Eq. (A.9) shows that the squared combined standard uncertainty Δf of the parameter of interest F, is a weighted sum of the squared standard uncertainties of the input experimental parameters $\{x, y, ...\}$. The partial derivatives are called sensitivity coefficients [10].

In Section 3.3.2.1, the cross- and in-plane thermal conductivity of thin films is determined by Eq. (3.33) and Eq. (3.34). Since the first harmonic voltage V_ω is (about) three orders of magnitude greater than the 3ω voltage $V_{3\omega}$ and the fact that a high-purity signal generator and digital lock-in amplifier utilized in the 3ω measurements are highly accurate, uncertainties in the first harmonic voltage V_ω, the power per unit length P_l, and the heating frequency f, are normally negligible [11]. Due to the accurate measurement of every 3ω heater structure, the heaters dimensions l and $2b$ can also be neglected. Furthermore, for the 3ω Microscopy technique the voltage V_ω, the power per unit length P_l, the thermal exchange radius r_{th}, and the frequency f were also neglected.

Therefore, in 3ω measurements, the uncertainty of the measured film thermal conductivity k_f mostly originates from the uncertainties of the measurement of the film thickness d_f, the metal heaters temperature coefficient of resistance α and the measured amplitude of the 3ω voltage $V_{3\omega}$.

Then considering uncertainties in the calibration of the thin film sample of interest and the reference sample (if needed), and assuming that the variables d_f, α and $V_{3\omega}$ are uncorrelated, the uncertainty Δk_f of our differential 3ω measurements can be estimated by [9]:

$$\Delta k_f = \sqrt{\left(\frac{\partial k_f}{\partial V_{3\omega}}\Delta V_{3\omega}\right)_{r+f}^{2} + \left(\frac{\partial k_f}{\partial V_{3\omega}}\Delta V_{3\omega}\right)_{r}^{2} + \left(\frac{\partial k_f}{\partial \alpha}\Delta \alpha\right)_{r+f}^{2} + \left(\frac{\partial k_f}{\partial \alpha}\Delta \alpha\right)_{r}^{2} + \left(\frac{\partial k_f}{\partial d_f}\Delta d_f\right)^{2}} \tag{A.10}$$

Table A.5 lists the partial derivatives of the differential 3ω measurements considered for the uncertainty analysis as well as their corresponding sensitivity coefficients.

Table A.5: Partial derivatives for the uncertainty propagation of the differential 3ω method.

Coefficient of sensitivity	Partial derivative
$\left(\frac{\partial k_f}{\partial V_{3\omega}}\right)_{r+f}$	$-\frac{d_f}{4}\left(\frac{b}{P_l \cdot \alpha \cdot V_\omega}\right)_{r+f}\left[\left(\frac{V_{3\omega} \cdot b}{P_l \cdot \alpha \cdot V_\omega}\right)_{r+f} - \left(\frac{V_{3\omega} \cdot b}{P_l \cdot \alpha \cdot V_\omega}\right)_{r}\right]^{-2}_{avg}$
$\left(\frac{\partial k_f}{\partial V_{3\omega}}\right)_{r}$	$\frac{d_f}{4}\left(\frac{b}{P_l \cdot \alpha \cdot V_\omega}\right)_{r}\left[\left(\frac{V_{3\omega} \cdot b}{P_l \cdot \alpha \cdot V_\omega}\right)_{r+f} - \left(\frac{V_{3\omega} \cdot b}{P_l \cdot \alpha \cdot V_\omega}\right)_{r}\right]^{-2}_{avg}$
$\left(\frac{\partial k_f}{\partial \alpha}\right)_{r+f}$	$\frac{d_f}{4}\left(\frac{V_{3\omega} \cdot b}{P_l \cdot \alpha^2 \cdot V_\omega}\right)_{r+f}\left[\left(\frac{V_{3\omega} \cdot b}{P_l \cdot \alpha \cdot V_\omega}\right)_{r+f} - \left(\frac{V_{3\omega} \cdot b}{P_l \cdot \alpha \cdot V_\omega}\right)_{r}\right]^{-2}_{avg}$
$\left(\frac{\partial k_f}{\partial \alpha}\right)_{r}$	$-\frac{d_f}{4}\left(\frac{V_{3\omega} \cdot b}{P_l \cdot \alpha^2 \cdot V_\omega}\right)_{r}\left[\left(\frac{V_{3\omega} \cdot b}{P_l \cdot \alpha \cdot V_\omega}\right)_{r+f} - \left(\frac{V_{3\omega} \cdot b}{P_l \cdot \alpha \cdot V_\omega}\right)_{r}\right]^{-2}_{avg}$
$\left(\frac{\partial k_f}{\partial d_f}\right)$	$\frac{1}{4}\left[\left(\frac{V_{3\omega} \cdot b}{P_l \cdot \alpha \cdot V_\omega}\right)_{r+f} - \left(\frac{V_{3\omega} \cdot b}{P_l \cdot \alpha \cdot V_\omega}\right)_{r}\right]^{-1}$

Although the sample preparation process results in repeatable and uniform 3ω heater structures, small differences in the heater width, length and the temperature coefficient of resistance are always present from one sample to another and cannot be avoided. Therefore, these parameters are measured separately for every film-on-substrate sample, as demonstrated in Section 4.3.1.3. Therefore, it is obvious that the uncertainty of the film thermal conductivity strongly depends on the investigated film-on-substrate sample. One example of the uncertainty analysis for the cross-plane thermal conductivity measurement of a γ-CuI thin

film with a thickness of 200 nm is demonstrated in Table A.6. For this example the heating power per unit length P_l (3.99 and 4.01 Wm^{-1}), the heater half-width b (12.14 and 11.92 µm) and first harmonic voltage V_ω (1.51 V) of the γ-CuI film sample and the Si_3N_4 reference sample must be known.

Table A.6: Example of an experimental uncertainty analysis of a 200 nm thin γ-CuI thin film investigated by the differential 3ω method.

	Value	Sensitivity coefficient		Standard deviation		Weighted uncertainty
$\boldsymbol{V_{3\omega,r+f}}$	334 µV	$\left(\frac{\partial k_f}{\partial V_{3\omega}}\Delta V_{3\omega}\right)_{r+f}$	-63.6×10^3	$\Delta V_{3\omega,r+f}$	1.0×10^{-9}	1.31×10^{-14}
$\boldsymbol{V_{3\omega,r}}$	297 µV	$\left(\frac{\partial k_f}{\partial V_{3\omega}}\Delta V_{3\omega}\right)_{r}$	62.8×10^3	$\Delta V_{3\omega,r}$	1.5×10^{-7}	9.55×10^{-3}
$\boldsymbol{\alpha_{r+f}}$	0.00434 K^{-1}	$\left(\frac{\partial k_f}{\partial \alpha}\Delta\alpha\right)_{r+f}$	4.90	$\Delta\alpha_{r+f}$	1.5×10^{-7}	9.41×10^{-3}
$\boldsymbol{\alpha_r}$	0.00430 K^{-1}	$\left(\frac{\partial k_f}{\partial \alpha}\Delta\alpha\right)_{r}$	-4.33	$\Delta\alpha_r$	9.9×10^{-6}	4.85×10^{-4}
$\boldsymbol{d_f}$	200 nm	$\left(\frac{\partial k_f}{\partial d_f}\Delta d_f\right)$	13.1×10^{-6}	Δd_f	9.6×10^{-6}	4.16×10^{-4}
$\boldsymbol{k_f}$	0.51 $Wm^{-1}K^{-1}$			Δk_f		1.34×10^{-2}

The last column of Table A.6 shows the contribution of the weighted uncertainty of each experimental variable to the standard overall uncertainty of k_f. For this example, the propagation of uncertainty from the input experimental variables result in an overall uncertainty of $\Delta k_f = 1.34 \times 10^{-2}$, which is equal to 2.63%. For the other 3ω film-on-substrate samples, the combined standard uncertainty was always below 3%, which is tolerable for differential 3ω measurements [8].

D. Experimental parameters

The experimental parameters and values of the 3ω measurements corresponding to the macroscopic 3ω method and the 3ω Microscopy technique are listed in Tables A.7 to A.14 and Tables A.15 to A.16, respectively.

Table A.7: Experimental values of the macroscopic 3ω method to determine the cross-plane thermal conductivity of SiO_2 thin films using Eq. (3.33).

Parameter	Unit	SiO_2 (cross-plane)				
		1	2	3	4	5
$\boldsymbol{d_f}$	nm	92	291	499	690	1002
$\boldsymbol{P}$	mW	30.1	30.6	30.6	31.9	31.5
$\boldsymbol{\Delta T_f}$	K	0.0527	0.146	0.237	0.377	0.504
$\boldsymbol{2b}$	µm	6.64	6.74	6.87	6.18	6.33
$\boldsymbol{l}$	mm	9.0	9.0	9.0	9.0	9.0

Table A.8: Experimental values of the macroscopic 3ω method to determine the cross-plane thermal conductivity of Si_3N_4 thin films using Eq. (3.33).

Parameter	Unit	Si_3N_4 (cross-plane)				
		6	7	8	9	10
$\boldsymbol{d_f}$	nm	298	500	601	698	1001
$\boldsymbol{P}$	mW	57.8	56.6	57.4	55.9	55.2
$\boldsymbol{\Delta T_f}$	K	0.396	0.429	0.451	0.464	0.597
$\boldsymbol{2b}$	µm	6.07	6.07	6.44	6.17	
$\boldsymbol{l}$	mm	9.0	9.0	9.0	9.0	9.0

Table A.9: Experimental values of the macroscopic 3ω method to determine the cross-plane thermal conductivity of AlN thin films using Eq. (3.33).

Parameter	Unit	AlN (cross-plane)				
		11	12	13	14	15
$\boldsymbol{d_f}$	nm	99	304	511	710	1009
$\boldsymbol{P}$	mW	45.5	55.3	45.2	56.1	44.6
$\boldsymbol{\Delta T_f}$	K	0.0262	0.0350	0.0383	0.0529	0.0548
$\boldsymbol{2b}$	µm	5.92	6.25	6.10	6.38	6.10
$\boldsymbol{l}$	mm	9.0	9.0	9.0	9.0	9.0

Table A.10: Experimental values of the macroscopic 3ω method to determine the in-plane thermal conductivity of AlN thin films using Eq. (3.33).

Parameter	Unit	AlN (in-plane)				
		11	12	13	14	15
$\boldsymbol{d_f}$	nm	99	304	511	710	1009
$\boldsymbol{P}$	mW	161.5	160.5	158.2	158.1	163.3
$\boldsymbol{\Delta T_f}$	K	0.176	0.439	0.646	0.759	0.985
$\boldsymbol{2b}$	µm	0.99	0.99	1.0	1.0	1.0
$\boldsymbol{l}$	mm	9.0	9.0	9.0	9.0	9.0

Table A.11: Experimental values of the macroscopic 3ω method to determine the cross-plane thermal conductivity of γ-CuI thin films using Eq. (3.34).

Parameter	Unit	γ-CuI (cross-plane)		
		16	17	18
$\boldsymbol{d_f}$	nm	70	200	400
$\boldsymbol{P}$	mW	35.3	35.9	35.6
$\Delta\boldsymbol{T_f}$	K	0.0247	0.0649	0.114
$\boldsymbol{2b}$	µm	25.01	24.28	25.05
$\boldsymbol{l}$	mm	9	9	9

Table A.12: Experimental values of the macroscopic 3ω method to determine the in-plane thermal conductivity of γ-CuI thin films using Eq. (3.34).

Parameter	Unit	γ-CuI (in-plane)		
		16	17	18
$\boldsymbol{d_f}$	nm	70	200	400
$\boldsymbol{P}$	mW	45.2	47.1	47.1
$\Delta\boldsymbol{T_f}$	K	0.72	1.91	3.56
$\boldsymbol{2b}$	µm	0.98	1.0	0.99
$\boldsymbol{l}$	mm	9	9	9

Table A.13: Experimental values of the macroscopic 3ω method to determine the cross-plane thermal conductivity of Si_3N_4 reference films using Eq. (3.33).

Parameter	Unit	Si_3N_4 (reference)
		19
$\boldsymbol{d_f}$	nm	200
$\boldsymbol{P}$	mW	36.1
$\Delta\boldsymbol{T_f}$	K	0.055
$\boldsymbol{2b}$	µm	23.84
$\boldsymbol{l}$	mm	9

Table A.14: Experimental values of the macroscopic 3ω method to determine the in-plane thermal conductivity of Si_3N_4 reference films using Eq. (3.33).

Parameter	Unit	Si_3N_4 (reference)
		19
$\boldsymbol{d_f}$	nm	200
$\boldsymbol{P}$	mW	47.4
$\Delta\boldsymbol{T_f}$	K	1.396
$\boldsymbol{2b}$	µm	0.99
$\boldsymbol{l}$	mm	9

Table A.15: Experimental values of the 3ω Microscopy technique to determine the local cross-plane thermal conductivity of γ-CuI thin films using Eq. (4.3).

Parameter	Unit	γ-CuI (3ω Microscopy)					
		16		17		18	
		M1	M2	M1	M2	M1	M2
d_f	nm	70	70	200	200	400	400
P/l	Wm^{-1}	0.4	0.4	0.4	0.4	0.4	0.4
ΔT_f	K	1.22	0.452	2.76	1.14	5.52	2.05
r_{th}	nm	100	100	100	100	100	100

Table A.16: Experimental values of the 3ω Microscopy technique to determine the local cross-plane thermal conductivity of AlN thin films using Eq. (4.3).

Parameter	Unit	AlN (3ω Microscopy)					
		12		13		14	
		M3	M4	M3	M4	M3	M4
d_f	nm	304	304	511	511	710	710
P/l	Wm^{-1}	0.4	0.4	0.4	0.4	0.4	0.4
ΔT_f	K	0.276	0.077	0.417	0.114	0.546	0.144
r_{th}	nm	100	100	100	100	100	100

E. FEM Simulation

The quantitative local thermal conductivity $k_{f,local}$ of thin films can be determined from Eq. (4.3), if the amplitude of the heating power P_l applied in the thin film is known. Therefore, a simplified two-dimensional FEM model of the 3ω Microscopy setup, including the thermo-resistive probe and the film-on-substrate sample was designed (see Figure 7.2 and Figure A.1). Numerical FEM simulations within the time-domain were performed to study the dissipated heating power value as a function of the sample's thermal conductivity. The FEM simulations were developed and performed using COMSOL Multiphysics software. Figure A.1(a) shows the geometry of the two-dimensional FEM model. A thin film with a thickness of 100 nm was deposited on a Si substrate. In order to study the dissipated heating power value as a function of the film's thermal conductivity k_f was varied between 0.1 and 10000 $Wm^{-1}K^{-1}$.

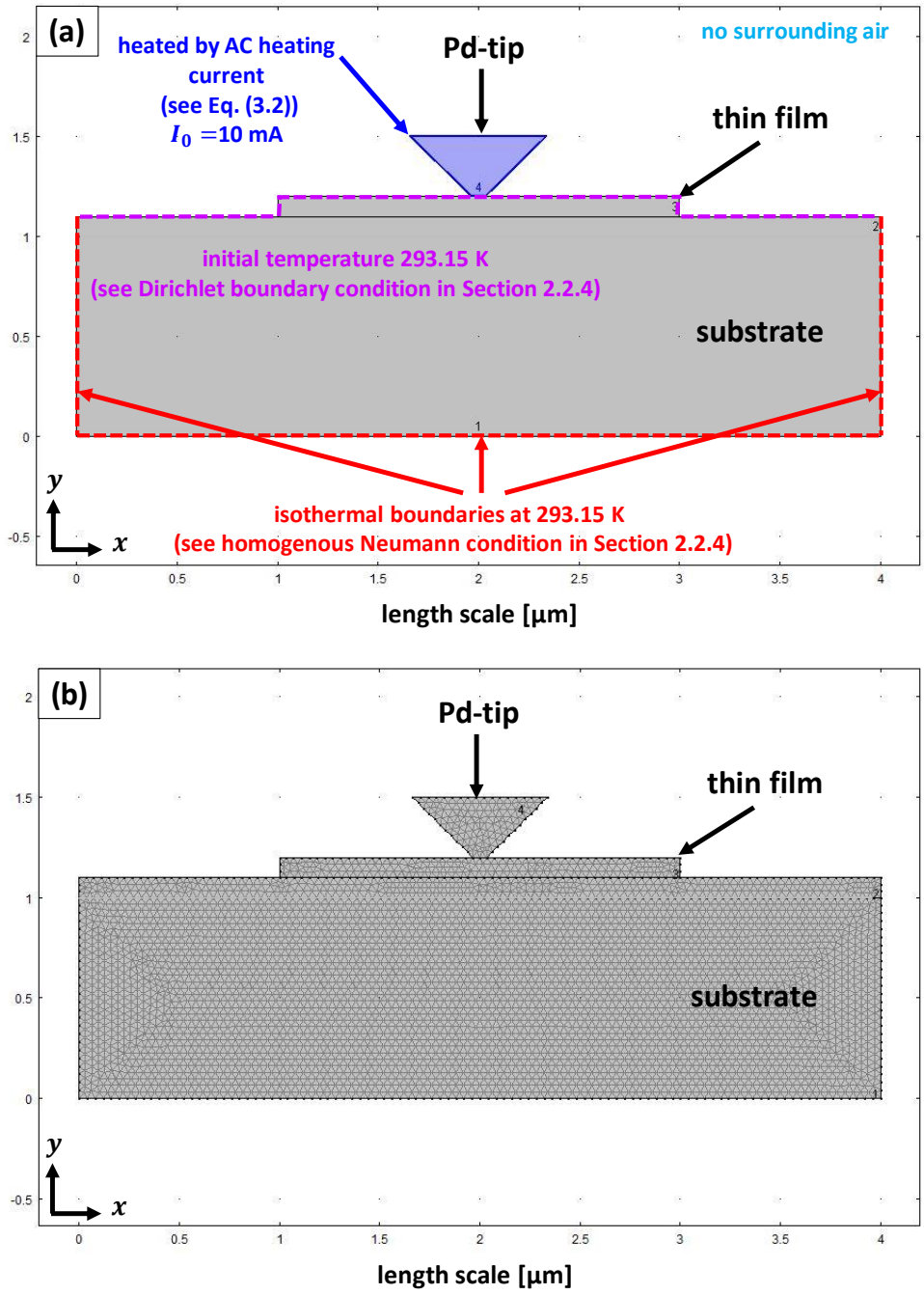

Figure A.1: Simplified two-dimensional FEM simulation of the 3ω Microscopy setup, including the thermo-resistive Pd-tip and the investigated film-on-substrate structure: (a) FEM model including the heat source and boundary conditions; (b) mesh structure of the film-on-substrate sample generated using COMSOL Multiphysics software. The Pd-tip was heated by an AC heating current (see Eq. (3.3)) and both sides and the bottom of the FEM model were assumed as isothermal (293.15 K).

For the density ρ_f and specific heat capacity $c_{p,f}$ of the thin film we defined values of 2200 kgm^{-3} and 730 $Jkg^{-1}K^{-1}$, respectively. The Si substrate has a constant thermal

conductivity k_s = 147 $Wm^{-1}K^{-1}$ [7], density ρ_s = 2330 kgm^{-3} [7] and specific heat capacity $c_{p,s}$ = 711 $Jkg^{-1}K^{-1}$ [7]. For the Pd-tip we used values of k_h = 72 $Wm^{-1}K^{-1}$, ρ_h = 12023 kgm^{-3} and specific heat capacity $c_{p,h}$ = 240 $Jkg^{-1}K^{-1}$.

After defining the basic geometries, a mesh for the investigated film-on-substrate structure and the thermo-resistive Pd-tip was applied, as illustrated in Figure A.1(b). For our FEM simulations we used an extremely fine mesh structure (highest mesh element density of COMSOL Multiphysics software) to assure a sufficiently high accuracy within the contact area between the thermo-resistive tip and the thin film. The value of the heating current applied to the metallic line was 10 mA. The frequency for 3ω Microscopy measurements was chosen to be 1000 Hz (see Section 7.2.1). Figure A.1(a) illustrates the boundary conditions and heat source of the FEM model. The thin film, substrate and Pd-tip were considered as isotropic. Furthermore, ideal thermal contacts between the thin film and substrate were assumed. As introduced in Section 2.3, radiation of the Pd-tip (3ω heater) can be neglected [3,12].

Numerical Simulations were performed using the Joule heating module of the COMSOL Multiphysics software. The basic equations of the Joule heating model, applied for the Pd-tip and the film-on-substrate structure can be written as (see also differential equation of heat conduction, Eq. (2.11)) [13]:

$$\frac{\partial}{\partial x}\left(k_f \frac{\partial T_f}{\partial x}\right) + \frac{\partial}{\partial y}\left(k_f \frac{\partial T_f}{\partial y}\right) - c_{p,f}\rho_f \frac{\partial T_f}{\partial t} = 0 \tag{A.11}$$

$$\frac{\partial}{\partial x}\left(\frac{\partial T_s}{\partial x}\right) + \frac{\partial}{\partial y}\left(\frac{\partial T_s}{\partial y}\right) - \frac{1}{a_s}\frac{\partial T_f}{\partial t} = 0 \tag{A.12}$$

$$\frac{\partial}{\partial x}\left(\frac{\partial T_h}{\partial x}\right) + \frac{\partial}{\partial y}\left(\frac{\partial T_h}{\partial y}\right) - \frac{1}{a_h}\frac{\partial T_h}{\partial t} + \frac{P(t)}{k_h} = 0 \tag{A.13}$$

where $P(t)$ is the time-dependent heating power (see Eq. (3.3)), a the diffusivity and k the thermal conductivity. The subscripts f, s, and h refer to the thin film, substrate and Pd-tip

(3ω heater), respectively. Results of the thermal conductivity-dependent heating power values obtained by FEM analysis are provided in Section 7.2.1.

F. References

[1] H.S. Carslaw, J.C. Jaeger, Conduction of heat in solids, 2nd ed., Clarendon, Oxford, (1959) 1-92.

[2] C.P. Chen, C. Mortici, New sequence converging towards the Euler–Mascheroni constant, Computers & Mathematics with Applications 64 (4) (2012) 391–398.

[3] D.G. Cahill, Thermal conductivity measurement from 30 to 750 K: The 3ω method, Review of Scientific Instruments 61 (2) (1990) 802–808.

[4] T. Borca-Tasciuc, A.R. Kumar, G. Chen, Data reduction in 3ω method for thin-film thermal conductivity determination, Review of Scientific Instruments 72 (4) (2001) 2139–2147.

[5] D. Koninck, Thermal Conductivity Measurements using the 3-Omega Technique: Application to Power Harvesting Microsystems, McGill University, Montréal, Canada (2008) 2-1 - 2-18.

[6] S.M. Lee, D.G. Cahill, Heat transport in thin dielectric films, Journal of Applied Physics 81 (6) (1997) 2590–2595.

[7] R. Hull, Properties of crystalline silicon, INSPEC, London, (1999) p. 58, 98.

[8] C. Dames, Measuring the Thermal Conductivity of Thin Films: 3 Omega and related Electrothermal Methods, Annual Review of Heat Transfer 16 (1) (2013) 7–49.

[9] S.J. Kline, F.A. McClintock, Describing uncertainties in single-sample experiments, Mechanical Engineering 75 (1) (1953) 3–8.

[10] I. Farrance, R. Frenkel, Uncertainty of Measurement: A Review of the Rules for Calculating Uncertainty Components through Functional Relationships, The Clinical Biochemist Reviews 33 (2) (2012) 49–75.

[11] J.P. Feser, Scalable Routes to Efficient Thermoelectric Materials, University of California, Berkeley Ph.D. thesis (2010) 62–63.

[12] M. Bogner, A. Hofer, G. Benstetter, H. Gruber, R.Y. Fu, Differential 3ω method for measuring thermal conductivity of AlN and Si3N4 thin films, Thin Solid Films 591 (2015) 267–270.

[13] M. Feuchter, C. Jooss, M. Kamlah, The 3ω-method for thermal conductivity measurements in a bottom heater geometry, Physica status solidi A 213 (3) (2016) 649–661.